Magnesium and Silicon Isotope Fractionation in Magma Oceans: Seeking New Constraints on Primitive Mantle Heterogeneity.

Bram de Winter

University College
University of Oxford

A thesis submitted for the degree of Doctor of Philosophy

Trinity 2026

Abstract

Understanding the processes controlling early Earth differentiation is essential for interpreting the present-day structure and composition of the mantle. In particular, crystallisation of a global magma ocean may have generated chemical and isotopic heterogeneity, the preservation of which remains debated. This thesis investigates Mg and Si isotope fractionation during magmatic processes. It aims to quantify the extent to which primordial mantle reservoirs could survive to the present day. A combined approach of high-temperature experiments, molecular dynamics (MD) simulations, and density functional theory (DFT) calculations is employed to constrain equilibrium isotope fractionation and the underlying structural controls of this process. Experimental results in basaltic systems show that mineral–melt Mg isotope fractionation at magmatic temperatures is small but measurable. Complementary atomistic simulations reveal that isotope fractionation in silicate melts is primarily governed by bond length and coordination number, with structural heterogeneity between melts and minerals playing a key role in generating non-zero fractionation. Extending this approach to lower-mantle conditions, MD and DFT calculations are used to determine Mg and Si isotope fractionation between bridgmanite and silicate melt at pressures of 40–80 GPa and temperatures up to 4000 K. These results show that pressure-induced structural differences between crystalline and molten phases generate measurable isotopic contrasts even at high temperatures. Crystallisation models incorporating these fractionation factors predict the development of isotopically distinct bridgmanite-rich cumulates and a residual melt, while comparison with the isotopic similarity between the Bulk Silicate Earth and the Moon constrains the volume of preserved primordial bridgmanite-rich material to ≤ 5 wt%. These results imply that large-scale primordial reservoirs were either not preserved or were efficiently mixed during mantle evolution. Overall, this thesis shows that stable Mg and Si isotopes place new constraints on the origin and evolution of Earth's deep mantle, providing a quantitative framework that links atomic-scale processes to planetary differentiation and indicating that large primordial reservoirs are unlikely to have been preserved.

Magnesium and Silicon Isotope Fractionation in Magma Oceans: Seeking New Constraints on Primitive Mantle Heterogeneity.



Bram de Winter

University College

University of Oxford

A thesis submitted for the degree of

Doctor of Philosophy

Trinity 2026

Acknowledgements

Completing this PhD has been both an intellectual and a personal journey. Over the past few years, I have had the opportunity to explore challenging questions in Earth and planetary science. This work would not have been possible without the support, guidance, and encouragement of many people, whom I would like to thank here.

First and foremost, I would like to thank my supervisor, **Andrew Walker**. Your guidance throughout this PhD has fundamentally shaped my scientific thinking. I am especially grateful for the time you took to meet with me in your office and for your support with my writing. I am grateful that you took a chance on a prospective PhD student with no computational experience and taught me to perform DFT calculations independently. Your critical and rigorous approach, together with your ability to dissect large planetary questions with outstanding foundational knowledge, has been immensely supportive throughout this project.

I am also deeply thankful to **Elena Melekhova** for her support, especially her assistance with experiments and career guidance. Following the classic motto, "Hardened in the training grounds, ready for the battlefield" (which still resonates with me after our first meetings), I remain grateful for her relentless encouragement and valuable advice, from the beginning of my PhD through to applying for postdoctoral positions.

I would also like to thank my unofficial third supervisor, **Prof. Tim Elliott**, from the University of Bristol. I greatly enjoyed our discussions, which often opened up new research questions and could inspire many future projects. Your extraordinary experience and knowledge of isotope and planetary systems deeply influenced my approach to research. This work would also not have been possible without the financial support of the ERC Advanced Grant NONUNE awarded to Tim.

I am also grateful to two collaborators from Bristol, **Xiao-Ning Liu** and **Isaac Onyett**. This work would not have been possible without your expertise and the time you invested in measuring Mg and Si isotopes from my experiments. Even with the lab delays, we produced valuable data that fuelled the work in this PhD.

Next, I would like to thank the technical staff and researchers from the University of Oxford who made the experimental (**Richard Thomas**) and analytical (**Andrew Matzen** and **Krystof Sokol**) components of this thesis possible.

I sincerely thank University College Oxford for its financial support. I am grateful for the Oxford-Radcliffe Scholarship that I received and for the travel

grants from University College that allowed me to present at conferences. In addition, I want to thank the Royal Astronomical Society (RAS) for their financial support for the travel grants.

Because I am concerned about missing some PhD students, I would like to acknowledge the entire postgraduate community of the Department of Earth Sciences at Oxford; you truly made me feel at home here. However, some people deserve special mention. My office mates: Rebekah, Justina, Asri, Bassam, Daniel, Ian, and Xiangying: thank you for making this journey far more enjoyable. **Justin Leung**, my fellow deep-Earth PhD student, thank you for making my time here so enjoyable. Even though you are a geophysicist, we could always find common ground and support each other in our deep-Earth PhD journeys. **Hannah Sanderson**, I really enjoyed our time together in the department and at conferences. Your advice and encouragement have always been a source of support for me. I also thank **Bei-Bei Morrison-Evans** for being my lab buddy during the first years of my PhD. **Lara Boudinot**, even though you are half the time looking for animals in Africa, you have always supported me. I also thank the members of the research groups that I have been part of (Planetary Science and ExPet), the Oxford Volleyball Team for four years of amazing accomplishments and countless memorable matches against other universities, and everyone who took part in the many space events that I organised.

Additionally, I would like to thank **Justin Leung** and **Rhiannon Ackland** for proofreading my thesis.

Finally, I am going to switch for a moment to my native language, Dutch:

Deze thesis draag ik op aan **mijn familie en Vera**, die mij gedurende mijn vier jaar in Oxford met eindeloos geduld en onvoorwaardelijke steun hebben bijgestaan, zowel in goede als in moeilijke tijden. Ik ben jullie ontzettend dankbaar; zonder jullie vertrouwen, aanmoediging en steun had ik dit niet kunnen bereiken.

In het bijzonder wil ik **Vera** bedanken. Dank je wel voor je geduld, je vertrouwen en de onvoorwaardelijke steun die je mij gedurende dit traject hebt gegeven. Je stond altijd voor me klaar, wist me moed in te spreken wanneer dat nodig was en hebt alle hoogte- en dieptepunten van dit avontuur met mij gedeeld. Dat heeft voor mij meer betekend dan ik in woorden kan uitdrukken.

Tot slot wil ik **mijn opa, Wim**, bedanken. Jouw fascinatie voor geologie en andere wetenschappen heeft mij al van jongs af aan geïnspireerd en mijn nieuwsgierigheid aangewakkerd. Hoewel je zelf nooit de kans hebt gehad om geologie te studeren, voelt het door de oprechte interesse die je altijd in mijn studie en onderzoek hebt getoond alsof je zelf bijna een half diploma hebt behaald. Ik hoop dat deze thesis jullie allemaal trots maakt.

Dank jullie wel voor alles.

Abstract [English version]

Understanding the processes controlling early Earth differentiation is essential for interpreting the present-day structure and composition of the mantle. In particular, crystallisation of a global magma ocean may have generated chemical and isotopic heterogeneity, the preservation of which remains debated. This thesis investigates Mg and Si isotope fractionation during magmatic processes. It aims to quantify the extent to which primordial mantle reservoirs could survive to the present day. A combined approach of high-temperature experiments, molecular dynamics (MD) simulations, and density functional theory (DFT) calculations is employed to constrain equilibrium isotope fractionation and the underlying structural controls of this process. Experimental results in basaltic systems show that mineral–melt Mg isotope fractionation at magmatic temperatures is small but measurable. Complementary atomistic simulations reveal that isotope fractionation in silicate melts is primarily governed by bond length and coordination number, with structural heterogeneity between melts and minerals playing a key role in generating non-zero fractionation. Extending this approach to lower-mantle conditions, MD and DFT calculations are used to determine Mg and Si isotope fractionation between bridgmanite and silicate melt at pressures of 40–80 GPa and temperatures up to 4000 K. These results show that pressure-induced structural differences between crystalline and molten phases generate measurable isotopic contrasts even at high temperatures. Crystallisation models incorporating these fractionation factors predict the development of isotopically distinct bridgmanite-rich cumulates and a residual melt, while comparison with the isotopic similarity between the Bulk Silicate Earth and the Moon constrains the volume of preserved primordial bridgmanite-rich material to ≤ 5 wt%. These results imply that large-scale primordial reservoirs were either not preserved or were efficiently mixed during mantle evolution. Overall, this thesis shows that stable Mg and Si isotopes place new constraints on the origin and evolution of Earth's deep mantle, providing a quantitative framework that links atomic-scale processes to planetary differentiation and indicating that large primordial reservoirs are unlikely to have been preserved.

Abstract [Dutch version]

Het begrijpen van hoe de aarde zich in haar vroege geschiedenis heeft gedifferentieerd, is belangrijk om de huidige structuur en samenstelling van de mantel te verklaren. Tijdens deze vroege fase kan een globale magma-oceaan zijn gekristalliseerd, waardoor chemische en isotopische verschillen zijn ontstaan. Het is echter nog onduidelijk in hoeverre deze vroege (primordiale) verschillen tot op heden bewaard zijn gebleven. In dit proefschrift wordt onderzocht hoe magnesium (Mg) en silicium (Si) isotopen fractioneren tijdens magmatische processen. Het doel is om te bepalen of en hoe lang zulke vroege mantelreservoirs behouden kunnen blijven. Hiervoor wordt een combinatie gebruikt van hogetemperatuurexperimenten, moleculair-dynamische simulaties (MD) en density-functional-theory-berekeningen (DFT). Met deze aanpak worden zowel de grootte van de isotopenfractionatie als de onderliggende structurele oorzaken bepaald. De experimenten laten zien dat Mg-isotopenfractionatie tussen mineralen en smelt bij magmatische temperaturen klein maar meetbaar is. Simulaties op atomaire schaal tonen aan dat deze fractionatie vooral wordt bepaald door bindingslengtes en coördinatiegetallen (het aantal naburige atomen rond een element). Omdat silicaatsmelten structureel chaotisch zijn, ontstaat hierdoor een kleine maar duidelijke isotopenfractionatie. Wanneer deze benadering wordt toegepast op de omstandigheden van de mantel van Aarde, laten de berekeningen zien dat Mg- en Si-isotopenfractionatie ook bij zeer hoge drukken (40–80 GPa) en temperaturen (tot 4000 K) aanwezig blijft. Ondanks de extreme temperaturen zorgen drukgeïnduceerde structurele verschillen tussen vaste en gesmolten fasen voor meetbare isotopische verschillen. Modellen van magma-oceaankristallisatie, waarin deze fractionatiefactoren zijn opgenomen, voorspellen dat er isotopisch verschillende bridgmanite-rijke structuren kunnen ontstaan. Door deze modelresultaten te vergelijken met de vrijwel gelijke isotopensamenstelling van de aarde en de maan, kan worden afgeleid dat slechts een zeer klein deel van dergelijk primordiaal materiaal bewaard is gebleven (maximaal $\leq \sim$5 wt%). Deze resultaten suggereren dat grote, oude mantelreservoirs waarschijnlijk niet intact zijn gebleven, maar in de loop van de tijd zijn gemengd. Samengevat laat dit proefschrift zien dat stabiele Mg- en Si-isotopen belangrijke nieuwe inzichten geven in de oorsprong en evolutie van de diepe aardmantel. Het werk verbindt processen op atomaire schaal met planetaire differentiatie en helpt beter te begrijpen hoe de aarde zich heeft ontwikkeld.

Contents

List of Figures **x**

List of Abbreviations **xii**

1 Introduction **1**

1.1 General Introduction 2
1.2 Background: From Planetary Accretion to Magma-Ocean Solidification 3
1.2.1 Magma Ocean Formation and Crystallisation 6
1.2.2 Preservation of primordial mantle reservoirs 8
1.2.3 Tracing primordial mantle heterogeneities with isotopic systems 9
1.3 Theoretical Framework of High-Temperature Isotope Fractionation . 10
1.3.1 Generalities 10
1.3.2 Gibbs free energy and equilibrium 12
1.3.3 α and β Fractionation Factor 13
1.3.4 Calculation of Fractionation Factor 13
1.3.5 Experimental Fractionation Factor 15
1.4 Magnesium Isotopes 15
1.4.1 Magnesium Geochemistry 15
1.4.2 Magnesium Stable Isotopes 16
1.4.3 Measurement of Mg Isotopes 16
1.4.4 Parameters Controlling Fractionation 16
1.4.5 Use in Earth Sciences 17
1.4.6 Magnesium Isotopic Fractionation at High Temperature . . . 19
1.5 Silicon Geochemistry and Isotopes 21
1.5.1 Silicon Geochemistry 21
1.5.2 Silicon Stable Isotopes 21
1.5.3 Measurement of Si Isotopes 22
1.5.4 Parameters Controlling Si Fractionation 22
1.5.5 Applications in Earth Sciences 23
1.5.6 High-Temperature Silicon Isotope Fractionation 23
1.6 Key Knowledge Gaps 25
1.7 Structure of the Thesis 27

2 Methodology – Computational **36**
2.1 Density functional theory . . . 39
2.1.1 Hohenberg–Kohn theorems . . . 40
2.1.2 Kohn–Sham approach . . . 41
2.1.3 Exchange–correlation functionals and approximations . . . 42
2.1.4 Choice of exchange–correlation functional for this study . . . 43
2.1.5 Bloch theorem . . . 43
2.1.6 Basis set . . . 44
2.1.7 CASTEP implementation . . . 44
2.2 Geometry optimisation . . . 46
2.2.1 Potential energy surface . . . 46
2.2.2 Geometry optimisation . . . 47
2.2.3 Optimisation algorithms . . . 48
2.2.4 Dispersion forces . . . 49
2.2.5 CASTEP implementation . . . 50
2.3 Lattice dynamics . . . 51
2.3.1 Vibrational motion in crystalline solids . . . 51
2.3.2 Harmonic approximation . . . 52
2.3.3 Dynamical matrix and phonon frequencies . . . 53
2.3.4 Isotope fractionation and vibrational properties . . . 54
2.3.5 Limitations of the harmonic approximation . . . 55
2.3.6 CASTEP implementation . . . 55
2.4 Molecular dynamics . . . 56
2.4.1 Moving atoms in the liquid state . . . 56
2.4.2 Ergodicity principle . . . 57
2.4.3 Equations of motion . . . 57
2.4.4 Thermodynamic particle ensembles . . . 58
2.4.5 Thermostats . . . 58
2.4.6 Snapshot techniques versus other techniques . . . 59
2.4.7 CASTEP implementation . . . 61

3 Methodology – Experiments **64**
3.1 Overview of Experimental Methods . . . 64
3.2 Stable Isotopes Petrological Experiments . . . 65
3.3 Experimental Objectives . . . 66
3.4 Experimental Setup . . . 67
3.4.1 Olivine capsules . . . 67
3.4.2 Natural crystal – melt interaction . . . 68
3.4.3 Growing forsterite crystals from bulk composition . . . 69

3.5 Starting Composition 69
3.6 Sample Holder 71
3.7 1 atm furnace experiments 71

4 The magnitude of equilibrium isotope fractionation 74
4.1 Introduction 77
4.2 Methods 80
4.2.1 Experiments 81
4.2.2 Analytical techniques 84
4.2.3 First-principles calculations 85
4.3 Results 87
4.3.1 Experimental run products 87
4.3.2 Experimental isotope analysis 89
4.3.3 Ab initio calculations 90
4.3.4 Comparison between experimental and theoretical results . . 97
4.4 Discussion 98
4.4.1 Assessment of isotopic equilibrium 98
4.4.2 Comparison with literature data for Mg isotopic fractionation between olivine and clinopyroxene in naturally occurring samples 100
4.4.3 Constraints on $\Delta^{26}Mg_{ol/melt}$ from experiments 103
4.5 Conclusions 104

5 Five-fold Mg in silicate melts drives non-zero Mg isotope fractionation 119
5.1 MD–DFT Modelling Framework 124
5.2 Magnesium isotope fractionation in silicate melt 126
5.3 Silicon isotope fractionation: bond-length dominated behaviour . . 128
5.4 A Structural–Chemical Framework for Mineral–Melt Isotope Fractionation 130

6 Mg–Si isotopes tightly constrain the primordial bridgmanite reservoirs 156
6.1 Introduction 159
6.2 Methods 161
6.3 Results 162
6.3.1 Equilibrium isotope fractionation at lower mantle conditions 162
6.3.2 Relationship to structural melt parameters 163
6.4 Discussion 165
6.4.1 High-pressure isotope fractionation 165
6.4.2 Magma ocean differentiation 166

6.4.3 Limits on primordial reservoirs 168
6.4.4 Finding traces of primordial bridgmanite 169
6.4.5 Implications for lower mantle structure 171
6.5 Conclusion 172

7 Conclusions and Outlook **202**
7.1 Conclusions 202
7.2 Future Work 205

List of Figures

1.1 Mg and Si isotope compositions of Solar System materials 4
1.2 Si-isotope metal-silicate fractionation literature data 5
1.3 Silicon and magnesium isotope compositions of the BSE, Moon, enstatite chondrites, and ordinary chondrites 7
1.4 Magnesium isotope compositions of various geological reservoirs . . 18
1.5 Silicon isotope compositions of various geological reservoirs 24

2.1 Convergence of the total energy of a diopside structure 46
2.2 Two-dimensional visualisation of a potential energy surface. 48
2.3 Diatomic linear harmonic chain representing a line of atoms. 52

3.1 Forsterite-Diopside-Anorthite Ternary system 70

4.1 Ternary diagram of Diopside-Anorthite-Forsterite with experiments 82
4.2 BSE images of experimental run products 89
4.3 Mg isotopic difference mineral-melt and mineral-mineral 91
4.4 Cell parameters crystal structures 92
4.5 Reduced partitioning function for magnesium isotopes in diopside and forsterite. 94
4.6 Reduced partitioning function with thermal expansion correction . . 96
4.7 Inter-mineral Mg isotope fractionation between diopside and forsterite 98
4.8 Inter-mineral Mg isotopic differences compared to xenoliths 103
4.9 SEM images of samples with compositions BDW-S1 and BDW-S2. . 111
4.10 Experiment EMPA pictures 112
4.11 Compilation of literature data cpx-olivine 113
4.12 Reduced partitioning function for magnesium isotopes in literature . 116
4.13 SEM images of experimental samples for Si isotopes 118

5.1 Mg isotope fractionation (Δ^{26}Mg) between olivine, clinopyroxene and melt. Lines show MD–DFT predictions 134
5.2 Predicted Si isotope fractionation (Δ^{30}Si) between olivine, clinopyroxene, and melt from MD–DFT 136
5.3 Schematic overview of the molecular dynamics–density functional theory workflow 142

5.4 Cation–oxygen radial distribution functions for Si, Al, Mg, and Ca of the molecular-dynamics trajectory 145
5.5 MSD of full molecular-dynamics trajectory 146
5.6 Ionic-model residuals (β_{residual}) plotted against local structural descriptors 151

6.1 Temperature dependence of equilibrium isotopic fractionation between bridgmanite and melt 179
6.2 Relationship between average bond length and isotopic fractionation expressed as $1000\ln(\beta)$ for (a) Si- and (b) Mg-bearing phases. . . . 180
6.3 Evolution of isotopic composition during fractional crystallisation as a function of melt fraction. 181
6.4 Schematic of planetary differentiation from magma ocean onset to long-term mantle evolution. 183
6.5 Temperature dependence of reduced partition function ratios ($1000\ln\beta$) for Mg (top) and Si (bottom) at 0 GPa for bridgmanite. 190
6.6 Cation–oxygen radial distribution functions, high-pressure melt . . 191
6.7 MSD of high-pressure melt 192
6.8 Compilation of published BSE and BSM isotope compositions for Mg and Si. 197
6.9 Evolution of isotopic composition during fractionation crystallisation as a function of melt fraction (All pressures). 198

List of Abbreviations

BSE . . . . . Bulk Silicate Earth

BSM . . . . . Bulk Silicate Moon

BEAMS . . . . . Bridgmanite-Enriched Ancient Mantle Structures

BMO . . . . . Basal Magma Ocean

DFT . . . . . Density Functional Theory

DFT–MD . . . . Density Functional Theory Molecular Dynamics

DFPT . . . . . Density Functional Perturbation Theory

MD . . . . . Molecular Dynamics

NVT . . . . . Canonical ensemble (constant number of particles, volume, temperature)

NPT . . . . . Isothermal–isobaric ensemble (constant number of particles, pressure, temperature)

CN . . . . . Coordination Number

β . . . . . Reduced partition function ratio

α . . . . . Isotope fractionation factor

Δ . . . . . Isotopic difference between phases

δ . . . . . Isotopic composition relative to a standard

PBESOL . . . . . Perdew–Burke–Ernzerhof for solids functional

PBE . . . . . Perdew–Burke–Ernzerhof functional

LDA . . . . . Local Density Approximation

CASTEP . . . . . Cambridge Sequential Total Energy Package

MC-ICP-MS . . . Multi-Collector Inductively Coupled Plasma Mass Spectrometry

SEM . . . . . Scanning Electron Microscope

EMPA . . . . . Electron Microprobe Analysis

OIB . . . . . Ocean Island Basalt

MORB . . . . . Mid-Ocean Ridge Basalt

"Geologists have a saying - rocks remember."

— Neil Armstrong

1 Introduction

Contents

1.1 General Introduction 2
1.2 Background: From Planetary Accretion to Magma-Ocean Solidification 3
1.2.1 Magma Ocean Formation and Crystallisation 6
1.2.2 Preservation of primordial mantle reservoirs 8
1.2.3 Tracing primordial mantle heterogeneities with isotopic systems 9
1.3 Theoretical Framework of High-Temperature Isotope Fractionation 10
1.3.1 Generalities 10
1.3.2 Gibbs free energy and equilibrium 12
1.3.3 α and β Fractionation Factor 13
1.3.4 Calculation of Fractionation Factor 13
1.3.5 Experimental Fractionation Factor 15
1.4 Magnesium Isotopes 15
1.4.1 Magnesium Geochemistry 15
1.4.2 Magnesium Stable Isotopes 16
1.4.3 Measurement of Mg Isotopes 16
1.4.4 Parameters Controlling Fractionation 16
1.4.5 Use in Earth Sciences 17
1.4.6 Magnesium Isotopic Fractionation at High Temperature 19
1.5 Silicon Geochemistry and Isotopes 21
1.5.1 Silicon Geochemistry 21
1.5.2 Silicon Stable Isotopes 21
1.5.3 Measurement of Si Isotopes 22
1.5.4 Parameters Controlling Si Fractionation 22
1.5.5 Applications in Earth Sciences 23
1.5.6 High-Temperature Silicon Isotope Fractionation 23

1.6 Key Knowledge Gaps 25
1.7 Structure of the Thesis 27

1.1 General Introduction

The current structure and composition of Earth preserves evidence of the earliest stages of planetary formation. Among these, details about magma-ocean crystallisation, a crucial differentiation event in Earth's history, are particularly significant. Large-scale melting during accretion of Earth and the Moon-forming giant impact likely generated a deep or global magma ocean (Boukaré et al., 2025; Labrosse et al., 2007). As this magma ocean cooled, high-pressure minerals crystallised and segregated, creating the mantle's chemical architecture and composition.

Geodynamic models predict that this crystallisation occurred in a bottom-up process, initiating in the lower mantle and progressing upward. This leads to the formation of bridgmanite-rich cumulates in the mid-mantle (Ballmer et al., 2017, 2025; Gülcher et al., 2021). Depending on density contrasts between bridgmanite and melt phases and the efficiency of mantle convection, such structures may have been gravitationally stable and capable of surviving until the present day. These early reservoirs have been used as input parameters to explain present-day large low-shear-velocity provinces (LLSVPs), ultra-low-velocity zones (ULVZs), and deep-mantle density anomalies (Koelemeijer et al., 2018; Moulik & Ekström, 2016; Ritsema et al., 2011).

However, the survival of primordial heterogeneities remains debated. Seismic tomography provides indirect constraints on mantle structure. This method, based on analysing P- and S-wave structures, cannot uniquely determine composition. Furthermore, 4.5 billion years of mantle convection could potentially substantially mix early-formed layers.

Stable isotope geochemistry provides a complementary test. If magma-ocean crystallisation generated equilibrium isotope fractionation between melt and high-pressure silicate minerals, then segregation and preservation of early cumulates

should have produced isotopic heterogeneity in the mantle. The absence of such heterogeneity places quantitative limits on the volume and persistence of primordial domains.

Magnesium (Mg) and silicon (Si) isotopes are particularly well suited to this problem. Both elements are major components of mantle minerals, and their stable isotopes fractionate in predictable, mass-dependent ways controlled by the bonding environment. High-precision measurements show near-homogeneity in present-day mantle-derived rocks (X.-N. Liu et al., 2023, 2025). Reconciling this homogeneity with models predicting preserved magma-ocean cumulates requires quantitative knowledge of equilibrium mineral–melt fractionation at the relevant pressure–temperature conditions.

This thesis investigates the question: Can Mg and Si isotope fractionation during magma-ocean crystallisation preserve large primordial bridgmanite-rich reservoirs consistent with modern isotopic observations?

1.2 Background: From Planetary Accretion to Magma-Ocean Solidification

Earth's formation was characterised by a series of highly energetic events that set its initial thermal state, internal structure, and isotopic composition. Each of these processes has left a distinct isotopic signature (Figure 1.3). These events began within the protoplanetary disk, where gas and dust gradually condensed into solid particles that grew into increasingly larger bodies. Through collisions and gravitational forces, these materials formed kilometre-scale planetesimals and planetary embryos, which eventually gave rise to terrestrial planets via giant impacts (Chambers & Wetherill, 1998; Morbidelli et al., 2012; Raymond et al., 2009). Alternative formation pathways, such as pebble accretion, have been suggested to accelerate planetary formation (Lambrechts & Johansen, 2012; Lambrechts et al., 2014). However, the significance of these mechanisms for terrestrial planet formation remains debated (see, for example, Morbidelli et al., 2025).

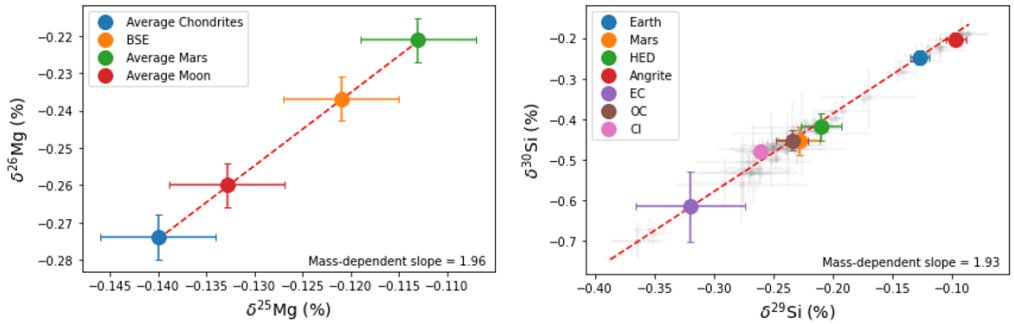


Figure 1.1: (a) Mg (Hin et al., 2017) and (b) Si isotope compositions of Solar System materials (Onyett et al., 2023). Both systems define mass-dependent fractionation lines (slopes ≈ 1.96 for Mg and 1.93 for Si), indicating that isotopic variations among planetary bodies arise from mass-dependent processes during planet formation, not from nucleosynthetic or outer Solar System inputs.

The isotopic compositions of Solar System materials provide key constraints on these early stages of planetary formation. Mg and Si isotopes exhibit systematic, mass-dependent relationships across meteorites, planetary bodies, and Bulk Silicate Earth. As illustrated in Figure 1.1, these relationships define linear trends consistent with equilibrium or kinetic mass-dependent fractionation, indicating that isotopic variations arise primarily from physical and chemical processes such as condensation, evaporation, and differentiation, rather than from nucleosynthetic heterogeneity (Armytage et al., 2011; Dauphas et al., 2015). The offset between chondritic meteorites and the Bulk Silicate Earth further suggests that high-temperature processes during, or before accretion, modified the Earth's initial isotopic composition (Bourdon et al., 2010; Chakrabarti & Jacobsen, 2010; Dauphas, 2017).

These accretionary events were fundamentally energetic. Frequent impacts between growing bodies generated significant thermal energy, complemented by other heat sources, such as radiogenic decay of short-lived isotopes, such as ^{26}Al, and the heat released during metal–silicate differentiation. These factors helped sustain high internal temperatures (Elkins-Tanton et al., 2011). As planetary embryos grew, the combined heat sources caused widespread melting, triggering large-scale differentiation.

Early differentiation leads to the separation of a metallic core from a silicate mantle. Studies, both experimental and theoretical, suggest that silicon can partition

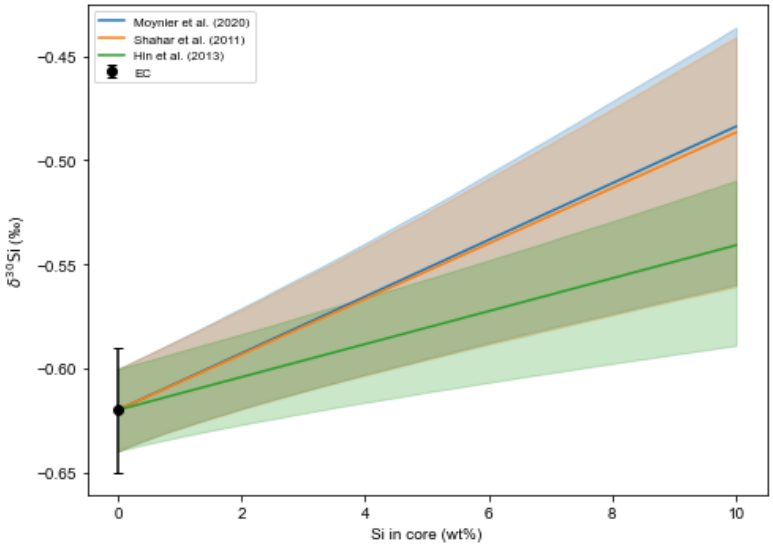


Figure 1.2: Predicted change in δ^{30}Si of Bulk Silicate Earth (BSE) as a function of silicon partitioning into the core (Si in the core, wt%). Coloured lines show model predictions from Moynier et al. (2020) (blue), Shahar et al. (2011) (orange), and Hin et al. (2014) (green); the semi-transparent bands around each line display the corresponding uncertainty ranges. The starting point is the enstatite chondrite data measured by Onyett et al. (2023). Enstatite chondrites are shown because their bulk isotopic and elemental compositions closely resemble those inferred for Earth's building materials, despite mineral-scale fractionation caused by highly reducing conditions, which partitions Si and other elements into metal and sulfide phases. Alternatively, different chondrite groups could be chosen which have less pronounced light isotopic signatures.

into the core under high-pressure conditions, thereby affecting the silicon isotopic composition of silicate Earth (Georg et al., 2007; Kempl et al., 2016; Shahar et al., 2009, 2011). Conversely, lithophile magnesium remains largely excluded from the core, so Mg isotopes mainly reflect silicate processes. Model predictions of δ^{30}Si variation based on silicon partitioning into the core are presented in Figure 1.2, showing both the extent of fractionation and the uncertainties linked to core formation.

The final stages of Earth's accretion were likely dominated by giant impacts, culminating in the Moon-forming collision between the proto-Earth and a Mars-sized impactor (Theia). This event had profound consequences for Earth's thermal and chemical evolution, generating a global or near-global magma ocean and promoting extensive mixing and equilibration between impactor and target material (Canup, 2004; Ćuk & Stewart, 2012). The close similarity in Mg and Si isotope compositions

between Earth and the Moon, typically within $< 0.04\,‰$, provides strong evidence for efficient equilibration during or following this event (Armytage et al., 2011; Hin et al., 2017) unless Theia was identical to the proto-Earth.

The evolution of isotopic compositions is summarised schematically in Figure 1.3, which illustrates different isotopic solar-system reservoirs of δ^{30}Si and δ^{26}Mg with proposed mechanisms that could fractionate stable isotopes. Together with the meteorite data shown in Figure 1.1, these observations show that Mg and Si isotopes are sensitive tracers of high-temperature planetary processes and provide a framework for linking early Earth evolution to present-day mantle composition.

As accretion progressed, the Giant Impact occurred, and internal temperatures increased; conditions within the early Earth exceeded the liquidus of silicate materials over large depth ranges. This led to the formation of a global magma ocean, marking a fundamental transition in Earth's evolution from a partially molten accreting body to a differentiated planet dominated by large-scale melting and crystallisation processes.

1.2.1 Magma Ocean Formation and Crystallisation

The formation of a magma ocean represents one of the most important differentiation events in Earth's history. Following large-scale melting induced by accretionary heating and the Moon-forming giant impact, the mantle likely existed as a vigorously convecting silicate liquid, with temperatures exceeding 4000 K along a mantle adiabat (Stixrude et al., 2009). As the magma ocean cooled, crystallisation was governed by the intersection of the adiabat with the solidus, determining both the sequence of mineral formation and the resulting chemical stratification.

Most models predict that crystallisation initiated in the deep mantle, where pressures reach approximately 40–80 GPa, leading to the formation of high-pressure phases such as bridgmanite ($MgSiO_3$) and ferropericlase (MgO) (Ballmer et al., 2017; Gülcher et al., 2021; Labrosse et al., 2007). This bottom-up crystallisation sequence would have produced dense cumulates that segregated and accumulated near the core–mantle boundary. In some scenarios, this process results in the

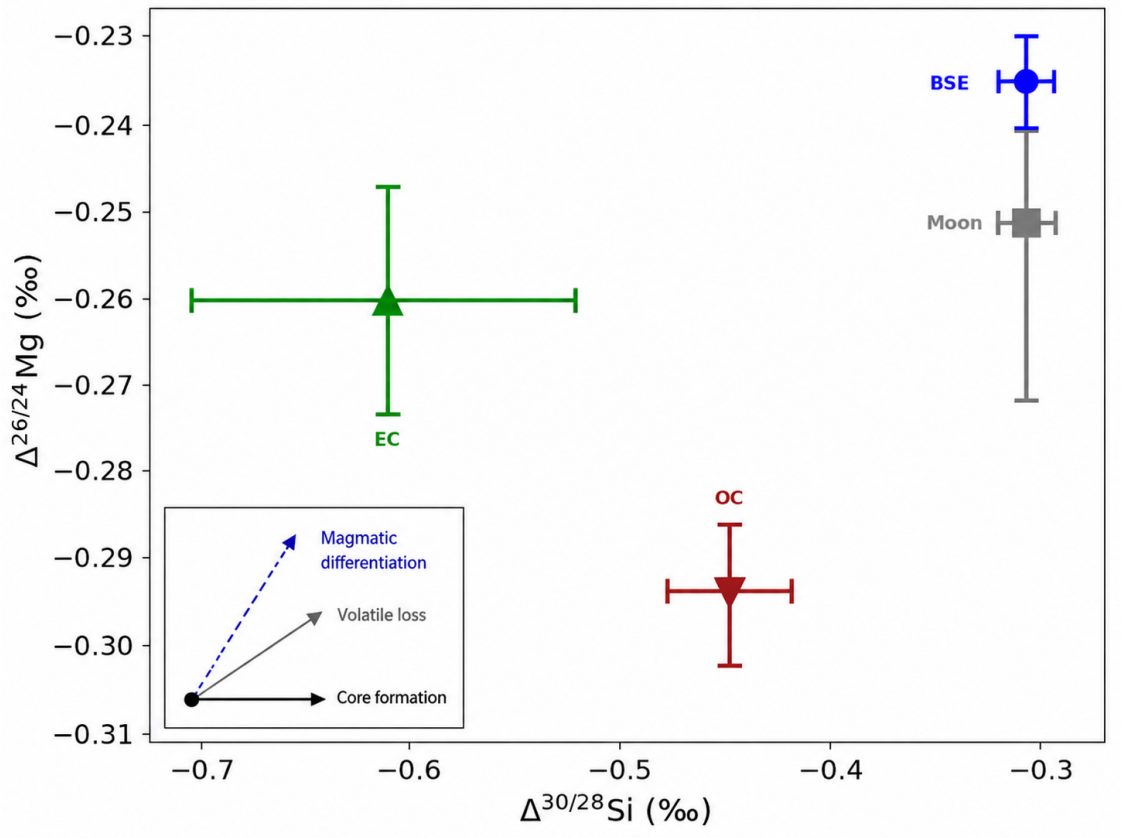


Figure 1.3: Comparison of the coupled silicon and magnesium isotope compositions ($\Delta^{30/28}$Si versus $\Delta^{26/24}$Mg) of the Bulk Silicate Earth (BSE), the Moon, enstatite chondrites (EC), and ordinary chondrites (OC). Error bars represent 1σ uncertainties. The inset illustrates the expected directions of isotopic fractionation associated with core formation, volatile loss, and magmatic differentiation. The volatile-loss vector is based on the models of Hin et al. (2017), whereas the magmatic differentiation vector is based on the framework of Walker et al. (2026) and will be quantitatively evaluated in this thesis. Magnesium isotope compositions for EC and OC are from Hin et al. (2017), while silicon isotope compositions for EC and OC are from Onyett et al. (2023). The BSE Mg isotope composition is from X.-N. Liu et al. (2023), and the BSE Si isotope composition is from X.-N. Liu et al. (2025). Lunar Mg isotope data are from Klaver et al. (2024), and lunar Si isotope data are from Dauphas et al. (2015)

formation of a basal magma ocean (BMO), a partially molten layer that may persist over extended timescales (Boukaré et al., 2025; Labrosse et al., 2007).

However, magma ocean crystallisation may not have been a purely stratified process. More recent models suggest dynamic behaviour in which crystals form, sink, remelt, and are redistributed within the convecting magma ocean, producing a heterogeneous “marble-cake” mantle structure (Boukaré et al., 2025). In this framework, dense bridgmanite-rich cumulates may still accumulate at depth, while

other material is mixed throughout the mantle. The resulting structure depends sensitively on crystallisation kinetics, density contrasts, and convective efficiency.

The isotopic consequences of magma ocean crystallisation are hinted in Figure 1.3 and in studies by F. Huang et al. (2014) and Walker et al. (2026), which highlights the potential for equilibrium fractionation between minerals and melts during cooling. If such fractionation is significant, then early-formed cumulates may develop distinct isotopic signatures relative to the residual melt, providing a mechanism for generating chemical and isotopic heterogeneity within the mantle.

1.2.2 Preservation of primordial mantle reservoirs

The long-term preservation of magma-ocean cumulates depends on their physical properties and on subsequent mantle dynamics. Numerical simulations indicate that compositionally distinct domains with modest density contrasts (on the order of a few per cent) may remain stable over billions of years, particularly if they are anchored at the core–mantle boundary (Ballmer et al., 2017; B. Li et al., 2014). In this context, bridgmanite-enriched ancient mantle structures (BEAMS) have been proposed as potential long-lived reservoirs formed during magma ocean crystallisation.

Seismological observations provide indirect evidence for such deep-mantle heterogeneity. Global tomographic models reveal large low shear velocity provinces (LLSVPs) beneath Africa and the Pacific, which extend upward from the core–mantle boundary and are interpreted as thermochemical anomalies (Moulik & Ekström, 2016; Ritsema et al., 2011). Smaller-scale ultra-low velocity zones (ULVZs), characterised by extreme reductions in seismic velocity (>20%), are also observed near the core–mantle boundary and represent partial melt or iron-rich residues associated with basal magma ocean processes (Labrosse et al., 2007; McNamara, 2019).

Despite these observations, the origin of deep-mantle structures remains debated. While some models interpret LLSVPs and ULVZs as remnants of early differentiation, others attribute them to recycled crustal material or ongoing mantle convection. Because seismic observations primarily constrain physical properties rather than composition, they cannot uniquely determine whether these structures are primordial

or secondary. As a result, complementary geochemical approaches are required to test the preservation of early-formed mantle reservoirs.

1.2.3 Tracing primordial mantle heterogeneities with isotopic systems

While seismic and geodynamic observations reveal the physical complexity of Earth's deep mantle, isotopic systems provide complementary chemical evidence to trace the remnants of Earth's magma ocean. The decay of short-lived ^{182}Hf to ^{182}W (with a half-life of about 9 million years) serves as a marker for early silicate differentiation and magma ocean crystallisation. Since Hf is lithophile and W is siderophile, any metal-silicate separation within the first 50 million years of Earth's history can produce detectable μ^{182}W anomalies. Ocean Island Basalts (OIBs) from Hawaii, Samoa, and Iceland show deficits of up to 19 ppm compared to BSE (Mundl et al., 2017). At the same time, basalts from Baffin Island and Ontong Java display positive μ^{182}W (Rizo et al., 2016). These findings suggest that some parts of the mantle have remained isolated from convection since the Hadean, consistent with primordial signatures of bridgmanite-rich cumulates or a buried magma ocean. Another relevant isotopic system is based on the extinct radionuclide ^{146}Sm, which decays to ^{142}Nd. Boyet and Carlson (2005) first showed that terrestrial samples show an excess compared to chondrites, indicating global differentiation within 30 million years of solar system formation. Subsequent analyses reveal that Archean rocks from Isua, Acasta, and Barbeto (Caro, 2011) exhibit both positive and negative μ^{142}Nd anomalies, suggesting the preservation of multiple ancient reservoirs. Combined with ^{182}W anomalies, this strengthens the interpretation that traces of an early basal magma ocean could be preserved in these isotopic signatures.

Helium and neon isotopes provide complementary constraints on the existence of long-lived mantle heterogeneity. Several OIBs exhibit high ^{3}He/^{4}He ratios, indicating a mantle source with low time-integrated U + Th/He ratios and therefore limited accumulation of radiogenic ^{4}He (Jackson & Carlson, 2011). When considered together with primordial Ne isotope signatures, these observations are consistent

with sampling ancient mantle domains that have remained relatively isolated from convective mixing and extensive degassing.

In contrast, Mg and Si isotopes have yet to provide strong evidence for ancient deep-mantle reservoirs, even though they could serve as effective tracers of differentiation dominated by bridgmanite (Walker et al., 2026). Currently, their main importance is in complementing radiogenic isotope systems. With future improvements in measurement accuracy and in high-pressure partitioning studies, subtle yet diagnostic Mg–Si isotopic differences between lower- and upper-mantle reservoirs may be uncovered. Combining these stable isotope insights with ^{182}W, ^{142}Nd, and Fe isotopes offers a promising path to investigate the long-term preservation and sampling of Earth's earliest mantle components.

1.3 Theoretical Framework of High-Temperature Isotope Fractionation

Understanding isotope fractionation in high-temperature magmatic systems requires linking large-scale planetary processes to atomic-scale behaviour. At equilibrium, isotopes partition between phases according to differences in their bonding environments and vibrational properties. These effects can be described using thermodynamic and statistical mechanical principles, which provide a framework for quantifying isotope fractionation.

1.3.1 Generalities

Isotope exchange reactions can occur through chemical reactions or changes in conditions, such as temperature or pressure. For example, in these reactions, a heavier isotope (Y) can be replaced by a lighter isotope (Y') between two distinct phases. This replacement results in one phase becoming enriched in a specific isotope relative to the other phase. There are two types of isotope fractionation to consider when studying isotope fractionation:

1. **Mass-dependent isotope fractionation**. Isotopic fractionation usually aligns with mass-dependent fractionation, meaning the changes in isotopic ratios depend on the mass differences of the isotopes involved. This form of fractionation can take place through various processes:

   - **Equilibrium fractionation**. Equilibrium fractionation takes place when a system with isotopic exchange reaches complete thermodynamic equilibrium. In this state, the ratio of isotopes depends on thermodynamic conditions, including temperature. This process is vital in fields like mantle geochemistry, palaeoclimatology, and hydrology.
   - **Non-equilibrium fractionation, or kinetic fractionation**. Non-equilibrium fractionation, or kinetic fractionation, happens when a system is not in equilibrium. Since lighter isotopes generally react or diffuse more quickly than heavier ones, this results in isotopic differences across various stages. Examples include evaporation, condensation, and diffusion between growth zones in minerals.

2. **Mass-independent fractionation / non-mass-dependent fractionation** In some cases, isotopic fractionation does not scale with isotope mass differences and is therefore described as mass-independent fractionation (MIF). Well-known examples include photochemical reactions that produce anomalous isotope signatures, such as the oxygen isotope anomalies observed in atmospheric chemistry. In addition, some heavy elements, including mercury (Hg) and uranium (U), exhibit non-mass-dependent fractionation arising from nuclear volume (field shift) effects, where differences in nuclear size and shape, rather than isotope mass, influence isotopic partitioning.

   Thus, it is essential to acknowledge that isotope fractionation is inherently mass-dependent on the involved atoms. This study primarily focuses on mass-dependent equilibrium isotope fractionation using ab initio calculations and experimental petrology.

1.3.2 Gibbs free energy and equilibrium

The relative Gibbs free energies of isotopic exchange reactions between phases govern equilibrium isotope fractionation. This thermodynamic preference can be described in terms of the Gibbs free energy change, ΔG, which represents the difference in potential energy between the phases involved in a particular reaction. For isotope exchange at thermodynamic equilibrium, ΔG can be expressed as:

$$\Delta G = -k_{\mathrm{B}} T \ln K_{\mathrm{eq}}, \tag{1.1}$$

where T is the temperature, k_{B} is the Boltzmann constant, and K_{eq} is the equilibrium constant. K_{eq} is defined by the free energy in the system at the time of isotopic exchange and depends on temperature:

$$K_{\mathrm{eq}} = e^{-\frac{\Delta F}{k_{\mathrm{B}} T}}, \tag{1.2}$$

where ΔF is the Helmholtz free energy variation, k_{B} is the Boltzmann constant, and T is the temperature. The Helmholtz free energy (F) describes the thermodynamic potential of a system at constant volume and temperature, whereas the Gibbs free energy (G) is defined at constant pressure and temperature; for condensed phases under high-pressure conditions, both formulations are closely related, but the Helmholtz free energy is more directly linked to statistical mechanical treatments based on partition functions. With consideration of statistical quantum physics, Equation 1.2 can be expressed in terms of the partition function:

$$Q = \sum_{n} e^{-\frac{E_n}{k_{\mathrm{B}} T}}, \tag{1.3}$$

where Q is the partition function over the set of states n, and E_n is the energy of state n. As a result, K_{eq} can be formulated as a function of Q:

$$K_{\mathrm{eq}} = \frac{Q_{\mathrm{products}}}{Q_{\mathrm{reactants}}} \tag{1.4}$$

1.3.3 α and β Fractionation Factor

The fractionation factor (α) represents the relative isotope enrichment between two phases and depends on quantum-mechanical effects (Q). The fractionation factor α is defined as:

$$\alpha_{AY-BY} = \frac{\beta_{AY}}{\beta_{BY}}, \tag{1.5}$$

where β is the individual phase fractionation factor, expressed as:

$$\beta_{AY} = \frac{Q_{AY}}{Q_{AY'}}, \tag{1.6}$$

where Q represents the quantum-mechanical partition functions of phases A and B, and isotopes Y and Y'.

Absolute values for isotope fractionation are typically small, and α values are very close to 1. An $\alpha > 1$ indicates enrichment of heavy isotopes, while $\alpha < 1$ indicates enrichment of light isotopes in phase A relative to phase B. To improve readability, α is often expressed in logarithmic form as:

$$10^3 \ln \alpha_{AY-BY} = x \text{‰} \tag{1.7}$$

1.3.4 Calculation of Fractionation Factor

Theoretical and computational fractionation factors utilise *ab initio* calculations, such as Density Functional Theory (DFT). The fundamentals of DFT are described in detail in Chapter 2. *Ab initio* calculations compute phonon frequencies from thermodynamic calculations, which are then used to determine equilibrium isotope ratios. The approach to isotope fractionation calculations used here follows previous studies of stable isotopes (Blanchard et al., 2009; Javoy et al., 2012; X. Li et al., 2009; Méheut et al., 2007; Rustad & Dixon, 2009) and studies specifically addressing Si isotope fractionation (F. Huang et al., 2014; Méheut et al., 2009) and Mg isotope fractionation (F. Huang et al., 2013; Schauble, 2011; Walker et al., 2026; W. Wang, Walter, et al., 2023; Wu et al., 2015; Young et al., 2009).

The translation from phonon frequencies (outputs of DFT calculations) to isotope fractionation ratios used here is based on previous work (Walker et al., 2026). The aim is to compute the reduced partition function, $\beta(X, Y, Y')$. This function represents the equilibrium constant between two isotopes in a single mineral phase (Y and Y') and an ideal gas (X) (Urey, 1947). Within the harmonic approximation, the phonon frequencies of a crystal can be used to calculate the reduced partition function $\beta(X, Y, Y')$. (Schauble, 2004) for crystal X:

$$\beta\left(X, Y, \mathrm{Y}'\right) = \prod_{i=1}^{\mathrm{n}^q} \left[\prod_{j=1}^{3\,\mathrm{N}^{at}} \left(\frac{\omega'_{\mathrm{i\ ,j}}}{\omega_{i,j}} \frac{e^{-h\omega'_{i,\mathrm{j}}/(2kT)}}{1 - e^{-h\omega'_{i,\mathrm{j}}/(2kT)}} \frac{1 - e^{-h\omega_{i,\mathrm{j}}/(2kT)}}{e^{-h\omega_{i,\mathrm{j}}/(2kT)}} \right) \right]^{\omega_i} \tag{1.8}$$

where $\omega_{i,j}$ and $\omega'_{i,j}$ represent the phonon frequencies at the ith point in the reciprocal lattice and jth vibrational branch, h is the Planck constant, k_B is the Boltzmann constant, and T is the temperature. The calculation is performed over $3N_\mathrm{at}$ vibrational modes for each of the N_q points in the first Brillouin zone. The Brillouin zone comprises the set of points accessible from the origin in reciprocal space without crossing any Bragg plane. Symmetry is used to avoid double-counting in the reciprocal lattice and thereby reduce computational cost. The phonon frequencies $\omega_{i,j}$ and $\omega'_{i,j}$ are obtained from CASTEP thermodynamic calculations and constitute the primary input for Equation 1.8.

The isotope fractionation factor between two solid phases, such as forsterite and diopside, is defined as $\alpha(X_1, X_2, Y, Y')$, where X_1 and X_2 represent two mineral phases and Y and Y' represent two isotopes. It can be expressed in logarithmic form as:

$$\Delta_{Y'} = 10^3 \ln \alpha(X_1, X_2, Y, Y') = 10^3 \ln \beta(X_1, Y, Y') - 10^3 \ln \beta(X_2, Y, Y'), \tag{1.9}$$

where $\Delta_{Y'}$ represents the difference (in ‰) in heavy isotope enrichment between phases X_1 and X_2.

1.3.5 Experimental Fractionation Factor

Empirical measurements of stable isotopes are commonly reported using δ notation. Isotope ratios are defined as the deviation of the isotope ratio of a sample from that of a standard (e.g., BHVO-2). These ratios are expressed in parts per mil (‰). For example, for Mg:

$$\delta^{26}\mathrm{Mg}_x = \left(\frac{(^{26}\mathrm{Mg}/^{24}\mathrm{Mg})_x}{(^{26}\mathrm{Mg}/^{24}\mathrm{Mg})_{\mathrm{BHVO-2}}} - 1 \right) \times 10^3, \tag{1.10}$$

where x represents the sample and BHVO-2 is the standard. In this thesis, heavy isotope ratios are systematically used as the numerator so that enrichment in heavy isotopes corresponds to positive δ values.

Experimental data can be expressed in terms of fractionation factors comparable to computational modelling results. The fractionation factor α between two phases A and B can be approximated from δ values as:

$$10^3 \ln \alpha_{A-B} \approx \delta^{26}\mathrm{Mg}_A - \delta^{26}\mathrm{Mg}_B \tag{1.11}$$

1.4 Magnesium Isotopes

1.4.1 Magnesium Geochemistry

Magnesium is the fourth most abundant element in Earth and the eighth most abundant element in Earth's crust (McDonough & Sun, 1995). It plays a fundamental role in the Earth and other terrestrial planets as a major component of key mantle minerals such as olivine $(\mathrm{Mg,Fe})_2\mathrm{SiO}_4$ and diopside $\mathrm{CaMgSi_2O_6}$, as well as high-pressure mineral phases like ringwoodite $\mathrm{Mg_2SiO_4}$ and bridgmanite $\mathrm{MgSiO_3}$. Thus, magnesium directly influences mantle composition, seismic behaviour, and mantle dynamics. It occurs naturally only in the 2+ oxidation state and readily forms MgO.

1.4.2 Magnesium Stable Isotopes

Magnesium has three naturally occurring stable isotopes: ^{24}Mg, ^{25}Mg, and ^{26}Mg. Its atomic weight is 24.305 u, corresponding to abundances of 78.88% ^{24}Mg, 9.988% ^{25}Mg, and 10.96% ^{26}Mg. Magnesium isotope compositions in this thesis are expressed using δ notation:

$$\delta^{26}\mathrm{Mg} = \left(\frac{(^{26}\mathrm{Mg}/^{24}\mathrm{Mg})_{\mathrm{sample}}}{(^{26}\mathrm{Mg}/^{24}\mathrm{Mg})_{\mathrm{standard}}} - 1 \right) \times 10^3 \tag{1.12}$$

$$\delta^{25}\mathrm{Mg} = \left(\frac{(^{25}\mathrm{Mg}/^{24}\mathrm{Mg})_{\mathrm{sample}}}{(^{25}\mathrm{Mg}/^{24}\mathrm{Mg})_{\mathrm{standard}}} - 1 \right) \times 10^3 \tag{1.13}$$

Values of δ^{26}Mg and δ^{25}Mg are multiplied by a factor of 10^3 to express them in per mil (‰).

1.4.3 Measurement of Mg Isotopes

Magnesium isotopes are predominantly measured using multi-collector inductively coupled plasma mass spectrometry (MC-ICP-MS). Following the work of Galy et al. (2001), a high-accuracy sample–standard bracketing approach has become widely adopted. While these techniques have enabled the use of magnesium isotopes as tracers of various geological processes, previous studies have reported unexplained variability in results from similar samples. This scatter can be attributed, in part, to biases arising from discrepancies between the sample matrix and the standard used in sample–standard bracketing.

To address these limitations, Coath et al. (2017) and later Hin et al. (2017) introduced the double-spiking method, which mitigates the influence of instrumental mass bias on measurements. As a result, double spiking allows magnesium isotope measurements with an accuracy of approximately 0.01 ‰ in modern analyses.

1.4.4 Parameters Controlling Fractionation

The primary parameter controlling Mg isotope fractionation, as for most stable isotope systems, is temperature (Chapter 1.3.2). Additional parameters influencing

magnesium isotope fractionation have been investigated through both theoretical and experimental studies. Three key factors have been identified:

1. **Bond length.** Phases with shorter (stronger) Mg–O bond lengths are enriched in heavy Mg isotopes, whereas longer (weaker) bonds preferentially incorporate light isotopes. An exponential relationship between the reduced partition function β for $^{26}Mg/^{24}Mg$ and bond length has been shown in theoretical studies (Walker et al., 2026).

2. **Coordination number.** The coordination number (CN) exhibits an inverse relationship with $\delta^{26}Mg$. Phases with lower CN tend to display heavier isotopic compositions than those with higher CN. This relationship reflects the increased stiffness of Mg–O bonds at lower coordination numbers. Theoretical studies suggest that the magnitude of this fractionation between mantle phases exceeds analytical detection limits, even at chondritic liquidus temperatures (Walker et al., 2026).

3. **Electronegativity of surrounding atoms.** The electronegativity of neighbouring elements has been proposed as an additional control on Mg isotope fractionation. Greater enrichment in heavy Mg isotopes is associated with lower electronegativity of the cation bonded to Mg (Méheut & Schauble, 2014). However, the limited evidence for this effect in natural samples (Armytage et al., 2011) raises questions about its overall significance.

1.4.5 Use in Earth Sciences

Magnesium isotopes are a powerful tool for understanding processes on Earth and within the Solar System (Figure 1.4). The isotopic system exhibits measurable variability in natural samples while analytical precision can reach $\delta^{26}Mg < 0.1\,‰$. The largest Mg isotope fractionations are typically observed at low temperatures, particularly in studies of weathering and alteration of igneous and continental rocks (Brewer et al., 2018; K.-J. Huang et al., 2012, 2018; X.-M. Liu et al., 2014; Teng et al., 2010) and in glacial systems (Cuozzo et al., 2020; K.-J. Huang et al., 2016).

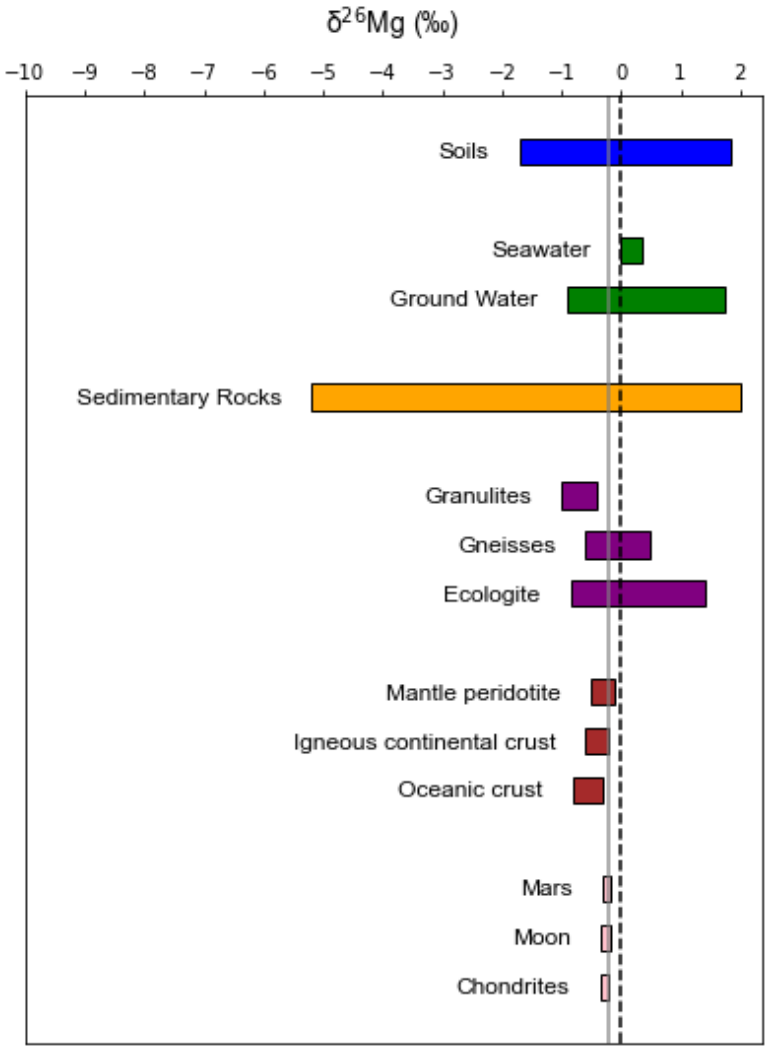


Figure 1.4: Magnesium isotope compositions of various geological reservoirs relative to the BHVO-2 standard. The grey line represents the BSE composition from Hin et al. (2017). Data is compiled by Guo et al. (2019)

Magnesium isotopes have also been widely applied to investigate magmatic differentiation processes (F. Huang et al., 2011; W.-Y. Li et al., 2016; Teng et al., 2007; S.-J. Wang et al., 2012, 2016). In addition, they provide key constraints on the formation and evolution of the Solar System. Chondrites, the building blocks of planets, have been extensively analysed for Mg isotopes, with δ^{26}Mg values ranging between -0.285 and $-0.219\,‰$ (Bourdon et al., 2010; Chakrabarti & Jacobsen, 2010; Hin et al., 2017; Pogge von Strandmann et al., 2011; Sikdar & Rai, 2021; Teng et al., 2010).

1.4.6 Magnesium Isotopic Fractionation at High Temperature

The advancement of double-spiking techniques in MC-ICPMS has significantly enhanced the ability to resolve small Mg isotope fractionations at high temperatures. Although isotopic variations are subtle under these conditions, they provide critical insights into mantle processes and geodynamics.

Magmatic Processes

The behaviour of magnesium isotopes during magmatic processes has been extensively reviewed by Guo et al. (2019). Most magmatic rocks exhibit limited variation in δ^{26}Mg, suggesting that high-temperature processes are generally inefficient at fractionating Mg isotopes. Instead, Mg isotope compositions largely reflect those of their source regions, with minor modifications arising from specific processes:

1. **Partial melting.** Partial melting has been proposed to increase δ^{26}Mg values in tholeiitic basalts and pyroxenites (Stracke et al., 2018; Zhong et al., 2017). However, X.-N. Liu et al. (2023) reported negligible fractionation effects ($< 0.002\,‰$) in residual peridotites using high-precision double-spiking techniques.

2. **Diffusion and Mg–Fe exchange.** At high temperatures, one of the mechanisms to achieve isotope fractionation arises from kinetic effects during diffusion. Light isotopes diffuse more rapidly than heavy isotopes, potentially resulting in lower δ^{26}Mg values compared to equilibrium predictions (X.-N. Liu et al., 2023).

Recent studies have also focused on Mg isotope mobility in subduction zones, highlighting the role of fluid-mediated transport (X. Deng et al., 2024; P.-P. Liu et al., 2017). Significant variations in arc lavas have been documented, ranging from $-0.31 \pm 0.04\,‰$ in Costa Rica to $-0.01 \pm 0.18\,‰$ in the Philippines (P.-P. Liu et al., 2017). Heavier Mg isotope signatures are generally linked to recycled carbonates

from subducting slabs, whereas lighter signatures are attributed to aqueous fluids derived from peridotite dehydration (X. Deng et al., 2024).

The temperature dependence of Mg isotope fractionation between mineral pairs (e.g., clinopyroxene–garnet, calcite–dolomite) suggests that Mg isotopes can be used as geothermometers. This application has been explored in several studies (Gou et al., 2022; X. Li et al., 2025). However, these approaches rely on a robust understanding of equilibrium fractionation, which remains poorly constrained. Consequently, further work is required to validate Mg isotopes as reliable geothermometers.

Mineral–Mineral and Mineral–Melt Fractionation Factors

The dataset of Mg isotope compositions for high-temperature silicate minerals remains limited (F. Huang et al., 2013; Schauble, 2011; Walker et al., 2026; Y. Wang et al., 2023). Table 1.1 summarises available β-factors for key mantle minerals derived from *ab initio* studies.

High-precision determinations of mineral–mineral fractionation factors have been reported by X.-N. Liu et al. (2022) and X.-N. Liu et al. (2023). Earlier work by Hu et al. (2020) measured Mg isotope ratios between pyroxenes and olivine; however, these results are associated with larger analytical uncertainties due to the use of simple sample–standard bracketing.

Only a limited number of studies have examined Mg isotope fractionation between silicate minerals and melt (Liao et al., 2022; Schiller et al., 2017; Teng et al., 2007). The most precise natural measurements of olivine phenocrysts in basaltic melt yield $\Delta^{26}\mathrm{Mg}_{\mathrm{Ol/melt}} = -0.071 \pm 0.010\,‰$ (Liao et al., 2022). However, X.-N. Liu et al. (2022) concluded that reproducing these results experimentally remains challenging due to temperature fluctuations of up to 10 degrees between the rims and the core in the piston–cylinder apparatus. Furthermore, Mg β-factors have not been calculated in existing silicate melt models that were used for Si and Fe isotopes (Rabin et al., 2023).

Table 1.1: Magnesium β-factor of minerals relevant to the Earth's mantle from *ab initio* studies.

		$10^3 \ln(\beta) = Ax + Bx^2 + Cx^3$		$(x = 10^3/T^2)$	Functional
Study	Formula	A	B	C	
Huang et al. (2013)					
Olivine	Mg_2SiO_4	2.0748	0.1052	-0.0119	LDA
Diopside	$CaMgSi_2O_6$	2.2442	0.1028	-0.0117	
Orthopyroxene	$MgSiO_3$	2.2501	0.0665	-0.0081	
Wang et al. (2013)					
Olivine	Mg_2SiO_4	2.565	-0.01735	0.0001947	LDA
Diopside	$CaMgSi_2O_6$	2.767	-0.01812	0.0001877	
Bridgmanite	$MgSiO_3$	2.510	-0.01930	0.0002489	
Duan et al. (2023)					
Olivine	Mg_2SiO_4	2.4265	-0.01555	0.00015	PBE
Diopside	$CaMgSi_2O_6$	2.3365	-0.01415	0.00010	
$10^3 \ln(\beta) = AT^{-6} + BT^{-4} + CT^{-2}$					(T = K)
Schauble et al. (2011)					
Olivine	Mg_2SiO_4	1.5614×10^{14}	-1.5115×10^{10}	2.3547×10^6	PBE
Diopside	$CaMgSi_2O_6$	1.4032×10^{14}	-1.4915×10^{10}	2.4806×10^6	

1.5 Silicon Geochemistry and Isotopes

1.5.1 Silicon Geochemistry

Silicon is one of the most abundant elements on Earth, comprising approximately 15.1% of the Earth's crust by weight (McDonough & Sun, 1995). Due to its lithophile character, silicon readily bonds with oxygen. Typically, silicon exhibits an oxidation state of +4, forming tetrahedral structures (SiO_4), which serve as fundamental building blocks for silicate minerals in both the crust and mantle. In silicate melt, silicon plays a crucial role as a polymerisation factor and is widely recognised as the dominant network-former controlling structural connectivity (Mysen et al., 1982).

1.5.2 Silicon Stable Isotopes

Silicon has three stable isotopes: ^{28}Si, ^{29}Si, and ^{30}Si. Its atomic mass is 28.085 u, with natural abundances of 92.223% ^{28}Si, 4.685% ^{29}Si, and 3.092% ^{30}Si. Isotope

compositions are expressed using δ notation:

$$\delta^{30}\mathrm{Si} = \left(\frac{\left(^{30}\mathrm{Si}/^{28}\mathrm{Si}\right)_{\mathrm{sample}}}{\left(^{30}\mathrm{Si}/^{28}\mathrm{Si}\right)_{\mathrm{standard}}} - 1 \right) \times 10^3 \tag{1.14}$$

$$\delta^{29}\mathrm{Si} = \left(\frac{\left(^{29}\mathrm{Si}/^{28}\mathrm{Si}\right)_{\mathrm{sample}}}{\left(^{29}\mathrm{Si}/^{28}\mathrm{Si}\right)_{\mathrm{standard}}} - 1 \right) \times 10^3 \tag{1.15}$$

Values are reported in per mil (‰). Positive δ values indicate enrichment in heavy isotopes relative to the standard.

1.5.3 Measurement of Si Isotopes

Measurement techniques for silicon isotopes are similar to those used for magnesium (Section 1.3.3). Multicollector inductively coupled plasma mass spectrometry (MC-ICP-MS), with correction for instrumental mass bias, is commonly employed (Savage, 2011; Zambardi & Poitrasson, 2011). These methods typically achieve analytical precision better than 0.1 ‰.

To improve accuracy, particularly at high temperatures where isotopic variations are small, double-spiking techniques have been developed. Originally introduced by Coath et al. (2017) and refined by X.-N. Liu et al. (2024), these methods allow silicon isotope measurements with a precision of approximately 0.03 ‰.

1.5.4 Parameters Controlling Si Fractionation

Silicon isotope fractionation is primarily controlled by temperature, Si–O bond length (F. Huang et al., 2014; Rabin et al., 2021), and the electronegativity of surrounding cations (Méheut & Schauble, 2014). One additional factor compared to Mg is:

1. **Polymerisation degree.** A positive correlation between δ^{30}Si and melt polymerisation has been proposed (Poitrasson & Zambardi, 2015). However, this relationship remains debated due to limited supporting evidence in natural systems (Savage, 2011).

1.5.5 Applications in Earth Sciences

Silicon isotopes are widely used to investigate geological and biogeochemical processes (Figure 1.5). They serve as tracers in low-temperature systems, including soil formation (Pogge von Strandmann et al., 2012), glacial–ocean interactions (Frings et al., 2016), and the global silicon cycle (Savage et al., 2013).

At high temperatures, silicon isotopes provide insights into igneous differentiation (Rabin et al., 2023; Savage, 2011; Savage et al., 2012; Zambardi et al., 2014) and mantle heterogeneity (H. Deng et al., 2019; Savage, 2011; Yu et al., 2018). They are also used to study metal–silicate fractionation and core formation processes (Poitrasson & Zambardi, 2015; Pringle et al., 2014; Shahar et al., 2009, 2011). Combined mass-dependent and mass-independent silicon isotope systems have been applied to investigate the origins of chondrites (Dauphas et al., 2015; Kadlag et al., 2019, 2021; Onyett et al., 2023, 2024; Sikdar & Rai, 2021; Tanaka et al., 2021; Villeneuve et al., 2020).

1.5.6 High-Temperature Silicon Isotope Fractionation

Magmatic Differentiation

Silicon isotopes show greater variability in magmatic systems compared to magnesium isotopes. Basaltic rocks typically exhibit δ^{30}Si values around $-0.3\,‰$, whereas more evolved magmas display heavier compositions near $-0.1\,‰$. These variations suggest that isotope fractionation occurs during magmatic differentiation.

Fractional crystallisation has been proposed as a key mechanism (Qin et al., 2016; Rabin et al., 2023), supported by empirical observations (Savage, 2011). As magmas cool, silicon incorporation into solid phases can shift isotopic compositions.

Additional processes, including melt polymerisation, cation effects, and thermal diffusion, have been proposed to explain observed variations (Poitrasson & Zambardi, 2015). However, interpretation remains limited by the lack of well-constrained equilibrium fractionation factors.

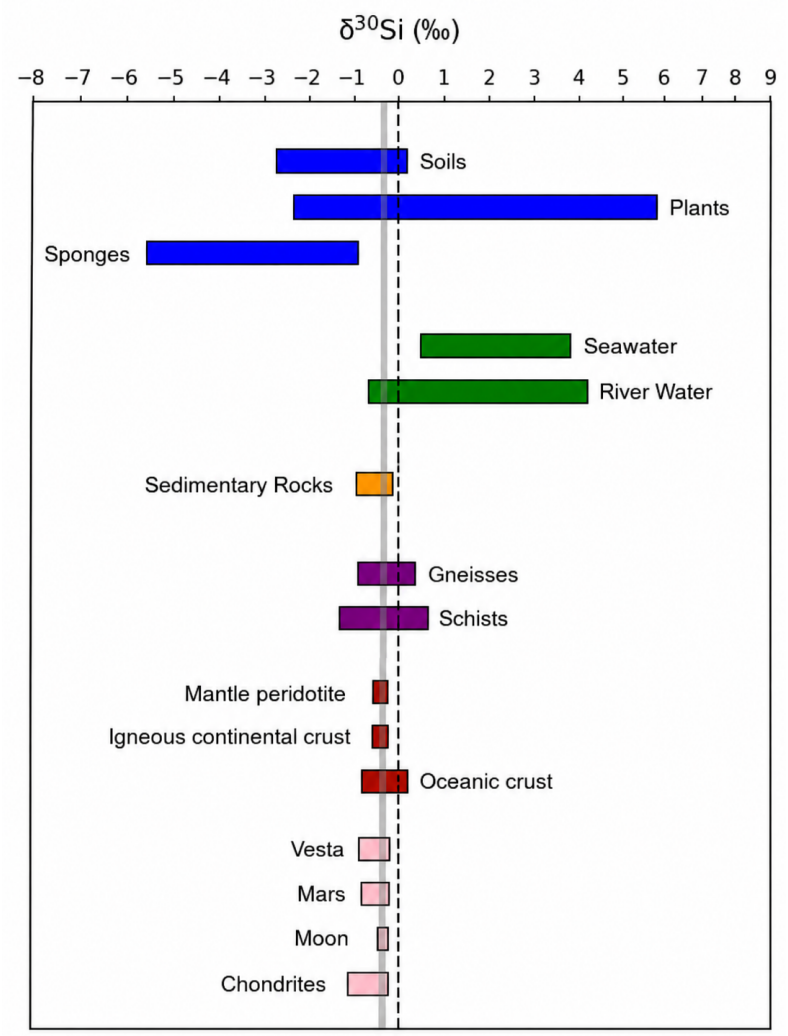


Figure 1.5: Silicon isotope compositions of various geological reservoirs relative to the NBS-28 standard. The grey line represents the BSE composition from Onyett et al. (2023). Figure modified based on data compiled from W. Wang et al. (2019)

Mineral–Mineral and Mineral–Melt Fractionation

High-temperature silicon isotope fractionation is primarily constrained by theoretical studies (F. Huang et al., 2014; Méheut & Schauble, 2014; Méheut et al., 2009; Qin et al., 2016; Rabin et al., 2021, 2023). Experimental constraints remain limited, particularly for mantle conditions.

Recent work by X.-N. Liu et al. (2025) reports small fractionation between minerals and melt, with $\Delta^{30}\mathrm{Si}_{\mathrm{ol/melt}} = -0.001 \pm 0.029\,‰$. Computational approaches combining DFT and molecular dynamics have also been developed (Rabin et al., 2023).

Metal–silicate silicon isotope fractionation has been investigated experimentally

(Hin et al., 2014; Kempl et al., 2016; Shahar et al., 2009, 2011). These studies indicate that equilibrium may be difficult to achieve, although Hin et al. (2014) showed equilibration over time, with Δ^{30}Si values of $-1.48\,‰$ at 1450 °C and $-1.11\,‰$ at 1750 °C.

Table 1.2: Silicon β-factor of minerals relevant to the Earth's mantle from *ab initio* studies.

		$10^3 \ln(\beta) = Ax + Bx^2 + Cx^3 \quad (x = 10^3/T^2)$			Functional
Study	Formula	A	B	C	
Huang et al. (2014)					
Olivine	Mg_2SiO_4	-0.952	1.417	6.749	LDA
Diopside	$CaMgSi_2O_6$	-0.645	0.94	6.795	
Orthopyroxene	$MgSiO_3$	-0.455	0.647	6.985	
Bridgmanite	$MgSiO_3$	-1.264	2.131	3.462	
Qin et al. (2016)					
Olivine	Mg_2SiO_4	7.72691	-0.20034	0.00729	LDA
Diopside	$CaMgSi_2O_6$	7.56179	-0.20489	0.00815	
Rabin et al. (2021)					
Olivine	Mg_2SiO_4	0.0029	-0.1546	7.2781	PBE
Diopside	$CaMgSi_2O_6$	0.0028	-0.1455	6.9465	
Wu et al. (2015)					
Olivine	Mg_2SiO_4	-0.091	7.484	-0.1424	LDA
Bridgmanite	$MgSiO_3$	-0.141	4.542	-0.0214	

1.6 Key Knowledge Gaps

Despite the importance of Si and Mg isotopes as tracers of planetary evolution, several key knowledge gaps remain regarding their behaviour and the models that describe them:

1. **Equilibrium mineral–melt fractionation at high-temperature.** Equilibrium fractionation between minerals and melt remains incompletely constrained. Early experimental studies suggested negligible Mg isotope fraction-

ation (Teng et al., 2007), whereas recent double-spike measurements show measurable, non-zero $\Delta^{26}Mg_{ol-melt}$ (X.-N. Liu et al., 2022).

2. **Validation of DFT calculations at high temperatures.** The accuracy of calculated β-factors depends on several methodological choices, including the exchange–correlation functional, treatment of thermal expansion, and site averaging for different cation sites in minerals (Schauble, 2011; Walker et al., 2026; W. Wang, Wu, et al., 2023). Experimental validation under relevant conditions remains limited.

3. **Lack of a framework for melt β-factors.** A limited established framework exists for calculating melt β-factors directly from atomistic melt structures and probing individual sites. Molecular dynamics studies reveal significant structural heterogeneity in silicate melt (Guillot & Sator, 2007; Rabin et al., 2023), but the isotopic consequences, particularly Mg, of this heterogeneity remain poorly quantified.

4. **Linking isotope fractionation to planetary-scale processes.** The connection between isotope fractionation and the long-term survival of planetary reservoirs remains poorly constrained. In this thesis, I investigate whether equilibrium Mg and Si isotope fractionation during magma ocean crystallisation permits the preservation of large primordial bridgmanite-rich reservoirs consistent with present-day isotopic observations.

This work aims to extend and improve previous Mg- and Si-based DFT fractionation calculations by validating them against experimentally measured mineral–melt fractionation factors. I compare these results with new *ab initio* calculations to improve our understanding of Mg and Si isotope fractionation during magma ocean cooling and to identify potential primordial isotopic signatures that persist to the present day. Ultimately, this study links microscopic isotope–structure relationships with planetary-scale processes, showing how early Earth events have shaped the isotopic composition observed today.

1.7 Structure of the Thesis

This thesis comprises seven chapters built around the key questions outlined in Section 1.1. The structure is as follows:

- **Chapter 1: Introduction**

  Overview of Mg and Si isotope systems, their geochemical behaviour, and key knowledge gaps.

- **Chapter 2: Computational Methods**

  Description of the atomic-scale modelling techniques used in this thesis, including density functional theory, lattice dynamics, and molecular dynamics simulations.

- **Chapter 3: Experimental Methods**

  Description of the experimental approaches used to measure isotope fractionation between minerals and melt.

- **Chapter 4: The magnitude of equilibrium isotope fractionation of Mg between forsterite, diopside, and melt at liquidus temperatures.**

  This chapter quantifies equilibrium Mg isotope fractionation between forsterite, diopside, and melt at liquidus conditions using a combination of experimental and *ab initio* approaches. Experimental results yield $\Delta^{26}\mathrm{Mg}_{\mathrm{ol/melt}} = -0.058\,‰$ and $\Delta^{26}\mathrm{Mg}_{\mathrm{cpx/melt}} = 0.060\,‰$, corresponding to $\Delta^{26}\mathrm{Mg}_{\mathrm{cpx/ol}} = 0.131\,‰$ at 1300 °C, consistent with natural basalt–olivine systems. Atomic-scale modelling using the PBESOL functional, including thermal expansion and site averaging, accurately reproduces experimental results, whereas alternative approaches introduce significant biases. Site averaging in forsterite is shown to be essential to avoid deviations of up to $\pm 0.08\,‰$.

- **Chapter 5: Five-fold Mg in silicate melts drives non-zero Mg isotope fractionation**

This chapter presents a combined molecular dynamics and density functional theory (MD–DFT) framework to quantify isotope fractionation between mantle minerals and silicate melt. Simulations reveal a heterogeneous coordination environment in melt, with Mg predominantly in five- and six-fold coordination. Site-specific calculations show that lower-coordination environments preferentially incorporate heavy Mg isotopes. Weighted averaging of these environments reproduces experimentally observed non-zero mineral–melt fractionation ($\Delta^{26}\mathrm{Mg}_{\mathrm{ol-melt}} \approx 0.02$–$0.08\,‰$). In contrast, Si remains predominantly four-fold coordinated, resulting in negligible equilibrium Si isotope fractionation.

- **Chapter 6: Mg–Si isotopes tightly constrain the primordial bridgmanite reservoir in the present-day Earth's mantle**

  This chapter combines MD–DFT calculations with crystallisation models to quantify Mg and Si isotope fractionation between bridgmanite and melt during early magma ocean crystallisation. Results indicate that significant isotope fractionation develops during early solidification, producing large isotopic contrasts between melt and bridgmanite-rich cumulates. Preservation of such reservoirs would generate mantle-scale isotopic offsets exceeding observed differences between the (accessible) Bulk Silicate Earth and Moon. These findings suggest that large, long-lived primordial reservoirs are unlikely.

- **Chapter 7: Conclusions and Outlook**

  This chapter summarises the thesis and discusses future projects that flow from its results.

Together, these chapters form the thesis entitled:

> *Magnesium and Silicon Isotope Fractionation in Magma Oceans: Seeking New Constraints on Primitive Mantle Heterogeneity.*

Bibliography

Armytage, R. M., Georg, R. B., Savage, P. S., Williams, H. M., & Halliday, A. N. (2011). Silicon isotopes in meteorites and planetary core formation. *Geochimica et Cosmochimica Acta*, *75*(13), 3662–3676.

Ballmer, M. D., Houser, C., Hernlund, J. W., Wentzcovitch, R. M., & Hirose, K. (2017). Persistence of strong silica-enriched domains in the Earth's lower mantle. *Nature Geoscience*, *10*(3), 236–240.

Ballmer, M. D., Spaargaren, R. J., Mallik, A., Manjón-Cabeza Córdoba, A., Nakajima, M., & Vilella, K. (2025). Present-day Earth mantle structure set up by crustal pollution of the basal magma ocean. *Science Advances*, *11*(29), eadu2072.

Blanchard, M., Poitrasson, F., Méheut, M., Lazzeri, M., Mauri, F., & Balan, E. (2009). Iron isotope fractionation between pyrite (FeS2), hematite (Fe2O3) and siderite (FeCO3): A first-principles density functional theory study. *Geochimica et Cosmochimica Acta*, *73*(21), 6565–6578.

Boukaré, C.-É., Badro, J., & Samuel, H. (2025). Solidification of Earth's mantle led inevitably to a basal magma ocean. *Nature*, 1–6.

Bourdon, B., Tipper, E. T., Fitoussi, C., & Stracke, A. (2010). Chondritic Mg isotope composition of the Earth. *Geochimica et Cosmochimica Acta*, *74*(17), 5069–5083.

Boyet, M., & Carlson, R. W. (2005). ^{142}Nd Evidence for Early (>4.53 Ga) Global Differentiation of the Silicate Earth. *Science*, *309*(5734), 576–581.

Brewer, A., Teng, F.-Z., & Dethier, D. (2018). Magnesium isotope fractionation during granite weathering. *Chemical Geology*, *501*, 95–103.

Canup, R. M. (2004). Simulations of a late lunar-forming impact. *Icarus*, *168*(2), 433–456.

Caro, G. (2011). Early Silicate Earth Differentiation. *Annual Review of Earth and Planetary Sciences*, *39*(Volume 39, 2011), 31–58.

Chakrabarti, R., & Jacobsen, S. B. (2010). The isotopic composition of magnesium in the inner Solar System. *Earth and Planetary Science Letters*, *293*(3), 349–358.

Chambers, J. E., & Wetherill, G. W. (1998). Making the Terrestrial Planets: N-Body Integrations of Planetary Embryos in Three Dimensions. *Icarus*, *136*(2), 304–327.

Coath, C. D., Elliott, T., & Hin, R. C. (2017). Double-spike inversion for three-isotope systems. *Chemical Geology*, *451*, 78–89.

Ćuk, M., & Stewart, S. T. (2012). Making the Moon from a Fast-Spinning Earth: A Giant Impact Followed by Resonant Despinning. *Science*, *338*(6110), 1047–1052.

Cuozzo, N., Sletten, R. S., Hu, Y., Liu, L., Teng, F.-Z., & Hagedorn, B. (2020). Silicate weathering in antarctic ice-rich permafrost: Insights using magnesium isotopes. *Geochimica et Cosmochimica Acta*, *278*, 244–260.

Dauphas, N. (2017). The isotopic nature of the Earth's accreting material through time. *Nature*, *541*(7638), 521–524.

Dauphas, N., Poitrasson, F., Burkhardt, C., Kobayashi, H., & Kurosawa, K. (2015). Planetary and meteoritic Mg/Si and δ^{30}Si variations inherited from solar nebula chemistry. *Earth and Planetary Science Letters*, *427*, 236–248.

Deng, H., Ballmer, M. D., Reinhardt, C., Meier, M. M. M., Mayer, L., Stadel, J., & Benitez, F. (2019). Primordial Earth Mantle Heterogeneity Caused by the Moon-forming Giant Impact? *The Astrophysical Journal*, *887*(2), 211.

Deng, X., Chen, Y.-X., Wang, W., Li, Y., Xiao, Z., & Wu, Z. (2024). Heavy magnesium isotopic signatures in arc lavas may be attributed to dehydration of subducting hydrated mantle. *Communications Earth & Environment*, *5*(1), 1–12.

Elkins-Tanton, L. T., Weiss, B. P., & Zuber, M. T. (2011). Chondrites as samples of differentiated planetesimals. *Earth and Planetary Science Letters*, *305*(1), 1–10.

Frings, P. J., Clymans, W., Fontorbe, G., De La Rocha, C. L., & Conley, D. J. (2016). The continental Si cycle and its impact on the ocean Si isotope budget. *Chemical Geology*, *425*, 12–36.

Galy, A., Belshaw, N. S., Halicz, L., & O'Nions, R. K. (2001). High-precision measurement of magnesium isotopes by multiple-collector inductively coupled plasma mass spectrometry. *International Journal of Mass Spectrometry*, *208*(1), 89–98.

Georg, R. B., Halliday, A. N., Schauble, E. A., & Reynolds, B. C. (2007). Silicon in the Earth's core. *Nature*, *447*(7148), 1102–1106.

Gou, L.-L., Zhai, M.-G., Zhang, C.-L., George, P., Huang, K.-J., Xu, X.-F., Lu, J.-S., Zhao, Y., Ao, W.-H., Hu, Y.-H., & Zhou, F. (2022). Validation of clinopyroxene-garnet magnesium isotope geothermometer to constrain the peak metamorphic temperature in ultrahigh-temperature ultramafic-mafic granulites. *American Mineralogist*, *107*(9), 1697–1708.

Guillot, B., & Sator, N. (2007). A computer simulation study of natural silicate melts. Part II: High pressure properties. *Geochimica et Cosmochimica Acta*, *71*(18), 4538–4556.

Gülcher, A. J. P., Ballmer, M. D., & Tackley, P. J. (2021). Coupled dynamics and evolution of primordial and recycled heterogeneity in Earth's lower mantle. *Solid Earth*, *12*(9), 2087–2107.

Guo, B., Zhu, X., Dong, A., Yan, B., Shi, G., & Zhao, Z. (2019). Mg isotopic systematics and geochemical applications: A critical review. *Journal of Asian Earth Sciences*, *176*, 368–385.

Hin, R. C., Coath, C. D., Carter, P. J., Nimmo, F., Lai, Y. J., Pogge von Strandmann, P. A., Willbold, M., Leinhardt, Z. M., Walter, M. J., & Elliott, T. (2017). Magnesium isotope evidence that accretional vapour loss shapes planetary compositions. *Nature*, *549*(7673), 511–527.

Hin, R. C., Fitoussi, C., Schmidt, M. W., & Bourdon, B. (2014). Experimental determination of the Si isotope fractionation factor between liquid metal and liquid silicate. *Earth and Planetary Science Letters*, *387*, 55–66.

Hu, Y., Teng, F.-Z., & Ionov, D. A. (2020). Magnesium isotopic composition of metasomatized upper sub-arc mantle and its implications to Mg cycling in subduction zones. *Geochimica et Cosmochimica Acta*, *278*, 219–234.

Huang, F., Chen, L., Wu, Z., & Wang, W. (2013). First-principles calculations of equilibrium Mg isotope fractionations between garnet, clinopyroxene, orthopyroxene, and olivine: Implications for Mg isotope thermometry. *Earth and Planetary Science Letters*, *367*, 61–70.

Huang, F., Wu, Z., Huang, S., & Wu, F. (2014). First-principles calculations of equilibrium silicon isotope fractionation among mantle minerals. *Geochimica et Cosmochimica Acta*, *140*, 509–520.

Huang, F., Zhang, Z., Lundstrom, C. C., & Zhi, X. (2011). Iron and magnesium isotopic compositions of peridotite xenoliths from Eastern China. *Geochimica et Cosmochimica Acta*, *75*(12), 3318–3334.

Huang, K.-J., Teng, F.-Z., Plank, T., Staudigel, H., Hu, Y., & Bao, Z.-Y. (2018). Magnesium isotopic composition of altered oceanic crust and the global Mg cycle. *Geochimica et Cosmochimica Acta*, *238*, 357–373.

Huang, K.-J., Teng, F.-Z., Shen, B., Xiao, S., Lang, X., Ma, H.-R., Fu, Y., & Peng, Y. (2016). Episode of intense chemical weathering during the termination of the 635 Ma Marinoan glaciation. *Proceedings of the National Academy of Sciences of the United States of America*, *113*(52), 14904–14909.

Huang, K.-J., Teng, F.-Z., Wei, G.-J., Ma, J.-L., & Bao, Z.-Y. (2012). Adsorption- and desorption-controlled magnesium isotope fractionation during extreme weathering of basalt in Hainan Island, China. *Earth and Planetary Science Letters*, *359–360*, 73–83.

Jackson, M. G., & Carlson, R. W. (2011). An ancient recipe for flood-basalt genesis. *Nature*, *476*(7360), 316–319.

Javoy, M., Balan, E., Méheut, M., Blanchard, M., & Lazzeri, M. (2012). First-principles investigation of equilibrium isotopic fractionation of O- and Si-isotopes between refractory solids and gases in the solar nebula. *Earth and Planetary Science Letters*, *319–320*, 118–127.

Kadlag, Y., Tatzel, M., Frick, D. A., & Becker, H. (2019). The origin of unequilibrated EH chondrites – Constraints from in situ analysis of Si isotopes, major and trace elements in silicates and metal. *Geochimica et Cosmochimica Acta*, *267*, 300–321.

Kadlag, Y., Tatzel, M., Frick, D. A., Becker, H., & Kühne, P. (2021). In situ Si isotope and chemical constraints on formation and processing of chondrules in the Allende meteorite. *Geochimica et Cosmochimica Acta*, *304*, 234–257.

Kempl, J., Vroon, P., Van Der Wagt, B., Zinngrebe, E., Frost, D., & Van Westrenen, W. (2016). Silicon stable isotope fractionation between metal and silicate at high-pressure, high-temperature conditions as a tracer of planetary core formation. *Geologie en Mijnbouw/Netherlands Journal of Geosciences*, *95*(2), 113–129.

Klaver, M., Klemme, S., Liu, X.-N., Hin, R. C., Coath, C. D., Anand, M., Lissenberg, C. J., Berndt, J., & Elliott, T. (2024). Titanium-rich basaltic melts on the Moon modulated by reactive flow processes. *Nature Geoscience*, 1–6.

Koelemeijer, P., Schuberth, B. S. A., Davies, D. R., Deuss, A., & Ritsema, J. (2018). Constraints on the presence of post-perovskite in Earth's lowermost mantle from tomographic-geodynamic model comparisons. *Earth and Planetary Science Letters*, *494*, 226–238.

Labrosse, S., Hernlund, J. W., & Coltice, N. (2007). A crystallizing dense magma ocean at the base of the Earth's mantle. *Nature*, *450*(7171), 866–869.

Lambrechts, M., & Johansen, A. (2012). Rapid growth of gas-giant cores by pebble accretion. *Astronomy & Astrophysics*, *544*, A32.

Lambrechts, M., Johansen, A., & Morbidelli, A. (2014). Separating gas-giant and ice-giant planets by halting pebble accretion. *Astronomy & Astrophysics*, *572*, A35.

Li, B., Kung, J., Liu, W., & Liebermann, R. C. (2014). Phase transition and elasticity of enstatite under pressure from experiments and first-principles studies. *Physics of the Earth and Planetary Interiors*, *228*, 63–74.

Li, W.-Y., Teng, F.-Z., Halama, R., Keller, J., & Klaudius, J. (2016). Magnesium isotope fractionation during carbonatite magmatism at Oldoinyo Lengai, Tanzania. *Earth and Planetary Science Letters*, *444*, 26–33.

Li, X., Zhu, G., Ai, Y., Zhang, Z., Chen, W., Li, T., Zhang, Y., & Duan, P. (2025). Using Mg isotopes to constrain the formation temperature of dolomite. *Scientific Reports*, *15*, 10910.

Li, X., Zhao, H., Tang, M., & Liu, Y. (2009). Theoretical prediction for several important equilibrium Ge isotope fractionation factors and geological implications. *Earth and Planetary Science Letters*, *287*(1), 1–11.

Liao, R., Zhu, H., Zhang, L., Li, H., Li, C., He, Y., Sun, W., & Liu, H. (2022). Unusual δ^{26}Mg values in oceanic crust basalts from the South China Sea. *GSA Bulletin*, *135*(1-2), 523–533.

Liu, P.-P., Teng, F.-Z., Dick, H. J. B., Zhou, M.-F., & Chung, S.-L. (2017). Magnesium isotopic composition of the oceanic mantle and oceanic Mg cycling. *Geochimica et Cosmochimica Acta*, *206*, 151–165.

Liu, X.-M., Teng, F.-Z., Rudnick, R. L., McDonough, W. F., & Cummings, M. L. (2014). Massive magnesium depletion and isotope fractionation in weathered basalts. *Geochimica et Cosmochimica Acta*, *135*, 336–349.

Liu, X.-N., Hin, R., Coath, C., van Soest, M., Melekhova, E., & Elliott, T. (2022). Equilibrium olivine-melt Mg isotopic fractionation explains high δ^{26}Mg values in arc lavas. *Geochemical Perspectives Letters*, *22*, 42–47.

Liu, X.-N., Hin, R. C., Coath, C. D., Bizimis, M., Su, L., Ionov, D. A., Takazawa, E., Brooker, R., & Elliott, T. (2023). The magnesium isotopic composition of the mantle. *Geochimica et Cosmochimica Acta*, *358*, 12–26.

Liu, X.-N., Klaver, M., Hin, R. C., Coath, C. D., Bizimis, M., Ionov, D. A., & Elliott, T. (2025). Si isotope composition of Earth's mantle and oceanic basalts. *Geochimica et Cosmochimica Acta*.

Liu, X.-N., Klaver, M., Hin, R. C., Coath, C. D., Ng, H. C., & Elliott, T. (2024). High-precision, mass dependent Si isotope measurements via the critical mixture double-spiking technique. *Journal of Analytical Atomic Spectrometry*, *39*(11), 2799–2808.

McDonough, W., & Sun, S. (1995). The composition of the Earth. *Chemical Geology*, *120*(3-4), 223–253.

McNamara, A. K. (2019). A review of large low shear velocity provinces and ultra low velocity zones. *Tectonophysics*, *760*, 199–220.

Méheut, M., Lazzeri, M., Balan, E., & Mauri, F. (2007). Equilibrium isotopic fractionation in the kaolinite, quartz, water system: Prediction from first-principles density-functional theory. *Geochimica et Cosmochimica Acta*, *71*(13), 3170–3181.

Méheut, M., Lazzeri, M., Balan, E., & Mauri, F. (2009). Structural control over equilibrium silicon and oxygen isotopic fractionation: A first-principles density-functional theory study. *Chemical Geology*, *258*(1), 28–37.

Méheut, M., & Schauble, E. A. (2014). Silicon isotope fractionation in silicate minerals: Insights from first-principles models of phyllosilicates, albite and pyrope. *Geochimica et Cosmochimica Acta*, *134*, 137–154.

Morbidelli, A., Kleine, T., & Nimmo, F. (2025). Did the terrestrial planets of the solar system form by pebble accretion? *Earth and Planetary Science Letters*, *650*, 119120.

Morbidelli, A., Lunine, J., O'Brien, D., Raymond, S., & Walsh, K. (2012). Building Terrestrial Planets. *Annual Review of Earth and Planetary Sciences*, *40*(1), 251–275.

Moulik, P., & Ekström, G. (2016). The relationships between large-scale variations in shear velocity, density, and compressional velocity in the Earth's mantle. *Journal of Geophysical Research: Solid Earth*, *121*(4), 2737–2771.

Moynier, F., Deng, Z., Lanteri, A., Martins, R., Chaussidon, M., Savage, P., & Siebert, J. (2020). Metal-silicate silicon isotopic fractionation and the composition of the bulk Earth. *Earth and Planetary Science Letters*, *549*, 116468.

Mundl, A., Touboul, M., Jackson, M. G., Day, J. M. D., Kurz, M. D., Lekic, V., Helz, R. T., & Walker, R. J. (2017). Tungsten-182 heterogeneity in modern ocean island basalts. *Science*, *356*(6333), 66–69.

Mysen, B. O., Virgo, D., & Seifert, F. A. (1982). The structure of silicate melts: Implications for chemical and physical properties of natural magma. *Reviews of Geophysics*, *20*(3), 353–383.

Onyett, I. J., Schiller, M., Makhatadze, G. V., Deng, Z., Johansen, A., & Bizzarro, M. (2023). Silicon isotope constraints on terrestrial planet accretion. *Nature*, *619*(7970), 539–544.

Onyett, I. J., Schiller, M., Stokholm, M., Bollard, J., & Bizzarro, M. (2024). Silicon isotope compositions of chondritic components: Insights into early disk processes. *Earth and Planetary Science Letters*, *646*, 118985.

Pogge von Strandmann, P. A. E., Elliott, T., Marschall, H. R., Coath, C., Lai, Y.-J., Jeffcoate, A. B., & Ionov, D. A. (2011). Variations of Li and Mg isotope ratios in bulk chondrites and mantle xenoliths. *Geochimica et Cosmochimica Acta*, *75*(18), 5247–5268.

Pogge von Strandmann, P. A. E., Opfergelt, S., Lai, Y.-J., Sigfússon, B., Gislason, S. R., & Burton, K. W. (2012). Lithium, magnesium and silicon isotope behaviour accompanying weathering in a basaltic soil and pore water profile in Iceland. *Earth and Planetary Science Letters*, *339–340*, 11–23.

Poitrasson, F., & Zambardi, T. (2015). An Earth–Moon silicon isotope model to track silicic magma origins. *Geochimica et Cosmochimica Acta*, *167*, 301–312.

Pringle, E. A., Moynier, F., Savage, P. S., Badro, J., & Barrat, J.-A. (2014). Silicon isotopes in angrites and volatile loss in planetesimals. *Proceedings of the National Academy of Sciences*, *111*(48), 17029–17032.

Qin, T., Wu, F., Wu, Z., & Huang, F. (2016). First-principles calculations of equilibrium fractionation of O and Si isotopes in quartz, albite, anorthite, and zircon. *Contributions to Mineralogy and Petrology*, *171*(11), 91.

Rabin, S., Blanchard, M., Pinilla, C., Poitrasson, F., & Gregoire, M. (2021). First-principles calculation of iron and silicon isotope fractionation between Fe-bearing minerals at magmatic temperatures: The importance of second atomic neighbors. *Geochimica et Cosmochimica Acta*, *304*, 101–118.

Rabin, S., Blanchard, M., Pinilla, C., Poitrasson, F., & Grégoire, M. (2023). Iron and silicon isotope fractionation in silicate melts using first-principles molecular dynamics. *Geochimica et Cosmochimica Acta*, *343*, 212–233.

Raymond, S. N., O'Brien, D. P., Morbidelli, A., & Kaib, N. A. (2009). Building the terrestrial planets: Constrained accretion in the inner Solar System. *Icarus*, *203*(2), 644–662.

Ritsema, J., Deuss, A., van Heijst, H. J., & Woodhouse, J. H. (2011). S40RTS: A degree-40 shear-velocity model for the mantle from new Rayleigh wave dispersion, teleseismic traveltime and normal-mode splitting function measurements. *Geophysical Journal International*, *184*(3), 1223–1236.

Rizo, H., Walker, R. J., Carlson, R. W., Touboul, M., Horan, M. F., Puchtel, I. S., Boyet, M., & Rosing, M. T. (2016). Early Earth differentiation investigated

through ^{142}Nd, ^{182}W, and highly siderophile element abundances in samples from Isua, Greenland. *Geochimica et Cosmochimica Acta*, *175*, 319–336.

Rustad, J. R., & Dixon, D. A. (2009). Prediction of Iron-Isotope Fractionation Between Hematite (α-Fe2O3) and Ferric and Ferrous Iron in Aqueous Solution from Density Functional Theory. *The Journal of Physical Chemistry A*, *113*(44), 12249–12255.

Savage, P. S. (2011). *Silicon isotopes and the development of the Earth* [http://purl.org/dc/dcmitype/Text]. Oxford University, UK.

Savage, P. S., Georg, R. B., Williams, H. M., & Halliday, A. N. (2013). The silicon isotope composition of the upper continental crust. *Geochimica et Cosmochimica Acta*, *109*, 384–399.

Savage, P. S., Georg, R. B., Williams, H. M., Turner, S., Halliday, A. N., & Chappell, B. W. (2012). The silicon isotope composition of granites. *Geochimica et Cosmochimica Acta*, *92*, 184–202.

Schauble, E. A. (2004). Applying Stable Isotope Fractionation Theory to New Systems. *Reviews in Mineralogy and Geochemistry*, *55*(1), 65–111.

Schauble, E. A. (2011). First-principles estimates of equilibrium magnesium isotope fractionation in silicate, oxide, carbonate and hexaaquamagnesium(2+) crystals. *Geochimica et Cosmochimica Acta*, *75*(3), 844–869.

Schiller, M., Dallas, J., Creech, J., Bizzarro, M., & Baker, J. (2017). Tracking the formation of magma oceans in the Solar System using stable magnesium isotopes. *Geochemical Perspectives Letters*, 22–31.

Shahar, A., Hillgren, V. J., Young, E. D., Fei, Y., Macris, C. A., & Deng, L. (2011). High-temperature Si isotope fractionation between iron metal and silicate. *Geochimica et Cosmochimica Acta*, *75*(23), 7688–7697.

Shahar, A., Ziegler, K., Young, E. D., Ricolleau, A., Schauble, E. A., & Fei, Y. (2009). Experimentally determined Si isotope fractionation between silicate and Fe metal and implications for Earth's core formation. *Earth and Planetary Science Letters*, *288*(1), 228–234.

Sikdar, J., & Rai, V. K. (2021). Mg isotope variations in microphases of unequilibrated enstatite chondrites. *Meteoritics & Planetary Science*, *56*(8), 1459–1477.

Stixrude, L., de Koker, N., Sun, N., Mookherjee, M., & Karki, B. B. (2009). Thermodynamics of silicate liquids in the deep Earth. *Earth and Planetary Science Letters*, *278*(3), 226–232.

Stracke, A., Tipper, E. T., Klemme, S., & Bizimis, M. (2018). Mg isotope systematics during magmatic processes: Inter-mineral fractionation in mafic to ultramafic Hawaiian xenoliths. *Geochimica et Cosmochimica Acta*, *226*, 192–205.

Tanaka, R., Potiszil, C., & Nakamura, E. (2021). Silicon and Oxygen Isotope Evolution of the Inner Solar System. *The Planetary Science Journal*, *2*(3), 102.

Teng, F.-Z., Li, W.-Y., Rudnick, R. L., & Gardner, L. R. (2010). Contrasting lithium and magnesium isotope fractionation during continental weathering. *Earth and Planetary Science Letters*, *300*(1), 63–71.

Teng, F.-Z., Wadhwa, M., & Helz, R. T. (2007). Investigation of magnesium isotope fractionation during basalt differentiation: Implications for a chondritic composition of the terrestrial mantle. *Earth and Planetary Science Letters*, *261*(1), 84–92.

Urey, H. C. (1947). The thermodynamic properties of isotopic substances. *Journal of the Chemical Society (Resumed)*, (0), 562–581.

Villeneuve, J., Marrocchi, Y., & Jacquet, E. (2020). Silicon isotopic compositions of chondrule silicates in carbonaceous chondrites and the formation of primordial solids in the accretion disk. *Earth and Planetary Science Letters*, *542*, 116318.

Walker, A. M., Hin, R. C., & Elliott, T. (2026). Controls on Mg isotopic fractionation between deep mantle phases and relict signatures of a terrestrial magma ocean. *Geochimica et Cosmochimica Acta*, *425*, 131–142.

Wang, S.-J., Teng, F.-Z., & Scott, J. M. (2016). Tracing the origin of continental HIMU-like intraplate volcanism using magnesium isotope systematics. *Geochimica et Cosmochimica Acta*, *185*, 78–87.

Wang, S.-J., Teng, F.-Z., Williams, H. M., & Li, S.-G. (2012). Magnesium isotopic variations in cratonic eclogites: Origins and implications. *Earth and Planetary Science Letters*, *359–360*, 219–226.

Wang, W., Wei, H.-Z., Jiang, S.-Y., Liu, X., Lei, F., Lin, Y.-B., & Zhao, Y. (2019). Silicon Isotope Geochemistry: Fractionation Linked to Silicon Complexations and Its Geological Applications. *Molecules*, *24*(7), 1415.

Wang, W., Walter, M. J., Brodholt, J. P., Huang, S., & Petaev, M. I. (2023). Chalcogen isotopes reveal limited volatile contribution from late veneer to Earth. *Science Advances*, *9*(49), eadh0670.

Wang, W., Wu, Z., Huang, S., & Huang, F. (2023). First-principles investigation of equilibrium magnesium isotope fractionation among mantle minerals: Review and new data. *Earth-Science Reviews*, *237*, 104315.

Wang, Y., Deng, J., Liao, R., Chen, L., Li, D., Liu, H., & Sun, W. (2023). Magnesium isotopic composition of the Mariana forearc serpentinite: Implications for Mg isotopic composition of the mantle wedge and Mg isotopic fractionation during mantle wedge serpentinization. *Chemical Geology*, *624*.

Wu, Z., Huang, F., & Huang, S. (2015). Isotope fractionation induced by phase transformation: First-principles investigation for Mg2SiO4. *Earth and Planetary Science Letters*, *409*, 339–347.

Young, E. D., Tonui, E., Manning, C. E., Schauble, E., & Macris, C. A. (2009). Spinel-olivine magnesium isotope thermometry in the mantle and implications for the Mg isotopic composition of Earth. *Earth and Planetary Science Letters*, *288*(3-4), 524–533.

Yu, H.-M., Li, Y.-H., Gao, Y.-J., Huang, J., & Huang, F. (2018). Silicon isotopic compositions of altered oceanic crust: Implications for Si isotope heterogeneity in the mantle. *Chemical Geology*, *479*, 1–9.

Zambardi, T., Lundstrom, C. C., Li, X., & McCurry, M. (2014). Fe and Si isotope variations at Cedar Butte volcano; insight into magmatic differentiation. *Earth and Planetary Science Letters*, *405*, 169–179.

Zambardi, T., & Poitrasson, F. (2011). Precise Determination of Silicon Isotopes in Silicate Rock Reference Materials by MC-ICP-MS. *Geostandards and Geoanalytical Research*, *35*(1), 89–99.

Zhong, Y., Chen, L.-H., Wang, X.-J., Zhang, G.-L., Xie, L.-W., & Zeng, G. (2017). Magnesium isotopic variation of oceanic island basalts generated by partial melting and crustal recycling. *Earth and Planetary Science Letters*, *463*, 127–135.

"In theory, there is no difference between theory and practice. In practice, there is."

— Richard P. Feynman

2

Methodology – Computational

Contents

2.1 Density functional theory 39
2.1.1 Hohenberg–Kohn theorems 40
2.1.2 Kohn–Sham approach 41
2.1.3 Exchange–correlation functionals and approximations . 42
2.1.4 Choice of exchange–correlation functional for this study 43
2.1.5 Bloch theorem 43
2.1.6 Basis set 44
2.1.7 CASTEP implementation 44
2.2 Geometry optimisation 46
2.2.1 Potential energy surface 46
2.2.2 Geometry optimisation 47
2.2.3 Optimisation algorithms 48
2.2.4 Dispersion forces 49
2.2.5 CASTEP implementation 50
2.3 Lattice dynamics 51
2.3.1 Vibrational motion in crystalline solids 51
2.3.2 Harmonic approximation 52
2.3.3 Dynamical matrix and phonon frequencies 53
2.3.4 Isotope fractionation and vibrational properties 54
2.3.5 Limitations of the harmonic approximation 55
2.3.6 CASTEP implementation 55
2.4 Molecular dynamics 56
2.4.1 Moving atoms in the liquid state 56
2.4.2 Ergodicity principle 57
2.4.3 Equations of motion 57
2.4.4 Thermodynamic particle ensembles 58
2.4.5 Thermostats 58
2.4.6 Snapshot techniques versus other techniques 59

2.4.7 CASTEP implementation 61

This thesis combines quantum-mechanical theory, first-principles computational modelling, molecular dynamics simulations, and high-temperature experimental petrology to investigate equilibrium isotope fractionation of magnesium (Mg) and silicon (Si) in minerals and silicate melts under conditions relevant to planetary interiors. Because isotope fractionation at high temperatures is governed by subtle differences in atomic bonding environments and vibrational behaviour, a rigorous theoretical and methodological framework is required to link atomic-scale processes to measurable isotopic signatures.

Over the past decades, first-principles computational methods have become the primary tool for addressing this problem. Among these, density functional theory (DFT) has become the standard approach for calculating the electronic structure of condensed matter systems. The formal foundations of DFT were established by Hohenberg and Kohn (Hohenberg & Kohn, 1964), who demonstrated that its electron density uniquely determines the ground-state properties of an interacting electron system, and by Kohn and Sham (Kohn & Sham, 1965), who introduced a practical scheme for solving the resulting equations. Although the theoretical framework has been in place for several decades, the widespread application of DFT has been enabled by advances in computational power and the development of efficient numerical implementations, particularly for periodic systems using plane-wave basis sets and pseudopotentials (Payne et al., 1992; Vanderbilt, 1990). DFT is now widely used across physics, chemistry, and materials science to investigate crystal structures, phase stability, elastic properties, and vibrational behaviour. In the geosciences, it has been applied extensively to study mineral properties at high pressures and temperatures and to calculate equilibrium isotope fractionation factors from first principles (Huang et al., 2013, 2014; Schauble, 2004).

More detailed explanations of the theoretical foundations of DFT can be found in textbooks such as Martin, 2020; Parr, 1980; Sholl and Steckel, 2022, while broader perspectives on its development and application can be found in review articles

by Jones, 2015; Kohn, 1999. These works provide the necessary background for the more detailed discussions presented in the following sections.

This chapter outlines the computational methodology used throughout this study. Section 2.1 introduces the key principles of density functional theory relevant to the calculation of energies and forces in periodic systems. Section 2.2 describes geometry optimisation and the determination of equilibrium structures. Section 2.3 develops lattice dynamics, focusing on the harmonic approximation and the calculation of vibrational frequencies. Section 2.4 presents molecular dynamics as a method for modelling atomic motion in silicate melts. Detailed theoretical formulations are provided within each section, with emphasis on the aspects most relevant to isotope fractionation.

All calculations in this study were performed using the CASTEP computational code. CASTEP (Cambridge Sequential Total Energy Package) was developed in the late 1980s and early 1990s at the University of Cambridge (Segall et al., 2002), building on earlier advances in plane-wave density functional theory and pseudopotential methods, as well as on the Car–Parrinello framework for ab initio molecular dynamics (Car & Parrinello, 1985). The code has since evolved into a robust, widely used platform for first-principles simulations of condensed-matter systems. Its implementation of plane-wave basis sets and periodic boundary conditions makes it particularly well suited to modelling crystalline minerals, while its capabilities for phonon calculations and ab initio molecular dynamics allow for a consistent treatment of vibrational and finite-temperature properties.

In this work, CASTEP is used to calculate total energies, optimise crystal structures, compute phonon frequencies, and perform molecular dynamics simulations for both minerals and silicate melts. These calculations provide the fundamental quantities required to determine equilibrium isotope fractionation factors and to investigate their dependence on pressure, temperature, and atomic-scale structure. The following sections describe the theoretical framework and computational implementation in detail. Specific parameter choices and implementations are described in Chapters 4, 5, & 6.

2.1 Density functional theory

The description of isotope fractionation at the atomic scale requires an accurate determination of the electronic ground state and the interatomic forces that arise from it. Within the Born–Oppenheimer approximation (Born & Oppenheimer, 1927), this problem reduces to solving the Schrödinger equation for a system of interacting electrons in the field of fixed nuclei. However, for systems of practical relevance, such as crystalline minerals or silicate melts, the direct solution of the many-body Schrödinger equation is computationally intractable due to the exponential scaling of the many-electron wavefunction with system size. A more efficient formulation is therefore required to make first-principles calculations feasible.

Density functional theory (DFT) provides such a framework by reformulating the quantum-mechanical problem in terms of the electron density rather than the many-electron wavefunction. This represents a fundamental simplification, as the electron density depends only on three spatial coordinates, regardless of the number of electrons in the system. In doing so, DFT retains the essential physics governing electron interactions while reducing the computational complexity to a level that allows practical calculations for periodic solids and complex silicate systems.

In this study, DFT serves as the foundation for all first-principles calculations. It provides total energies and interatomic forces, which define the potential energy surface of a system. These quantities are central to the subsequent methodology: the equilibrium structure of a mineral is obtained by minimising the total energy, while the forces acting on atoms determine their vibrational behaviour. In particular, the second derivatives of the total energy with respect to atomic displacements yield force constants that determine vibrational frequencies. Since equilibrium isotope fractionation depends directly on differences in these vibrational frequencies, DFT provides the critical link between electronic structure and isotope systematics.

A further advantage of DFT is its natural compatibility with periodic boundary conditions, which are required for modelling crystalline materials. Minerals are inherently periodic, and their electronic structure must reflect this symmetry. In practical implementations, this periodicity is exploited through reciprocal-space

formulations, enabling efficient plane-wave calculations. When combined with molecular dynamics, the same framework can be extended to disordered systems such as silicate melts, enabling a consistent treatment of both solid and liquid phases within a unified approach.

Despite this conceptual simplification, DFT does not eliminate all the challenges associated with the quantum-mechanical problem. In particular, the exact relationship between electron density and total energy is not known and must be approximated. The success of DFT, therefore, depends on the formulation of appropriate energy functionals and on practical schemes for solving the resulting equations. These aspects are introduced in the following sections: first, the Hohenberg–Kohn theorems, which provide the formal basis of the theory; and second, the Kohn–Sham approach, which enables its practical implementation.

2.1.1 Hohenberg–Kohn theorems

Calculating wave functions to approach electron density is overly complex without approximations or supporting theorems. DFT takes a different approach by reformulating the problem in terms of electron density. First described by Pierre Hohenberg and Walter Kohn (Hohenberg & Kohn, 1964), the Hohenberg–Kohn theorems describe two fundamental principles of DFT:

1. For a system of interacting electrons in an external potential, the ground-state electron density uniquely determines that potential, up to a constant (Hohenberg & Kohn, 1964). This implies that the ground-state wave functional can be written as a function of the electron density and, subsequently, the ground-state energy.

2. The ground-state energy is obtained by minimising the energy functional with respect to the electron density (Sholl & Steckel, 2022).

By applying these principles, DFT maps energy to electron density and replaces the many-electron wavefunction with the electron density as the fundamental variable. Here, DFT involves simplifying steps that transform a multidimensional

problem into a scalar field, resulting in an energy function (Segall et al., 2002). The theory of DFT provides a formal guarantee that the electron density determines the ground-state energy, but in practice, the exact form of the energy functional remains unknown.

2.1.2 Kohn–Sham approach

To use DFT for practical molecular modelling, the Kohn–Sham (KS) equations are needed, which are used when the second principle of DFT is coupled to the energy functional of Eq. (2.1) (Kohn & Sham, 1965). Kohn and Sham identified a lack of a kinetic-energy functional in traditional DFT, which prevented accurate calculations. They solve this problem by reintroducing wave functions, since the density is written in terms of the electrons that are not interacting with each other, i.e. the non-interacting KS electrons. This is necessary to incorporate kinetic energy into the equation fully. The KS equations, therefore, represent a total energy functional for the sum of the molecular orbital kinetic part and a functional of density for the rest of the energy.

$$E[n] = E_{\text{kin,KS}}[n] + E_{\text{coul}}[n] + E_{\text{ext}}[n] + \Big(E_{\text{kin}}[n] - E_{\text{kin,KS}}[n]\Big) + E_{\text{xc}}[n] \qquad (2.1)$$

Where the term $E_{\text{kin,KS}}[n]$ has been added as the energy of non-interacting Kohn–Sham electrons.

The Kohn–Sham method enables the solution of the Schrödinger equation with a certain degree of simplicity. However, problems still arise as a result of $E'_{\text{xc}}[n]$, which is the exchange-correlation function that relies on the Hartree potential, $E_{\text{hartree}}[n]$. This term is the potential arising from the electron charge distribution and is therefore dependent on the electron density. To determine this electron density, the Kohn–Sham equations need to be solved. This leads to a self-consistent problem requiring iterative solution.

2.1.3 Exchange–correlation functionals and approximations

The addition of Kohn–Sham non-interacting electrons introduces additional complexity that requires approximation. To solve the $E'_{\mathrm{xc}}[n]$ functional, a suitable approximation must be introduced to calculate the exchange-correlation contribution and solve the DFT equation. The initial approximation used in studies is the Local Density Approximation (LDA), which was introduced alongside the previously discussed Kohn–Sham equation (Kohn & Sham, 1965). This approximation states that $E'_{\mathrm{xc}}[n]$ can be represented as the exchange-correlation energy of a uniform electron gas for each infinitesimal element of density in the DFT equations. Electron density, however, is in most cases non-uniform around atoms and therefore the LDA approximation is often inaccurate. Nevertheless, LDA has historically been an important approximation that has enabled DFT calculations while still producing results that can be justified.

Since the development of LDA, many other exchange-correlation approximations have become available, notably the Perdew–Burke–Ernzerhof (PBE: Perdew et al. (1996)) and the revised version, Perdew–Burke–Ernzerhof for solids (PBEsol: Perdew et al. (2008)). These approximations are based on Generalised Gradient Approximations (GGA), a variation of LDA that incorporates the density gradient to compensate for LDA's lack of spatial variation (Perdew et al., 1992). Traditional GGA-based methods, such as PBE, thus compute the density and its gradient at each point within the system. PBE, however, has its limitations. It overestimates lattice constants by about 1% (Perdew et al., 2008) and therefore overestimates equilibrium properties related to lattice constants. Phonon frequencies and bulk modulus are often underestimated. PBEsol addresses this by restoring the gradient expansion for exchange in slowly varying densities, which results in better approximations for $E'_{\mathrm{xc}}[n]$ in solid-state systems. In summary, the choice of exchange–correlation functional introduces systematic uncertainty into predicted structural and vibrational properties, potentially affecting calculated isotope fractionation factors.

2.1.4 Choice of exchange–correlation functional for this study

In this thesis, our CASTEP calculations were performed using the PBEsol exchange–correlation functional, a revised GGA functional specifically designed to improve the description of equilibrium properties of solids. PBEsol restores the density-gradient expansion for exchange, resulting in more accurate lattice constants, bulk moduli, and phonon frequencies for crystalline materials.

Previous studies have demonstrated that accurate vibrational frequencies are critical for reliable equilibrium isotope fractionation calculations, as fractionation factors depend sensitively on force constants and vibrational spectra (Huang et al., 2013, 2014; Schauble, 2011). By improving the structural and vibrational description of minerals, PBEsol provides a more reliable basis for calculating reduced partition function ratios and mineral–melt fractionation factors.

The use of PBEsol in this study, therefore, represents a deliberate methodological choice aimed at minimising systematic errors in vibrational properties and enhancing the robustness of calculated isotope fractionation factors. The implications of this choice, along with comparisons to alternative functionals, are discussed where relevant in later chapters.

2.1.5 Bloch theorem

To solve the Schrödinger equation, and subsequently DFT, for crystalline minerals, which are periodic systems, one must use Bloch's theorem. This theorem (Bloch, 1929) states that an electronic wavefunction can be expressed as a plane wave multiplied by a periodic function. This introduces the idea of k-point sampling for the supercell. As the effect of k-point sampling becomes limited when k-points are close together, we can approximate our calculations using a finite number of k-points. In DFT codes, the wavefunctions are therefore used in combination with Bloch's theorem, and k-points are sampling points in reciprocal space used to integrate over the Brillouin zone.

2.1.6 Basis set

The k-point grids are chosen by fixing a geometry optimisation for each mineral and varying the k-point grid to minimise numerical error during convergence testing. In general, a larger k-point grid for a chosen mineral (e.g. $2\times1\times2$ or $4\times2\times4$) increases the accuracy of the calculation that is needed for convergence. However, large k-point grids result in longer calculation times; therefore, a balance between accuracy and computational cost is necessary. For each mineral structure, the k-point cell is tested before further geometry optimisations. The reciprocal k vectors are defined in three dimensions, $\mathbf{b}_1$, $\mathbf{b}_2$, $\mathbf{b}_3$, and are linked to real lattice vectors. An increase in real lattice vectors results in a decrease in reciprocal lattice vectors. The volume of reciprocal space can be expressed with Ω_{BZ}, otherwise known as the first Brillouin zone (BZ). For each mineral structure, the number of k-points can be reduced by applying symmetry and therefore lessening the number of irreducible k-points.

2.1.7 CASTEP implementation

The DFT implementation in CASTEP uses the plane-wave pseudopotential formalism (Milman et al., 2010). In this approach, the valence electronic wavefunctions are expanded in a plane-wave basis, while pseudopotentials represent the core electrons. The use of pseudopotentials greatly reduces the number of explicitly treated electrons, thereby lowering computational cost without sacrificing the accuracy required for structural and vibrational calculations. For the systems considered here, this is particularly important because Mg- and Si-bearing minerals contain relatively light elements with well-defined valence structures, making them especially amenable to pseudopotential treatment. The pseudopotentials used in CASTEP are designed to reproduce the scattering properties of an all-electron system within the valence region, thereby retaining the material's essential chemistry while avoiding the prohibitive cost of a full all-electron calculation.

A key numerical parameter in any plane-wave calculation is the kinetic cut-off energy, which determines the maximum energy of the plane waves included in the basis set. Low cut-off energies reduce computational expense, but if the cut-off is

too low, the basis set becomes incomplete, and the calculated energies, forces, and vibrational frequencies may become inaccurate. Conversely, higher cut-off energies improve numerical convergence but substantially increase computational cost. For this reason, the cut-off energy must be carefully tested for each mineral structure before production calculations are carried out. In this study, convergence tests were performed by monitoring the total energy as a function of cut-off energy, as illustrated by the example convergence curve shown in Figure 2.1. The chosen cut-off energy was taken from the plateau region of the curve, where further increases in cut-off produced only negligible changes in the total energy. This ensures that the basis set is sufficiently complete for reliable geometry optimisation and phonon calculations.

The choice of cut-off energy is closely linked to the pseudopotentials used in the calculation. Softer pseudopotentials generally allow lower cut-off energies, whereas harder pseudopotentials require larger basis sets to achieve convergence. The final choice, therefore, reflects a balance between computational efficiency and accuracy. Because isotope fractionation depends on subtle differences in vibrational frequencies, even small numerical errors can propagate into the calculated reduced partition function ratios. It is therefore essential that the cut-off energy is high enough to ensure convergence not only of total energies, but also of forces, stresses, and phonon frequencies (Gonze & Lee, 1997).

The reciprocal-space formulation used by CASTEP also requires careful sampling of the Brillouin zone using k-points. As discussed earlier in this chapter, the density of the k-point grid controls the accuracy of the calculated electronic structure. In practice, the k-point mesh was converged for each structure by increasing the grid density until changes in total energy and forces became negligible. Smaller unit cells require denser k-point sampling than larger ones, whereas symmetry can substantially reduce the number of irreducible k-points that must be calculated. The final k-point meshes were therefore selected based on convergence tests for each mineral system before geometry optimisation.

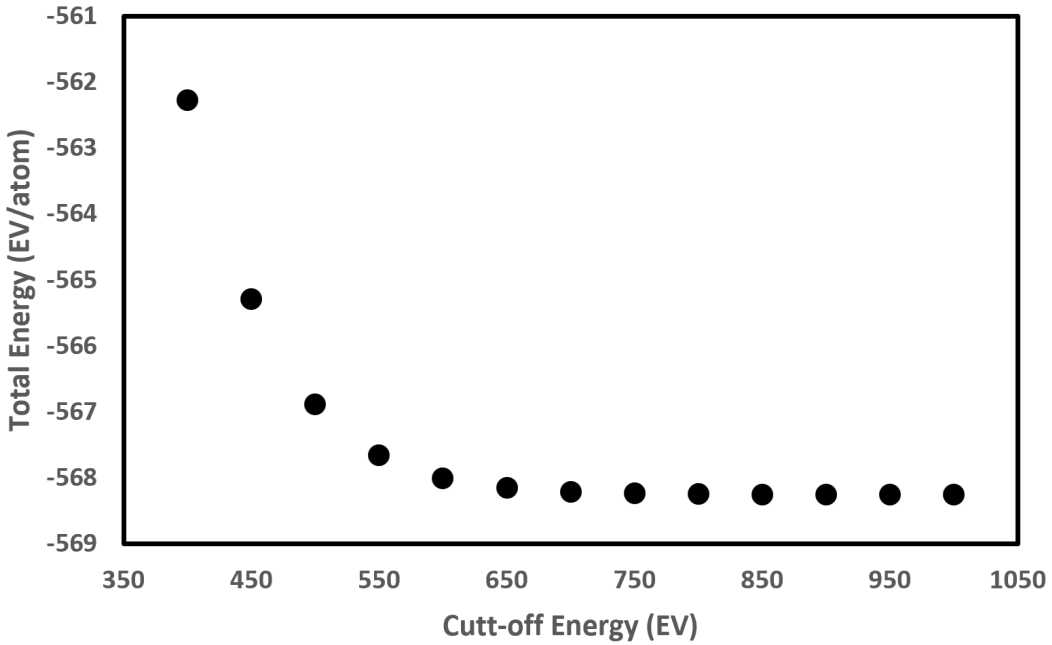


Figure 2.1: Convergence of the total energy of a diopside structure with respect to plane-wave cut-off energy, used to calibrate CASTEP calculations in this study.

2.2 Geometry optimisation

2.2.1 Potential energy surface

To investigate atomic structures under conditions relevant to planetary interiors, such as those in magma oceans, it is necessary to describe how the system's energy depends on atomic configuration. At high temperatures and pressures, minerals can adopt multiple structural arrangements, each associated with a distinct total energy. Determining which of these configurations is stable requires a formal description of the relationship between atomic positions and system energy.

This relationship is expressed through the potential energy surface (PES), a multidimensional function that maps the system's total energy as a function of its nuclear coordinates. Any displacement of atoms, whether through bond stretching, bending, or rotational motion, results in a change in the total energy. These changes reflect variations in interatomic distances and bonding environments, which ultimately determine the stability of a given structure. The concept of the potential

energy surface was first introduced by Marcellin (1913) and later developed in the context of chemical reaction theory by Eyring (1935).

For a system containing N atoms, the PES depends on all atomic coordinates. In Cartesian space, this corresponds to $3N$ degrees of freedom, while in internal coordinates (excluding overall translation and rotation), the number reduces to $3N-6$. Even for relatively simple mineral systems, this results in a high-dimensional energy landscape. Despite this complexity, the key features of the PES can be understood in terms of its stationary points, where the energy gradient with respect to atomic positions vanishes.

Among these stationary points, minima correspond to stable or metastable configurations, while saddle points represent transition states between different structures. In this study, the primary objective is to identify the minimum-energy configurations corresponding to equilibrium crystal structures under specified pressure and temperature conditions. These configurations provide the structural basis for subsequent calculations of vibrational properties and isotope fractionation.

Figure 2.2 illustrates a simplified two-dimensional representation of a potential energy surface, highlighting the location of energy minima and the pathways connecting them. Although real systems exist in a much higher-dimensional space, this schematic provides a useful conceptual framework for understanding the optimisation process.

2.2.2 Geometry optimisation

Geometry optimisation is the numerical procedure used to locate minima on the potential energy surface. In practice, this involves solving a multidimensional minimisation problem in which the total energy is expressed as a function of atomic coordinates. The equilibrium configuration of a system is defined by vanishing first derivatives of the energy with respect to all coordinates, together with a positive-definite Hessian, indicating a stable minimum.

Starting from an initial atomic configuration, the optimisation proceeds iteratively. At each step, the forces acting on the atoms are calculated and used

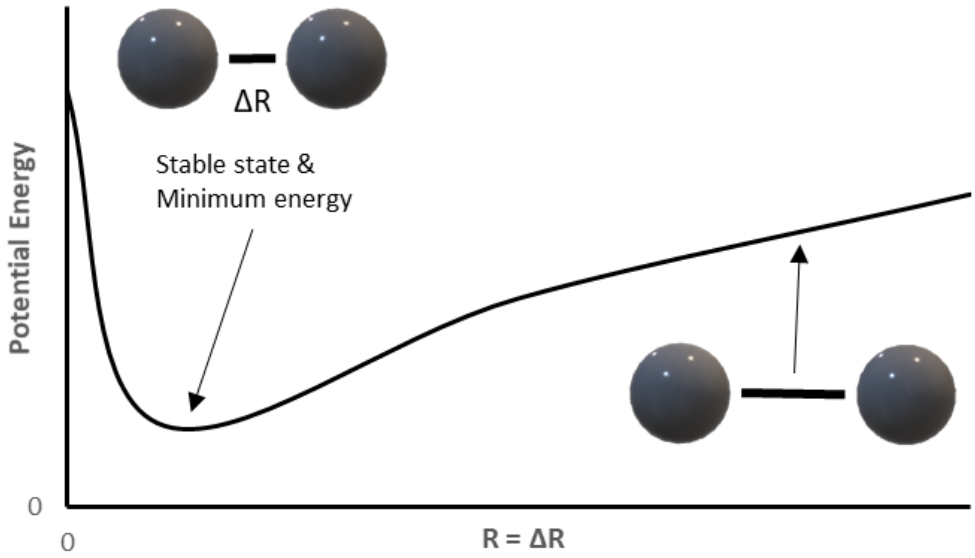


Figure 2.2: Two-dimensional visualisation of a potential energy surface.

to update their positions in a direction that reduces the total energy. These forces correspond to the negative gradient of the potential energy surface and therefore point towards lower-energy configurations. The process is repeated until convergence is achieved, typically defined by thresholds on forces, total energy changes, and, in periodic systems, stress.

The accuracy of the final optimised structure depends on both the quality of the underlying electronic structure calculation and the robustness of the minimisation algorithm. Because the optimised geometry defines the equilibrium bonding environment, it directly influences all subsequent calculations, including vibrational frequencies and isotope fractionation factors. Ensuring that the system has reached a true minimum on the PES is therefore essential.

2.2.3 Optimisation algorithms

A variety of numerical methods exist for solving the energy minimisation problem. These methods can broadly be classified into non-derivative and derivative-based approaches. Historically, non-derivative methods were often employed due to limited computational resources, as they do not require explicit calculation of forces.

However, with modern computational capabilities and the availability of analytical forces in DFT, derivative-based methods have become standard.

Among these, conjugate gradient methods have been widely used in early implementations of plane-wave DFT (Payne et al., 1992). In this approach, the search direction at each iteration is constructed from the current energy gradient and the previous search direction, ensuring that successive directions are conjugate. This significantly improves convergence compared to simple steepest-descent methods, particularly in high-dimensional systems.

The conjugate gradient method proceeds by performing a line search along a chosen direction to locate the minimum energy along that path. Once this point is found, the search direction is updated based on the new gradient, and the process is repeated. This method efficiently navigates the potential energy surface by avoiding redundant exploration of previously minimised directions.

In modern implementations, quasi-Newton methods such as the Broyden–Fletcher–Goldfarb–Shanno (BFGS) algorithm are preferred. These methods construct an approximate Hessian matrix, which describes the curvature of the potential energy surface. By incorporating information about both gradients and curvature, BFGS provides more accurate search directions and step sizes, leading to faster and more reliable convergence. Additionally, the method allows for the simultaneous optimisation of atomic positions and lattice parameters, making it particularly suitable for modelling crystalline materials under varying pressure conditions.

2.2.4 Dispersion forces

Density functional theory offers a solid basis for understanding interatomic forces, but some types are harder to model accurately. Specifically, long-range dispersion interactions, also called London dispersion forces, result from correlated fluctuations in electron density that create temporary dipoles between atoms. Since these interactions are non-local, standard exchange–correlation functionals like LDA or GGA often fail to describe them effectively.

In many mineral systems, dispersion forces are weaker than main bonding interactions like ionic or covalent bonds. Consequently, their impact on the total energy is usually minor and unlikely to influence the optimised structure significantly. However, in systems where weak interactions play a larger role, ignoring dispersion can lead to systematic errors in the computed geometries and energies.

To address these effects, dispersion corrections can be added either using empirical methods or advanced exchange–correlation functionals that incorporate non-local interactions. In this study, dispersion effects are deemed secondary for the Mg- and Si-bearing minerals examined. However, their potential impact highlights a limitation of standard DFT methods and is taken into account when assessing the accuracy of the results.

2.2.5 CASTEP implementation

Geometry optimisation calculations in this study were performed using the CASTEP code within the framework of density functional theory. The optimisation procedure relies on the calculation of atomic forces, obtained directly from the electronic ground state via the Hellmann–Feynman theorem. These forces correspond to the gradient of the total energy with respect to atomic positions and are used iteratively to locate the minimum of the potential energy surface.

In CASTEP, geometry optimisation is carried out using efficient numerical minimisation algorithms, most commonly the Broyden–Fletcher–Goldfarb–Shanno (BFGS) method. This quasi-Newton approach constructs and updates an approximate Hessian matrix during the optimisation, allowing both the direction and magnitude of atomic displacements to be determined more accurately than in simple gradient-based methods. As a result, the BFGS algorithm typically achieves rapid and stable convergence, even for systems with many degrees of freedom.

For crystalline materials, both atomic coordinates and lattice parameters can be optimised simultaneously. This is particularly important for mineral systems at high pressure, where the equilibrium structure depends not only on atomic positions but also on the unit-cell geometry. In the present study, geometry optimisation

was therefore performed under conditions of fixed external pressure or stress, as appropriate, allowing the lattice vectors to relax along with the atomic positions.

The accuracy of geometry optimisation depends on the numerical parameters used in the underlying DFT calculation. In particular, the plane-wave cut-off energy and k-point sampling must be sufficiently converged to ensure reliable forces and stresses. If these parameters are not adequately converged, errors in the calculated forces can lead to incorrect optimisation pathways or convergence to non-physical structures. For this reason, convergence testing with respect to cut-off energy and k-point density was performed before optimisation, and the same parameters were consistently used in subsequent phonon and molecular dynamics calculations.

The convergence of the geometry optimisation itself was assessed using standard criteria in CASTEP, including thresholds on the maximum force acting on any atom, the total energy change between iterations, and the residual stress in the system. Only structures that satisfied all convergence criteria were used for further analysis. This ensures that the optimised configurations correspond to true minima on the potential energy surface and provide a reliable basis for subsequent lattice dynamics and isotope fractionation calculations.

2.3 Lattice dynamics

2.3.1 Vibrational motion in crystalline solids

Lattice dynamics describes the vibrational behaviour of atoms in a crystal lattice under the assumption that the system is at equilibrium. In practice, this means that lattice dynamics calculations are performed on structures that have already been geometry-optimised, so that the forces acting on all atoms are near-zero and the system corresponds to a minimum on the potential energy surface. The vibrational properties are then obtained by considering small displacements of atoms about these equilibrium positions. As a result, lattice dynamics provides a description of atomic motion that is strictly valid only in the vicinity of an equilibrium configuration.

Within this framework, atoms do not move freely through the lattice but instead undergo small oscillations around their equilibrium positions. Even at absolute

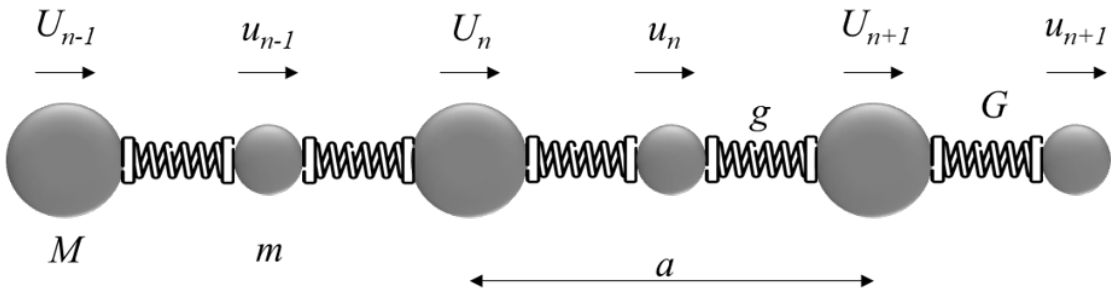


Figure 2.3: Diatomic linear harmonic chain representing a line of atoms.

zero temperature, atoms exhibit quantum mechanical zero-point motion, while at finite temperatures, thermal energy leads to continuous vibrational motion. These vibrations are not independent but are coupled through interatomic forces, giving rise to collective modes that propagate through the crystal.

Because the system is treated as a perturbation about equilibrium, the restoring forces acting on displaced atoms are determined by the curvature of the potential energy surface at the minimum. This curvature determines the force constants, which in turn control the system's vibrational frequencies. The collective vibrational modes can therefore be described in terms of normal modes, which form the basis for the quantised lattice vibrations known as phonons.

These vibrational properties provide the foundation for calculating reduced partition function ratios and, ultimately, equilibrium isotope fractionation factors. As discussed in Chapter 1, equilibrium isotope fractionation arises from differences in vibrational behaviour between isotopically substituted systems. Since isotope substitution affects atomic mass but not the equilibrium bonding environment, it leads to systematic shifts in vibrational frequencies while leaving the underlying force constants largely unchanged. Lattice dynamics, therefore, provides the essential link between equilibrium crystal structure and isotope fractionation.

2.3.2 Harmonic approximation

To describe lattice vibrations quantitatively, the potential energy surface is expanded as a Taylor series about the equilibrium configuration. Retaining terms up to

second order leads to the harmonic approximation, in which the potential energy is expressed as a quadratic function of atomic displacements.

Within this approximation, the system behaves as a set of coupled harmonic oscillators, for which analytical solutions exist. The first-order term vanishes at equilibrium, leaving the second-order term to define the curvature of the potential energy surface. This curvature is directly related to the force constants, which quantify the strength of interactions between atoms.

The harmonic approximation provides a tractable and widely used description of lattice vibrations. Although it neglects higher-order (anharmonic) effects, these are generally small for many solid-state systems and are often within the uncertainty of isotope fractionation calculations. As a result, the harmonic approximation forms the basis of most first-principles studies of vibrational properties and isotope fractionation.

2.3.3 Dynamical matrix and phonon frequencies

The vibrational properties of a crystalline solid can be obtained by solving the equations of motion for small atomic displacements about equilibrium. Within the harmonic approximation, this leads to an eigenvalue problem defined by the dynamical matrix, which contains information about the interatomic force constants and atomic masses. The eigenvalues of this matrix correspond to the squared vibrational frequencies, while the eigenvectors describe the corresponding atomic displacement patterns.

Because the system is periodic, these vibrational modes can be expressed as collective waves propagating through the crystal lattice. Each vibrational mode is therefore characterised not only by its frequency, but also by a wavevector that describes how the displacement varies across the lattice. These wavevectors are defined in reciprocal space and are commonly referred to as q-points, in direct analogy to the k-points used in electronic structure calculations.

Each q-point represents a specific vibrational wavelength and direction within the crystal. Sampling different q-points allows the full vibrational spectrum to be

constructed across the Brillouin zone. For a given q-point, the dynamical matrix is constructed and diagonalised to obtain a set of phonon frequencies corresponding to that wavevector. The complete vibrational behaviour of the system is then obtained by evaluating these frequencies over a grid of q-points spanning the Brillouin zone.

In practice, it is not necessary to sample all possible q-points. Instead, a finite grid of q-points is used, and convergence is tested to ensure that the vibrational properties are accurately represented. Denser q-point grids provide a more complete description of the phonon spectrum but increase computational cost. As with k-point sampling, symmetry can be exploited to reduce the number of unique q-points that must be evaluated.

The use of q-point sampling is particularly important for calculating thermodynamic properties and isotope fractionation factors. The vibrational partition function depends on contributions from all phonon modes across the Brillouin zone, meaning that incomplete sampling can lead to errors in calculated free energies. Accurate q-point sampling is therefore essential to ensure reliable determination of reduced partition function ratios and equilibrium isotope fractionation.

2.3.4 Isotope fractionation and vibrational properties

The connection between lattice dynamics and isotope fractionation arises from the dependence of vibrational energy on atomic mass. In quantum mechanics, vibrational modes have discrete energy levels, and their occupation depends on temperature. The distribution of vibrational states is described by the partition function, which incorporates contributions from all phonon modes.

When a heavier isotope substitutes for an atom, its vibrational frequencies decrease, leading to a change in the vibrational partition function. This leads to differences in free energy between isotopically substituted systems. At equilibrium, these free energy differences determine the partitioning of isotopes between phases.

The reduced partition function ratio, often referred to as the β-factor, provides a convenient measure of this effect for a single phase. Differences in β-factors between phases then define the equilibrium fractionation factor. Because these quantities

depend directly on phonon frequencies, accurate lattice-dynamics calculations are essential for reliable predictions of isotope fractionation.

2.3.5 Limitations of the harmonic approximation

Although the harmonic approximation provides a robust framework for describing lattice vibrations, it neglects anharmonic effects that become increasingly important at high temperatures. These effects include thermal expansion, phonon–phonon interactions, and deviations from purely quadratic potential energy surfaces.

At the extreme conditions relevant to magma oceans, such as temperatures approaching several 1000 K, anharmonicity may influence vibrational properties and isotope fractionation. However, previous studies have shown that, for many systems, the magnitude of anharmonic corrections is small compared to the overall uncertainty in first-principles calculations (Walker et al., 2026). As a result, the harmonic approximation remains a reasonable and widely adopted approach for modelling isotope fractionation in both minerals and melts.

2.3.6 CASTEP implementation

Lattice dynamics calculations in this study were performed using the CASTEP code, which provides efficient methods for determining vibrational properties within density functional theory. The starting point for these calculations is the fully optimised crystal structure obtained from geometry optimisation, ensuring that the system corresponds to a minimum on the potential energy surface.

In CASTEP, phonon calculations are typically performed using the finite-displacement (or "frozen phonon") method (Frank et al., 1995). In this approach, small displacements are applied to atoms in the unit cell, and the resulting forces are calculated using DFT. These forces are then used to construct the force constant matrix, which describes the second derivatives of the total energy with respect to atomic displacements (Parlinski et al., 1997). From this matrix, the dynamical matrix is assembled and diagonalised to obtain phonon frequencies and vibrational modes.

Because phonon frequencies depend sensitively on the accuracy of the underlying DFT calculation, it is essential that the numerical parameters, such as plane-wave cut-off energy and k-point sampling, are fully converged. The same parameters used in geometry optimisation were therefore employed in the lattice dynamics calculations to ensure consistency. In addition, symmetry was exploited to reduce the number of required atomic displacements, improving computational efficiency without compromising accuracy.

The calculated phonon frequencies were subsequently used to determine reduced partition function ratios and equilibrium isotope fractionation factors. By combining lattice dynamics with first-principles electronic structure calculations, CASTEP provides a direct link between atomic-scale vibrational properties and isotope systematics, forming a central component of the computational methodology used in this thesis.

2.4 Molecular dynamics

2.4.1 Moving atoms in the liquid state

"Imagine that an alien lands on Earth, hears about something called a bicycle, and wants to understand how it works, how to ride it, and how to fix it when it breaks. Figuring this out from just a picture of a bicycle would be challenging. Watching a movie of someone riding a bicycle would help. Even better, the alien would experiment with an actual bicycle, for example, by turning a pedal and seeing how the wheels respond." – Scott A. Hollingsworth

A mineralogist trying to understand silicate melts faced similar challenges. An atomic-level structure is beneficial and creates some insights. Many atomic-scale effects, however, depend on intermolecular interactions that can be studied only by tracking the motion of molecules in a dynamic environment. Unfortunately, observing atomic motion is difficult, if not nearly impossible. An alternative approach is an atomic-scale computational simulation known as molecular dynamics (MD). These simulations use the positions of atoms in a system to calculate the forces exerted on each atom by all the surrounding atoms. Using a set of Newton's

laws, one can predict, therefore, the spatial position of each atom at each point in time in one simulation. If this is repeated, a three-dimensional movie emerges that depicts the atomic-level configuration of large-scale moving systems such as liquids.

2.4.2 Ergodicity principle

Liquid systems are disordered and lack long-range periodicity. To accurately replicate natural liquid systems, the computational simulation box would need to exceed current computational limitations. To study the atomic structures of liquids, an ensemble of microstates must be introduced. These snapshots of an atomic structure represent the probability that a liquid system was in a similar state at that moment. Molecular dynamics can calculate these atomic positions within microstates at a series of time steps. To compute liquids accurately using molecular dynamics, one uses the ergodicity principle.

The ergodicity principle states that a system comprising different particles, over time, will cause each particle to sample the same energetic states that can be observed if multiple particle states are examined at a single point in time. In other words, the time average equals the ensemble average.

Molecular dynamics satisfies the ergodicity principle if the system is run long enough, allowing its molecules to visit all energetically relevant states. Here, this is described as the time required to reach equilibrium with a silicate melt.

2.4.3 Equations of motion

Molecular dynamics is a method that calculates the motion of each atom based on Newton's second law of motion. This law states that the acceleration of an object, in this case an atom, depends on its mass and the force acting on it:

$$\mathbf{F}_i = m_i \frac{d^2\mathbf{r}_i}{dt^2}. \tag{2.2}$$

One of the most widely used computational integrations of Newton's second law in molecular dynamics is the Verlet algorithm (Verlet, 1967). This algorithm

simplifies the motion equations by calculating the atomic positions at $t + \Delta t$. The basic formula for the Verlet algorithm is:

$$\mathbf{r}_i(t + \Delta t) = 2\mathbf{r}_i(t) - \mathbf{r}_i(t - \Delta t) + \frac{\mathbf{F}_i(t)}{m_i}\Delta t^2. \tag{2.3}$$

2.4.4 Thermodynamic particle ensembles

A set of thermodynamic ensembles exists to reproduce the experimental conditions needed. The ensemble is selected based on the modelling system's requirements and the parameters that must be fixed or controlled.

- **NVE** – This is the micro-canonical ensemble that consists of an isolated system where the number of particles N, the volume V, and total energy E are fixed. In this ensemble, there is no interchange between the experimental system and the environment. Therefore, this ensemble is not used in this study.

- **NVT** – The canonical ensemble NVT, with fixed number of particles N, fixed volume V, and fixed temperature T, provides the system at temperature equilibrium. This ensemble is used in the first simulations to keep the system at a fixed volume and temperature and study isotope fractionation.

- **NPT** – Ensemble with fixed number of particles N, fixed pressure P, and fixed temperature T. This ensemble is used to obtain equilibrium volumes for target pressures during silicate melt simulations.

2.4.5 Thermostats

In MD simulations, the temperature is crucial for determining physical properties and dynamic behaviour. As we saw in Equation 2.2, the classical equation of motion, based on Newton's second law, conserves energy and thus samples the microcanonical ensemble (NVE), where the number of particles N, volume V, and energy E are preserved. To simulate more relevant conditions, simulations should be performed under NVT ensembles, in which the system exchanges energy with an

external bath to maintain a constant temperature. This is achieved by connecting the system to thermostat algorithms. Several types of thermostats can be used in MD simulations, each with its own advantages and disadvantages. Some of the most commonly used thermostats include:

- **Nosé–Hoover thermostat**: The Nosé–Hoover thermostat offers a deterministic approach to NVT by adding a degree of freedom that acts as a thermal reservoir. This method produces correct canonical statistics and preserves dynamical trajectories, making it well-suited to simulations.
- **Berendsen thermostat**: The Berendsen thermostat introduces a first-order relaxation of the system towards the target temperature using time-dependent factors. This method is computationally inexpensive but does not yield a true canonical ensemble and is not recommended for accurate simulations.
- **Andersen thermostat**: This thermostat simulates collisions with a heat bath by randomly selecting particles and recalculating their velocities. This method correctly samples the canonical ensemble but violates the system's natural dynamics and momentum conservation.

2.4.6 Snapshot techniques versus other techniques

Determining isotopic signatures in silicate melts, especially for magnesium and silicon, is quite challenging in high-temperature isotope geochemistry. Because it is difficult to observe melt structures and atomic movements directly, silicate glasses are often used as substitutes for their liquid counterparts. However, these static models do not fully capture the dynamic behaviour of melts. Building on the work of Rabin et al. (2023), we employ first-principles MD simulations that combine MD and DFT methods to investigate isotope fractionations under conditions similar to those in natural magmatic systems.

Rabin et al. employed a method that we refer to as the "snapshot technique", in which a series of snapshots is extracted from the trajectory of an MD simulation at 1 ps intervals. Each snapshot structure is treated individually, as in the

mineral structures explained in previous sections. Each configuration is relaxed to 0 K and a finite pressure (typically 1 GPa), thereby enabling the calculation of vibrational frequencies using a frozen-phonon approach. These frequencies are then used to compute the reduced partition function ratios for each isotope system. Averaging over several snapshots yields representative β-factors for the melt, along with uncertainty estimates based on the snapshot-to-snapshot variance. This methodology, combined with DFT calculations for minerals such as olivine and orthopyroxene (Huang et al., 2013; Schauble, 2011; Wang et al., 2023, e.g), yields accurate results that are comparable to experimentally measured mineral–melt data (Li et al., 2025; Rabin et al., 2023).

An alternative method, the velocity autocorrelation function (VAF) approach similar to used in Luo et al. (2020), directly infers isotope fractionation from the vibrational density of states (VDOS), obtained via the Fourier transform of the atoms' velocity autocorrelation. This approach captures the melt's finite-temperature dynamics and accounts for anharmonic atomic motion. Nonetheless, in complex silicate systems, the VAF method faces practical hurdles: the low-frequency portion of the VDOS contains diffusive signals that must be carefully removed to avoid overestimating the kinetic energy. Implementing this correction for multi-component melts is difficult. Additionally, the uncertainties associated with the VAF method tend to be larger, as its precision relies heavily on long trajectory durations and dense sampling of atomic velocities.

Since both methods yield similar β-factors and force constants within the margin of error, and anharmonic effects appear insignificant relative to statistical uncertainty, the snapshot method was chosen for this study to ensure consistency and improve computational efficiency. This approach also allows for straightforward comparison with the silicon isotope calculations, which are based on the same static, frozen-phonon framework.

2.4.7 CASTEP implementation

Molecular dynamics simulations in this study were performed using the ab initio molecular dynamics (AIMD) framework implemented in CASTEP. In this approach, interatomic forces are calculated directly from density functional theory at each time step, providing a consistent description of atomic interactions without relying on empirical potentials. This is particularly important for silicate melts, where bonding environments are complex and variable.

The equations of motion were integrated using standard time-stepping algorithms with a time step of 1 fs (10^{-15} seconds), chosen to resolve atomic motion accurately. Simulations were carried out under controlled thermodynamic conditions, primarily using NVT and NPT ensembles. Temperature was regulated using a Nosé–Hoover thermostat, and pressure was controlled as needed to achieve equilibrium densities at target conditions.

As in the static calculations, the accuracy of the simulations depends on the convergence of the underlying DFT parameters, including cut-off energy and pseudopotentials. For large simulation cells, Brillouin zone sampling was typically restricted to the Γ-point, which provides a computationally efficient approximation for disordered systems.

Bibliography

Bloch, F. (1929). Über die Quantenmechanik der Elektronen in Kristallgittern. *Zeitschrift für Physik*, *52*(7), 555–600.

Born, M., & Oppenheimer, R. (1927). Zur Quantentheorie der Molekeln. *Annalen der Physik*, *389*(20), 457–484.

Car, R., & Parrinello, M. (1985). Unified Approach for Molecular Dynamics and Density-Functional Theory. *Physical Review Letters*, *55*(22), 2471–2474.

Eyring, H. (1935). The Activated Complex in Chemical Reactions. *Journal of Chemical Physics*, *3*, 107–115.

Frank, W., Elsässer, C., & Fähnle, M. (1995). Ab initio force-constant method for phonon dispersions in alkali metals, *Phys. Rev. Lett.*, *74*, 1791–1794.

Gonze, X., & Lee, C. (1997). Dynamical matrices, Born effective charges, dielectric permittivity tensors, and interatomic force constants from density-functional perturbation theory. *Physical Review B*, *55*(16), 10355–10368.

Hohenberg, P., & Kohn, W. (1964). Inhomogeneous electron gas. *Physical Review*, *136*(3B), B864.

Huang, F., Chen, L., Wu, Z., & Wang, W. (2013). First-principles calculations of equilibrium Mg isotope fractionations between garnet, clinopyroxene, orthopyroxene, and olivine: Implications for Mg isotope thermometry. *Earth and Planetary Science Letters*, *367*, 61–70.

Huang, F., Wu, Z., Huang, S., & Wu, F. (2014). First-principles calculations of equilibrium silicon isotope fractionation among mantle minerals. *Geochimica et Cosmochimica Acta*, *140*, 509–520.

Jones, R. (2015). Density functional theory: Its origins, rise to prominence, and future. *Reviews of Modern Physics*, *87*(3), 897–923.

Kohn, W. (1999). Nobel Lecture: Electronic structure of matter—wave functions and density functionals. *Reviews of Modern Physics*, *71*(5), 1253–1266.

Kohn, W., & Sham, L. J. (1965). Self-Consistent Equations Including Exchange and Correlation Effects. *Physical Review*, *140*(4A), A1133–A1138.

Li, Y., Hardin, J., Wang, W., Wu, Z., & Huang, S. (2025). Mineral-melt calcium isotope fractionation factors constrained using *ab initio* molecular dynamics simulations and their implications to calcium isotope effects during partial melting in the upper mantle. *Geochimica et Cosmochimica Acta*.

Luo, H., Karki, B. B., Ghosh, D. B., & Bao, H. (2020). First-principles computation of diffusional Mg isotope fractionation in silicate melts. *Geochimica et Cosmochimica Acta*, *290*, 27–40.

Martin, R. M. (2020). *Electronic Structure: Basic Theory and Practical Methods*. Cambridge University Press.

Milman, V., Winkler, B., White, J. A., Pickard, C. J., Payne, M. C., Akhmatskaya, E. V., & Nobes, R. H. (2010). Electronic structure, vibrational properties and spectroscopy of materials using density functional theory, plane waves and pseudopotentials: Castep implementation. *Journal of Physics: Condensed Matter*, *22*, 073201.

Parlinski, Li, & Kawazoe. (1997). First-principles determination of the soft mode in cubic ZrO_2. *Phys. Rev. Lett.*, *78*, 4063–4066.

Parr, R. G. (1980). Density Functional Theory of Atoms and Molecules. In K. Fukui & B. Pullman (Eds.), *Horizons of Quantum Chemistry* (pp. 5–15). Springer Netherlands.

Payne, M. C., Teter, M. P., Allan, D. C., Arias, T. A., & Joannopoulos, J. D. (1992). Iterative minimization techniques for ab initio total-energy calculations: Molecular dynamics and conjugate gradients. *Reviews of Modern Physics*, *64*(4), 1045–1097.

Perdew, J. P., Burke, K., & Ernzerhof, M. (1996). Generalized gradient approximation made simple. *Physical review letters*, *77*(18), 3865.

Perdew, J. P., Chevary, J. A., Vosko, S. H., Jackson, K. A., Pederson, M. R., Singh, D. J., & Fiolhais, C. (1992). Atoms, molecules, solids, and surfaces: Applications of the generalized gradient approximation for exchange and correlation. *Physical Review B*, *46*(11), 6671–6687.

Perdew, J. P., Ruzsinszky, A., Csonka, G., Vydrov, O. A., Scuseria, G. E., Constantin, L. A., Zhou, X., & Burke, K. (2008). Restoring the Density-Gradient Expansion for Exchange in Solids and Surfaces. *Physical Review Letters*, *100*(13), 136406.

Rabin, S., Blanchard, M., Pinilla, C., Poitrasson, F., & Grégoire, M. (2023). Iron and silicon isotope fractionation in silicate melts using first-principles molecular dynamics. *Geochimica et Cosmochimica Acta*, *343*, 212–233.

Schauble, E. A. (2004). Applying Stable Isotope Fractionation Theory to New Systems. *Reviews in Mineralogy and Geochemistry*, *55*(1), 65–111.

Schauble, E. A. (2011). First-principles estimates of equilibrium magnesium isotope fractionation in silicate, oxide, carbonate and hexaaquamagnesium(2+) crystals. *Geochimica et Cosmochimica Acta*, *75*(3), 844–869.

Segall, M. D., Lindan, P. J. D., Probert, M. J., Pickard, C. J., Hasnip, P. J., Clark, S. J., & Payne, M. C. (2002). First-principles simulation: Ideas, illustrations and the CASTEP code. *Journal of Physics: Condensed Matter*, *14*(11), 2717.

Sholl, D. S., & Steckel, J. A. (2022). *Density Functional Theory: A Practical Introduction*. John Wiley & Sons.

Vanderbilt, D. (1990). Soft self-consistent pseudopotentials in a generalized eigenvalue formalism. *Physical Review B*, *41*(11), 7892–7895.

Verlet, L. (1967). Computer "Experiments" on Classical Fluids. I. Thermodynamical Properties of Lennard-Jones Molecules. *Physical Review*, *159*(1), 98–103.

Walker, A. M., Hin, R. C., & Elliott, T. (2026). Controls on Mg isotopic fractionation between deep mantle phases and relict signatures of a terrestrial magma ocean. *Geochimica et Cosmochimica Acta*, *425*, 131–142.

Wang, W., Wu, Z., Huang, S., & Huang, F. (2023). First-principles investigation of equilibrium magnesium isotope fractionation among mantle minerals: Review and new data. *Earth-Science Reviews*, *237*, 104315.

"An experiment is a question which science poses to Nature."

— Max Planck

3 Methodology – Experiments

Contents

3.1 Overview of Experimental Methods 64
3.2 Stable Isotopes Petrological Experiments 65
3.3 Experimental Objectives 66
3.4 Experimental Setup 67
3.4.1 Olivine capsules 67
3.4.2 Natural crystal – melt interaction 68
3.4.3 Growing forsterite crystals from bulk composition . . . 69
3.5 Starting Composition 69
3.6 Sample Holder 71
3.7 1 atm furnace experiments 71

3.1 Overview of Experimental Methods

This chapter describes the experimental petrology methods used to measure Mg and Si isotope fractionation between coexisting minerals and silicate melt under controlled laboratory conditions. This section outlines the experimental petrology methods used to measure Mg and Si isotope fractionation between coexisting minerals and silicate melt under controlled lab conditions. These experiments support the equilibrium isotope fractionation calculations discussed in Chapter 5 and provide an experimental basis for testing and refining model predictions across

a range of temperatures and pressures.

The experiments were designed to simulate conditions characteristic of partial melting and crystallisation in magma ocean settings, focusing on both solid–solid and solid–melt equilibrium assemblages. The methods presented here include the preparation of starting materials, selection of experimental run conditions (pressure, temperature, and oxygen fugacity), and post-run analytical approaches to assess chemical and isotopic equilibrium. Emphasis is placed on techniques to minimise contamination and ensure equilibrium fractionation, including the design of capsule assemblies, selection of run durations, and quench strategies.

Together, these experiments provide critical constraints on the mechanisms and magnitudes of Mg and Si isotope fractionation among major mantle phases (e.g., olivine, pyroxene, bridgmanite) and silicate melt. The following sections outline the experimental protocols in detail, followed by the presentation and interpretation of results in the subsequent Results and Discussion chapters.

3.2 Stable Isotopes Petrological Experiments

To explore isotopic fractionation under controlled, high-temperature (and, where relevant, high-pressure) conditions, we employed an experimental approach tailored to different phase equilibria and element systems. In general, these isotope experiments strive to impose equilibrium exchange among minerals, melt, or fluids, then measure the resulting isotope ratios (e.g., by MC-ICP-MS or TIMS) to infer fractionation factors. However, doing so in practice involves significant methodological challenges:

1. Ensuring equilibrium (i.e. that kinetic effects and diffusion gradients are negligible).

2. Avoiding open-system isotope loss (e.g. by evaporation or boundary contamination).

3. Controlling redox, temperature, pressure, and chemical environment to isolate the isotope system of interest.

4. Growing phases sufficiently large to be individually extracted and measured afterwards.

5. Achieving high analytical precision for often tiny isotope differences.

To meet these challenges, experiments in literature employ multiple techniques, including long-duration diffusion or exchange runs in piston-cylinder or multi-anvil presses, rapid quenching or "pump-and-hold" thermal annealing, and laser-heating levitation methods combined with aerodynamic gas control. The results are cross-checked using internal consistency (e.g., three-isotope methods) and by comparison with theoretical or *ab initio* predictions. The classic review by Young et al. (2015) on high-temperature isotope fractionation outlines the general framework and caveats of such experimental designs. For high-pressure metal–silicate systems (e.g. Si isotopes), Kempl et al. (2013) and Shahar et al. (2011) provide key case studies on how these technical challenges have been addressed under extreme P–T conditions.

3.3 Experimental Objectives

The primary objective of the experiments used in this research is to generate empirical constraints on isotope fractionation between key rock-forming silicates that can be directly compared with *ab initio* calculations. Specifically, we investigate Mg and Si isotope partitioning between forsterite and diopside, two phases that coexist along the cotectic in the simplified $CaO–MgO–Al_2O_3–SiO_2$ (CMAS) system. This choice allows us to reproduce conditions under which both minerals crystallise from a residual melt of the same bulk composition, thereby isolating temperature-dependent equilibrium effects from compositional influences. The resulting isotopic data provide a crucial experimental basis for testing theoretical fractionation factors and refining models of isotope behaviour in planetary magma systems. Analytical procedures and isotope measurement protocols are described in Chapter 5; here, the rationale, experimental design, and sample-synthesis approach are outlined.

3.4 Experimental Setup

Achieving and confirming equilibrium between a crystalline phase and a coexisting silicate melt is essential for accurately determining isotope fractionation factors. In isotope exchange experiments, even slight disequilibrium can mask the true isotope signature, leading to inaccurate conclusions. Consequently, experimental design must ensure that both chemical and isotopic equilibrium are achieved and maintained throughout the process.

This section details the experimental setups used in this study to examine Mg and Si isotope fractionation between solid and molten silicate phases. It emphasises the selection of apparatus, sample assembly, and run conditions designed to achieve equilibrium, along with post-run methods for assessing the completeness of isotopic exchange.

3.4.1 Olivine capsules

One approach to measuring solid–melt isotope fractionation ratios involves designing an experimental setup in which a crystal serves as the capsule, with silicate powder inside. To address the common issue of Fe-loss in 1 atm gas-mixing experiments, Nash et al. (2016) developed a method to create crystalline olivine capsules. These capsules enable melting experiments saturated with olivine. Nash et al. (2016) prepared olivine starting compositions, pressed them into pellets, and heated them for at least 2 hours at 1300 °C. Two capsule types were produced: one for 1 atm tests and another for piston-cylinder presses. The 1 atm capsules had an outer diameter of 6 mm, an inner diameter of 3 mm, and contained 0.37 g of olivine. The researchers noted that the capsules were permeable, necessitating longer melting times or the use of bonding agents to reduce porosity. Producing a Fo_{100} capsule, free of Fe, eliminates the influence of fO_2 on isotope equilibrium. However, synthesising Fo_{100} is technically intricate and prone to leakage, making it less ideal. Because synthesising leak-free Fo_{100} capsules is technically demanding, this approach was not adopted in the present study.

3.4.2 Natural crystal – melt interaction

A more recent study by Jollands et al. (2020) introduces a method to assess the significance of measuring Mg stable-isotope diffusion ratios using LA-ICP-MS in experimental petrology samples. This research aims to improve the precision of Mg diffusion rates across varying silica activities. Prior studies show that silica activities notably influence the diffusion of both major elements (Zhukova et al., 2014) and trace elements (Jollands et al., 2016; Jollands et al., 2014). To explore this influence, the studies conducted experiments using a synthesised forsterite crystal and pressed-phase assemblage pellets.

The forsterite, grown via the artificial Czochralski method, was polished and placed into Pt crucibles. The Czochralski method is the primary industrial technique for growing large, high-purity single crystals. The phase mixtures, such as Mg_2SiO_4–$Mg_2Si_2O_6$ (forsterite–protoenstatite) or Mg_2SiO_4–MgO (forsterite–periclase), were designed to modify Si activities. These mixtures were sintered, pressed into pellets, and attached to the crystal surface. The setup was heated in a Pt crucible at 1250–1600 °C for up to 14 days, with a minimum of 1 day, in a CO–CO_2 gas mixture furnace. Mg isotopes (^{24}Mg, ^{25}Mg, and ^{26}Mg) were analysed via LA-ICP-MS at the Australian National University.

Results indicated that higher Mg activity increases Mg diffusion rates by roughly ten times. The study also observed anisotropy in Mg diffusion, with differences of 0.5 log units between mineral orientations (Jollands et al., 2020), aligning with earlier findings (Jollands et al., 2016). The oxygen fugacity of the furnace atmosphere had minimal impact, as shown by Chakraborty et al. (1994). Consequently, airflow effects are negligible, allowing for experiments in standard laboratory furnaces.

Overall, the research confirms that the experimental setup using single-crystal and melt powders can detect Mg isotope diffusion effects using LA-ICP-MS. It also emphasises the importance of measuring Mg isotopes in different mineral orientations to account for anisotropy. However, the technique relies on natural or synthetic Fo_{100} forsterite crystals, which are rare in nature and challenging to produce in the desired sizes synthetically. Therefore, we chose not to include this methodology in our study.

3.4.3 Growing forsterite crystals from bulk composition

A third method involves experiments focused on growing forsterite crystals large enough to surpass the 20 μm size limit for isotope analysis. In a study by Park and Hanson (1999), olivine crystals up to 150 μm were produced within 10 days at 1 atm. Instead of using the Fo–Di–An ternary system from Jollands et al. (2014), the authors chose an SiO_2–Al_2O_3–CaO–MgO, anorthite–enstatite–diopside (An-En-Di) basalt analogue system. Consistent with this study's aim, this ternary system was selected to avoid effects from Fe, Na, or K.

Operating within the Fo–An–Di basalt system (Figure 3.1), crystallisation occurs as low as 1274 °C, which is at a lower temperature than in the An–En–Di system, making them more suitable for experiments. Park and Hanson (1999) started with a composition just above the liquidus at 1300 °C for 2 hours to ensure homogeneity, then held it at 1275 °C for 48 hours to achieve equilibrium. Rapid quenching was done by dropping the capsule into distilled water.

The glass was ground into small crystals, pressed, and reheated at 1275 °C for 1–10 days. Quenched samples showed crystal sizes from 1 to 150 μm. Experiments exceeding 7 days showed undesirable clustering of forsterite crystals; thus, 7 days were optimal as they mitigated this effect while promoting heterogeneity. Growing crystals directly from the bulk composition allows olivine and diopside to crystallise in complete equilibrium with the host liquid. Therefore, we adopted this methodology and further developed it to enable experiments at low nucleation rates, thereby promoting the growth of significant mineral phases.

3.5 Starting Composition

For successful experimental petrology runs that measure $^{24}Mg/^{26}Mg$ isotopic fractionation between mineral and melt, the sample must be in complete chemical equilibrium. In this study, I focus on isolating isotope fractionation of stable Mg and Si isotopes, ensuring that potential confounding effects from other elements do not interact with our isotopic systems. A key control factor is preventing

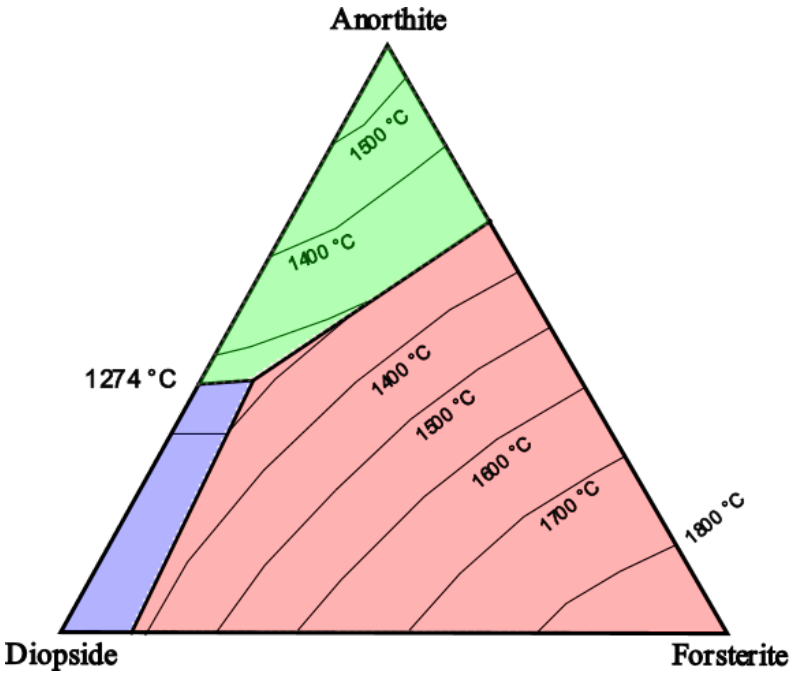


Figure 3.1: Forsterite-Diopside-Anorthite Ternary system (Morse, 1980).

chemical exchange between the forsterite crystals and the silicate phase. Variations in concentrations, such as SiO_2, can significantly influence Mg isotope diffusion in forsterite (Jollands et al., 2020; Zhukova et al., 2014). Furthermore, the nature of equilibrium isotope fractionation factors makes them challenging to measure and analyse. Therefore, the experiment starts with compositions within the Fo–An–Di system (Figure 3.1), ensuring the synthesised forsterite crystal remains in equilibrium with the silicate composition. The initial composition in the Fo–An–Di system is intentionally chosen because it lacks any Fe components. Removing Fe from the composition eliminates an additional factor that influences isotope fractionation. The presence of Fe and changes in fO_2 affect the octahedral vacancies in olivine, which have important implications for the stable isotope partitioning between olivines with different forsterite contents (Nakamura & Schmalzried, 1983). Forsterite diffusion coefficients increase with increasing oxygen fugacity (Dohmen et al., 2007). A small number of studies showed that external gas mixing furnace fO_2 does not influence Mg isotope diffusion (Chakraborty et al., 1994; Jollands et al., 2020). However, these studies do not account for fO_2 and Fe concentrations in the starting compositions and instead focus on external fO_2 conditions.

3.6 Sample Holder

All experiments were conducted using a custom-built platinum "chandelier-type" sample holder designed to maintain spatial uniformity and sample separation within the furnace. The chandelier configuration consists of a central platinum (Pt) ring in the shape of a regular pentagon, from which multiple Pt suspension wires extend. The pentagonal ring serves as the primary structural frame and is connected at its apex to a thicker Pt wire that terminates in a hook. This hook allows the entire assembly to be securely suspended beneath a glass support tube within the vertical box furnace, ensuring stable positioning in the central hot zone, where temperature gradients are minimal.

Beneath the pentagonal frame, three to five thinner Pt wires are attached, each terminating in a small loop. These loops act as individual sample mounts onto which experimental sample charges (forsterite or diopside starting compositions) are affixed using a minute amount of adhesive. Upon heating, the glue volatilises cleanly, leaving the samples firmly attached to the Pt loops through surface tension and partial fusion of the sample edges. This configuration ensures that each sample remains in a fixed position throughout the run, preventing contact between charges or capsule walls.

The chandelier arrangement provides several advantages over conventional single-wire suspensions. First, it allows multiple samples to be equilibrated simultaneously under identical thermal and chemical conditions, which is critical for directly comparing fractionation between coexisting phases. All mounted samples are positioned approximately 5 cm apart and at the same vertical height within the furnace, thereby minimising temperature gradients. The robust Pt construction provides mechanical stability at high temperatures ($> 1500°C$) while avoiding contamination or alloying with silicate melt.

3.7 1 atm furnace experiments

All crystallisation experiments were performed in a vertical box furnace at 1 atm. Before each series, the furnace temperature profile was calibrated using an external

type-S thermocouple placed at the location of the sample assembly. Comparing this external thermocouple with the internal one revealed a consistent offset of approximately 6 °C, which was used as a correction factor for all reported temperatures.

After calibration, the furnace was heated to about 10 °C above the nominal liquidus of the starting composition to ensure full melting of the materials. The system was held at the supraliquidus temperature for 2 hours to promote melt homogeneity and eliminate any residual crystalline phases. Subsequently, the temperature was lowered to the desired run conditions.

Our preliminary experiments showed that a controlled cooling rate of 0.1 °C per minute strikes the best balance between reducing excessive nucleation and encouraging the growth of large, well-formed mineral grains ideal for isotopic and textural studies. Consequently, each run was cooled at this rate until reaching the cotectic temperature of the forsterite–diopside system (ca 1280 °C), plus an extra 2 °C. Keeping the temperature just above the cotectic point ensured that only the targeted crystalline phases formed and prevented the nucleation of secondary mineral phases.

Once the final set point was reached, the experiments were maintained isothermally for seven days to facilitate chemical and isotopic equilibrium among the coexisting forsterite, diopside, and melt. Multiple experiments confirmed that this duration was sufficient to ensure homogeneity and equilibrium within the sample assemblage. At the end of the run, the furnace was switched off, and the sample was allowed to cool to room temperature under ambient atmospheric conditions before capsule removal and further processing. Analytical procedures for textural characterisation, major-element analysis, micro-sampling, chemical purification, and Mg/Si isotope measurements follow the protocols described in Chapters 4.

Bibliography

Chakraborty, S., Farver, J. R., Yund, R. A., & Rubie, D. C. (1994). Mg tracer diffusion in synthetic forsterite and San Carlos olivine as a function of P, T and fO2. *Physics and Chemistry of Minerals*, *21*(8), 489–500.

Dohmen, R., Becker, H.-W., & Chakraborty, S. (2007). Fe–Mg diffusion in olivine I: Experimental determination between 700 and 1,200°C as a function of composition, crystal orientation and oxygen fugacity. *Physics and Chemistry of Minerals*, *34*(6), 389–407.

Jollands, M. C., Hermann, J., O'Neill, H. S. C., Spandler, C., & Padrón-Navarta, J. A. (2016). Diffusion of Ti and some Divalent Cations in Olivine as a Function of Temperature, Oxygen Fugacity, Chemical Potentials and Crystal Orientation. *Journal of Petrology*, *57*(10), 1983–2010.

Jollands, M. C., O'Neill, H. S. C., & Hermann, J. (2014). The importance of defining chemical potentials, substitution mechanisms and solubility in trace element diffusion studies: The case of Zr and Hf in olivine. *Contributions to Mineralogy and Petrology*, *168*(3), 1055.

Jollands, M. C., Zhukova, I., O'Neill, H. S. C., & Hermann, J. (2020). Mg diffusion in forsterite from 1250–1600 °C. *American Mineralogist*, *105*(4), 525–537.

Kempl, J., Vroon, P. Z., Zinngrebe, E., & van Westrenen, W. (2013). Si isotope fractionation between Si-poor metal and silicate melt at pressure–temperature conditions relevant to metal segregation in small planetary bodies. *Earth and Planetary Science Letters*, *368*, 61–68.

Morse, S. A. (1980). *Basalts and phase diagrams*. Springer.

Nakamura, A., & Schmalzried, H. (1983). On the nonstoichiometry and point defects of olivine. *Physics and Chemistry of Minerals*, *10*(1), 27–37.

Nash, W., Smythe, D., & Wood, B. J. (2016). Synthetic olivine capsules for use in experiments. *American Mineralogist*, *101*(10), 2260–2263.

Park, Y., & Hanson, B. (1999). Experimental investigation of Ostwald-ripening rates of forsterite in the haplobasaltic system. *Journal of Volcanology and Geothermal Research*, *90*(1), 103–113.

Shahar, A., Hillgren, V. J., Young, E. D., Fei, Y., Macris, C. A., & Deng, L. (2011). High-temperature Si isotope fractionation between iron metal and silicate. *Geochimica et Cosmochimica Acta*, *75*(23), 7688–7697.

Young, E. D., Manning, C. E., Schauble, E. A., Shahar, A., Macris, C. A., Lazar, C., & Jordan, M. (2015). High-temperature equilibrium isotope fractionation of non-traditional stable isotopes: Experiments, theory, and applications. *Chemical Geology*, *395*, 176–195.

Zhukova, I., O'Neill, H., Campbell, I., & Kilburn, M. (2014). The effect of silica activity on the diffusion of Ni and Co in olivine. *Contributions to Mineralogy and Petrology*, *168*.

4

The magnitude of equilibrium isotope fractionation

This chapter addresses one of the central challenges in stable isotope geochemistry: quantifying equilibrium isotope fractionation at high temperatures. Although magnesium isotopes are widely used to trace mantle processes, their interpretation depends critically on well-constrained equilibrium fractionation factors between minerals and melt. At magmatic temperatures, these fractionations are small and often approach analytical precision limits, making them difficult to resolve unambiguously in natural systems.

Previous work has relied on two main approaches: empirical observations from natural samples and theoretical predictions from first-principles calculations. However, both approaches suffer from limitations. Natural samples may record kinetic effects such as diffusion or incomplete equilibration, while theoretical calculations depend sensitively on computational assumptions, including the choice of exchange–correlation functional and treatment of thermal expansion. As a result, discrepancies persist between empirical, experimental, and theoretical estimates of Mg isotope fractionation.

The paper presented in this chapter tackles this problem by combining high-temperature petrological experiments with density functional theory (DFT) cal-

culations. The experimental design explicitly aims to minimise kinetic effects, particularly Soret diffusion, by reducing thermal gradients and working in an Fe-free system. In parallel, atomic-scale simulations explore how methodological choices influence predicted fractionation factors. This dual approach provides a rare opportunity to directly compare experimentally derived equilibrium fractionation with ab initio predictions under controlled conditions.

By focusing on the relatively simple CMAS system and the mineral pair forsterite–diopside, this study establishes a benchmark for Mg isotope fractionation at liquidus conditions. In doing so, it addresses a key gap in the field: the lack of experimentally validated equilibrium fractionation factors for major mantle phases. This chapter, therefore, provides the methodological and conceptual foundation for the subsequent chapters, in which these constraints are extended to more complex systems and broader geodynamic contexts.

This manuscript will be resubmitted to Geochimica et Cosmochimica Acta (GCA)

Statement of Authorship for joint/multi-authored papers for PGR thesis is attached in the appendix at the end of the thesis

The magnitude of equilibrium isotope fractionation of Mg between forsterite, diopside and melt at liquidus temperatures.

Bram de Winter[a,*], Andrew M. Walker[a], Elena Melekhova[a], Xiao-Ning Liu[b], Tim Elliott[b]

[a] Department of Earth Sciences, University of Oxford, South Parks Road, Oxford, OX1 3AN, UK
[b] School of Earth Sciences, University of Bristol, Wills Memorial Building, Queen's Road, Bristol, BS8 1RJ, UK

*Corresponding Author: bram.dewinter@earth.ox.ac.uk

Abstract

We examine the equilibrium fractionation of Mg isotopes between forsterite, diopside, and a coexisting melt at liquidus temperatures using a combination of analyses of petrological-experiment products and atomic-scale simulations. Our experiment yields $\Delta^{26}Mg_{ol/melt} = -0.071 \pm 0.032$ ‰ (2s.e.) and $\Delta^{26}Mg_{cpx/melt} = 0.060 \pm 0.034$ ‰ (2s.e.) at 1300 °C for crystals grown from a near-cotectic basaltic melt in the CMAS system, which combine to give $\Delta^{26}Mg_{cpx/ol} = 0.131 \pm 0.045$ ‰ at 1300 °C. The value of $\Delta^{26}Mg_{ol/melt}$ is within the uncertainty of the mean olivine–melt fractionation determined for unzoned phenocrysts and naturally quenched glass from ocean island and mid-ocean ridge basalts. We compare the experimentally determined Mg isotope fractionation between olivine and clinopyroxene with *ab initio* calculations using different density functional theory (DFT) exchange-correlation functionals. We demonstrate that when using the revised Perdew–Burke–Ernzerhof (PBESOL) functional, accounting for thermal expansion, and site-averaging for forsterite, our *ab initio* results are in good agreement with our experiments, yielding $\Delta^{26}Mg_{cpx/ol} = 0.134$ ‰ at 1300 °C. Using the Local Density Approximation (LDA) or other Generalised Gradient Approximation (GGA) functionals, or neglecting thermal expansion, lowers $\Delta^{26}Mg_{cpx/ol}$ values to approximately 0.03–0.06 ‰ below the experimentally measured values. Neglecting site-averaging in forsterite results in

positive (using only M1) or negative (using only M2) deviations in fractionation of 0.08 ‰ from averaged isotope ratios. Comparison of our experimentally and theoretically derived $\Delta^{26}Mg_{cpx/ol}$ values with empirical estimates from natural samples reveals a systematic offset, underscoring the need to distinguish equilibrium mineral–mineral fractionation from empirically derived relationships that may incorporate kinetic or compositional effects.

Keywords: Mg isotopes, equilibrium isotope fractionation, density functional theory, high-temperature experiments.

4.1 Introduction

Atomic-scale simulations are increasingly used to provide information on isotopic fractionation driven by deep-Earth and planetary processes (Young et al., 2015a). Validating these simulations has been challenging due to the small, predicted effects (Blanchard et al., 2017; Schauble, 2011) relative to the limits of traditional analytical reproducibility and the difficulty of acquiring suitable natural samples or experiments that demonstrate pure equilibrium isotope fractionation. Here, we focus on the relatively simple case of equilibrium fractionation of magnesium isotopes between high-temperature silicate phases at ambient pressure. Magnesium is a major rock-forming element, representing a fundamental building block of geological reservoirs. The stable isotopes of magnesium (approx. 79% ^{24}Mg, 10% ^{25}Mg, 11% ^{26}Mg) exhibit a notable relative mass difference of up to 8%, which promotes significant isotopic fractionation, as has been documented in igneous systems that can operate on planetary scales (Hin et al., 2017; Sedaghatpour & Teng, 2016; Teng et al., 2010).

Atomic-scale simulations based on density functional theory (DFT) suggest significant equilibrium fractionation of Mg isotopes among major mantle minerals (Huang et al., 2013; Schauble, 2011; Wang et al., 2023), broadly consistent with observations of Mg isotopic differences in apparently equilibrated natural samples (Young et al., 2009). While such simulations are ideally *ab initio* (i.e., based on first principles without adjustable parameters), important choices must be made that may

affect their reliability. For example, it is necessary to choose the exchange-correlation functional and to decide how to incorporate thermal expansion or the presence of different crystallographic sites in the minerals being studied. Previous studies have made use of the local density approximation (LDA; Perdew and Zunger (1981)) or the PBE (Perdew et al. (1996)), semi-local generalised gradient approximation (GGA) for exchange-correlation functional, but newer functionals are now routinely available (Perdew et al., 2008). PBESOL was created to model the equilibrium properties of solids better and has proven to more accurately reproduce the lattice parameters and elastic properties of silicate minerals than previous GGA functionals. Moreover, many studies have overlooked the effect of thermal expansion. Wang et al. (2023) demonstrate that thermal expansion alters the equilibrium fractionation of Mg isotopes between different minerals. Given the sensitivity of equilibrium isotope fractionation to both exchange-correlation functional and thermal expansion, thorough validation against well-constrained measurements is needed.

Analysis of natural samples, including inter-mineral Mg isotope fractionations preserved in mantle peridotites, as well as mineral–melt isotope fractionations recorded in mid-ocean ridge basalts (MORB), ocean island basalts (OIB), and chondritic meteorites, has provided an empirical foundation for understanding high-temperature isotope fractionation in planetary materials (Pogge von Strandmann et al., 2011; Stracke et al., 2018; Teng et al., 2010; Yang et al., 2009). Early studies provided valuable information but were limited in their ability to resolve these effects because equilibrium fractionations at magmatic temperatures are small and approach the precision limits of sample-standard bracketing techniques (Teng et al., 2015). Recent development of the critical mixture double-spiking technique (Coath et al., 2017) has substantially improved analytical reproducibility, enabling more robust detection of subtle Mg isotope fractionations (Liu et al., 2023) and small but significant Mg isotope differences between chondrites and Earth (Hin et al., 2017).

Interpreting isotopic variations requires well-constrained equilibrium fractionation factors, especially the key equilibrium melt–solid fractionation factors. Particularly, the recent argument of the widely occurring diffusion-driven Mg isotope

fractionations in the MORB samples was based mainly on the empirically determined non-zero melt–olivine fractionation factor (Liu et al., 2023), while others, adopting a zero value of melt–olivine fractionation factor, concluded equilibrium isotope fractionations (Soderman et al., 2024). Despite this, a non-zero melt–olivine fractionation factor was carefully determined previously (Liu et al., 2022). Given the difficulties in obtaining fully equilibrated glass–mineral pairs from natural samples and the fact that diffusion processes can easily influence Mg isotopes (Lai et al., 2015; Richter et al., 2009; Teng et al., 2011), further constraints from theoretical prediction, and petrological experimental work are necessary. Direct comparison between measured Mg isotope fractionation in natural samples and *ab initio* calculations of equilibrium fractionation remains nontrivial.

Petrological experiments offer an alternative method for studying equilibrium isotope fractionation, as they theoretically enable control over key variables like temperature, pressure, and composition. However, in practice, this potential is not always achieved because experimental samples, like natural ones, can experience kinetic fractionation, especially in the form of Soret diffusion, caused by temperature gradients within the experiments, as reported by Liu et al. (2022). The Soret effect is a thermodiffusion process in which isotopes migrate along a temperature gradient, with heavier isotopes tending to concentrate on the cooler side. This can impose very significant isotopic fractionations (Richter et al., 2008). To address this, experiments should explicitly aim to minimise kinetic effects by ensuring minimal thermal gradients across the experimental charge and by homogenising initial compositions. The current lack of controlled studies that can truly isolate equilibrium isotope fractionation between major silicate minerals and co-existing melt highlights the necessity for such research.

This study assesses the influence of various DFT parameters on calculated equilibrium isotope fractionation factors for Mg between forsterite–melt, diopside–melt, and forsterite–diopside, by comparing modelling results with experimental results. Forsterite and diopside were synthesised at near-liquidus conditions at 1 atm in the CMAS system (Ca–Mg–Al–Si). Additionally, DFT calculations are performed

from 0 to 4000 K at 1 atm, using different exchange-correlation functionals, site-averaging methods, and thermal expansion factors (following the approach of Walker et al. (2026)) to calculate isotopic differences between forsterite and diopside. These paired experimental and theoretical results provide a basis for evaluating Mg isotope fractionation at high temperatures.

4.2 Methods

We use two complementary methods to assess equilibrium Mg isotope fractionation between forsterite and diopside. We do this because atomic-scale simulations are most reliable for fractionation between crystalline solids; in this case, the fractionation is driven by mass-dependent changes in crystal vibrations, which lattice dynamics can describe. This approach is not directly applicable to liquids. In our first approach, we used samples from a pair of experiments in which we grew forsterite or diopside crystals from a melt composition at a temperature designed to leave a residual melt near the CMAS cotectic. We measured $\Delta^{26}Mg_{ol/melt}$ and $\Delta^{26}Mg_{cpx/melt}$. Because the residual melt compositions are similar, we can use these experiments to determine $\Delta^{26}Mg_{cpx/ol}$. Since diopside and forsterite are endmembers of clinopyroxene (cpx) and olivine (ol), we label this fractionation as $\Delta^{26}Mg_{cpx/ol}$ (Eq. 1) throughout the text for consistency with literature conventions:

$$\Delta^{26}Mg_{cpx/ol} = \Delta^{26}Mg_{cpx/melt} - \Delta^{26}Mg_{ol/melt} \tag{4.1}$$

Our experiments are designed to minimise the influence of non-equilibrium isotope fractionation processes. We aimed to eliminate the effects of Soret diffusion and Fe–Mg interdiffusion by working in an iron-free system with minimal temperature gradients, and by using long durations to ensure phase homogeneity. With this approach, we create a situation designed to achieve near-equilibrium isotope fractionation.

In our second approach, we utilise atomic-scale simulations to constrain the equilibrium fractionation of ^{24}Mg relative to ^{26}Mg in cpx and ol as a function of

temperature. By design, these simulations yield only equilibrium fractionation and are not sensitive to other processes that cause isotopic fractionation. In this approach, $\Delta^{26}\mathrm{Mg}_{\mathrm{cpx/ol}}$ is derived from the reduced partition function, $\beta(X,\ ^{24}\mathrm{Mg},\ ^{26}\mathrm{Mg})$, which is the equilibrium constant for the isotopic exchange reaction between the phase of interest, X, and an ideal gas (Urey, 1947). The equilibrium isotope fractionation factor between two solid mineral phases (cpx and ol) and two isotopes of an element (^{24}Mg, ^{26}Mg) can be determined as the ratio of β or as the difference in expected measured isotopic content:

$$\Delta^{26}\mathrm{Mg}^{\mathrm{DFT}}_{\mathrm{cpx/ol}} \approx \ln\Big(1000\,\beta(\mathrm{Di},\ ^{24}\mathrm{Mg},\ ^{26}\mathrm{Mg})\Big) - \ln\Big(1000\,\beta(\mathrm{Fo},\ ^{24}\mathrm{Mg},\ ^{26}\mathrm{Mg})\Big) \quad (4.2)$$

where $\Delta^{26}\mathrm{Mg}_{\mathrm{cpx/ol}}$ is the isotopic difference between cpx and ol. In our calculations, β is obtained from the phonon density of states via atomic-scale simulations. However, important choices must be made when undertaking these calculations, and different implementations can yield systematically different fractionation factors. While numerous studies have compared such calculations with isotopic measurements in natural systems (Liu et al., 2023; Soderman et al., 2024), uncertainties remain regarding the sensitivity of the results to computational parameters and assumptions. Our combined approach offers an opportunity to explore the impact of these choices and to further evaluate the computational framework in a system with experimental constraints.

4.2.1 Experiments

We synthesised forsterite and diopside crystals from starting compositions within the CaO–MgO–Al_2O_3–SiO_2 (CMAS) system. We selected starting compositions and equilibration temperatures near the liquidus to achieve melt fractions of 65 vol.% and 80 vol.% for diopside and forsterite experiments, respectively, to keep the residual melt composition close to the eutectic (Figure 4.1).

Starting compositions were synthesised using high-purity oxide and carbonate reagents: calcium oxide (CaO), magnesium oxide (MgO), aluminium oxide (Al_2O_3),

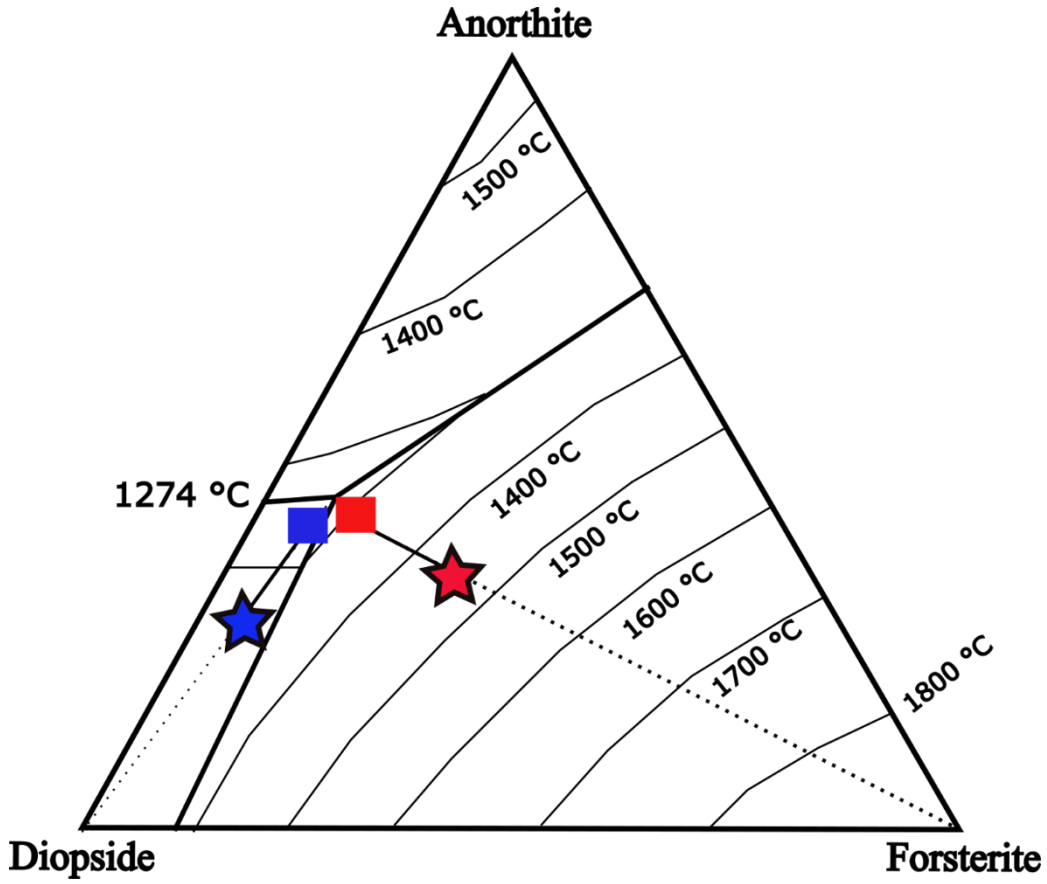


Figure 4.1: Ternary diagram of Diopside-Anorthite-Forsterite after (Morse, 1980). Starting composition (stars) and the measured residual melt (squares) are joined by tie lines for experiments that crystallise diopside (blue) and forsterite (red).

silicon dioxide (SiO_2), and calcium carbonate ($CaCO_3$). $CaCO_3$ was included during initial mixing to promote homogenisation of the starting material and was subsequently decarbonated at high temperature to yield CaO. All oxides were subjected to a drying process at 1000 °C for 12 hours to eliminate any absorbed moisture (H_2O). The dried oxides were then accurately weighed, mixed and ground for 30 minutes to ensure a uniform distribution of components. Following this grinding, $CaCO_3$ was added, and the starting mixture was then decarbonated at 1000 °C overnight. After decarbonation, the mixture was subjected to a second grinding to enhance homogeneity. Starting composition mixtures were glassed at 1375 °C for glass BDW-S2 (used to grow Di) and 1500 °C for glass BDW-S1 (used to grow Fo) for 2 hours in a Gera vertical box furnace (HTRV 70-250/18) at the Earth Science Department of the University of Oxford. Subsequently, the molten starting

composition was quenched in water. To ensure a consistent and homogeneous starting composition, two cycles of melting and grinding were performed (Table 4.1).

Table 4.1: Experimental starting composition measured by EPMA at the University of Oxford. Elemental concentrations are given as wt% oxide.

Experiment	n^a	MgO	s.d.	SiO_2	s.d.	Al_2O_3	s.d.	CaO	s.d.	Total
BDW-S2 (Di)	12	15.43	0.17	50.86	0.22	10.36	0.13	22.96	0.13	99.62
BDW-S1 (Fo)	25	21.36	0.13	47.15	0.18	12.37	0.10	17.59	0.09	99.47

[a]Compositions are given as the average of n analyses.

The crystal growth experiments were conducted in a vertical furnace under atmospheric pressure in air. A "chandelier" assembly was designed to accommodate four platinum loops, each containing a mixture of starting material and a small amount of PVA glue to ensure attachment of the starting material to the loop. In prior experiments, the hot spot and temperature gradient in the furnace were carefully calibrated. We observed a 2 °C temperature gradient over a 10 cm vertical distance within the hotspot using an external Type B thermocouple. The beads in our setup are spaced 1 cm apart. Assuming similar thermal gradients along the horizontal axis, we expect temperatures to vary by < 0.2 °C between beads within a single experiment.

A "chandelier" was positioned at the vertical hotspot at 1500 ± 2.5 °C for 2 hours to ensure thermal equilibration. Subsequently, the temperature was gradually decreased to the target endpoint at a controlled rate of 1 °C/min, as outlined by (Mallmann & O'Neill, 2009). The furnace was then held at the final temperature (Table 4.2) for seven days to allow the growth of crystals exceeding 100 μm. The experiments were quenched in water. Subsequently, the quench beads were extracted, mounted in Araldite epoxy resin, and first polished with abrasive paper and then with a series of diamond pastes. In Figure 4.2, we present backscattered SEM images of two run products, BDW-S2-1 (Di) and BDW-S1-4 (Fo).

The experimental numbering scheme sequentially indicates: the starting composition (BDW-S1 or BDW-S2), the experimental run (e.g., BDW-S2-1), the bead from each experimental run (e.g., BDW-S2-1-1), and a letter for the individual drill site (e.g., BDW-S2-1-1A).

4.2.2 Analytical techniques

The morphology and size of recovered forsterite and diopside crystals were determined using a FEI Quanta 650 scanning electron microscope (SEM) at the Department of Earth Sciences, University of Oxford. Backscatter images of all recovered beads are given in Figure 4.9.

The major element compositions of starting compositions and experimental run products were analysed by Electron Microprobe Analysis (EMPA) using a CAMECA SX-5 FE system at the University of Oxford's Department of Earth Sciences, operating at 10 nA and 20 kV with a spot size of 1 μm. For calibration, we used natural albite (Si, Al, Mg) and andradite (Ca) standards. To ensure that experimental run products are homogeneous, transect lines were set up across minerals and melt pools (see Figure 4.10).

For magnesium isotope analysis, beads BDW-S1-4 (Fo) and BDW-S2-1 (Di) were chosen because they contained the largest mineral phases (Figure 4.9). The material drilling and isotope analysis follow the procedures detailed by Liu et al. (2022, 2023). In brief, a New Wave Research microdrill was used to obtain two samples each of forsterite and diopside, as well as four samples of silicate melt from BDW-S2-1 (Di) and two from BDW-S1-4 (Fo). The sample material was drilled in a droplet of approximately 5 μL of Milli-Q water placed on the surface mount. The water containing the drilled powder was then recovered using a pipettor and transferred to a cleaned Teflon beaker. The drilled samples were subsequently digested in a mixture of ultra-pure concentrated HNO_3, HCl, and HF in a 3:1:1 volume ratio on a hotplate at 150 °C. Following complete digestion, the samples were dissolved in 1 M HNO_3 for magnesium column chemistry.

Magnesium was purified using two-column cation-exchange chromatography with BioRad AG50W-X12 resin. Aliquots of 1 mL of eluent were taken before and after the Mg collection window to check the yield, which exceeded 99.8% for all samples. Magnesium isotope measurements were performed on a Thermo-Finnigan Neptune MC-ICPMS. Jet sample cone and H skimmer cone were used. The sample solution was aspirated into the mass spectrometer in a 0.3 M HNO_3

solution containing 1 μg/ml Mg, using the combination of a Savillex PFA nebuliser and Apex HF (Element Inc.).

The instrumental mass bias is corrected through the ^{25}Mg–^{26}Mg critical mixture double spike method (Coath et al., 2017; Hin et al., 2017; Liu et al., 2023). Mg isotope data are reported as δ^{26}Mg DSM-3 (the relative difference of ^{26}Mg/^{24}Mg between the sample and the reference standard DSM-3), and are subsequently abbreviated as δ^{26}Mg. Analyses of the rock standard BHVO-2 and BIR-1 yielded a δ^{26}Mg value of -0.206 ± 0.035 ‰ and -0.206 ± 0.023 ‰, respectively, consistent with previous reports (He et al., 2022; Liu et al., 2023).

4.2.3 First-principles calculations

The *ab initio* approach for isotope fractionation is similar to previous studies of Mg isotope fractionation (Huang et al., 2013; Schauble, 2011; Wang et al., 2023; Wu et al., 2015; Young et al., 2009) as well as other isotope systems (Blanchard et al., 2009; Javoy et al., 2012; X. Li & Liu, 2011; X. Li et al., 2009; Rustad & Dixon, 2009). To calculate $\Delta^{26}\mathrm{Mg}_{\mathrm{cpx/ol}}$, we use plane waves and pseudopotential (Payne et al., 1992) approach to density functional theory (DFT: (Hohenberg & Kohn, 1964; Kohn & Sham, 1965)) and lattice dynamics in CASTEP (Clark et al., 2005).

Our reference calculations are undertaken in two steps. First, we determine the equilibrium structure of forsterite and diopside. These calculations were performed using a generalised gradient approximation functional designed to give improved equilibrium properties of solids (PBESOL; (Perdew et al., 2008)), and initial crystal structures of forsterite and diopside were obtained from the American Mineralogist Crystal Structure Database (Downs & Hall-Wallace, 2003). These structures were refined by minimising the static energy with respect to atomic positions and cell parameters, with convergence assumed when the maximum force on each atom was below 1.0×10^{-4} eV/Å, maximum stress 0.05 GPa and total energy changes less than 1.0×10^{-5} eV.

All our calculations were performed with norm-conserving pseudopotentials for core electrons and the 2p electrons for O, the 3s and 3p electrons for Si, and

the 3s electrons for Ca and Mg included in the valence. The electron density was expanded on a plane-wave basis with a cutoff energy of 1000 eV and sampled in reciprocal space with $4 \times 2 \times 4$ and $4 \times 4 \times 2$ Monkhorst-Pack grids (Monkhorst & Pack, 1976) for forsterite and diopside, respectively (these parameters were chosen by convergence testing of the phonon frequencies).

In the second step, we calculate the phonon frequencies of both minerals with one magnesium atom substituted for either the heavy (^{26}Mg) or light (^{24}Mg) isotope and the masses of all other atoms set according to their natural isotopic abundances. We used variational Density Functional Perturbation Theory (DFPT: (Gonze, 1997; Gonze & Lee, 1997; Refson et al., 2006)) to calculate phonon frequencies on a shifted grid (to include the gamma point) in reciprocal space, as used for the expansion of the electronic wavefunctions. These were supplemented using Fourier interpolation (Giannozzi et al., 1991) to interpolate frequencies at wave vectors between those included in the DFPT calculation.

We calculated the $\beta(X, Y, Y^*)$ for diopside and forsterite (Kieffer, 1982; Schauble, 2004):

$$\beta(X, Y, Y^*) = \prod_{i=1}^{N_q} \left[\prod_{j=1}^{3N_{\mathrm{at}}} \left(\frac{\omega^*_{i,j}}{\omega_{i,j}} \frac{e^{-h\omega^*_{i,j}/(2kT)}}{1 - e^{-h\omega^*_{i,j}/(2kT)}} \frac{1 - e^{-h\omega_{i,j}/(2kT)}}{e^{-h\omega_{i,j}/(2kT)}} \right) \right]^{w_i} \tag{3}$$

, where $\omega_{i,j}$ and $\omega^*_{i,j}$ are the vibrational frequencies calculated for the two different isotopes in phase X at the ith reciprocal lattice sampling point for the jth branch within the simulation cell that contains N_{at} atoms in the crystal unit cell. T is the temperature in Kelvin, and k is Boltzmann's constant. At a large grid of N_q points sampled in the first Brillouin Zone, we run the second product of Eq. (3) over all modes. We utilised the symmetry of the reciprocal lattice to reduce computational costs. This symmetry is applied to equivalent points with weighting factors w_i, ensuring proper accounting for points on the edges of the sampled irreducible volume. The aim is, therefore, to compute $\omega_{i,j}$ and $\omega^*_{i,j}$ with enough accuracy within the available computational limitations.

The reference calculations are supplemented by others where different choices are made for the calculation of equilibrium isotope fractionation. We alter the

exchange correlation functional using the LDA (Perdew & Zunger, 1981), or a common generalised gradient approximation due to PBE (Perdew et al., 1996). We also explore altering the site in forsterite where the Mg isotope substitution is made. Duan et al. (2023) show that accounting for the presence of two different Mg sites in forsterite is important when calculating isotope fractionation factors. These sites have different polyhedron volumes, affecting isotope fractionation up to 0.5‰ at 900 K (Duan et al., 2023).

Finally, we account for the thermal expansion of the forsterite and diopside crystals. In this study, we employ the approach described by Walker et al. (2026) to investigate the differential thermal expansion of forsterite and also apply it to diopside. For each cell volume, V (calculated by performing geometry optimisation with various pressures while neglecting temperature effects), we calculate phonon frequencies to evaluate the Helmholtz free energy. The volume-energy data obtained are used to fit isothermal third-order Birch-Murnaghan equations of state (EOS), incorporating temperature dependence for parameters such as the zero-pressure volume (V_0), the zero-pressure bulk modulus (K_0), and its pressure derivative (K_0').

Before comparing with experimental data, it is essential to define the theoretical setup most likely to produce accurate predictions of equilibrium isotope fractionation. In cases where direct experimental data is unavailable, we consider the combination of the PBESOL exchange–correlation functional, explicit thermal expansion treatment, and averaging across the two distinct Mg sites in forsterite as the most physically sound and consistent methodological approach. This setup offers the best overall representation of the structural and vibrational properties in silicate minerals and is thus used as the reference model for further analysis.

4.3 Results

4.3.1 Experimental run products

We selected the two beads with the biggest crystals for isotope analysis: BDW-S2-1 (Di), comprising diopside crystals with diameters ≥ 400 μm, and BDW-S1-4 (Fo), containing forsterite crystals with diameters ≥ 250 μm (Figure 4.2). Several

Table 4.2: Experimental run conditions, phase proportions and compositions of runs analysed for their isotopic compositions.

Experiment	Phase	T (K)	Duration (days)	Phase proportions (wt%)	n^a	MgO	SiO_2	Al_2O_3	CaO	Total	n^a	δ^{26}Mg	2 s.e.
S2-1 (Di)		1573	7	Glass (64), Di (36)									
	melt				10	11.61 (5)	49.11 (3.7)	17.47 (9)	22.21 (2.6)	100.41	12	-1.372	0.023
	diopside				14	17.62 (2.7)	52.93 (3.6)	5.27 (8.1)	25.01 (2.1)	100.83	12	-1.312	0.023
S1-4 (Fo)		1560	7	Glass (80), Di (20)									
	melt				10	13.86 (0.9)	48.72 (2.3)	15.7 (0.7)	21.62 (0.6)	99.9	36	-1.362	0.018
	forsterite				20	56.95 (2.4)	42.7 (1.3)	0.08 (0.1)	0.68 (0.1)	100.42	18	-1.42	0.025

[a] Compositions are given as the averages of n analyses.
Mass fraction phase proportions obtained by mass-balance calculations.
Major element compositions reported as weight percentages with uncertainties given in parentheses as 10^{-1} (s.e).

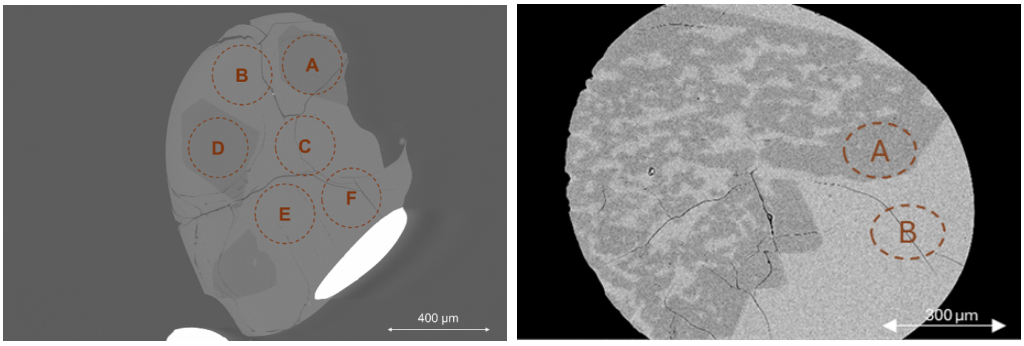


Figure 4.2: BSE images of experimental run products: a) bead BDW-S1-4 containing three Fo crystals and b) bead BDW-S2-1 containing a large Di crystal. These beads were used for micro drilling and isotope analysis. Orange dotted circles show the drill sites with letters corresponding to isotope samples reported in Table 4.5

additional experimental charges were created during this study; however, most produced crystals too small for reliable microdrilling or isotope analysis, leaving only two charges suitable for determining equilibrium fractionation factors. A representative backscattered electron image (BSE) of a polished cross-section is shown in Figure 4.2. Neither the melt nor the mineral phases show any heterogeneity, despite the skeletal textures of the diopside crystals (Table 4.2, Figure 4.9 & Figure 4.10). Mass balance calculations reveal that the mineral phases comprise 19.57 wt% for S1 (Fo) and 36.56 wt% for S2 (Di), within 1 wt% of the proportions expected by applying the lever rule to the phase diagram shown in Figure 4.1.

4.3.2 Experimental isotope analysis

Liu et al. (2022) observed that, in the experimental materials, the isotope ratio varied systematically with position within experimental charges that experience significant temperature differences, suggesting the occurrence of Soret diffusion, making the experimental runs less reliable for providing convincing isotope fractionation factors. In contrast, our measurements (Table 4.5) show homogeneity (2 s.e. $= \pm 0.025\,‰$, comparable to the analytical precision limit of $\pm 0.027\,‰$, (Liu et al., 2023)) across multiple sites within a single sample, as expected in a system near isotopic equilibrium. This is in contrast to the up to 0.6 ‰ δ^{26}Mg variance seen in Liu et al. (2022) as a result of larger temperature variations within the sample. Therefore,

we believe our samples do not exhibit thermal gradients or the Soret effect under the current analytical precision.

We drilled six melt samples from the beads (Figure 2, orange dotted circles). Fractionation factors are calculated directly from the individual analyses reported in Table 4.5. The average Mg isotope composition for each phase in each bead is reported in Table 2. Average Δ^{26}Mg for ol–melt and cpx–melt are $\Delta^{26}Mg_{ol/melt} = -0.058 \pm 0.032$ at 1573 ± 2.5 K and $\Delta^{26}Mg_{cpx/melt} = 0.060 \pm 0.034$ at 1560 ± 2.5 K. Assuming this fractionation varies as $1/T^2$ (where T is temperature in K) and tends to zero as the temperature tends to infinity (expected for equilibrium fractionation: Urey (1947)) results in $\Delta^{26}Mg_{cpx/melt} = (1.49 \pm 0.84) \times 10^5/T^2$ and $\Delta^{26}Mg_{ol/melt} = (-1.44 \pm 0.79) \times 10^5/T^2$ (Figure 4.3a&b). We then corrected the $\Delta^{26}Mg_{ol/melt}$ at 1560 K using the temperature-dependent equation, resulting in $\Delta^{26}Mg_{ol/melt} = -0.071 \pm 0.032$. Our $\Delta^{26}Mg_{ol/melt}$ value is in good consistency with previously reported $\Delta^{26}Mg_{ol/melt}$ values obtained from naturally quenched olivine–glass pairs (Liu et al., 2022) (Figure 4.3a). Furthermore, based on these obtained $\Delta^{26}Mg_{ol/melt}$ and $\Delta^{26}Mg_{cpx/melt}$ values, we can then derive $\Delta^{26}Mg_{cpx/ol} = 0.131 \pm 0.045$ at a temperature of 1560 ± 2.5 K, yielding $\Delta^{26}Mg_{cpx/ol} = (2.93 \pm 1.15) \times 10^5/T^2$ (Figure 4.3c).

4.3.3 Ab initio calculations

First, we evaluate the influence of the chosen exchange-correlation functionals on the mineral structures of diopside and forsterite. Our calculations were conducted using the LDA, GGA, and PBESOL exchange-correlation functionals. Results following geometry optimisation show that the calculated cell parameters (Table 4.7) and the Mg–O bond lengths (Table 4.6) for the PBESOL functional are much closer to experimental values than those obtained with LDA or PBE functionals (Figure 4.4).

Figure 4.11 illustrates the temperature dependence of the averaged reduced partition function (β) of forsterite and diopside using E_{xc} PBESOL, LDA and PBE compared to previous studies (Huang et al., 2013; Schauble, 2011; Wang et al., 2023). An overview of the methodologies used in the literature is given

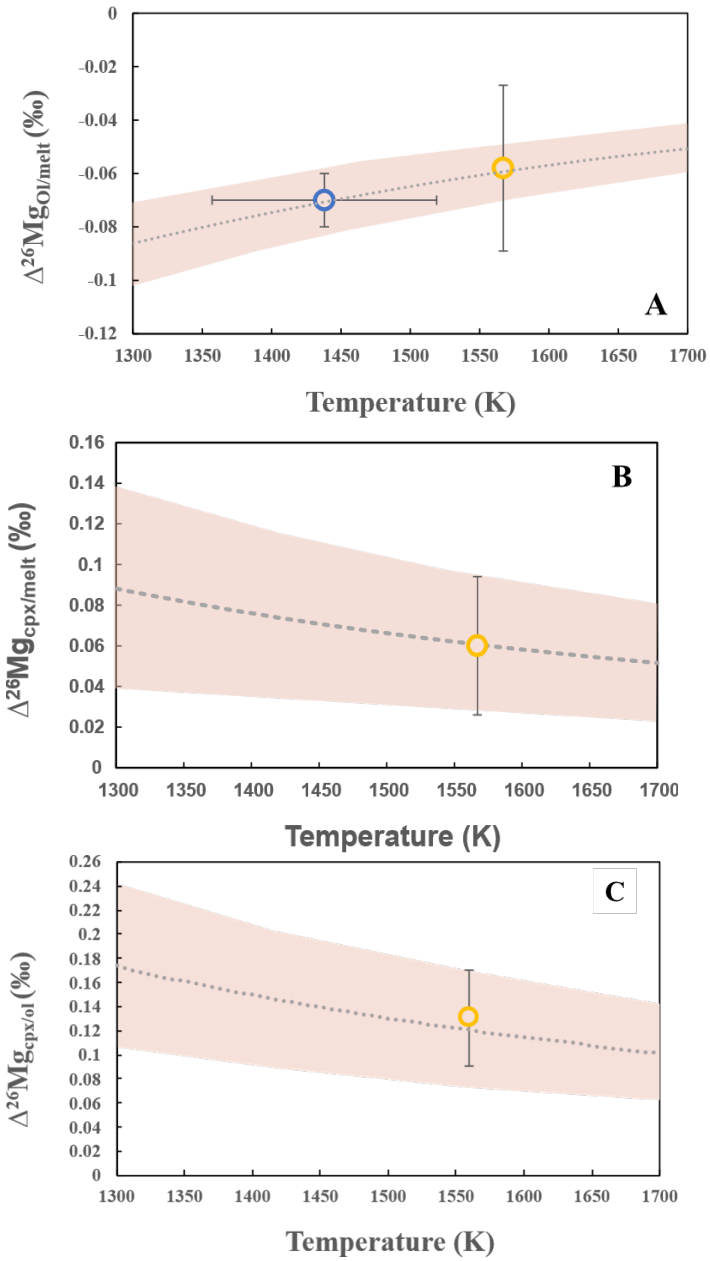


Figure 4.3: Mg isotopic difference between: (a) olivine–melt plotted against temperature for this study (yellow symbol) and compared with data from (Liu et al., 2022) (blue symbol). Temperature uncertainties in experiments are expected to be < 2.5 K (°C) and therefore not plotted as error bars. Dashed line represents the estimated $\Delta^{26}Mg_{ol/melt}$ as a function of temperature from (Liu et al., 2022) with uncertainties in orange. (b) clinopyroxene–melt plotted against temperature with $\Delta^{26}Mg_{cpx/melt}$ calculated in this study. (c) clinopyroxene–olivine plotted against temperature.

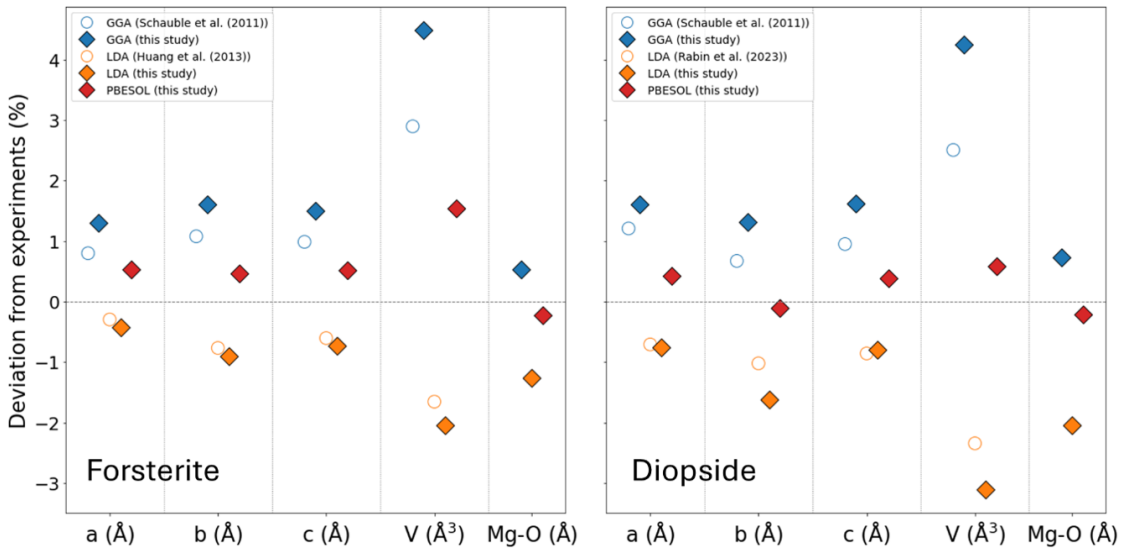


Figure 4.4: Deviation of calculated cell parameters and Mg–O bond lengths (Table 4.7) from experimentally determined crystal structures, with static (0 K) DFT results compared to experimental studies at the lowest temperature found. Diopside at 10 K (Prencipe et al., 2000), forsterite at 77 K (Hazen, 1976). PBESOL shows the smallest deviation across all metrics, indicating better agreement with the experimental crystal structure.

in Table 4.8. The polynomial fit parameters of the β-values calculated in this study are detailed in Table 4.3.

It is important to understand how the choice of exchange–correlation functional affects the relative reduced partition functions that enter isotope fractionation factors, and to distinguish this effect from differences that arise solely from changes in the calculated crystal structure. To explore this, we conducted additional calculations using the PBESOL, PBE, and LDA exchange-correlation functionals for forsterite while fixing the unit cell volume to its experimental value. First, we used fixed-volume calculations for forsterite and observed differences in $\beta(^{26}\mathrm{Mg}/^{24}\mathrm{Mg})$ of 0.04 ‰ (LDA) and −0.02 ‰ (PBE) relative to PBESOL.

To assess how structural differences influence isotope fractionation independently of the exchange–correlation functional, we conducted PBESOL calculations to examine the effect of variations in Mg–O bond lengths on the reduced partition function. Small bond length changes were induced by applying different external pressures, which systematically altered the unit-cell volume while maintaining a fixed functional. These calculations revealed a Mg isotope fractionation sensitivity

of 0.00375 ‰ for every 0.001 Å change in Mg–O bond length.

Using the sensitivity of Mg isotope fractionation to Mg–O bond length derived from the PBESOL pressure-dependent calculations, and the differences in average Mg–O bond length between the fixed-volume PBESOL, LDA, and PBE structures (Table 4.6), we estimate that only $\sim$ 0.003 ‰ (LDA) and $\sim$ 0.0006 ‰ (PBE) of the total offset can be attributed to bond length differences. The remaining offsets, therefore, arise from the direct effect of the exchange–correlation functional force constants.

Table 4.3: Polynomial fitted constants for $1000\ln(\beta(X, {}^{24}\mathrm{Mg}, {}^{26}\mathrm{Mg})) = AT^{-6} + BT^{-4} + CT^{-2}$ as a function of T in Kelvin from 1000–4000 K.

	A	B	C
Forsterite PBESOL M1	2.809×10^{14}	-1.766×10^{10}	2.523×10^{6}
Forsterite PBESOL Average	2.613×10^{14}	-1.642×10^{10}	2.346×10^{6}
Forsterite PBESOL M2	2.416×10^{14}	-1.519×10^{10}	2.170×10^{6}
Forsterite PBE	2.325×10^{14}	-1.464×10^{10}	2.134×10^{6}
Forsterite LDA	2.447×10^{14}	-1.541×10^{10}	2.247×10^{6}
Diopside PBESOL	2.163×10^{14}	-1.565×10^{10}	2.518×10^{6}
Diopside PBE	1.535×10^{14}	-1.218×10^{10}	2.188×10^{6}
Diopside LDA	2.720×10^{14}	-1.880×10^{10}	2.783×10^{6}

Here, we approach the different cation sites in forsterite, similar to (Duan et al., 2023), where we calculate the M1 and M2 sites and average them to produce a single $10^3 \ln\beta$ for δ^{26}Mg in forsterite (Figure 4.6). We observe a 14% difference in $10^3 \ln\beta$ for δ^{26}Mg between the M1 and M2 sites. Diopside has only one cation site for Mg, so it does not require averaging.

Lastly, recent studies have shown the impact of thermal expansion on phonon frequencies and, consequently, on isotope fractionation (Walker et al., 2026; Wang et al., 2023). Our calculated temperature dependent third-order Birch-Murnaghan parameters were fitted to fifth-order polynomials (Equation 4.9). These were then used to evaluate cell volume as a function of temperature and pressure. In addition, we calculated β as a function of temperature. We fitted this to a polynomial in volume and temperature (Table 4.4).

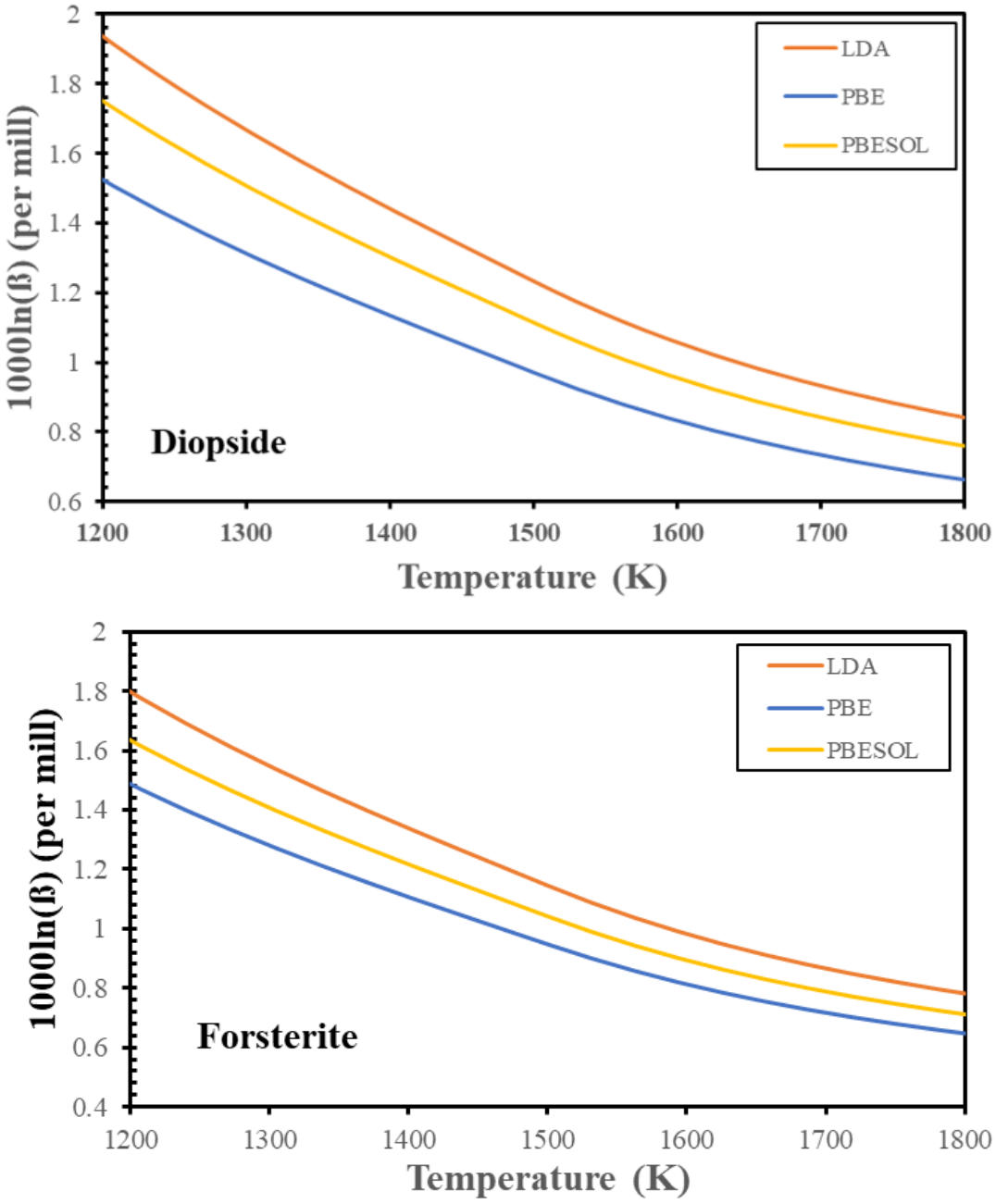


Figure 4.5: Reduced partitioning function for magnesium isotopes in (a) diopside and (b) forsterite for LDA (orange), PBE (blue) and PBESOL (yellow) functionals.

Figure 4.6 illustrates the $10^3 \ln\beta$ for δ^{26}Mg for Fo and Di, accounting for thermal expansion. The correction for thermal expansion is significant, as this slight change in unit-cell parameters leads to larger differences in $\Delta^{26}\mathrm{Mg}_{\mathrm{cpx/ol}}$ values. Thermal expansion was treated using the quasi-harmonic approximation, whereby the equilibrium cell volume and thermal expansivity vary continuously with temperature. The values quoted here represent the average thermal expansivity over the investigated temperature range and are provided only for comparison with previous studies. The expansion factors calculated for forsterite, $\alpha = 4.92\times10^{-5}$ K^{-1}; for diopside, $\alpha = 2.50\times10^{-5}$ K^{-1} between 1200 - 1800 K. These values are consistent with those found in previous experimental studies (Bouhifd et al., 1996; Finger & Ohashi, 1976). In contrast, the *ab initio* study of Wang et al. (2023) reported that diopside ($\alpha = 7.22\times10^{-5}$ K^{-1}) expands more than forsterite ($\alpha = 6.44\times10^{-5}$ K^{-1}), which leads to opposite effects in their $\Delta^{26}\mathrm{Mg}_{\mathrm{cpx/ol}}$ calculations using different exchange-correlation functionals (LDA). This discrepancy highlights how the choice of exchange functional and the thermal expansion correction significantly influence the accuracy of isotope fractionation predictions.

Table 4.4: Coefficients of the polynomial $1000\ln(\beta(V,T)) = (A_1 + A_2V^{-1})T^{-6} + (B_1 + B_2V^{-1} + B_3V^{-2})T^{-4} + (C_1 + C_2V^{-1} + C_3V^{-2})T^{-2}$ to calculate the reduced partition functions with thermal expansion correction between 300–1900 K with respective cell volumes.

	Fo	Di
A1 (K^6)	-1.5252×10^{15}	-9.4405×10^{14}
A2 (K^{6}Å^3)	5.2452×10^{17}	5.1513×10^{17}
B1 (K^4)	-1.2555×10^{11}	-2.8136×10^{11}
B2 (K^{4}Å^3)	9.1326×10^{13}	2.7616×10^{14}
B3 (K^{4}Å^6)	-1.7484×10^{16}	-7.0174×10^{16}
C1 (K^2)	1.1904×10^{6}	9.5665×10^{6}
C2 (K^{2}Å^3)	-1.3578×10^{9}	-9.7941×10^{9}
C3 (K^{2}Å^6)	5.0313×10^{11}	2.9521×10^{12}

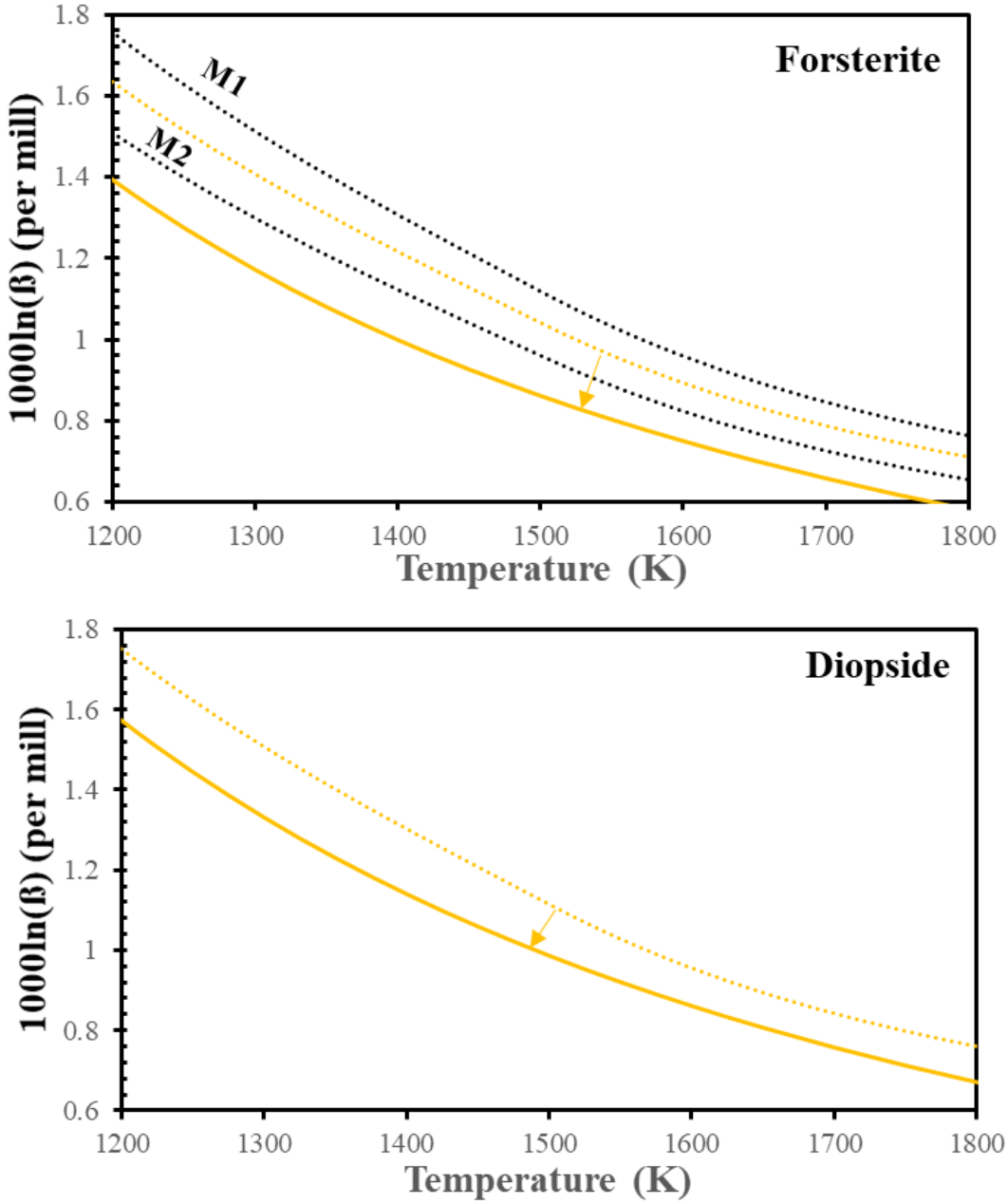


Figure 4.6: Reduced partitioning function with thermal expansion correction (yellow solid line) and without thermal expansion (yellow dotted line). The M1 and M2 sites (black dotted line) are averaged and then corrected for thermal expansion.

4.3.4 Comparison between experimental and theoretical results

We demonstrate a good agreement between the $\Delta^{26}Mg_{cpx/ol}$ ratios obtained from our experiments and those predicted by our PBESOL *ab initio* calculations performed with thermal expansion correction (Figure 4.7). The experimentally determined $\Delta^{26}Mg_{cpx/ol}$ ratios offer a reference point to evaluate the impacts of various exchange-correlation functionals, site averaging, and thermal expansion treatments on calculated equilibrium isotope fractionation. Notably, the calculated isotope fractionation ratios utilising the PBESOL functional with thermal expansion correction fall within the uncertainty range of the measured $\Delta^{26}Mg_{cpx/ol}$ values (Figure 4.7). Our study here evaluates which functional best reproduces Mg isotope fractionation rather than asserting that PBESOL is universally superior.

In contrast, calculations based on other exchange–correlation functionals, including LDA (Huang et al., 2013), LDA + QHA (Wang et al., 2023), and GGA (Schauble, 2011), yield $\Delta^{26}Mg_{cpx/ol}$ values that are lower than our experimentally constrained value by $\sim 0.02\,‰$ at 1573 K. These studies do not explicitly account for thermal expansion in the calculation of inter-mineral fractionation factors. Our results show that thermal expansion introduces a correction due to the reduced partition functions of olivine being relatively larger compared to diopside, suggesting that neglecting this effect is likely to contribute substantially to the apparent offset between these calculations and experimental constraints.

Interestingly, the calculations performed by Schauble (2011) using GGA as E_{xc} do not agree with our GGA (PBE) calculations. The variations between our calculations and Schauble (2011) reflect instead a difference in approach to translating phonon frequencies to reduced partition function ratios (β). Previously, it was a common approach to use a scale factor to correct vibrational frequencies for softening in the functional group when comparing results with those from vibrational spectroscopy (Schauble, 2011). More recent work (Huang et al., 2013; Walker et al., 2026; Young et al., 2015b) shows that computational methods have improved and remove the need for empirical corrections without losing predictive accuracy.

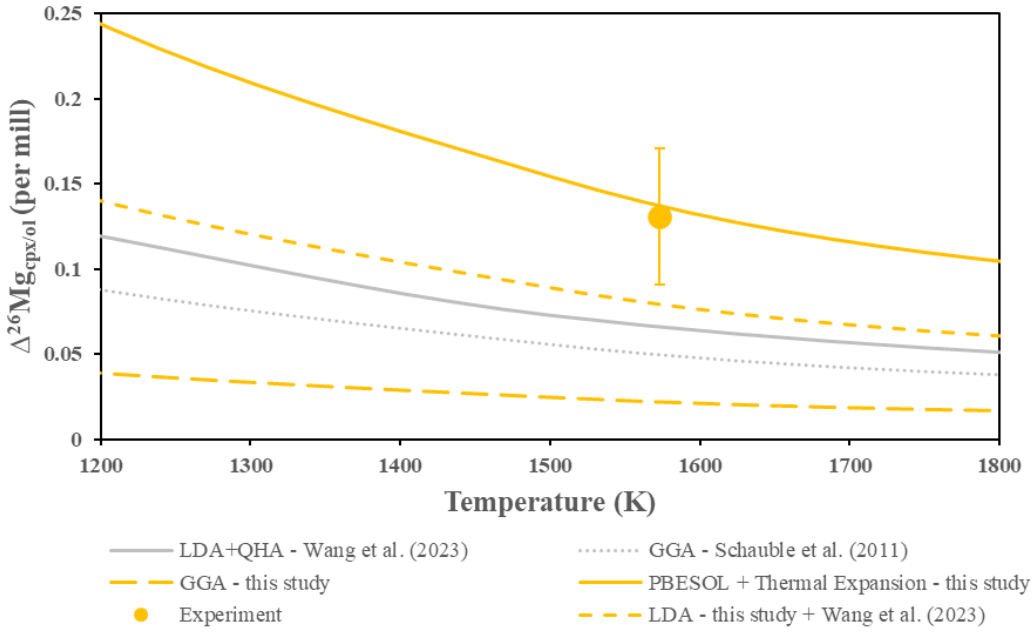


Figure 4.7: Inter-mineral Mg isotope fractionation between diopside and forsterite plotted as a function of temperature and compared with density functional theory calculations at 0 GPa from this study and from the literature. Static-volume calculations using GGA/PBE (yellow striped) and LDA (yellow dotted) are shown. LDA results from this study and from (Wang et al., 2023) overlap within the resolution of the figure and are therefore represented by the same symbol.

4.4 Discussion

Our results show good agreement between experimental determination of a value of $\Delta^{26}Mg_{cpx/ol}$ and its DFT Mg calculation (Figure 4.7). The PBESOL functional, when combined with thermal expansion and site averaging in forsterite, reproduces the measured $\Delta^{26}Mg_{cpx/ol}$ values most accurately, suggesting that this approach provides the most reliable basis for modelling equilibrium isotope behaviour in silicate minerals. In comparison, LDA and PBE underestimate Mg isotope fractionation in diopside and forsterite.

4.4.1 Assessment of isotopic equilibrium

A critical requirement for interpreting the measured Mg isotope fractionation factors is that the experimental measurements record equilibrium rather than kinetic isotope effects. Several processes can potentially drive non-equilibrium isotope fractionation

in high-temperature experiments, including intracrystalline diffusion and mineral–melt exchange, thermal diffusion (Soret effect), and melt heterogeneity (Liu et al., 2022; Richter et al., 2008, 2009; Teng et al., 2011).

Intracrystalline diffusion and mineral–melt exchange are expected to overprint equilibration isotope signatures over time, but their effectiveness depends on the relative rates of diffusion to crystal size and the experiment duration. Using published Mg diffusion coefficients for olivine and clinopyroxene (Chakraborty, 1997; Dohmen et al., 2007; Zhang et al., 2010), diffusion lengths over the 7-day dwell period at experimental temperatures are estimated to be limited to the outer few micrometres of the crystals. Given that the analysed crystals are 100–400 μm in diameter, diffusive re-equilibration only affects the crystal rims and is unlikely to dominate the bulk compositions in our drilled sections. This interpretation is supported by the absence of measurable major-element zoning in EMPA transects across both minerals and adjacent melt (Figure 4.10). While the resolution and coverage of these traverses do not preclude very small-scale heterogeneity, they demonstrate that no large compositional gradients are preserved at the scale relevant to isotopic analysis.

Thermal diffusion, also known as the Soret effect, can generate measurable isotopic fractionation when temperature gradients occur in experimental samples (Liu et al., 2022; Richter et al., 2008). However, this effect is unlikely to have influenced the experiments presented here. The temperature gradient across the experimental charge is estimated to be ca. 0.2 °C. In addition, we obtained melt samples from spatially distinct melt pools within the same experimental bead, and these show indistinguishable δ^{26}Mg values within analytical uncertainty ($\pm$0.025 ‰, 2 s.e.). This contrasts with experiments in which Soret diffusion produces systematic spatial variations in δ^{26}Mg of up to $\sim$ 0.6 ‰ (Liu et al., 2022), whereas no such isotopic variations are observed here. Therefore, we conclude that thermal gradients did not affect our measurement of the samples.

Lastly, melt homogeneity and boundary layer effects can lead to disequilibrium if minerals exchange with local melt reservoirs during growth. However, melt

compositions measured along multiple transects are homogeneous within analytical uncertainty and show no systematic gradients adjacent to mineral phases (Figure 4.10), indicating equilibration with a chemically uniform melt. Although the skeletal morphology of diopside indicates rapid growth under near-liquidus conditions, such textures do not necessarily imply isotopic disequilibrium. In the present experiments, the absence of both major-element zoning and intra-sample isotopic variability indicates that any initial growth-related heterogeneity was effectively homogenised during the dwell period.

In summary, these observations suggest that large kinetic isotope effects are unlikely to have impacted the measured fractionation factors. Despite this, diffusive processes can, in many cases, act to reduce isotopic contrasts between phases by promoting exchange with the surrounding melt (Richter et al., 2009; Teng et al., 2011). However, if diffusion or growth-related processes affect one phase more strongly than another, for example, due to differences in crystal morphology or diffusivity, then apparent inter-mineral fractionation could also be enhanced. The lack of resolvable compositional and isotopic gradients in the present experiments suggests that such phase-specific kinetic effects are not dominant.

We therefore conclude that the measured $\Delta^{26}Mg_{cpx-ol}$ value closely approximates equilibrium isotope fractionation under the experimental conditions. While minor deviations from perfect equilibrium cannot be excluded, the combined textural, compositional, and isotopic evidence indicates that any kinetic contributions are small relative to analytical uncertainty.

4.4.2 Comparison with literature data for Mg isotopic fractionation between olivine and clinopyroxene in naturally occurring samples

Previous studies (Chen et al., 2018; Hu et al., 2020; Liu et al., 2022, 2023; Pogge von Strandmann et al., 2011; Stracke et al., 2018; Yang et al., 2009) have investigated magnesium isotopic fractionation across various mineral phases in natural samples. $\Delta^{26}Mg_{cpx/ol}$ from most studies relying on sample–standard bracketing exhibit significant analytical uncertainties ($> \pm 0.1\,‰$, 2sd; Table 4.5) and are therefore not

well suited for quantitative testing of *ab initio* predictions. Nevertheless, despite their limited precision, such measurements have consistently shown fractionation factors of the same sign and order of magnitude as those predicted by atomic-scale simulations (Stracke et al., 2018; Young et al., 2009).

The recent dataset from Liu et al. (2022, 2023), which employs a critical mixture double-spiking method, provides a higher precision benchmark against which our experimental findings can be compared (Figure 4.8). While our measurements show a $\Delta^{26}Mg_{cpx/ol}$ value that closely matches Liu et al. (2023), who reported 0.131 ± 0.045 ‰, our experimental temperature is roughly 300 K higher than the temperatures estimated for their natural samples. Our theoretical calculations of equilibrium fractionation predict that at temperatures around 1300 K, we would expect the $\Delta^{26}Mg_{cpx/ol}$ values to be approximately 0.2 ‰ higher between the diopside–olivine phases. This suggests that other processes influence isotope ratios beyond equilibrium isotope fractionation. The similarity between experimentally determined fractionation at 1570 K and xenolith values recorded at lower equilibration temperatures is therefore unlikely to represent true equilibrium. Instead, it probably reflects partial kinetic resetting during ascent or cooling, which suppresses the equilibrium fractionation predicted by theory.

This conclusion is further supported when the data are evaluated using relative olivine–clinopyroxene Mg#. We calculated the relative Mg# differences between coexisting olivine and clinopyroxene in the samples used by Liu et al. (2023), following Sen (1988). Most samples exhibit small Mg# differences, usually within ±0.5 Mg#, suggesting near-equilibrium Fe–Mg partitioning between olivine and cpx. A smaller group of samples shows slight positive offsets, with olivine containing more Mg than cpx, up to +2 Mg#. Importantly, however, even samples that show near-equilibrium Fe–Mg partitioning yield $\Delta^{26}Mg_{cpx/ol}$ values that are systematically lower than our experimentally determined equilibrium fractionation. This indicates that agreement in Fe–Mg exchange does not guarantee equilibrium Mg-isotope fractionation and suggests that kinetic effects or incomplete isotopic equilibrium may persist in natural systems even where major-element partitioning appears equilibrated.

Minor but systematic deviations from equilibrium Mg isotope fractionation may arise during xenolith ascent, when decreasing temperature shifts the equilibrium Fe–Mg partitioning between olivine and clinopyroxene. Experimental and thermodynamic studies show that cooling favors an increase in Mg# of clinopyroxene relative to olivine, driving Mg diffusion from olivine into clinopyroxene as the system attempts to re-equilibrate (Putirka, 2008; Sen, 1988). Because Mg diffusion is faster than complete Fe–Mg re-equilibration, this process may halt before equilibrium is fully achieved. Diffusion-driven isotope fractionation then results in isotopically light Mg being concentrated in clinopyroxene rims, while olivine rims become relatively heavy, leading to a net reduction in $\Delta^{26}Mg_{cpx/ol}$ compared to the high-temperature equilibrium value. Such kinetic isotope effects during mineral diffusion are well documented in a range of mineral systems (Oeser et al., 2015; Richter et al., 2009; Sio et al., 2013). However, the effect in Hawaiian xenoliths studied by Liu et al. (2023) is likely limited, since these samples erupted explosively and cooled quickly, reducing the time for post-entrapment diffusion. The small $\Delta^{26}Mg_{cpx/ol}$ values and lack of major-element disequilibrium in mineral cores indicate that Fe–Mg re-equilibration was minimal, and that diffusive changes mostly dampened, rather than overprinted, the original Mg isotope signatures.

Alternatively, differences in $\Delta^{26}Mg_{cpx/ol}$ between natural and experimental mineral pairs could reflect the simplified, iron-free nature of the experimental system. However, our results show that both $\Delta^{26}Mg_{ol/melt}$ and $\Delta^{26}Mg_{cpx/melt}$ determined in this iron-free system are consistent, within uncertainty, with values from natural, Fe-bearing samples (Liu et al., 2022, 2023). This suggests that iron content does not exert a first-order control on equilibrium Mg isotope fractionation between mineral phases and melt and therefore is unlikely to dominate olivine–clinopyroxene fractionation either. While theoretical frameworks have proposed that cation electronegativity and bonding environment may influence isotope fractionation (Méheut & Schauble, 2014), direct experimental constraints on the effect of iron on Mg isotope fractionation remain limited. Further experiments incorporating

iron would nonetheless be valuable for testing for any subtle or second-order effects beyond the scope of this study.

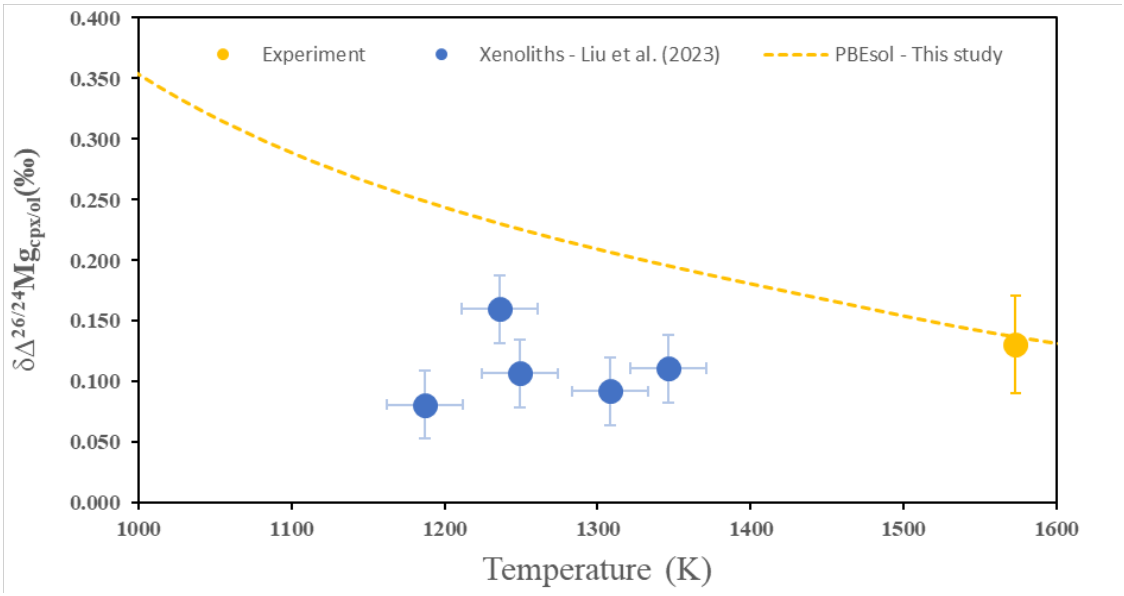


Figure 4.8: Inter-mineral Mg isotopic differences for clinopyroxene–olivine with PBESOL + site averaging + thermal expansion (tallow line) plotted against temperature in Kelvin and compared to xenoliths from (Liu et al., 2023).

4.4.3 Constraints on $\Delta^{26}Mg_{ol/melt}$ from experiments

Unlike the $\Delta^{26}Mg_{cpx/ol}$, our $\Delta^{26}Mg_{ol/melt}$ matches the ratio reported by Liu et al. (2022) (Figure 4.3). Although the compositions of residual melt and mineral phases in our experiments differ from those in the natural samples analysed by Liu et al., our results are complementary and consistent with the observed $\Delta^{26}Mg_{ol/melt} = (-1.46 \pm 0.26) \times 10^5/T^2$. This contrasts with the assumption of $\Delta^{26}Mg_{ol/melt} = 0$ (Soderman et al., 2024; Stracke et al., 2018) based on the work of Teng et al. (2007). The difficulty of accounting for the $\delta^{26}Mg$ of many mantle-derived basalts using equilibrium melting processes with the olivine–melt fractionation factor of Liu et al. (2022) led Soderman et al. (2024) to argue for the continued use of $\Delta^{26}Mg_{ol/melt} = 0$. That our new experimental results strongly support the $\Delta^{26}Mg_{ol/melt}$ reported by Liu et al. (2022), this emphasises the need to consider diffusive fractionation during magma migration to the surface in shaping erupted $\delta^{26}Mg$ (and $\delta^{57}Fe$) of mantle-derived melt (Liu et al., 2024).

Future research should focus on refining mineral–melt Mg isotope fractionation factors by expanding high-temperature experimental datasets to include a wider range of melt compositions, pressures, and redox conditions. Additionally, better constraints on the isotopic equilibrium between crystals and coexisting melt are needed. Specifically, systematic experiments that isolate compositional effects such as melt polymerisation, impurities (e.g Cr) in crystal lattice, and Mg coordination, and exclude kinetic overprints are important for enhancing the accuracy of mineral–melt fractionation factors and precise modelling of Mg isotope fractionation during large-scale differentiation in larger planetary bodies, where the pressure–temperature conditions and crystallisation timescales substantially differ from those studied in this research.

4.5 Conclusions

In this study, we assess the magnitude of Mg equilibrium isotope fractionation between forsterite and diopside at liquidus temperatures, using both data from petrological experiments and theoretical calculations. Our measurements of $\Delta^{26}\mathrm{Mg}_{\mathrm{ol/melt}} = -0.058 \pm 0.032$ and $\Delta^{26}\mathrm{Mg}_{\mathrm{cpx/melt}} = 0.060 \pm 0.034$ at 1300 °C / 1573 K allow us to calculate the first experimentally derived isotope fractionation factor for this mineral pair, with $\Delta^{26}\mathrm{Mg}_{\mathrm{cpx/ol}} = 0.131 \pm 0.04$ at 1576 K.

Our findings align well with *ab initio* calculations based on density functional theory (DFT), particularly emphasising the effectiveness of the PBESOL exchange-correlation functional and the thermal expansion correction in accurately modelling the $\Delta^{26}\mathrm{Mg}_{\mathrm{cpx/ol}}$ ratio. These consistent constraints emphasise the value of precise computational methods and experimentally obtained fractionation factors by producing a single, experimentally anchored $\Delta^{26}\mathrm{Mg}_{\mathrm{cpx/ol}}$ ratio.

Acknowledgements

We thank Krzystof Sokol and Andrew Matzen for their assistance with electron microscopy at the University of Oxford, and Chris Coath for his help in analysing

isotopic data at the University of Bristol. This research was funded by ERC Advanced Grant 883351 NONUNE to TE and BdW received financial support through an Oxford Radcliffe Scholarship from University College, Oxford. For the purpose of Open Access, the authors have applied a CC BY public copyright licence to any Author Accepted Manuscript (AAM) version arising from this submission. The authors would like to acknowledge the use of the University of Oxford Advanced Research Computing (ARC) facility and the ARCHER2 UK National Supercomputing Service (`https://www.archer2.ac.uk`) in carrying out this work.

Data availability

Density functional theory calculations were performed using the CASTEP code, available via `https://www.castep.org/`. Input and output files for these calculations are available through Zenodo via `https://doi.org/10.5281/zenodo.18195898`.

Bibliography

Blanchard, M., Balan, E., & Schauble, E. A. (2017). Equilibrium Fractionation of Non-traditional Isotopes: A Molecular Modeling Perspective. *Reviews in Mineralogy and Geochemistry*, *82*(1), 27–63.

Blanchard, M., Poitrasson, F., Méheut, M., Lazzeri, M., Mauri, F., & Balan, E. (2009). Iron isotope fractionation between pyrite (FeS2), hematite (Fe2O3) and siderite (FeCO3): A first-principles density functional theory study. *Geochimica et Cosmochimica Acta*, *73*(21), 6565–6578.

Bouhifd, M. A., Andrault, D., Fiquet, G., & Richet, P. (1996). Thermal expansion of forsterite up to the melting point. *Geophysical Research Letters*, *23*(10), 1143–1146.

Chakraborty, S. (1997). Rates and mechanisms of Fe-Mg interdiffusion in olivine at 980°–1300°C. *Journal of Geophysical Research: Solid Earth*, *102*(B6), 12317–12331.

Chen, H.-W., Claydon, J. L., Elliott, T., Coath, C. D., Lai, Y.-J., & Russell, S. S. (2018). Chronology of formation of early solar system solids from bulk Mg isotope analyses of CV3 chondrules. *Geochimica et Cosmochimica Acta*, *227*, 19–37.

Clark, S. J., Segall, M. D., Pickard, C. J., Hasnip, P. J., Probert, M. I. J., Refson, K., & Payne, M. C. (2005). First principles methods using CASTEP. *Zeitschrift für Kristallographie - Crystalline Materials*, *220*(5-6), 567–570.

Coath, C. D., Elliott, T., & Hin, R. C. (2017). Double-spike inversion for three-isotope systems. *Chemical Geology*, *451*, 78–89.

Dohmen, R., Becker, H.-W., & Chakraborty, S. (2007). Fe–Mg diffusion in olivine I: Experimental determination between 700 and 1,200°C as a function of composition, crystal orientation and oxygen fugacity. *Physics and Chemistry of Minerals*, *34*(6), 389–407.

Downs, R. T., & Hall-Wallace, M. (2003). The American Mineralogist crystal structure database. *American Mineralogist*, *88*(1), 247–250.

Duan, H., Yang, B., & Huang, F. (2023). Site-specific isotope effect: Insights from equilibrium magnesium isotope fractionation in mantle minerals. *Geochimica et Cosmochimica Acta*.

Finger, L. W., & Ohashi, Y. (1976). The thermal expansion of diopside to 800 degrees C and a refinement of the crystal structure at 700 degrees C. *American Mineralogist*, *61*(3-4), 303–310.

Gao, C., Cao, X., Liu, Q., Yang, Y., Zhang, S., He, Y., Tang, M., & Liu, Y. (2018). Theoretical calculation of equilibrium Mg isotope fractionations between minerals and aqueous solutions. *Chemical Geology*, *488*, 62–75.

Giannozzi, P., de Gironcoli, S., Pavone, P., & Baroni, S. (1991). Ab initio calculation of phonon dispersions in semiconductors. *Physical Review B*, *43*(9), 7231–7242.

Gonze, X. (1997). First-principles responses of solids to atomic displacements and homogeneous electric fields: Implementation of a conjugate-gradient algorithm. *Physical Review B*, *55*(16), 10337–10354.

Gonze, X., & Lee, C. (1997). Dynamical matrices, Born effective charges, dielectric permittivity tensors, and interatomic force constants from density-functional perturbation theory. *Physical Review B*, *55*(16), 10355–10368.

Hazen, R. M. (1976). Effects of temperature and pressure on the crystal structure of forsterite. *American Mineralogist*, *61*(11-12), 1280–1293.

He, Y., Sun, A.-Y., Zhang, Y.-C., Yang, R.-Y., Ke, S., Wang, Y., & Teng, F.-Z. (2022). High-precision and high-accuracy magnesium isotope analysis on multiple-collector inductively coupled plasma mass spectrometry using a critical mixture double spike technique. *Solid Earth Sciences*, *7*(3), 188–199.

Hin, R. C., Coath, C. D., Carter, P. J., Nimmo, F., Lai, Y. J., Pogge von Strandmann, P. A., Willbold, M., Leinhardt, Z. M., Walter, M. J., & Elliott, T. (2017). Magnesium isotope evidence that accretional vapour loss shapes planetary compositions. *Nature*, *549*(7673), 511–527.

Hohenberg, P., & Kohn, W. (1964). Inhomogeneous electron gas. *Physical Review*, *136*(3B), B864.

Hu, Y., Teng, F.-Z., & Ionov, D. A. (2020). Magnesium isotopic composition of metasomatized upper sub-arc mantle and its implications to Mg cycling in subduction zones. *Geochimica et Cosmochimica Acta*, *278*, 219–234.

Huang, F., Chen, L., Wu, Z., & Wang, W. (2013). First-principles calculations of equilibrium Mg isotope fractionations between garnet, clinopyroxene, orthopyroxene, and olivine: Implications for Mg isotope thermometry. *Earth and Planetary Science Letters*, *367*, 61–70.

Javoy, M., Balan, E., Méheut, M., Blanchard, M., & Lazzeri, M. (2012). First-principles investigation of equilibrium isotopic fractionation of O- and Si-isotopes between refractory solids and gases in the solar nebula. *Earth and Planetary Science Letters*, *319–320*, 118–127.

Kieffer, S. W. (1982). Thermodynamics and lattice vibrations of minerals: 5. Applications to phase equilibria, isotopic fractionation, and high-pressure thermodynamic properties. *Reviews of Geophysics*, *20*(4), 827–849.

Kohn, W., & Sham, L. J. (1965). Self-Consistent Equations Including Exchange and Correlation Effects. *Physical Review*, *140*(4A), A1133–A1138.

Lai, Y.-J., Pogge von Strandmann, P. A. E., Dohmen, R., Takazawa, E., & Elliott, T. (2015). The influence of melt infiltration on the Li and Mg isotopic composition of the Horoman Peridotite Massif. *Geochimica et Cosmochimica Acta*, *164*, 318–332.

Li, W.-Y., Teng, F.-Z., Xiao, Y., & Huang, J. (2011). High-temperature inter-mineral magnesium isotope fractionation in eclogite from the Dabie orogen, China. *Earth and Planetary Science Letters*, *304*(1), 224–230.

Li, X., & Liu, Y. (2011). Equilibrium Se isotope fractionation parameters: A first-principles study. *Earth and Planetary Science Letters*, *304*(1), 113–120.

Li, X., Zhao, H., Tang, M., & Liu, Y. (2009). Theoretical prediction for several important equilibrium Ge isotope fractionation factors and geological implications. *Earth and Planetary Science Letters*, *287*(1), 1–11.

Liu, X.-N., Hin, R., Coath, C., van Soest, M., Melekhova, E., & Elliott, T. (2022). Equilibrium olivine-melt Mg isotopic fractionation explains high δ^{26}Mg values in arc lavas. *Geochemical Perspectives Letters*, *22*, 42–47.

Liu, X.-N., Hin, R. C., Coath, C. D., Bizimis, M., Su, L., Ionov, D. A., Takazawa, E., Brooker, R., & Elliott, T. (2023). The magnesium isotopic composition of the mantle. *Geochimica et Cosmochimica Acta*, *358*, 12–26.

Liu, X.-N., Hin, R. C., Coath, C. D., & Elliott, T. (2024). Mg and Fe isotope compositions of mid-ocean ridge basalts modified by Mg-Fe inter-diffusion during melt transport. *Earth and Planetary Science Letters*, *642*, 118868.

Mallmann, G., & O'Neill, H. S. C. (2009). The Crystal/Melt Partitioning of V during Mantle Melting as a Function of Oxygen Fugacity Compared with some other

Elements (Al, P, Ca, Sc, Ti, Cr, Fe, Ga, Y, Zr and Nb). *Journal of Petrology*, *50*(9), 1765–1794.

Méheut, M., & Schauble, E. A. (2014). Silicon isotope fractionation in silicate minerals: Insights from first-principles models of phyllosilicates, albite and pyrope. *Geochimica et Cosmochimica Acta*, *134*, 137–154.

Monkhorst, H. J., & Pack, J. D. (1976). Special points for Brillouin-zone integrations. *Physical Review B*, *13*(12), 5188–5192.

Morse, S. A. (1980). *Basalts and phase diagrams*. Springer.

Oeser, M., Dohmen, R., Horn, I., Schuth, S., & Weyer, S. (2015). Processes and time scales of magmatic evolution as revealed by Fe–Mg chemical and isotopic zoning in natural olivines. *Geochimica et Cosmochimica Acta*, *154*, 130–150.

Payne, M. C., Teter, M. P., Allan, D. C., Arias, T. A., & Joannopoulos, J. D. (1992). Iterative minimization techniques for ab initio total-energy calculations: Molecular dynamics and conjugate gradients. *Reviews of Modern Physics*, *64*(4), 1045–1097.

Perdew, J. P., & Zunger, A. (1981). Self-interaction correction to density-functional approximations for many-electron systems. *Physical Review B*, *23*(10), 5048–5079.

Perdew, J. P., Burke, K., & Ernzerhof, M. (1996). Generalized gradient approximation made simple. *Physical review letters*, *77*(18), 3865.

Perdew, J. P., Ruzsinszky, A., Csonka, G., Vydrov, O. A., Scuseria, G. E., Constantin, L. A., Zhou, X., & Burke, K. (2008). Restoring the Density-Gradient Expansion for Exchange in Solids and Surfaces. *Physical Review Letters*, *100*(13), 136406.

Pogge von Strandmann, P. A. E., Elliott, T., Marschall, H. R., Coath, C., Lai, Y.-J., Jeffcoate, A. B., & Ionov, D. A. (2011). Variations of Li and Mg isotope ratios in bulk chondrites and mantle xenoliths. *Geochimica et Cosmochimica Acta*, *75*(18), 5247–5268.

Prencipe, M., Tribaudino, M., Pavese, A., Hoser, A., & Reehuis, M. (2000). A SINGLE-CRYSTAL NEUTRON-DIFFRACTION INVESTIGATION OF DIOPSIDE AT 10 K. *The Canadian Mineralogist*, *38*(1), 183–189.

Putirka, K. D. (2008). Thermometers and barometers for volcanic systems. *Reviews in mineralogy and geochemistry*, *69*(1), 61–120.

Refson, K., Tulip, P. R., & Clark, S. J. (2006). Variational density-functional perturbation theory for dielectrics and lattice dynamics. *Physical Review B*, *73*(15), 155114.

Richter, F. M., Dauphas, N., & Teng, F.-Z. (2009). Non-traditional fractionation of non-traditional isotopes: Evaporation, chemical diffusion and Soret diffusion. *Chemical Geology*, *258*(1), 92–103.

Richter, F. M., Watson, E. B., Mendybaev, R. A., Teng, F.-Z., & Janney, P. E. (2008). Magnesium isotope fractionation in silicate melts by chemical and thermal diffusion. *Geochimica et Cosmochimica Acta*, *72*(1), 206–220.

Rustad, J. R., & Dixon, D. A. (2009). Prediction of Iron-Isotope Fractionation Between Hematite (α-Fe2O3) and Ferric and Ferrous Iron in Aqueous Solution from Density Functional Theory. *The Journal of Physical Chemistry A*, *113*(44), 12249–12255.

Schauble, E. A. (2004). Applying Stable Isotope Fractionation Theory to New Systems. *Reviews in Mineralogy and Geochemistry*, *55*(1), 65–111.

Schauble, E. A. (2011). First-principles estimates of equilibrium magnesium isotope fractionation in silicate, oxide, carbonate and hexaaquamagnesium(2+) crystals. *Geochimica et Cosmochimica Acta*, *75*(3), 844–869.

Sedaghatpour, F., & Teng, F.-Z. (2016). Magnesium isotopic composition of achondrites. *Geochimica et Cosmochimica Acta*, *174*, 167–179.

Sen, G. (1988). Petrogenesis of spinel lherzolite and pyroxenite suite xenoliths from the Koolau shield, Oahu, Hawaii: Implications for petrology of the post-eruptive lithosphere beneath Oahu. *Contributions to Mineralogy and Petrology*, *100*(1), 61–91.

Sio, C. K. I., Dauphas, N., Teng, F.-Z., Chaussidon, M., Helz, R. T., & Roskosz, M. (2013). Discerning crystal growth from diffusion profiles in zoned olivine by *in situ* Mg–Fe isotopic analyses. *Geochimica et Cosmochimica Acta*, *123*, 302–321.

Soderman, C. R., Matthews, S., Shorttle, O., Jackson, M. G., Day, J. M. D., Kamenetsky, V., & Williams, H. M. (2024). Global oceanic basalt sources and processes viewed through combined Fe and Mg stable isotopes. *Earth and Planetary Science Letters*, *638*, 118749.

Stracke, A., Tipper, E. T., Klemme, S., & Bizimis, M. (2018). Mg isotope systematics during magmatic processes: Inter-mineral fractionation in mafic to ultramafic Hawaiian xenoliths. *Geochimica et Cosmochimica Acta*, *226*, 192–205.

Teng, F.-Z., Dauphas, N., Helz, R. T., Gao, S., & Huang, S. (2011). Diffusion-driven magnesium and iron isotope fractionation in Hawaiian olivine. *Earth and Planetary Science Letters*, *308*(3), 317–324.

Teng, F.-Z., Li, W.-Y., Ke, S., Marty, B., Dauphas, N., Huang, S., Wu, F.-Y., & Pourmand, A. (2010). Magnesium isotopic composition of the Earth and chondrites. *Geochimica et Cosmochimica Acta*, *74*(14), 4150–4166.

Teng, F.-Z., Wadhwa, M., & Helz, R. T. (2007). Investigation of magnesium isotope fractionation during basalt differentiation: Implications for a chondritic composition of the terrestrial mantle. *Earth and Planetary Science Letters*, *261*(1), 84–92.

Teng, F.-Z., Yin, Q.-Z., Ullmann, C. V., Chakrabarti, R., Pogge von Strandmann, P. A. E., Yang, W., Li, W.-Y., Ke, S., Sedaghatpour, F., Wimpenny, J., Meixner, A., Romer, R. L., Wiechert, U., & Jacobsen, S. B. (2015). Interlaboratory comparison of magnesium isotopic compositions of 12 felsic to ultramafic igneous rock standards analyzed by MC-ICPMS. *Geochemistry, Geophysics, Geosystems*, *16*(9), 3197–3209.

Urey, H. C. (1947). The thermodynamic properties of isotopic substances. *Journal of the Chemical Society (Resumed)*, (0), 562–581.

Walker, A. M., Hin, R. C., & Elliott, T. (2026). Controls on Mg isotopic fractionation between deep mantle phases and relict signatures of a terrestrial magma ocean. *Geochimica et Cosmochimica Acta*, *425*, 131–142.

Wang, W., Wu, Z., Huang, S., & Huang, F. (2023). First-principles investigation of equilibrium magnesium isotope fractionation among mantle minerals: Review and new data. *Earth-Science Reviews*, *237*, 104315.

Wu, Z., Huang, F., & Huang, S. (2015). Isotope fractionation induced by phase transformation: First-principles investigation for Mg2SiO4. *Earth and Planetary Science Letters*, *409*, 339–347.

Yang, W., Teng, F.-Z., & Zhang, H.-F. (2009). Chondritic magnesium isotopic composition of the terrestrial mantle: A case study of peridotite xenoliths from the North China craton. *Earth and Planetary Science Letters*, *288*(3), 475–482.

Young, E. D., Tonui, E., Manning, C. E., Schauble, E., & Macris, C. A. (2009). Spinel-olivine magnesium isotope thermometry in the mantle and implications for

the Mg isotopic composition of Earth. *Earth and Planetary Science Letters*, *288*(3-4), 524–533.

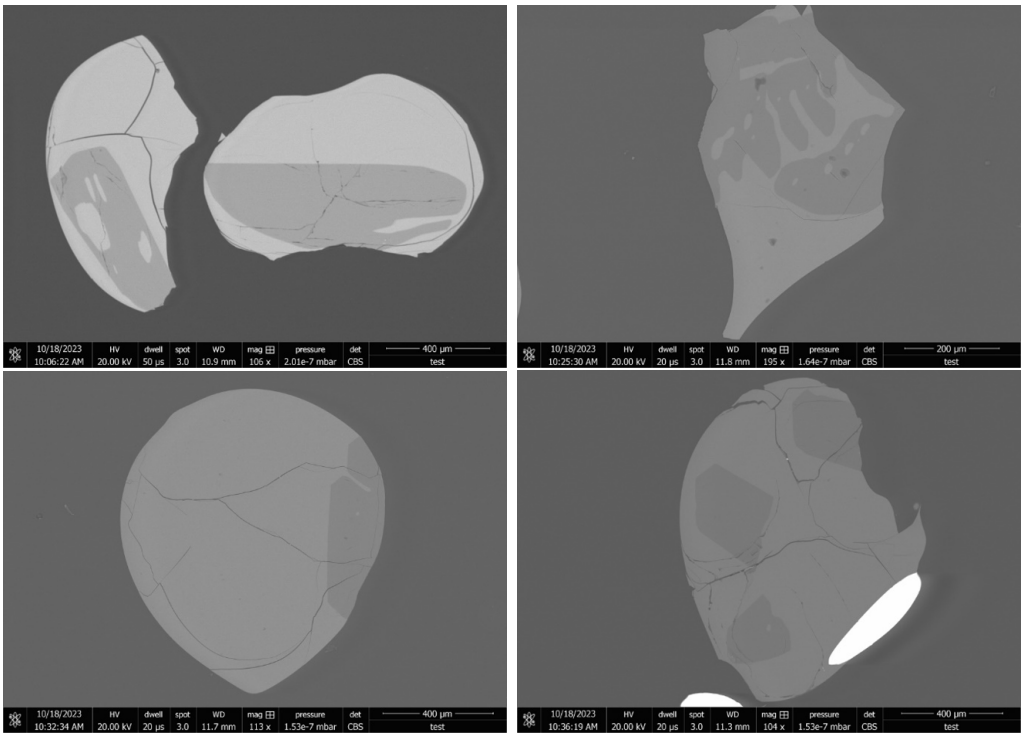
Young, E. D., Manning, C. E., Schauble, E. A., Shahar, A., Macris, C. A., Lazar, C., & Jordan, M. (2015a). High-temperature equilibrium isotope fractionation of non-traditional stable isotopes: Experiments, theory, and applications. *Chemical Geology*, *395*, 176–195.

Young, E. D., Manning, C. E., Schauble, E. A., Shahar, A., Macris, C. A., Lazar, C., & Jordan, M. (2015b). High-temperature equilibrium isotope fractionation of non-traditional stable isotopes: Experiments, theory, and applications. *Chemical Geology*, *395*, 176–195.

Zhang, X., Ganguly, J., & Ito, M. (2010). Ca–Mg diffusion in diopside: Tracer and chemical inter-diffusion coefficients. *Contributions to Mineralogy and Petrology*, *159*(2), 175–186.

Appendix: Supplementary Material

BDW-S1 composition



BDW-S2 composition

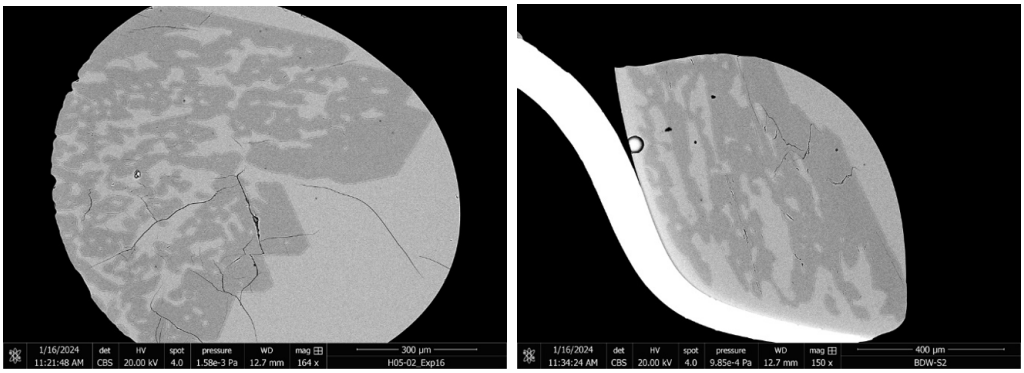


Figure 4.9: SEM images of samples with compositions BDW-S1 and BDW-S2.

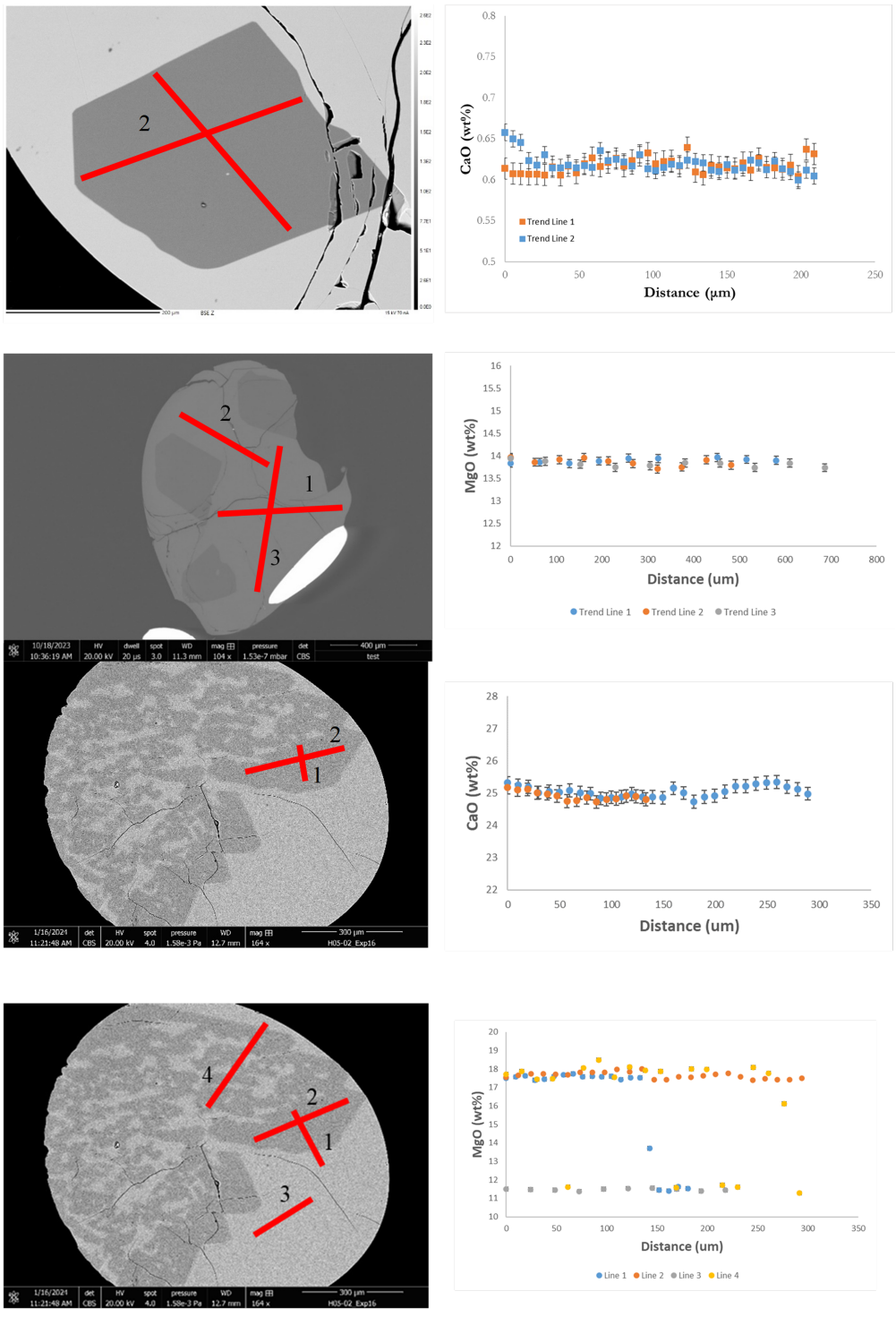


Figure 4.10: EMPA picture with highlighted lines that represent measurement analysis line stages through the forsterite crystal. Analyses were performed every 10 µm with a spot size of 5 µm. B) Concentration of CaO versus distance on the cross-section line stages. C) EMPA picture diopside crystal. D) Concentration of CaO versus distance on the cross-section line stages in diopside.

Table 4.5: Individual δ^{26}Mg measurements (‰) for olivine (Ol), diopside (Di), and coexisting melt from experiments BDW-S1-4 (Fo) and BDW-S2-1 (Di). Error bars represent two standard errors (2 s.e.).

Experiment	Drill site	Phase	δ^{26}Mg	2 s.e.	n^a
BDW-S1-4 (Fo)					
	A	Ol	-1.427	0.035	9
	B	Melt	-1.347	0.035	9
	C	Melt	-1.366	0.035	9
	D	Ol	-1.413	0.035	9
	E	Melt	-1.381	0.035	9
	F	Melt	-1.354	0.035	9
BDW-S2-1 (Di)					
	A	Di	-1.312	0.023	12
	B	Melt	-1.372	0.023	12

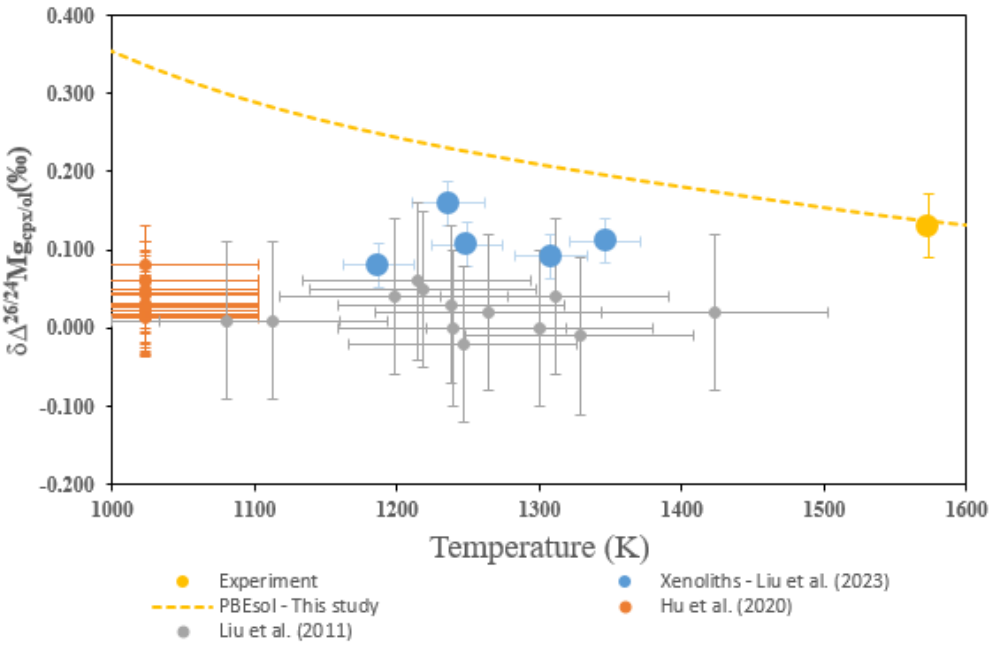


Figure 4.11: Compilation of literature data where both $\Delta^{26}Mg_{cpx/ol}$ and temperature of formation have been estimated. Note the large error bars on (Hu et al., 2020; W.-Y. Li et al., 2011), compared to the double-spiking methods of (Liu et al., 2023).

Table 4.6: Average Mg–O and Si–O bonds in Å, for 0 GPa calculations performed for diopside and forsterite mineral cells using LDA, GGA and PBESOL exchange-correlation functionals.

Mineral	Functional	Mg–O (Å)
Forsterite	LDA	2.0587
	GGA	2.0962
	PBESOL	2.0802
Diopside	LDA	2.0189
	GGA	2.0761
	PBESOL	2.0565

Table 4.7: Unit cell parameters and static volume at 0 K for different E_{xc} used in this study and literature studies. *Ab initio* studies are compared with experimentally determined unit cell volume parameters. Experiments are extrapolated towards 0 K unit cell parameters.

Mineral	E_{xc}	a	b	c	Static volume (Å^3)	Source
Forsterite	LDA	4.732	10.101	5.933	283.584	this study
	LDA	4.738	10.115	5.941	284.714	Huang et al. (2013)
	GGA	4.814	10.357	6.067	302.491	this study
	GGA	4.790	10.303	6.036	297.885	Schauble (2011)
	PBESOL	4.777	10.241	6.008	293.948	this study
	Experiments	4.758	10.190	5.982	290.000	Pamato et al. (2019)
Diopside	LDA	9.687	8.781	5.015	427.101	this study
	LDA	9.692	8.835	5.213	430.477	Wang et al. (2023)
	GGA	9.918	9.043	5.128	459.524	this study
	GGA	9.879	8.986	5.308	451.844	Schauble (2011)
	PBESOL	9.802	8.917	5.070	443.353	this study
	Experiments	9.749	8.925	5.252	439.465	Tribaudino et al. (2000)

Table 4.8: Polynomial fitted constants for $1000\ln(\beta(X, {}^{24}\mathrm{Mg}, {}^{26}\mathrm{Mg})) = AT^{-6} + BT^{-4} + CT^{-2}$ as a function of T in Kelvin for different studies, with $1000\ln\beta$ at 1000 K.

Mineral	E_{xc}	Study	T-exp	Site avg.	A	B	C	$1000\ln\beta$ (1000 K)
Diopside	LDA	(Wang et al., 2023)	Yes	N/A	2.767	-0.01812	0.0001877	2.7487
Diopside	LDA	(Huang et al., 2013)	No	N/A	2.2442	0.1052	-0.0117	2.3353*
Diopside	B3LYP	(Gao et al., 2018)	No	N/A	2.5287	-0.014671	0.00012343	2.5142
Diopside	PBE	(Duan et al., 2023)	No	No	2.3365	-0.01415	0.0001	2.3235
Forsterite	LDA	(Wang et al., 2023)	Yes	No	2.565	-0.01735	0.0001947	2.5478
Forsterite	LDA	(Huang et al., 2013)	No	No	2.0748	0.1052	-0.0119	2.1681*
Forsterite	LDA	(Wu et al., 2015)	No	No	-0.108	2.29	0.0094	2.1914
Forsterite	B3LYP	(Gao et al., 2018)	No	No	2.387	-0.015128	0.00014897	2.3720
Forsterite	PBE	(Duan et al., 2023)	No	Yes	2.4265	-0.01555	0.00015	2.4111
$1000\ln(\beta) = AT^{-6} + BT^{-4} + CT^{-2}$								
Forsterite	PBESOL	This study	Yes	Yes	2.61×10^{14}	-1.64×10^{10}	2.35×10^{6}	2.3964
Forsterite	PBE	This study	Yes	Yes	1.43×10^{14}	-1.43×10^{10}	2.32×10^{6}	2.2315
Forsterite	LDA	This study	Yes	Yes	2.45×10^{14}	-1.54×10^{10}	2.25×10^{6}	2.5642
Diopside	PBESOL	This study	Yes	N/A	2.16×10^{14}	-1.57×10^{10}	2.52×10^{6}	2.5024
Diopside	PBE	This study	Yes	N/A	1.54×10^{14}	-1.22×10^{10}	2.19×10^{6}	2.1763
Diopside	LDA	This study	Yes	N/A	2.72×10^{14}	-1.88×10^{10}	2.78×10^{6}	2.7647
Diopside	PBE	(Schauble, 2011)	No	N/A	1.4032×10^{14}	-1.4915×10^{10}	2.4806×10^{6}	2.4658
Forsterite	PBE	(Schauble, 2011)	No	Yes	1.5614×10^{14}	-1.5115×10^{10}	2.3547×10^{6}	2.3397
Forsterite	PBE	(Walker et al., 2026)	Yes	No	1.8414×10^{14}	-1.6279×10^{10}	2.4312×10^{6}	2.4151

* Huang et al. (2013) polynomials provide different $1000\ln\beta$ at 1000 K compared to their supplementary data.

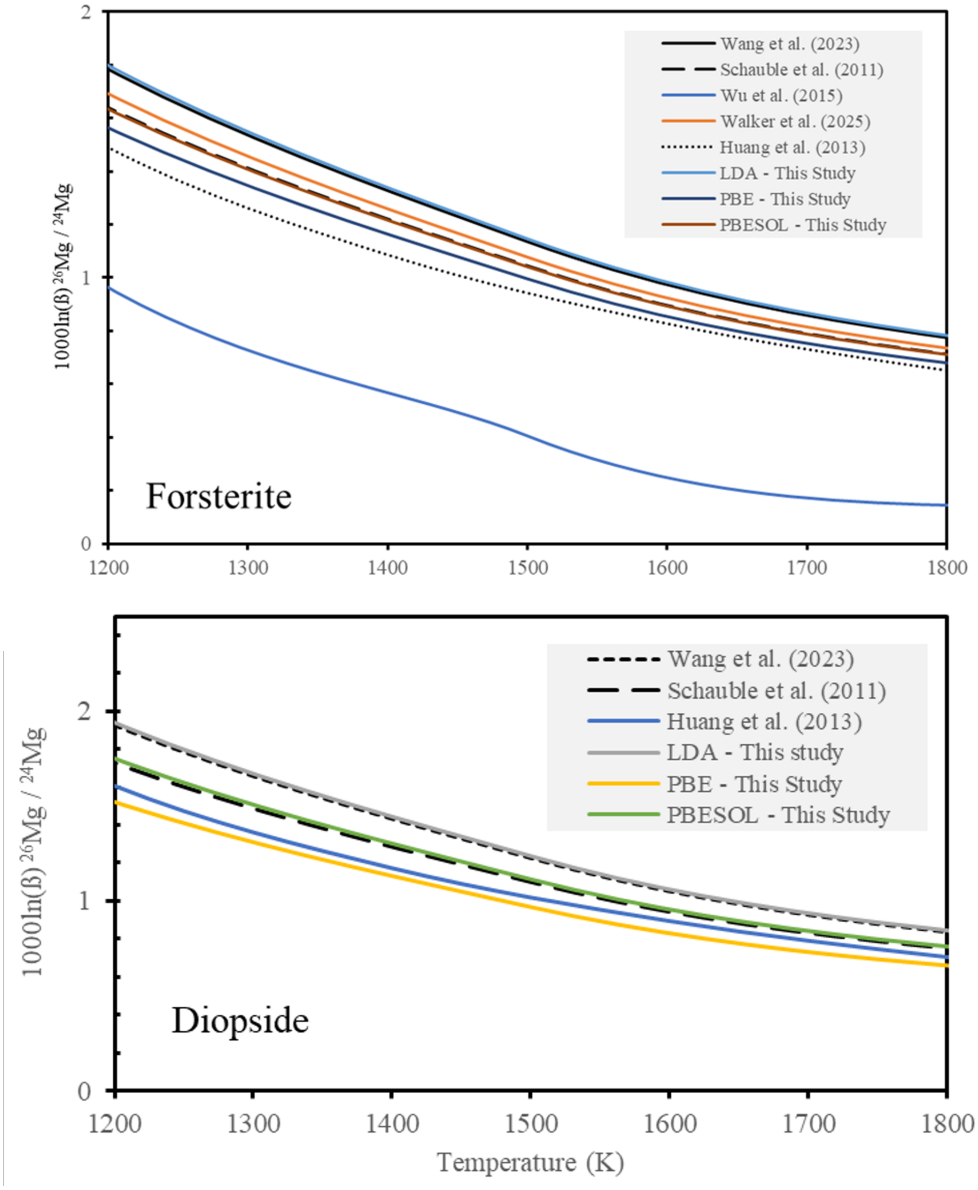


Figure 4.12: Reduced partitioning function for magnesium isotopes in a) forsterite and b) Diopside. An overview of the literature is given in the Supplementary table S2-3.

Table 4.9: Birch-Murnaghan equation of state (EOS) for forsterite and diopside using PBESOL exchange-correlation functional.

$$F(V) = F_0 + \frac{9V_0K_0}{16}\left\{\left[\left(\frac{V_0}{V}\right)^{2/3} - 1\right]^3 K_0' + \left[\left(\frac{V_0}{V}\right)^{2/3} - 1\right]^2 \left[6 - 4\left(\frac{V_0}{V}\right)^{2/3}\right]\right\} \quad (1)$$

Parameter	Coefficient	Forsterite	Diopside
F_0	x_0	-8.96×10^{3}	-1.68×10^{4}
	x_1	1.06×10^{-3}	9.80×10^{-4}
	x_2	-9.68×10^{-6}	-1.33×10^{-5}
	x_3	2.85×10^{-9}	3.95×10^{-9}
	x_4	-5.15×10^{-13}	-7.16×10^{-13}
	x_5	3.61×10^{-17}	5.40×10^{-17}
V_0	x_0	2.96×10^{2}	4.47×10^{2}
	x_1	1.18×10^{-2}	7.31×10^{-3}
	x_2	1.48×10^{-5}	-1.06×10^{-5}
	x_3	1.83×10^{-8}	1.65×10^{-8}
	x_4	-7.20×10^{-12}	-5.98×10^{-12}
	x_5	9.99×10^{-16}	6.56×10^{-16}
K_0	x_0	1.22×10^{2}	9.70×10^{1}
	x_1	-8.41×10^{-3}	-1.65×10^{-3}
	x_2	-1.85×10^{-5}	-4.72×10^{-5}
	x_3	1.03×10^{-8}	-2.72×10^{-10}
	x_4	-2.89×10^{-12}	6.84×10^{-12}
	x_5	2.86×10^{-15}	-1.11×10^{-15}
K_0'	x_0	4.35	7.06
	x_1	1.88×10^{-3}	2.92×10^{-1}
	x_2	-4.60×10^{-6}	-9.88×10^{-4}
	x_3	4.17×10^{-9}	9.48×10^{-7}
	x_4	-1.48×10^{-12}	-3.08×10^{-10}
	x_5	1.85×10^{-16}	3.24×10^{-14}

Table 4.10: Fitted parameters with thermal expansion correction.

$$1000 \ln \beta(V,T) = (A_1 + A_2V^{-1})T^{-6} + (B_1 + B_2V^{-1} + B_3V^{-2})T^{-4} + (C_1 + C_2V^{-1} + C_3V^{-2})T^{-2} \quad (2)$$

	Forsterite M1	Forsterite M2	Forsterite average	Diopside
A1	-1.64×10^{15}	-1.41×10^{15}	-1.53×10^{15}	-9.44×10^{14}
A2	5.64×10^{17}	4.85×10^{17}	5.25×10^{17}	5.15×10^{17}
B1	-1.35×10^{11}	-1.16×10^{11}	-1.26×10^{11}	-2.81×10^{11}
B2	9.82×10^{13}	8.45×10^{13}	9.13×10^{13}	2.76×10^{13}
B3	-1.88×10^{16}	-1.62×10^{16}	-1.75×10^{16}	-7.02×10^{16}
C1	1.28×10^{6}	1.10×10^{6}	1.19×10^{6}	9.57×10^{6}
C2	-1.46×10^{9}	-1.26×10^{9}	-1.36×10^{9}	-9.79×10^{9}
C3	5.41×10^{11}	4.65×10^{11}	5.03×10^{11}	2.95×10^{12}

Work in Progress: Experimental Silicon Isotope Dataset

A complementary dataset investigating equilibrium Si isotope fractionation between minerals and melts was originally intended for inclusion in this thesis. This study was designed to extend the combined experimental–theoretical approach applied to Mg isotopes (Chapter 3) to the Si isotope system, thereby providing a direct test of the MD–DFT framework developed in Chapter 4.

Experimental runs were successfully completed (Figure 4.13), and the resulting materials were prepared for isotope analysis through microdrilling. At the time of submission, these samples are awaiting high-precision Si isotope measurement at the University of Bristol. As a result, the dataset could not be incorporated into the present thesis.

Once completed, these results are expected to provide a critical experimental benchmark for Si isotope fractionation in silicate systems and will be reported in a dedicated publication.

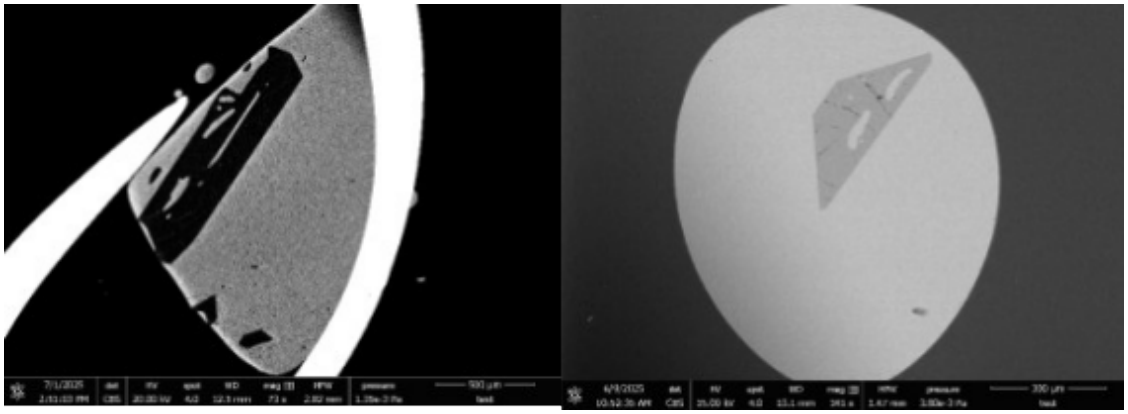


Figure 4.13: SEM images of experimental samples containing diopside (left) and forsterite (right) that are microdrilled and will be measured for Si isotopes.

5

Five-fold Mg in silicate melts drives non-zero Mg isotope fractionation

While Chapter 1 establishes the magnitude of equilibrium Mg isotope fractionation at high temperatures, it does not fully explain the physical origin of this fractionation, particularly the non-zero difference between minerals and melt. This issue is critical because many geochemical models implicitly assume that mineral–melt fractionation is negligible at magmatic conditions, an assumption that directly influences interpretations of mantle composition and melt generation.

The paper presented in this chapter addresses this problem by linking isotope fractionation to the atomic-scale structure of silicate melt. Unlike crystalline minerals, which have well-defined coordination environments, silicate melt are structurally heterogeneous. This heterogeneity introduces a distribution of local bonding environments that may significantly influence isotopic behaviour.

To investigate this, the study combines molecular dynamics (MD) simulations with site-specific DFT calculations, allowing isotope fractionation factors to be calculated for individual atomic environments within the melt. By explicitly accounting for variations in coordination number and bond geometry, this approach moves beyond bulk-averaged models and provides a mechanistic understanding of isotope fractionation in disordered systems.

This chapter, therefore, shifts the focus from measurement and validation to process-level understanding, addressing a key question: what structural features of melt control equilibrium isotope fractionation, and why does Mg behave differently from other elements such as Si?

This manuscript will be submitted to Geochemical Perspective Letters (GPL)

Statement of Authorship for joint/multi-authored papers for PGR thesis is attached in the appendix at the end of the thesis

Five-fold Mg in silicate melts drives non-zero Mg isotope fractionation.

Bram de Winter[a,*], Andrew M. Walker[a], Elena Melekhova[a], Tim Elliott[b]

[a] Department of Earth Sciences, University of Oxford, South Parks Road, Oxford, OX1 3AN, UK

[b] School of Earth Sciences, University of Bristol, Wills Memorial Building, Queen's Road, Bristol, BS8 1RJ, UK

*Corresponding Author: bram.dewinter@earth.ox.ac.uk

Abstract

Empirical observations imply small but resolvable Mg isotope differences between olivine and silicate melt at magmatic temperatures, although their interpretation as equilibrium fractionation is not universally accepted. Establishing a structural basis for these differences using *ab initio* calculations is therefore a critical next step. In this study, we employed molecular dynamics simulations in conjunction with density functional theory calculations to understand the structural controls that govern the non-zero Mg isotope fractionation between olivine and basaltic melt. Our calculations revealed that basaltic melts are rich in five-fold-coordinated Mg (∼50%), in contrast to the six-fold coordination in olivine and clinopyroxene. Five-fold coordinated Mg exhibits larger β-values than six-fold coordinated Mg systematically, resulting in a melt β distinct from mineral values and yielding a non-zero equilibrium $\Delta^{26}Mg_{ol-melt}$. This agrees with recent experimental and natural-sample constraints. In contrast, silicon in the melt is four-fold coordinated and thus exhibits near-zero $\Delta^{30}Si_{ol-melt}$. Our findings demonstrate that the presence of different coordination states in silicate melts provides the structural basis for non-zero equilibrium Mg isotope fractionation at magmatic temperatures.

Introduction

Stable isotope ratios can be excellent tracers of planetary differentiation, but the interpretation of measurements of isotopic ratios can be made more difficult by prior isotope equilibrium fractionation between minerals and melts on the liquidus. For example, estimates of the Mg isotope composition of the mantle are used to trace volatile loss (Hin et al., 2017) and mantle heterogeneity (Liu et al., 2023, 2026; Stracke et al., 2018). Ultimately, interpreting melt-derived Mg isotope compositions requires constraining the magnitude of $\Delta^{26}Mg_{ol-melt}$, which governs melt–mantle fractionation. Although small, equilibrium mineral–melt fractionations can significantly affect the isotopic composition of mantle-derived melts, particularly for compatible elements such as Mg, where mass-balance effects amplify melt–mineral differences. This is important because differences between mantle-derived melts may only amount to ∼0.03–0.10 ‰ (Liu et al., 2023; Zhong et al., 2017). Even minor equilibrium fractionation, however, can significantly bias interpretations of mantle composition and differentiation processes. In an earlier study, Teng et al. (2007) concluded that Mg isotopic fractionation between olivine and melt was negligible, based on a scattered dataset with limited analytical precision rather than discrete measurements of coexisting phases in equilibrium (SI). Their inferred $\Delta^{26}Mg_{ol-melt} = 0.07 \pm 0.10$ ‰ at temperatures $> 1050\,^{\circ}C$, which is well within their analytical error of zero, and further studies have used zero values as an assumption to interpret melt variations as lithological variations (Soderman et al., 2024; Stracke et al., 2018). Recent detailed studies of experiments and mantle xenoliths suggest that isotopic fractionation between olivine and melt might be more significant than previously thought. Specifically, $\Delta^{26}Mg_{ol-melt}$ are approximately in the range of ∼0.02–0.08 ‰ (De Winter et al., in review; Liu et al., 2022, 2023).

In contrast, silicon isotopes exhibit near-zero mineral–melt fractionation in natural samples ($\Delta^{30}Si_{ol-melt} = -0.001 \pm 0.029$ ‰; (Liu et al., 2025)). This indicates that equilibrium fractionation of Si is near zero within analytical uncertainty at conditions relevant for magmatic systems. Computational studies similarly find minimal Si isotope fractionation between minerals and melts (Rabin et al., 2023).

These observations have been interpreted as reflecting a weaker sensitivity of Si isotope fractionation to high-temperature processes (Huang et al., 2014). For both Mg and Si, improved analytical precision afforded by double-spike techniques (Coath et al., 2017) now allows these small fractionations to be resolved more reliably. Together, these observations suggest that Mg and Si isotope fractionation arises from the same equilibrium processes but differ in magnitude due to differences in their structural environments. However, the structural basis for these differences between Mg and Si isotope fractionation in silicate melts remains poorly constrained.

Because isotopes are isoelectronic, the isotopic partitioning between two phases at equilibrium is normally dominated by the vibrational entropy change associated with isotopic exchange. This can be conveniently described by the reduced partition function ratio (β) for each phase, which characterises the partitioning relative to an ideal gas. Equilibrium fractionation between phases is expressed as $\alpha = \beta_1/\beta_2$, and for small fractionation, overall, $\Delta \approx 1000 \ln \alpha$. For crystalline silicates, β can be calculated from an atomic-scale simulation of phonon frequencies (Huang et al., 2013, 2014; Méheut & Schauble, 2014; Schauble, 2011; Walker et al., 2026). For silicate melts, however, the environment of each atom varies. This variation arises from the lack of long-range order and the movement, or diffusion, of atoms in the melt. These configurations are characterised by a distribution of local environments rather than a single environment. Existing computational studies of isotopic fractionation have thus far focused solely on calculating bulk β values for silicate melts. Li et al. (2025) and Rabin et al. (2023) have limited their studies to the isotopes of Fe, Si, and Ca. Extending the methodology for Mg isotopes is interesting because the ion's local environment within a melt can vary with coordination numbers (Dufils et al., 2018; Guillot & Sator, 2007). In particular, this coordination number is affected by local parameters, such as local melt chemistry and therefore cannot be represented by a single average environment. Rather than calculating β values like Rabin et al. (2023), we represent bulk melt-isotopic behaviour as a weighted blend of multiple environments, each with its own distinct β value, allowing also the individual study of each site.

This raises the question: can the variations in local coordination environments in silicate melts account quantitatively for the difference between zero Si- and non-zero Mg isotope fractionation observed between olivine and basaltic melts? We address this question by explicitly linking the melt structure to Mg and Si isotope fractionation. Using molecular dynamics simulations and site-specific density functional theory calculations, we calculate β for different melt sites to determine β values for various Mg and Si environments. By averaging these values according to their abundance in the melts, we compute the bulk melt β and resulting mineral–melt Δ^{26}Mg and test whether it can fully explain the experimental differences in $\Delta^{26}\mathrm{Mg}_{\mathrm{ol-melt}}$ and $\Delta^{26}\mathrm{Mg}_{\mathrm{cpx-melt}}$. To explore this further, we also calculate Si isotope fractionation. This helps us determine the origin of the contrasting isotope fractionation between Mg and Si in olivine, cpx, and the coexisting melt.

5.1 MD–DFT Modelling Framework

We conducted molecular dynamics simulations combined with site-specific β calculations using DFT on a representative iron-free basaltic melt composition, similar to the residual melt composition after crystallisation of solid phases, as described by De Winter et al. (in review). A basaltic composition was selected because experimental constraints on Mg isotope fractionation currently exist only for basaltic systems, allowing direct validation of the calculations. Extension to pyrolitic or magma-ocean compositions is left for future work. These simulations were run at 4000 K and 1 GPa in cells containing 120 atoms. The structure was equilibrated under these conditions for 10 ps, similar to Rabin et al. (2023), to capture the full range of melt structural environments. Details of the equilibrium protocol, MD ensembles, and time-step controls are provided in the Supplementary Information (SI).

For the melt, we selected five static snapshots from the MD trajectories, following Rabin et al. (2023), who demonstrated convergence of isotope fractionation factors using five snapshots by comparison with path-integral molecular dynamics. We therefore adopted the same benchmarked approach to minimise computational

cost while retaining statistical convergence. Rabin et al. (2023) benchmarked this computationally efficient "snapshot" approach against path-integral molecular dynamics (PIMD). Whereas PIMD explicitly accounts for nuclear quantum effects and finite-temperature vibrational sampling, the snapshot method evaluates harmonic vibrational frequencies from static configurations; Rabin et al. (2023) showed that, at magmatic temperatures, both approaches yield indistinguishable Si isotope fractionation factors within uncertainty. Following the approach of Rabin et al. (2023), we collected four snapshots spanning 2–10 ps of simulation time, skipping the first 2 ps to allow the system to reach equilibrium in the liquid state. These snapshots were structurally relaxed by optimising atomic positions until the residual atomic forces dropped below 10^{-3} eV. We relaxed all atoms to part of the residual forces inherited from the MD configurations before phonon calculations. Although relaxing only the substituted isotope has been proposed for crystalline systems and could be explored in future work. Although the MD structures were generated at 4000 K, isotope fractionation was calculated from harmonic vibrational frequencies evaluated for each snapshot. These frequencies determine β as a continuous function of temperature through the partition function, allowing fractionation factors to be evaluated over a wide temperature range. The resulting MD–DFT melt structures exhibit parameters similar to those observed in experimental studies (see SI).

Site-specific calculations of β were performed by treating each distinct Mg ($n = 8$) and Si ($n = 6$) atomic site extracted from MD trajectories individually, thereby explicitly accounting for the local structural environment of each site. To assess both Si and Mg isotope fractionation, we calculated harmonic vibrational frequencies and β using DFT, employing the PBESOL functional (Perdew et al., 2008) and the CASTEP phonons module. We calculated β for Mg- and Si-sites in the structure, then averaged the site- and snapshot-level values to obtain a single β and its standard error for the basaltic melt. The computational setup, including plane-wave cutoffs, pseudopotentials, k-point sampling, and convergence criteria, is described in the SI.

Reduced partition function ratios (β) for crystalline forsterite and diopside were computed using the PBESOL functional at 1 GPa. These mineral β-factors are used

to calculate mineral–melt fractionation and to evaluate the agreement between theory and high-temperature experimental data. In both melt and mineral calculations, temperature-dependent β-values were fitted to simple polynomials for mineral–melt fractionation analysis (see Table 1). Complete sets of coefficients for all melt environments and mineral sites are provided in the SI. The predicted $\Delta^{26}\mathrm{Mg}_{\mathrm{ol-cpx}}$ at 1 GPa is consistent with values obtained in our previous work (De Winter et al., in review), providing an internal consistency check on the MD–DFT framework. Here, thermal expansion corrections were not applied because equivalent quasi-harmonic corrections for liquids are not yet established. Consequently, the calculations isolate structural effects associated with coordination.

5.2 Magnesium isotope fractionation in silicate melt

Figure 5.1 shows how $1000 \ln \beta$ varies with average Mg–O bond length for individual melt sites, grouped by coordination number. For Mg, β increases as bond length decreases, consistent with the expectation that heavier isotopes are preferentially stabilised in stiffer vibrational environments. The coordination number also exerts a systematic effect: five-fold coordinated Mg sites consistently exhibit higher β-values than six-fold coordinated sites.

Molecular dynamics simulations show that basaltic melt exhibits a broader range of local structural environments for Mg than crystalline phases. Most magnesium is found in five- or six-fold coordination (mean CN = 5.47; 53% five-fold, 47% six-fold), with Mg–O bond lengths ranging from 1.95 to 2.15 Å (Figure 5.1). In contrast, Mg in olivine and clinopyroxene is exclusively six-fold coordinated. This structural contrast provides the context for evaluating the role of melt structure in controlling Mg isotope fractionation.

When site-specific β-values are averaged over the complete melt structure, the presence of five-fold coordinated Mg results in a bulk melt β that is higher than that of olivine and clinopyroxene. Because Mg occupies only six-fold sites in these minerals, this coordination contrast leads to non-zero equilibrium Mg isotope

fractionation ($\Delta^{26}Mg_{ol-melt}$) between olivine and melt. The resulting $\Delta^{26}Mg$ differs between olivine–melt and clinopyroxene–melt pairs, reflecting differences in Mg–O bond lengths and site distortions between the two minerals. These predicted mineral–melt fractionations are shown in Figure 1. The magnitude of the calculated olivine–melt Mg isotope fractionation agrees with high-temperature experimental constraints within uncertainty (Figure 5.1), with a slight offset for cpx–melt. In particular, the MD–DFT-derived $\Delta^{26}Mg_{ol-melt}$ reproduces the non-zero fractionation ($\Delta^{26}Mg_{ol-melt} = -0.071 \pm 0.010‰$) reported by Liu et al. (2022) and supported by recent experimental results (De Winter et al., in review).

To assess whether additional structural factors influence Mg isotope fractionation beyond average bond length, site-specific β-values for both five- and six-fold coordinated Mg sites were regressed against the ionic model of Young et al. (2015). The difference between calculated β and ionic model values ($\beta_{residual}$) was analysed. We performed a statistical analysis of the $\beta_{residual}$ for CN = 6 sites, in conjunction with extracted structural melt parameters, to assess the influence of these parameters on β (see SI). Bond length explains approximately 80% of the variance in β across these sites. The remaining variance is dominated by polyhedral distortion, with more asymmetric Mg–O environments exhibiting higher $\beta_{residual}$ values, indicating local stiffening of the shortest bonds. Coordination number is not independent of bond length. Increasing coordination generally lengthens Mg–O bonds, making bond length the primary physical control on . Coordination number nevertheless remains useful because it captures systematic changes in bond-length distributions and polyhedral geometry. Because coordination number and bond length covary, the statistical analysis should not be interpreted as implying independent contributions from each parameter. Other factors, such as proximity to network-forming Si, non-bridging oxygen content, and local charge distribution, exert only minor effects. This analysis shows that while bond length is the dominant control on Mg isotope fractionation, coordination number and polyhedral distortion provide important secondary contributions. This agreement indicates that accounting for Mg coordination variability in melts is sufficient to reproduce the observed non-zero

mineral–melt Δ^{26}Mg at equilibrium. Models that exclude five-fold coordinated Mg or that approximate melt structures using crystalline analogues would instead predict Δ^{26}Mg values close to zero.

Overall, these results show that equilibrium Mg isotope fractionation between minerals and silicate melts can be understood in terms of variations in melt structure. The structural diversity captured in the MD simulations, including differences in coordination number and bond length, contrasts with the more uniform environments present in crystalline phases, consistent with earlier simulation studies showing that melts cannot be treated as crystalline analogues (Dufils et al., 2018; Guillot & Sator, 2007). Although our simulations focus on a single Fe-free basaltic composition at high temperature, the coordination-dependent controls identified here reflect general features of silicate melt structure observed across a wide range of basaltic systems for different pressure–temperature conditions (Rabin et al., 2023).

The dependence of site-specific β-values on coordination number matches earlier *ab initio* studies of crystalline phases (Duan et al., 2023; Schauble, 2011; Walker et al., 2026; Young et al., 2015) and shows that the same physical control operates in melts. In both crystals and melts, changes in coordination geometry alter Mg–O bond stiffness, which, in turn, sets site-β values and thus Mg isotope fractionation. Because melts host a distribution of site environments (notably five-fold sites absent from olivine and cpx), treating the melt as a single average coordination state or using crystalline analogues (Méheut & Schauble, 2014; Walker et al., 2026) omits high-β sites and underestimates equilibrium mineral–melt Δ^{26}Mg if the numerical abundance of different sites is not well represented.

5.3 Silicon isotope fractionation: bond-length dominated behaviour

In contrast to Mg, Si in the basaltic melt occupies a much narrower range of structural environments. Molecular dynamics simulations show that Si is almost exclusively four-fold coordinated (mean CN = 4.03), with only rare five-fold sites occurring in the melt. Average Si–O bond lengths are tightly clustered around

∼1.6 Å, reflecting the relatively rigid tetrahedral framework of the silicate melt. This restricted range of coordination environments provides the context for evaluating the structural controls on Si isotope fractionation.

Figure 5.2 shows the relationship between $1000 \ln \beta$ and average Si–O bond length for individual melt sites. For Si, β increases systematically with decreasing bond length, and the data define a single, continuous trend. Because the coordination number varies little for Si under the conditions studied here, bond length is the dominant control on Si isotope fractionation. Regression analysis indicates that approximately 75% of the variance in Si β-values within four-fold coordinated sites is explained by bond length alone. The remaining variance reflects secondary structural effects, including bond valence and local charge asymmetry. Previous studies have linked Si isotope fractionation to melt polymerisation (Poitrasson, 2017; Savage & Moynier, 2013), which affects Si–O bond lengths without altering coordination number. Our simulations span a limited range of melt polymerisation and do not resolve a systematic relationship between β and polymerisation under the conditions studied here. Unlike Mg, the coordination number does not exert a significant control on Si isotope fractionation under the conditions studied here.

The calculated Δ^{30}Si values for olivine–melt and clinopyroxene–melt pairs are shown in Figure 2a. At magmatic temperatures, these fractionations are close to zero, with opposite signs reflecting differences in average Si–O bond lengths between phases. The predicted olivine–melt fractionation is consistent, within uncertainty, with the available experimental constraint from Liu et al. (2025), as shown in Figure 5.2a.

These results allow comparison of our Si-isotope melt model with that of Rabin et al. (2023), reported a melt reduced partition function of $1000 \ln \beta = 3.202 \pm 0.056$ at 1500 K for an iron-depleted basalt composition (6.72 wt% FeO). This is slightly lower than the reported value here: 3.255 ± 0.064 at 1500 K, although an important methodological difference must be noted. Rabin et al. (2023) used the PBE functional (Perdew et al., 1996) to calculate β for melts, whereas we employ the PBESOL functional (Perdew et al., 2008). PBE is known to underestimate Mg

isotope fractionation in crystalline phases by approximately 0.05–0.07‰ at 1500 K between forsterite and diopside (De Winter et al., in review), with similar values expected for Si isotope fractionation. For this reason, direct quantitative comparison of melt β-values between the two studies is not straightforward, as the choice of exchange–correlation functional influences the predicted β-values.

5.4 A Structural–Chemical Framework for Mineral–Melt Isotope Fractionation

Stable-isotope fractionation between minerals and silicate melts is fundamentally controlled by bond length, which in turn depends on melt coordination. Although Mg fractionation is strongly influenced by coordination variability, both Mg and Si isotope fractionation ultimately reflect differences in bond stiffness. For Si, this is controlled primarily by bond length within a fixed coordination environment, whereas for Mg, coordination variability introduces additional high-β environments in the melt. In basaltic systems, Mg partitions between five- and six-fold coordinated environments, with five-fold sites exhibiting higher β-values. The bulk melt β therefore reflects a weighted average of these environments rather than a single coordination state. In contrast, Si in basaltic melt nearly always occupies fourfold-coordination sites, leading to limited $\Delta^{30}\mathrm{Si}_{\mathrm{min-melt}}$ between basaltic melts and four-coordinated silicate minerals.

This difference is governed by melt chemistry. Melt polymerisation, non-bridging oxygen content, and cation field strength regulate the distribution of coordination environments, thereby controlling the proportion of five- versus six-fold coordinated Mg (Guillot & Sator, 2007). Composition thus exerts a first-order control on Mg isotope fractionation by influencing melt structure. This creates a direct connection from composition to structure (including coordination, bond length, and distortion), then to site-specific β, and ultimately to bulk fractionation.

The ability to reproduce experimentally constrained mineral–melt fractionation at low pressure provides confidence in applying this framework to higher-pressure conditions, where direct constraints are limited. Our results suggest that at fixed

coordination, pressure shortens bonds, whereas increasing coordination lengthens them. These competing effects likely explain pressure-dependent isotope fractionation. These observations broadly agree with Wang et al. (2023), who also found bond length to dominate isotope fractionation within fixed coordination environments. This is particularly relevant for understanding isotope fractionation during magma ocean crystallisation, where coordination changes are expected to be more pronounced. Extending this approach to high-pressure phases offers a pathway to quantify isotope signatures generated during early planetary differentiation.

Acknowledgements

ERC Advanced Grant 883351 NONUNE funded this research to TE, and BdW received financial support through an Oxford Radcliffe Scholarship from University College, Oxford. For Open Access, the authors have applied a CC BY public copyright licence to any Author Accepted Manuscript (AAM) version arising from this submission. The authors would like to acknowledge the use of the University of Oxford Advanced Research Computing (ARC) facility and the ARCHER2 UK National Supercomputing Service (`https://www.archer2.ac.uk`) in carrying out this work.

Bibliography

Coath, C. D., Elliott, T., & Hin, R. C. (2017). Double-spike inversion for three-isotope systems. *Chemical Geology*, *451*, 78–89.

De Winter, B., Walker, A. M., Melekhova, E., Liu, X.-N., & Elliott, T. (in review). The magnitude of equilibrium isotope fractionation of Mg between forsterite, diopside and melt at liquidus temperatures. *Geochimica et Cosmochimica Acta*.

Duan, H., Yang, B., & Huang, F. (2023). Site-specific isotope effect: Insights from equilibrium magnesium isotope fractionation in mantle minerals. *Geochimica et Cosmochimica Acta*.

Dufils, T., Sator, N., & Guillot, B. (2018). Properties of planetary silicate melts by molecular dynamics simulation. *Chemical Geology*, *493*, 298–315.

Guillot, B., & Sator, N. (2007). A computer simulation study of natural silicate melts. Part II: High pressure properties. *Geochimica et Cosmochimica Acta*, *71*(18), 4538–4556.

Hin, R. C., Coath, C. D., Carter, P. J., Nimmo, F., Lai, Y. J., Pogge von Strandmann, P. A., Willbold, M., Leinhardt, Z. M., Walter, M. J., & Elliott, T. (2017). Magnesium isotope evidence that accretional vapour loss shapes planetary compositions. *Nature*, *549*(7673), 511–527.

Huang, F., Chen, L., Wu, Z., & Wang, W. (2013). First-principles calculations of equilibrium Mg isotope fractionations between garnet, clinopyroxene, orthopyroxene, and olivine: Implications for Mg isotope thermometry. *Earth and Planetary Science Letters*, *367*, 61–70.

Huang, F., Wu, Z., Huang, S., & Wu, F. (2014). First-principles calculations of equilibrium silicon isotope fractionation among mantle minerals. *Geochimica et Cosmochimica Acta*, *140*, 509–520.

Li, Y., Hardin, J., Wang, W., Wu, Z., & Huang, S. (2025). Mineral-melt calcium isotope fractionation factors constrained using *ab initio* molecular dynamics simulations and their implications to calcium isotope effects during partial melting in the upper mantle. *Geochimica et Cosmochimica Acta*.

Liu, X.-N., Hin, R., Coath, C., van Soest, M., Melekhova, E., & Elliott, T. (2022). Equilibrium olivine-melt Mg isotopic fractionation explains high δ^{26}Mg values in arc lavas. *Geochemical Perspectives Letters*, *22*, 42–47.

Liu, X.-N., Hin, R. C., Coath, C. D., Bizimis, M., Su, L., Ionov, D. A., Takazawa, E., Brooker, R., & Elliott, T. (2023). The magnesium isotopic composition of the mantle. *Geochimica et Cosmochimica Acta*, *358*, 12–26.

Liu, X.-N., Hin, R. C., Coath, C. D., Onyett, I., Rogers, B., Lewis, J., & Elliott, T. (2026). Magnesium isotope heterogeneity in oceanic island basalts. *Earth and Planetary Science Letters*, *684*, 120010.

Liu, X.-N., Klaver, M., Hin, R. C., Coath, C. D., Bizimis, M., Ionov, D. A., & Elliott, T. (2025). Si isotope composition of Earth's mantle and oceanic basalts. *Geochimica et Cosmochimica Acta*.

Méheut, M., & Schauble, E. A. (2014). Silicon isotope fractionation in silicate minerals: Insights from first-principles models of phyllosilicates, albite and pyrope. *Geochimica et Cosmochimica Acta*, *134*, 137–154.

Perdew, J. P., Burke, K., & Ernzerhof, M. (1996). Generalized gradient approximation made simple. *Physical review letters*, *77*(18), 3865.

Perdew, J. P., Ruzsinszky, A., Csonka, G., Vydrov, O. A., Scuseria, G. E., Constantin, L. A., Zhou, X., & Burke, K. (2008). Restoring the Density-Gradient Expansion for Exchange in Solids and Surfaces. *Physical Review Letters*, *100*(13), 136406.

Poitrasson, F. (2017). *Silicon isotope geochemistry* (Vol. 82).

Rabin, S., Blanchard, M., Pinilla, C., Poitrasson, F., & Grégoire, M. (2023). Iron and silicon isotope fractionation in silicate melts using first-principles molecular dynamics. *Geochimica et Cosmochimica Acta*, *343*, 212–233.

Savage, P. S., & Moynier, F. (2013). Silicon isotopic variation in enstatite meteorites: Clues to their origin and Earth-forming material. *Earth and Planetary Science Letters*, *361*, 487–496.

Schauble, E. A. (2011). First-principles estimates of equilibrium magnesium isotope fractionation in silicate, oxide, carbonate and hexaaquamagnesium(2+) crystals. *Geochimica et Cosmochimica Acta*, *75*(3), 844–869.

Soderman, C. R., Matthews, S., Shorttle, O., Jackson, M. G., Day, J. M. D., Kamenetsky, V., & Williams, H. M. (2024). Global oceanic basalt sources and processes viewed through combined Fe and Mg stable isotopes. *Earth and Planetary Science Letters*, *638*, 118749.

Stracke, A., Tipper, E. T., Klemme, S., & Bizimis, M. (2018). Mg isotope systematics during magmatic processes: Inter-mineral fractionation in mafic to ultramafic Hawaiian xenoliths. *Geochimica et Cosmochimica Acta*, *226*, 192–205.

Teng, F.-Z., Wadhwa, M., & Helz, R. T. (2007). Investigation of magnesium isotope fractionation during basalt differentiation: Implications for a chondritic composition of the terrestrial mantle. *Earth and Planetary Science Letters*, *261*(1), 84–92.

Walker, A. M., Hin, R. C., & Elliott, T. (2026). Controls on Mg isotopic fractionation between deep mantle phases and relict signatures of a terrestrial magma ocean. *Geochimica et Cosmochimica Acta*, *425*, 131–142.

Wang, W., Wu, Z., Huang, S., & Huang, F. (2023). First-principles investigation of equilibrium magnesium isotope fractionation among mantle minerals: Review and new data. *Earth-Science Reviews*, *237*, 104315.

Young, E. D., Manning, C. E., Schauble, E. A., Shahar, A., Macris, C. A., Lazar, C., & Jordan, M. (2015). High-temperature equilibrium isotope fractionation of non-traditional stable isotopes: Experiments, theory, and applications. *Chemical Geology*, *395*, 176–195.

Zhong, Y., Chen, L.-H., Wang, X.-J., Zhang, G.-L., Xie, L.-W., & Zeng, G. (2017). Magnesium isotopic variation of oceanic island basalts generated by partial melting and crustal recycling. *Earth and Planetary Science Letters*, *463*, 127–135.

Figures

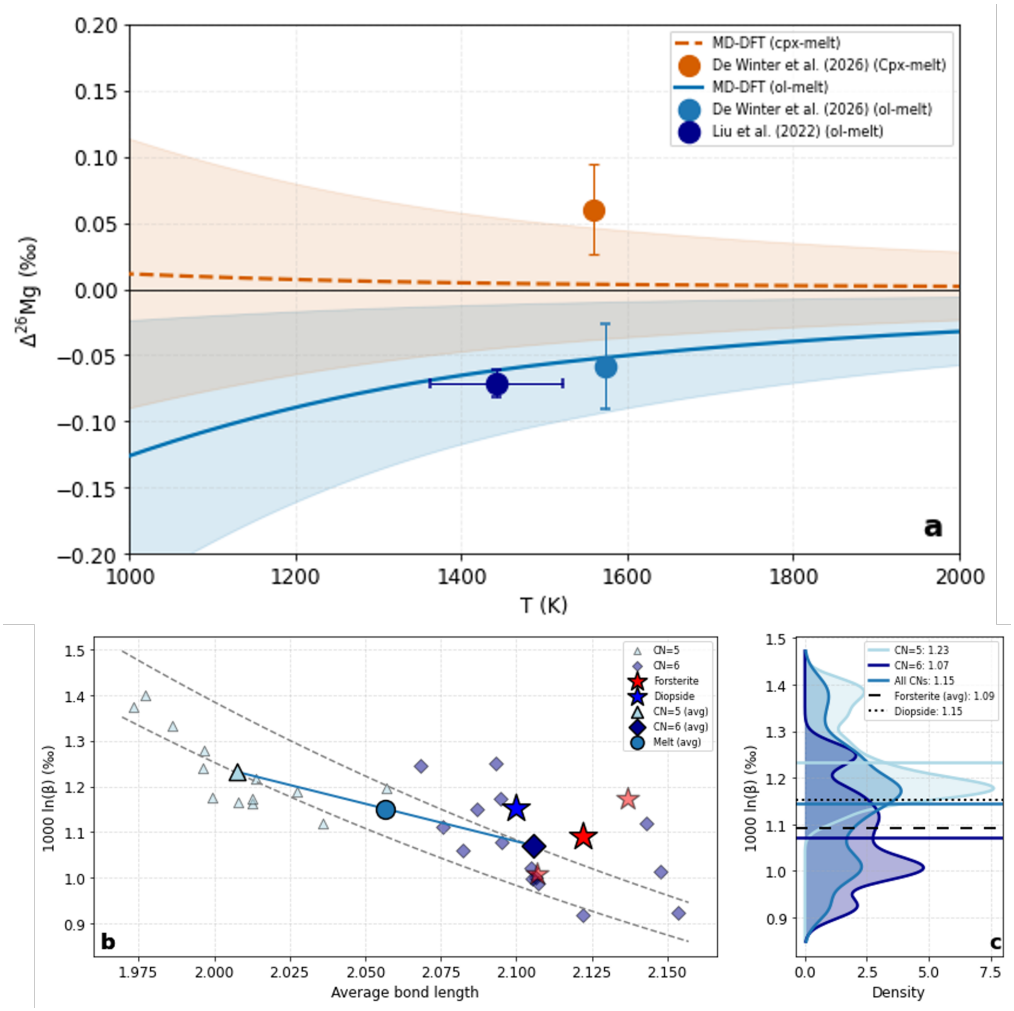


Figure 5.1: (a) Mg isotope fractionation (Δ^{26}Mg) between olivine, clinopyroxene and melt. Lines show MD–DFT predictions; shaded fields are 1σ uncertainties. Experimental data from (De Winter et al., in review; Liu et al., 2022) validate the olivine–melt predictions. (b) Plot of $1000 \ln \beta$ for Mg against average Mg–O bond length at individual melt sites, coloured by coordination number (CN = 5 and CN = 6). Larger symbols depict coordination-averaged melt β-values; Mg sites in forsterite (averaged between M1 and M2 site; smaller red stars) and diopside are included for comparison. Dashed grey lines represent ionic-model predictions (Young et al., 2015). (c) Kernel-density plots show the distribution of melt β-values for each coordination, with horizontal lines indicating average melt and mineral values.

Table 5.1: Polynomial fitted constants at 1 GPa for $1000\ln(\beta(X,\ ^{24}\mathrm{Mg},\ ^{26}\mathrm{Mg})) = AT^{-6} + BT^{-4} + CT^{-2}$ valid over the temperature range 1000–4000 K, where T is in Kelvin. Polynomial coefficients are reported for Mg and Si isotopic systems in forsterite (M1, M2, and average), diopside, and basaltic melt based on static calculations. The corresponding values of $1000\ln\beta$ evaluated at 1500 K are listed for comparison. Uncertainties (1σ), where reported, reflect regression errors of the polynomial fits. Also shown are mineral–melt equilibrium fractionation factors expressed as inverse-square temperature relationships.

	A	B	C	$1000\ln\beta$ (1500 K)
Mg				
Forsterite M2	3.12×10^{14}	-1.94×10^{10}	2.65×10^{6}	1.173
Forsterite Average	2.90×10^{14}	-1.80×10^{10}	2.46×10^{6}	1.091
Forsterite M1	2.68×10^{14}	-1.67×10^{10}	2.28×10^{6}	1.009
Diopside	2.34×10^{14}	-1.66×10^{10}	2.60×10^{6}	1.152
Basaltic Melt	$(3.88 \pm 0.015) \times 10^{14}$	$(-2.18 \pm 0.01) \times 10^{10}$	$(2.59 \pm 0.01) \times 10^{6}$	1.146 ± 0.004
Si				
Forsterite	7.43×10^{15}	-1.93×10^{11}	7.56×10^{6}	3.321
Diopside	8.16×10^{15}	-1.95×10^{11}	7.38×10^{6}	3.241
Basaltic Melt	$(9.12 \pm 0.02) \times 10^{15}$	$(-2.06 \pm 0.02) \times 10^{11}$	$(7.41 \pm 0.01) \times 10^{6}$	3.255 ± 0.064
Mineral–melt fractionation				
$\Delta^{26}\mathrm{Mg}_{\text{ol-melt}}$	$(-1.27 \pm 0.004) \times 10^5/T^2$			
$\Delta^{26}\mathrm{Mg}_{\text{cpx-melt}}$	$(0.11 \pm 0.01) \times 10^5/T^2$			
$\Delta^{30}\mathrm{Si}_{\text{ol-melt}}$	$(1.53 \pm 0.01) \times 10^5/T^2$			
$\Delta^{30}\mathrm{Si}_{\text{cpx-melt}}$	$(-0.29 \pm 0.01) \times 10^5/T^2$			

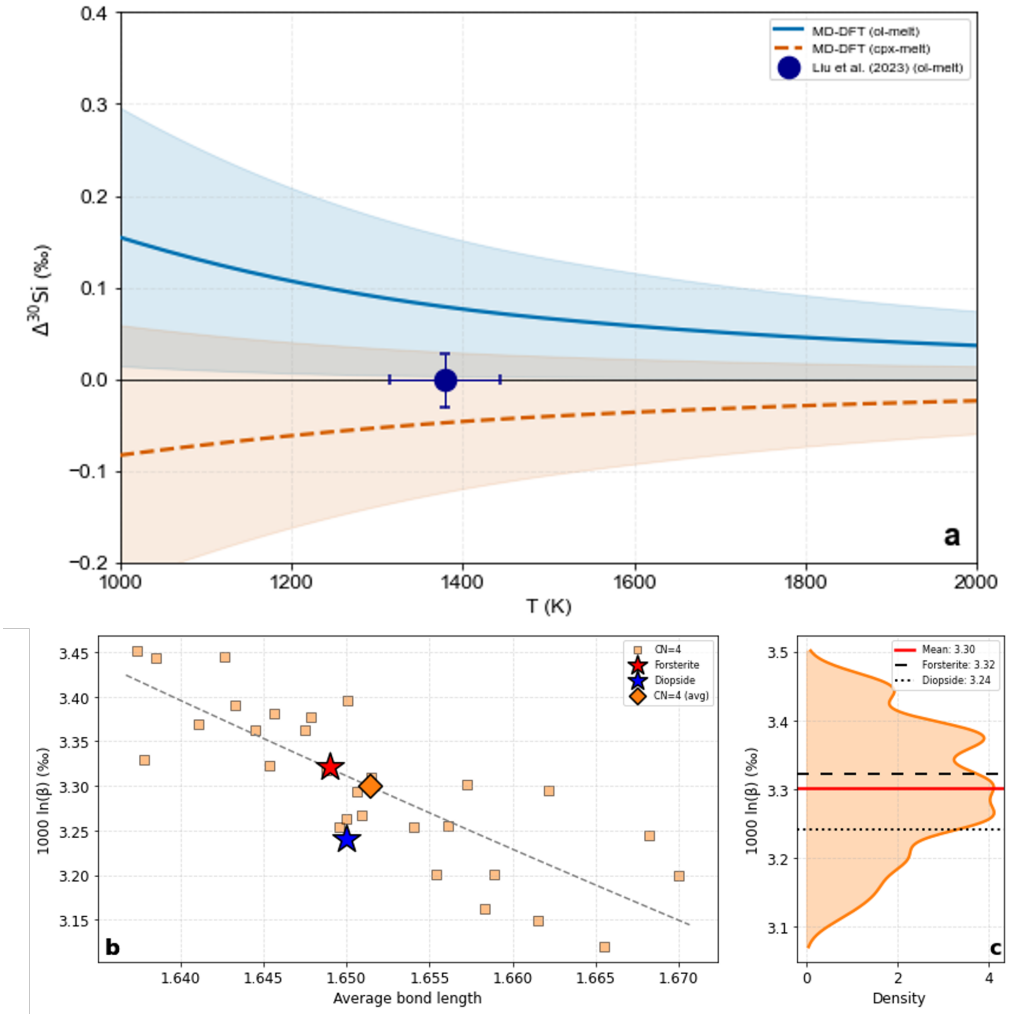


Figure 5.2: (a) Predicted Si isotope fractionation (Δ^{30}Si) between olivine, clinopyroxene, and melt from MD–DFT. Shaded fields show 1σ uncertainties. The cpx–melt measurement from (Liu et al., 2023) is shown for comparison. (b) displaying $1000 \ln \beta$ versus average Si–O bond length for CN = 4 melt sites, including coordination-averaged melt values and mineral references. (c) Density plots illustrate the variation of melt β-values relative to mineral benchmarks.

Appendix: Supplementary Information

1. Computational Methods: Molecular Dynamics and DFT

All calculations in this study were performed using a density functional theory (DFT) workflow using the CASTEP software code. As summarised schematically in Figure 5.3, *ab initio* molecular dynamics (DFT–MD) simulations were used to generate equilibrated silicate melt structures that sample the range of local coordination environments in the liquid. A series of atomic configurations were extracted from these MD trajectories and treated as static snapshots for site-specific DFT calculations to calculate vibrational properties, following the methodology developed by (Rabin et al., 2023). Equilibrium isotope fractionation factors (β) were calculated from these vibrational calculations using isotopic mass substitution, as seen in previous studies (Huang et al., 2013, 2014; Rabin et al., 2023; Schauble, 2011; Walker et al., 2026; Wang et al., 2023). This combined DFT–MD and snapshot-based DFT approach allows melt structure and isotope fractionation to be treated within a single first-principles framework, without reliance on crystalline analogues to study silicate melt.

First-principles calculations were performed using DFT (Hohenberg & Kohn, 1964; Kohn & Sham, 1965) within a plane-wave formalism (Payne et al., 1992) as implemented in CASTEP (Clark et al., 2005). Both mineral and melt DFT calculations were performed using the Perdew–Burke–Enzerhof for solids (PBESOL; (Perdew et al., 2008)). We used norm-conserving pseudopotentials (Troullier & Martins, 1991) with valence configurations including O 2p, Si 3s–3p, Mg 3s, Ca 3s, and Al 3s–3p electrons. The Brillouin-zone sampling was restricted to the Γ-point, appropriate for large, disordered simulation cells. Plane-wave energy cutoffs of 900 eV were chosen based on convergence testing to ensure reliable forces and vibrational frequencies.

Molecular Dynamics simulations

Molecular dynamics (MD) simulations were used to generate equilibrated silicate melt structures suitable for snapshot-based isotope fractionation calculations. All simulations began from a crystalline bridgmanite supercell containing 120 atoms, constructed to ensure realistic initial atomic separations and to avoid unphysical short-range interactions and subsequent failures. The supercell was generated using CrystalMaker®: a powder diffraction program for Mac and Windows (CrystalMaker Software Ltd, Oxford, England; `www.crystalmaker.com`), and exported as a CASTEP `.cell` file.

The initial crystalline structure was fully melted using canonical ensemble (NVT) simulations at 8000 K for 10 ps. Temperature control was achieved using a Nosé–Hoover thermostat (Hoover, 1985; Nosé, 1984), which provides correct sampling of the canonical ensemble and energy exchange between the system and the thermal reservoir. Melt equilibration was assessed through monitoring of equilibrated total energy, temperature stability, radial distribution functions (Figure 5.4), and atomic diffusion behaviour (see next section). When equilibration criteria were not satisfied, additional high-temperature NVT simulations were performed until a stable molten structure was obtained.

Target melt composition (residual melt of experiments based on De Winter et al., in review) was produced by atomic substitution applied to the equilibrated melt structure. Compositional adjustments were performed using a custom Python workflow that modifies cation proportions and writes `.cell` files, which are then used for MD simulations. Following atomic substitution, our melt structures were re-equilibrated at 8000 K to remove any artefacts introduced by the composition change. The simulation was then cooled to 4000 K. Additional NVT simulations at 4000 K (10 ps) were performed to ensure stability.

Because melt structure is strongly dependent on volume, simulation cell parameters were optimised using isothermal–isobaric (NPT) simulations at 4000 K. Pressure was controlled using a Parrinello–Rahman barostat (Parrinello & Rahman, 1981) with NPT simulations running for 10 ps and repeated until the average

pressure converged to 1 GPa. The final MD trajectories were produced in the NVT ensemble at 4000 K for up to 20 ps. Integration steps of 0.001 ps (1 fs) were chosen, following the methodology from (Rabin et al., 2023).

Snapshot selection and preparation

Our snapshot selection was extracted from the equilibrated NVT MD trajectories. These snapshots were selected at regular intervals (0.5 ps) to ensure statistical independence, as measured by (Rabin et al., 2023). We selected only a few snapshots for further calculations due to the computationally expensive DFT geometry optimisation steps. Because our snapshots contain multiple sites of Mg and Si we capture many different configurations that cover the limited amount of snapshots.

Melt snapshot calculations

Each melt snapshot was optimised at 1 GPa using an iterative procedure with progressively tighter electronic convergence criteria, beginning at 10^{-5} eV and refining to 10^{-9} eV. Optimisation continued until residual atomic forces were below 10^{-3} eV and pressures were less than 0.002 GPa. Although these optimised structures are formally glasses rather than liquids, previous studies have demonstrated that their local structural environments are representative of the parent melt, supporting their use in snapshot-based vibrational calculations.

The *ab initio* treatment of equilibrium isotope fractionation follows established approaches developed for Mg and Si isotopes in silicate minerals and melt (Huang et al., 2013, 2014; Rabin et al., 2021; Schauble, 2011; Walker et al., 2026). Density functional theory calculations were performed using CASTEP, and we used variational Density Functional Perturbation Theory (DFPT: (Gonze, 1997; Gonze & Lee, 1997; Refson et al., 2006)) on a Γ-centred $1 \times 1 \times 1$ q-point grid for the 120-atom melt supercells. Given the large real-space dimensions of the melt cells, Brillouin zone sampling is correspondingly small, and Γ-point phonons provide an adequate description of vibrational properties for isotope fractionation calculations.

Fourier interpolation was used to obtain vibrational frequencies throughout the Brillouin zone for crystalline phases.

Phonon frequencies were computed in a single CASTEP thermodynamics calculation for each structure. Isotope fractionation factors were subsequently derived using a custom post-processing script that applies isotopic mass substitution to the calculated vibrational frequencies while keeping force constants unchanged. This procedure allows reduced partition function ratios (β, Eq. 1) to be evaluated for all isotopes and crystallographic sites from a single phonon calculation, following the harmonic approximation and the Bigeleisen–Mayer equation (Young et al., 2015). Final β-values were obtained by averaging over all snapshots (or crystallographic sites, where applicable), with uncertainties estimated as the standard error of the mean.

$$\beta(X,Y,Y^*) = \prod_{i=1}^{N_q} \left[\prod_{j=1}^{3N_{\mathrm{at}}} \left(\frac{\omega^*_{i,j}}{\omega_{i,j}} \frac{e^{-h\omega^*_{i,j}/(2kT)}}{1-e^{-h\omega^*_{i,j}/(2kT)}} \frac{1-e^{-h\omega_{i,j}/(2kT)}}{e^{-h\omega_{i,j}/(2kT)}} \right) \right]^{w_i} \tag{1}$$

Mineral calculations (forsterite and diopside)

In addition to melt calculations, first-principles DFT calculations were performed on crystalline forsterite (Mg_2SiO_4) and diopside ($CaMgSi_2O_6$) to obtain equilibrium isotope fractionation factors for both magnesium and silicon. Initial crystal structures were obtained from the American Mineralogist Crystal Structure Database and fully optimised at 1 GPa. Geometry optimisation involved relaxing both atomic positions and cell parameters until residual forces were below 1×10^{-4} eV Å^{-1}, stresses were below 0.05 GPa, and total energy changes were below 1×10^{-5} eV.

Calculations employed the Perdew–Burke–Enzerhof for solids (PBESOL; (Perdew et al., 2008)) exchange–correlation functional, which is designed to reproduce equilibrium properties of solids accurately and has been shown to perform well for silicate minerals. Norm-conserving pseudopotentials and plane-wave cutoffs sufficient to converge phonon frequencies were used, and Brillouin-zone sampling employed Monkhorst–Pack grids appropriate for each crystal structure.

Phonon frequencies were calculated using density functional perturbation theory (Gonze & Lee, 1997). Isotopic fractionation factors for Mg and Si were obtained by

substituting isotopic masses at the relevant crystallographic sites while keeping force constants unchanged (Eq. 1). For forsterite, Mg isotopic substitution was performed independently on the distinct M1 and M2 Mg sites, and site-averaged β-values were calculated to obtain bulk mineral values. For diopside, which contains a single Mg site, no site averaging was required. Reduced partition function ratios were calculated over a wide temperature range using harmonic vibrational frequencies, allowing direct comparison with melt β-values and experimental constraints.

2. Structural Statistics of the Basaltic Melt

The short- and intermediate-range structure of the basaltic melt was characterised using radial distribution functions (RDFs), coordination-number (CN) statistics, and mean squared displacements (MSD) computed from the equilibrated portion of the molecular-dynamics trajectory (Figure 5.4 & Figure 5.5).

Si and Mg coordination environments and bond-length distributions

The Si–O RDF of the basaltic melt MD trajectory shows a sharp first peak around 1.6 Å, indicating tetrahedral silicon coordination. This matches well with the $\sim$ 1.63 Å Si–O bond length reported by Rabin et al., 2023 at low pressure, as well as with previous experimental and computational data (Guillot & Sator, 2007; Sanloup et al., 2013). The peak's narrow width and high intensity suggest a relatively rigid environment dominated by SiO_4 tetrahedra. Integrating the first shell yields an average Si–O coordination number of approximately 4 (CN = 4.03), with minor contributions from silicon in fivefold coordination.

The Mg–O RDF from the MD trajectory shows a broader first peak in the 2.0–2.2 Å range, indicating a more adaptable, varied local environment. The Mg–O bond-length distribution is notably wider than that of Si–O, in line with the weaker and more ionic nature of Mg–O bonds. The distribution of Mg coordination numbers spans both 5- and 6-fold coordination, reflecting the constant exchange of oxygen

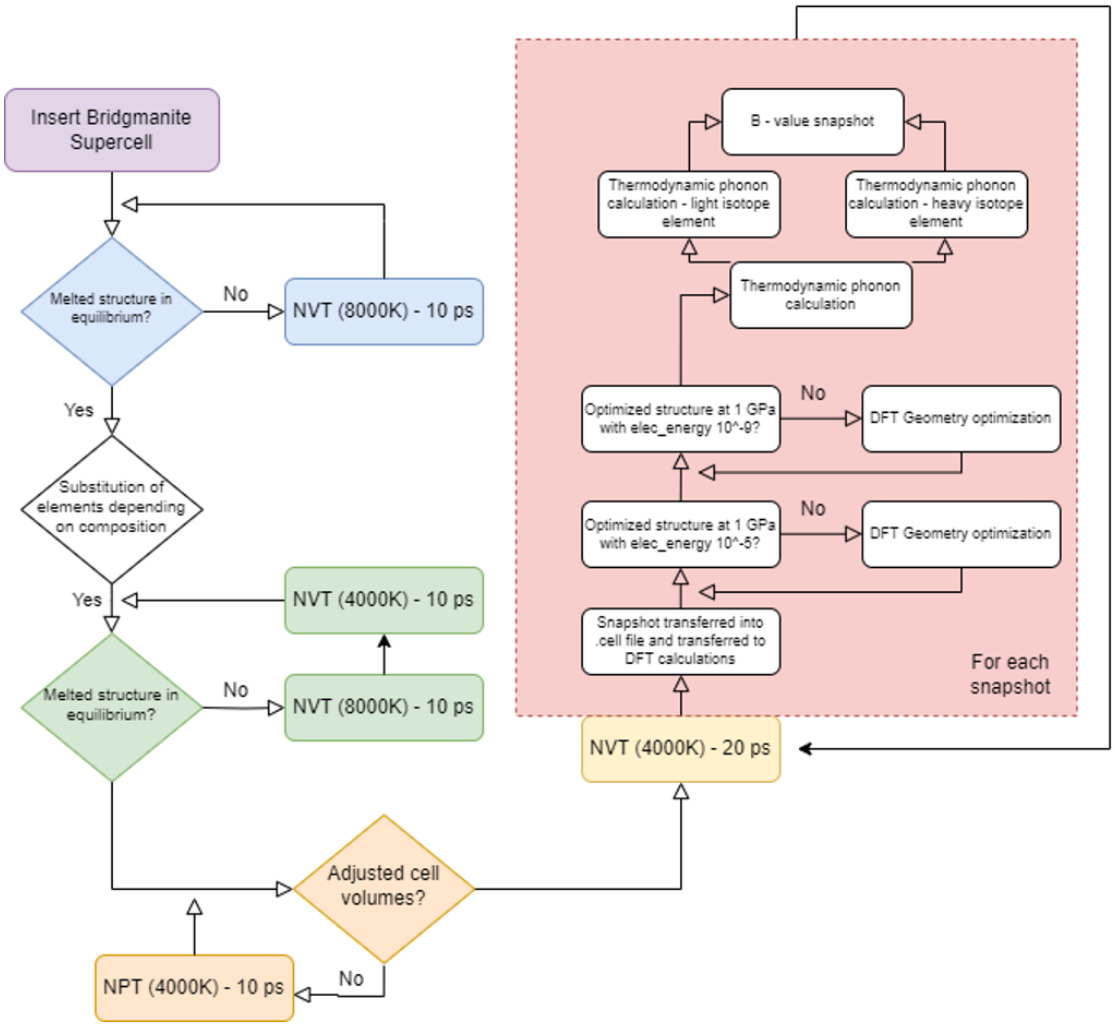


Figure 5.3: Schematic overview of the molecular dynamics–density functional theory workflow used to calculate equilibrium isotope fractionation factors. A bridgmanite supercell is inserted as the initial configuration and fully melted using NVT molecular dynamics simulations at 8000 K until structural equilibration is achieved. Target melt compositions are obtained through systematic atomic substitution, followed by re-equilibration at high temperature and cooling to 4000 K. Cell volumes are optimised using NPT simulations at 4000 K until the target pressure is reached, after which final production trajectories are generated in the NVT ensemble. Statistically independent snapshots are extracted from equilibrated trajectories and transferred to first-principles calculations. For each snapshot, density functional theory geometry optimisation is performed at 1 GPa using progressively tighter electronic convergence criteria, followed by harmonic phonon and thermodynamic calculations. Reduced partition function ratios (β-values) are derived from a single phonon calculation per snapshot using isotopic mass substitution, and final isotope fractionation factors are obtained by averaging over all snapshots.

atoms in the coordination sphere. The average Mg–O coordination number (CN = 5.47) is similar to low-pressure values reported by Rabin et al., 2023 (5.25–5.32).

Diffusion coefficients

Diffusion coefficients for individual atomic species were calculated from the MSD curves shown in Figure 5.5. Diffusion coefficients were derived using the Einstein relation:

$$D = \frac{1}{6}\frac{d}{dt}r^2(t) \tag{2}$$

by fitting to MSD curves over the 5–10 ps interval. Because MD simulations are limited in time, these diffusion coefficients should primarily be used to compare atomic species. The data show that Mg and Ca are the most mobile in the melt, with diffusion coefficients around 10^{-9} $m^2\,s^{-1}$. Oxygen has moderate mobility, whereas Si and Al have the lowest mobility, reflecting their roles in forming networks. A comparison with iron-depleted basalt at 1 GPa from Rabin et al., 2023 reveals that, although the absolute diffusion coefficients are lower in this study, the order of species mobility remains the same in both cases:

$$\mathrm{Ca} \geq \mathrm{Mg} > \mathrm{O} > \mathrm{Al} \geq \mathrm{Si} \tag{5.1}$$

Rabin et al., 2023 report higher absolute diffusion coefficients than those obtained here. Because the two studies differ in melt composition, temperature, and exchange-correlation functional, the origin of this offset cannot be uniquely attributed to any single factor. However, the relative trends in diffusion behaviour (e.g., ordering and temperature dependence) are similar across the two studies, indicating that the inferred transport mechanism is insensitive to the specific computational setup.

Network rigidity versus modifier flexibility

MD simulations reveal the contrasting local environments of Si and Mg, shedding light on the structures of basaltic melt. Silicon is mainly found in tetrahedral coordination, evidenced by the sharp Si–O RDF and narrow Si–O bond length

Table 5.2: Diffusion coefficients in basaltic melt.

Element	This study – D ($m^2 s^{-1}$)	(Rabin et al., 2023) – D ($m^2 s^{-1}$)
Mg	1.8×10^{-9}	3.8×10^{-9}
Ca	1.9×10^{-9}	4.5×10^{-9}
O	9.5×10^{-10}	3.5×10^{-9}
Si	7.0×10^{-10}	2.0×10^{-9}
Al	5.5×10^{-10}	3.3×10^{-9}

distribution around 1.6 Å. This indicates that SiO_4 tetrahedra form a stable, enduring framework in the melt, confirming that Si is the primary network-forming component.

In contrast, magnesium exhibits a broader range of local structural environments. The Mg–O RDF's broader first peak indicates variability in bond lengths and coordination geometry. Magnesium is found in both five- and six-coordinate environments, with oxygen atoms frequently occupying its coordination shell, creating a dynamic and adaptable local environment. This structural flexibility is also evidenced by magnesium's higher diffusivity relative to network-forming cations, suggesting that Mg forms transient bonds rather than a rigid structure.

These observations are consistent with previous *ab initio* MD studies, which identify Mg as a network-modifying cation whose coordination number is weakly dependent on melt composition but increases systematically with pressure (de Koker et al., 2008; Dufils et al., 2018; Guillot & Sator, 2007; Rabin et al., 2023; Stixrude et al., 2009). The coexistence of relatively rigid SiO_4 units and structurally flexible Mg–O polyhedra illustrates how silicate melt can sustain short-range network order while allowing substantial local structural disorder. This distinction offers crucial structural insight for understanding the different isotope fractionation behaviours of Mg and Si in melt, as discussed in the main text.

Although aluminium, calcium, and oxygen are not the main focus here, their structural behaviour generally aligns with previous research. Aluminium is found in environments between network formers and modifiers, while calcium shows broad RDF peaks and high coordination numbers typical of strongly modifying

cations. This supports the overall view of compositional and functional heterogeneity within the melt structure.

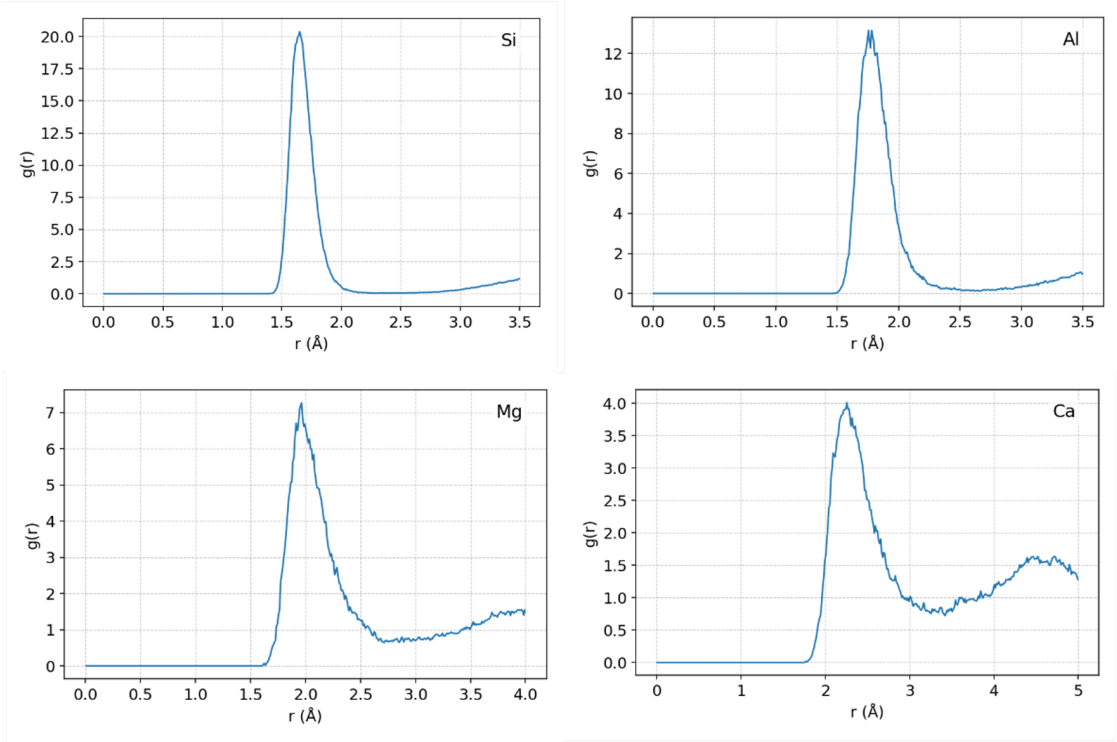


Figure 5.4: Cation–oxygen radial distribution functions for Si, Al, Mg, and Ca obtained from the equilibrated segment of the molecular-dynamics trajectory.

Snapshot melt structural parameters

Structural descriptors for regression and residual analysis (Section 3) were obtained directly from the geometry-optimised melt snapshots used in vibrational calculations, rather than from the MD trajectories. This is important because the MD trajectory captures a fluctuating liquid environment, while isotope fractionation calculations use energy-minimised snapshots. Consequently, all structural parameters were consistently derived from these optimised snapshot geometries at 1 GPa (Table 5.4).

1. **Coordination number (CN):** Coordination numbers were calculated using a distance-based criterion, taking the first minimum in the radial distribution function (RDF) from the MD trajectory (Figure S2). A cutoff of 2.00 Å was applied for Si–O bonds, and 2.60 Å for Mg–O bonds. Oxygen atoms within

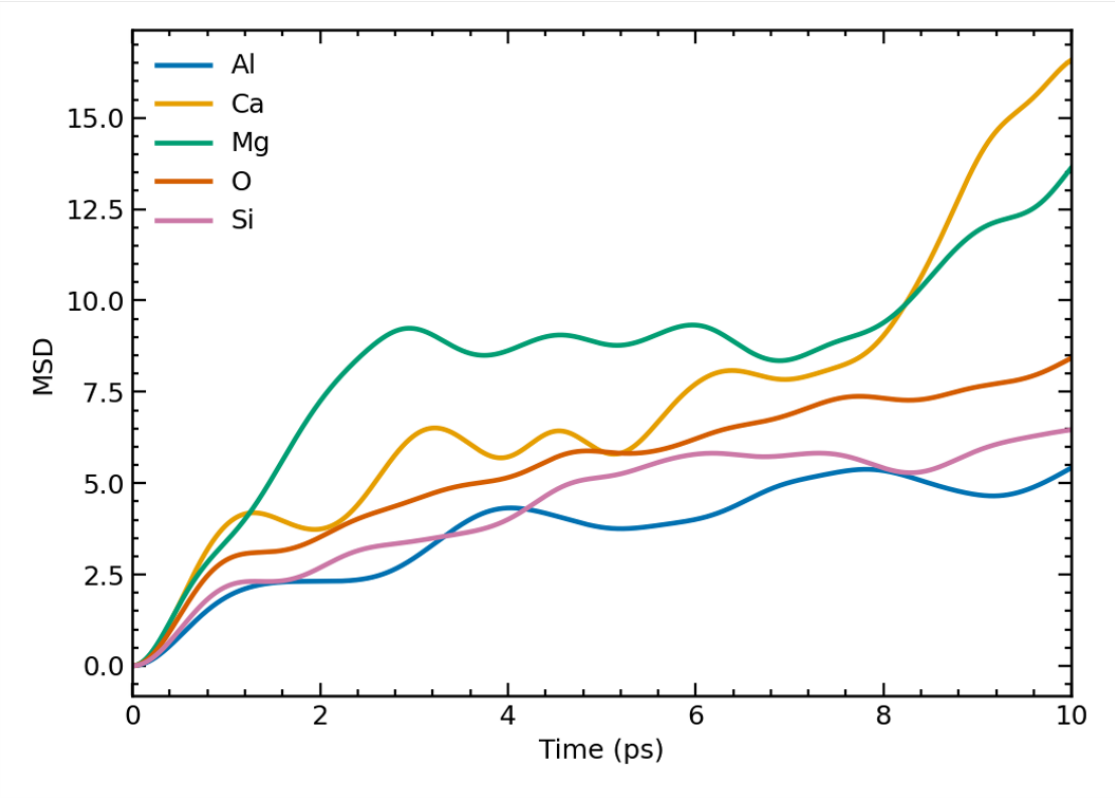


Figure 5.5: Mean squared displacement (MSD) of Al, Ca, Mg, O, and Si atoms as a function of time for the full molecular-dynamics trajectory. MSDs are computed relative to the initial configuration. The relative magnitudes of the MSDs indicate higher mobility of network-modifying cations (Mg, Ca) compared to network-forming species (Si, Al), with oxygen showing intermediate behaviour.

these cutoffs were deemed bonded. The coordination numbers for snapshots align with the definition used in the MD structural analysis.

2. **Average bond length:** For each site, the average element–oxygen bond length was determined by averaging all Si–O or Mg–O distances within the coordination cutoff. These values were computed separately for each site in every snapshot.

3. **Bond-length standard deviation:** Bond-length variability was measured by calculating the standard deviation of Mg–O and Si–O distances in the first coordination shell. This metric reflects the extent to which the actual structures deviate from perfect polyhedral symmetry.

4. **Non-bridging oxygen fraction (NBO_frac, Mg only):** For each Mg site, oxygen atoms in its coordination shell were classified as bridging (BO) if bonded to two network-forming cations (Si, Al) and non-bridging (NBO) if bonded to only one. The NBO fraction is defined as the ratio of NBOs to the total number of coordinating oxygen atoms.

5. Q^n **(Si only):** For Si sites, Q^n, or polymerisation, was identified by counting the bridging oxygens connected to the Si tetrahedron.

6. **Bond valence sum (BVS, Si only):** Bond valence sums were determined using standard parameters for Si–O bonds. BVS indicates local charge balance and bond strength.

7. **Nearest Si distance (Mg only):** The shortest distance to a Si atom was determined from the optimised snapshot geometry and served as an estimate of the electrostatic influence from second neighbours.

Quantification of Snapshot–Trajectory Structural Consistency

Since isotope fractionation calculations rely on geometry-optimised snapshots rather than thermally fluctuating MD configurations, it is crucial to verify that these optimised structures accurately represent the equilibrated melt sampled throughout the trajectory. To assess this, we compared mean structural parameters from the snapshot dataset (Table 5.4) with averages from the equilibrated MD trajectory (Section 2; Figure 5.4). Coordination numbers in the MD trajectory were obtained by integrating the first metal–oxygen RDF peak up to its first minimum, using the same cutoff distances as in the snapshot analysis to ensure consistency.

For silicon, the MD trajectory yields an average coordination number of 4.03, indicating predominantly tetrahedral environments. The mean coordination number from the optimised snapshots is CN = 4.056, a difference of just +0.026, suggesting little impact on the first-shell coordination. The average Si–O bond length in the optimised snapshots is 1.662 Å, compared with the MD RDF peak near 1.60 Å.

Rather than reflecting bulk thermal expansion, this small increase ($\Delta = +0.062$ Å, about 3.9%) occurs because geometry optimisation removes kinetic energy within a fixed simulation cell, allowing strain to be redistributed between local polyhedra.

In the same set of optimised snapshots, the Mg–O mean bond length decreases, with the Mg–O bond length in snapshots being $\langle \mathrm{Mg{-}O} \rangle = 2.050$ Å, compared to the MD RDF mid peak at 2.08 Å. Relative to the MD value ($\Delta = -0.030$ Å, roughly 5%), this indicates that relaxation transfers some of the local strain from Mg–O to Si–O bonds during energy minimisation.

Overall, these results show that local energy minimisation preserves the key structural features of the melt's first shell. Differences between average MD and snapshot metrics are small (≤ 0.06 Å in bond length and ≤ 0.03 in coordination number), confirming that the snapshot ensemble is a reliable structural proxy for the equilibrated melt and is suitable for site-specific vibrational and isotope fractionation studies.

Isotope Fractionation Calculations and Parameterisation

To quantify the structural controls on reduced partition function ratios (β) in the basaltic melt, we applied a two-stage statistical analysis to separate the dominant bond length and coordination number contributions to β from secondary geometric and electronic effects. All structural parameters used in the analysis were derived from the geometry-optimised melt snapshots, as detailed in the previous section (Table 5.4).

Within the harmonic approximation, equilibrium isotope fractionation depends primarily on vibrational force constants, which scale with bond stiffness and therefore inversely with bond length (Young et al., 2015). Following the classical Bigeleisen and Mayer (1947) formulation, the reduced partitioning function ratio for a given site can be expressed as:

$$\beta^{\text{ionic}} = 1 + \frac{1}{24}\left(\frac{h}{k_B T}\right)^2 \frac{K_f}{4\pi^2}\left(\frac{1}{\mu_i} - \frac{1}{\mu_0}\right) \tag{3}$$

where h is Planck's constant, k_B is the Boltzmann constant, T is temperature, and μ_i and μ_0 are the reduced masses of the substituted and reference isotopes, respectively. This equation can be used to express β in terms of an effective force constant K_f. For both Mg and Si, K_f was fitted separately for each coordination number (Table 5.3), thereby accounting for the systematic changes in force constants with coordination geometry. We compared the K_f with harmonically calculated force constants and concluded that they were in very close agreement.

To calculate the variance explained by the ionic model, and therefore bond length, we quantified it using the coefficient of determination:

$$R^2 = 1 - \frac{\sum_i (\beta_i - \hat{\beta}_i)^2}{\sum_i (\beta_i - \bar{\beta})^2} \tag{4}$$

where β_i is the DFT-calculated value, $\hat{\beta}_i$ is the value predicted from Eq. (3), and $\bar{\beta}$ is the mean β-value for the analysed subset. For six-fold coordinated Mg sites, this procedure yields $R^2 \approx 0.80$ ($n = 18$), indicating that eighty per cent of the variance of β is explained solely by variation in average Mg–O bond length within a fixed coordination geometry.

An analogous analysis was performed for silicon, restricting the dataset to fourfold coordination sites. In this case, the ionic fit yields $R^2 \approx 0.75$ ($n = 29$), demonstrating that bond length variation accounts for approximately 75% of the variance in Si β-values. These results confirm that bond stiffness represents the dominant first-order control on isotope fractionation within the melt.

To evaluate structural effects not captured by bond length, residual β-values were defined as:

$$\beta_i^{\text{residual}} = \beta_i^{\text{DFT}} - \beta_i^{\text{ionic}} \tag{5}$$

where β_i^{ionic} is the predicted value from the coordination-restricted ionic fit (Eq. 3). By construction, these residuals remove the dominant bond-length dependence and isolate secondary structural influences.

For six-fold coordination Mg sites, β_{residual} was examined as a function of additional structural descriptors derived from optimised snapshots (see previous section). Multivariate linear regression was applied:

$$\beta_j^{\text{residual}} = a_0 + \sum_i a_i x_{j,i} \tag{6}$$

where $x_{j,i}$ are local structural parameters including bond-length standard deviation (polyhedral distortion), non-bridging oxygen fraction, and nearest-Si distance.

To compare relative effect sizes across predictors, regression coefficients were standardised:

$$a_j^* = a_j \frac{\sigma_{x_j}}{\sigma_{\beta_{\text{residual}}}} \tag{7}$$

where σ denotes the standard deviation. The results are shown in Table 5.5.

These regressions show that bond-length variability is the dominant secondary control on β after the coordination-specific ionic trend is removed. For Mg in sixfold coordination, the standard deviation of the Mg–O bond lengths is the strongest predictor of residual β, indicating that polyhedral distortion has a larger effect than either non-bridging oxygen fraction or second-neighbour Si proximity. The negative coefficient on Mg–Si distance implies that shorter Mg–Si separations are associated with higher β residuals. For Si in fourfold coordination, bond-length variability is again the largest contributor, with bond valence sum providing a smaller additional effect and Q^n contributing negligibly. Together, these results indicate that local polyhedral distortion is the main structural variable governing the remaining β variance for both Mg and Si, beyond the first-order bond-length dependence.

The multivariate residual analysis was restricted to sixfold Mg because the coordination-specific ionic model is not directly comparable across five- and six-coordinate sites, and the six-coordinate subset is too limited to support a stable regression without introducing coordination as an additional predictor.

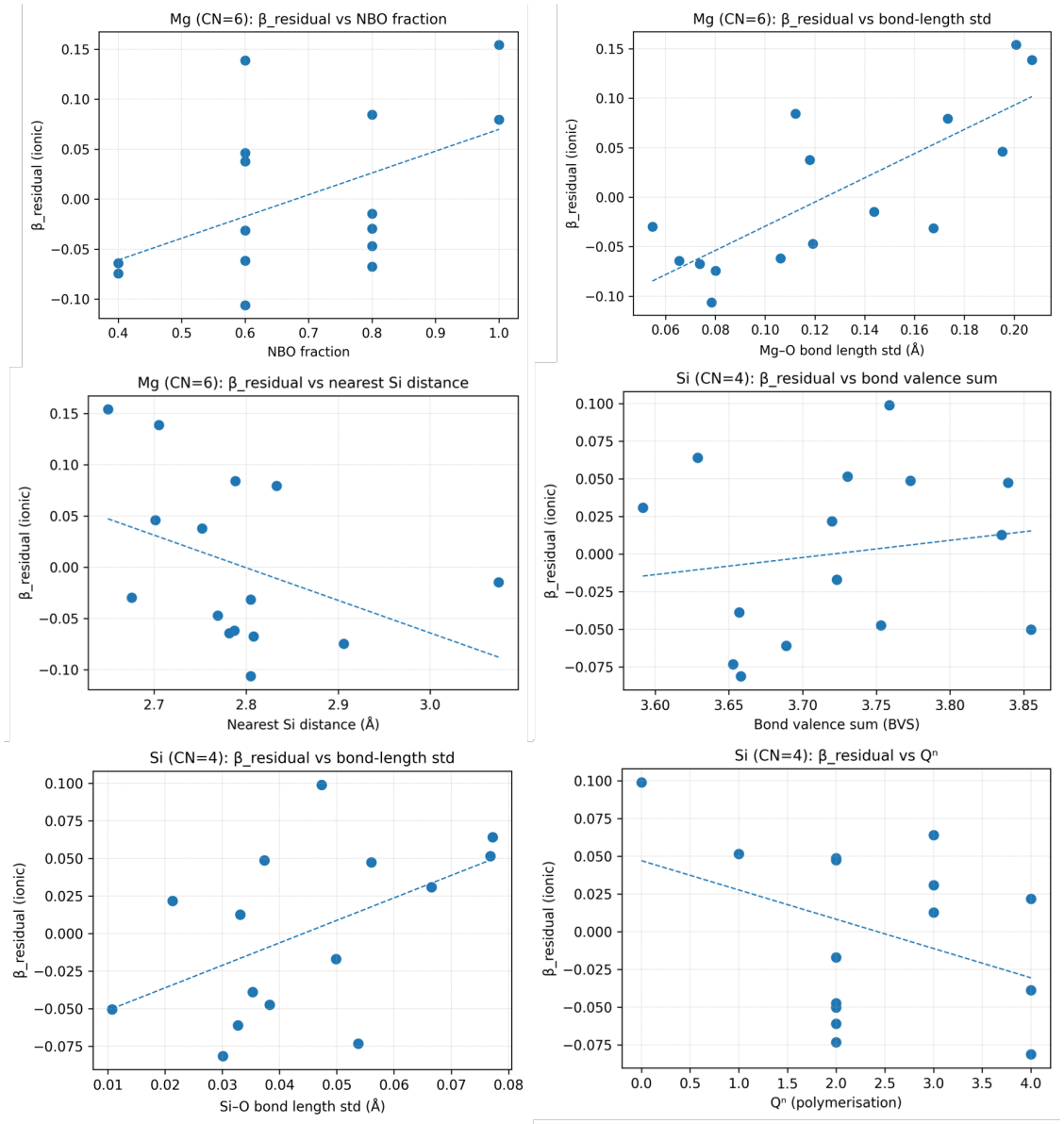


Figure 5.6: Ionic-model residuals (β_{residual}) plotted against local structural descriptors for Mg (CN = 6) and Si (CN = 4) sites. Residuals are defined relative to the coordination-restricted ionic fit (Eq. 3), removing the dominant bond-length dependence. Dashed lines indicate linear trends.

Table 5.3: Harmonic force constant (K_f) fitted to datasets.

Element	CN	K_f (N m^{-1})
Mg	5	589.979
Mg	6	512.505
Si	4	2133.404

Element	CN	Avg bond (Å)	Std	NBO	Si dist	β
Mg	5	1.999	0.0527	1.00	3.224	1.1748
Mg	5	1.973	0.0507	0.75	2.903	1.3734
Mg	5	2.013	0.0518	0.50	2.932	1.1624
Mg	5	2.028	0.0668	0.75	2.676	1.1876
Mg	5	1.966	0.0343	0.75	3.040	1.3743
Mg	5	1.966	0.0253	0.50	2.938	1.4627
Mg	5	1.974	0.0607	0.50	3.139	1.3477
Mg	5	1.999	0.0591	0.50	3.116	1.2511
Mg	5	2.057	0.1755	0.50	3.076	1.1956
Mg	5	1.977	0.0554	0.50	3.178	1.4000
Mg	6	2.105	0.1192	0.80	2.769	1.0206
Mg	6	2.087	0.1179	0.60	2.752	1.1506
Mg	6	2.122	0.0785	0.60	2.805	0.9201
Mg	6	2.153	0.1675	0.60	2.805	0.9250
Mg	6	2.107	0.1061	0.60	2.787	1.0019
Mg	6	2.093	0.2009	1.00	2.650	1.2505
Mg	6	2.095	0.1438	0.80	3.074	1.0772
Mg	6	2.068	0.1122	0.80	2.788	1.2459
			Si			
Element	CN	Q^n	Avg bond (Å)	Std	BVS	β
Si	3	0	1.571	0.0203	3.464	3.5759
Si	4	4	1.651	0.0213	3.720	3.3094
Si	4	2	1.638	0.0107	3.855	3.3289
Si	4	3	1.641	0.0331	3.835	3.3696
Si	4	2	1.661	0.0537	3.653	3.1495
Si	4	2	1.650	0.0383	3.753	3.2531
Si	4	2	1.654	0.0498	3.723	3.2539
Si	4	3	1.668	0.0772	3.629	3.2441
Si	4	0	1.650	0.0474	3.759	3.3963
Si	4	4	1.659	0.0353	3.657	3.2008
Si	5	4	1.785	0.1273	3.429	2.4572
Si	5	5	1.754	0.0467	3.548	2.4287

Table 5.4: Structural descriptors and β values for Mg and Si sites. Listed parameters include coordination number, average bond length, bond-length variability, measures of local connectivity or charge balance (NBO fraction for Mg; Q^n and bond valence sum for Si), and the corresponding β values used in regression analyses.

Mg model: $\beta = a_0 + a_1\sigma_{\mathrm{Mg-O}} + a_2\mathrm{NBO}_{\mathrm{frac}} + a_3 d_{\mathrm{Si}}$ $N = 15$, $R^2 = 0.727$ (of $\beta_{\mathrm{residual}}$ variance)		
Parameter	Coefficient	Std. Error
Intercept	0.364	0.368
Mg–O bond length std (Å)	+1.020	0.266
NBO fraction	+0.109	0.074
Nearest Si distance (Å)	-0.203	0.128
Si model: $\beta = a_0 + a_1\sigma_{\mathrm{Si-O}} + a_2\mathrm{BVS} + a_3 Q^n$ $N = 15$, $R^2 = 0.432$ (of $\beta_{\mathrm{residual}}$ variance)		
Parameter	Coefficient	Std. Error
Intercept	-1.300	0.861
Si–O bond length std (Å)	+2.063	0.879
Bond valence sum (BVS)	+0.324	0.219
Q^n	-0.001	0.014

Table 5.5: Multivariate linear regression coefficients describing the dependence of Mg and Si β on local structural descriptors. The average Mg–O bond length is the dominant control, while bond-length asymmetry, coordination number, and proximity to Si contribute significantly as secondary factors. The NBO fraction has a weaker but statistically significant effect. For silicon, dominant control arises from Si–O bond length and bond valence sum, with minor effects from tetrahedral distortion and polymerisation.

Bibliography

Bigeleisen, J., & Mayer, M. G. (1947). Calculation of Equilibrium Constants for Isotopic Exchange Reactions. *Journal of Chemical Physics*, *15*, 261–267 ADS Bibcode: 1947JChPh..15..261B.

Clark, S. J., Segall, M. D., Pickard, C. J., Hasnip, P. J., Probert, M. I. J., Refson, K., & Payne, M. C. (2005). First principles methods using CASTEP. *Zeitschrift für Kristallographie - Crystalline Materials*, *220*(5-6), 567–570.

de Koker, N. P., Stixrude, L., & Karki, B. B. (2008). Thermodynamics, structure, dynamics, and freezing of Mg2SiO4 liquid at high pressure. *Geochimica et Cosmochimica Acta*, *72*(5), 1427–1441.

De Winter, B., Walker, A. M., Melekhova, E., Liu, X.-N., & Elliott, T. (in review). The magnitude of equilibrium isotope fractionation of Mg between forsterite, diopside and melt at liquidus temperatures. *Geochimica et Cosmochimica Acta*.

Dufils, T., Sator, N., & Guillot, B. (2018). Properties of planetary silicate melts by molecular dynamics simulation. *Chemical Geology*, *493*, 298–315.

Gonze, X. (1997). First-principles responses of solids to atomic displacements and homogeneous electric fields: Implementation of a conjugate-gradient algorithm. *Physical Review B*, *55*(16), 10337–10354.

Gonze, X., & Lee, C. (1997). Dynamical matrices, Born effective charges, dielectric permittivity tensors, and interatomic force constants from density-functional perturbation theory. *Physical Review B*, *55*(16), 10355–10368.

Guillot, B., & Sator, N. (2007). A computer simulation study of natural silicate melts. Part II: High pressure properties. *Geochimica et Cosmochimica Acta*, *71*(18), 4538–4556.

Hohenberg, P., & Kohn, W. (1964). Inhomogeneous electron gas. *Physical Review*, *136*(3B), B864.

Hoover, W. G. (1985). Canonical dynamics: Equilibrium phase-space distributions. *Physical Review A*, *31*(3), 1695–1697.

Huang, F., Chen, L., Wu, Z., & Wang, W. (2013). First-principles calculations of equilibrium Mg isotope fractionations between garnet, clinopyroxene, orthopyroxene, and olivine: Implications for Mg isotope thermometry. *Earth and Planetary Science Letters*, *367*, 61–70.

Huang, F., Wu, Z., Huang, S., & Wu, F. (2014). First-principles calculations of equilibrium silicon isotope fractionation among mantle minerals. *Geochimica et Cosmochimica Acta*, *140*, 509–520.

Kohn, W., & Sham, L. J. (1965). Self-Consistent Equations Including Exchange and Correlation Effects. *Physical Review*, *140*(4A), A1133–A1138.

Nosé, S. (1984). A molecular dynamics method for simulations in the canonical ensemble. *Molecular Physics*, *52*(2), 255–268.

Parrinello, M., & Rahman, A. (1981). Polymorphic transitions in single crystals: A new molecular dynamics method. *Journal of Applied Physics*, *52*(12), 7182–7190.

Payne, M. C., Teter, M. P., Allan, D. C., Arias, T. A., & Joannopoulos, J. D. (1992). Iterative minimization techniques for ab initio total-energy calculations: Molecular dynamics and conjugate gradients. *Reviews of Modern Physics*, *64*(4), 1045–1097.

Perdew, J. P., Ruzsinszky, A., Csonka, G., Vydrov, O. A., Scuseria, G. E., Constantin, L. A., Zhou, X., & Burke, K. (2008). Restoring the Density-Gradient

Expansion for Exchange in Solids and Surfaces. *Physical Review Letters*, *100*(13), 136406.

Rabin, S., Blanchard, M., Pinilla, C., Poitrasson, F., & Gregoire, M. (2021). First-principles calculation of iron and silicon isotope fractionation between Fe-bearing minerals at magmatic temperatures: The importance of second atomic neighbors. *Geochimica et Cosmochimica Acta*, *304*, 101–118.

Rabin, S., Blanchard, M., Pinilla, C., Poitrasson, F., & Grégoire, M. (2023). Iron and silicon isotope fractionation in silicate melts using first-principles molecular dynamics. *Geochimica et Cosmochimica Acta*, *343*, 212–233.

Refson, K., Tulip, P. R., & Clark, S. J. (2006). Variational density-functional perturbation theory for dielectrics and lattice dynamics. *Physical Review B*, *73*(15), 155114.

Sanloup, C., Drewitt, J. W. E., Konôpková, Z., Dalladay-Simpson, P., Morton, D. M., Rai, N., van Westrenen, W., & Morgenroth, W. (2013). Structural change in molten basalt at deep mantle conditions. *Nature*, *503*(7474), 104–107.

Schauble, E. A. (2011). First-principles estimates of equilibrium magnesium isotope fractionation in silicate, oxide, carbonate and hexaaquamagnesium(2+) crystals. *Geochimica et Cosmochimica Acta*, *75*(3), 844–869.

Stixrude, L., de Koker, N., Sun, N., Mookherjee, M., & Karki, B. B. (2009). Thermodynamics of silicate liquids in the deep Earth. *Earth and Planetary Science Letters*, *278*(3), 226–232.

Troullier, N., & Martins, J. L. (1991). Efficient pseudopotentials for plane-wave calculations. *Physical Review B*, *43*(3), 1993–2006.

Walker, A. M., Hin, R. C., & Elliott, T. (2026). Controls on Mg isotopic fractionation between deep mantle phases and relict signatures of a terrestrial magma ocean. *Geochimica et Cosmochimica Acta*, *425*, 131–142.

Wang, W., Wu, Z., Huang, S., & Huang, F. (2023). First-principles investigation of equilibrium magnesium isotope fractionation among mantle minerals: Review and new data. *Earth-Science Reviews*, *237*, 104315.

Young, E. D., Manning, C. E., Schauble, E. A., Shahar, A., Macris, C. A., Lazar, C., & Jordan, M. (2015). High-temperature equilibrium isotope fractionation of non-traditional stable isotopes: Experiments, theory, and applications. *Chemical Geology*, *395*, 176–195.

6

Mg–Si isotopes tightly constrain the primordial bridgmanite reservoirs

The preceding chapters establish both the magnitude and the structural origin of equilibrium isotope fractionation at magmatic conditions. However, a key unresolved question is how these processes scale to planetary differentiation, particularly during the crystallisation of Earth's early magma ocean.

The paper presented in this chapter addresses this problem by applying first-principles calculations to lower mantle conditions, where pressures and temperatures far exceed those accessible in laboratory experiments. Under these conditions, bridgmanite, the dominant lower mantle mineral, plays a central role in controlling chemical and isotopic evolution.

A long-standing debate in Earth sciences concerns whether early-formed, compositionally distinct reservoirs could survive in the mantle over geological timescales. Geodynamic models suggest that such reservoirs may persist, yet observational constraints from seismic imaging and geochemistry provide limited evidence for their existence. Stable isotopes of major elements such as Mg and Si offer a potential means of resolving this discrepancy, as equilibrium fractionation during magma ocean crystallisation could generate detectable isotopic signatures.

This chapter, therefore, extends the framework developed in earlier chapters to a planetary scale, combining MD–DFT simulations with isotopic mass-balance modelling to evaluate the extent to which primordial heterogeneities can be preserved in the present-day mantle.

This manuscript will be submitted to Earth and Planetary Science Letters (EPSL)

Statement of Authorship for joint/multi-authored papers for PGR thesis is attached in the appendix at the end of the thesis

Mg–Si isotopes tightly constrain the primordial bridgmanite reservoir in the present-day Earth's mantle

Bram de Winter[a,*], Andrew M. Walker[a], Elena Melekhova[a], Tim Elliott[b]

[a] Department of Earth Sciences, University of Oxford, South Parks Road, Oxford, OX1 3AN, UK

[b] School of Earth Sciences, University of Bristol, Wills Memorial Building, Queen's Road, Bristol, BS8 1RJ, UK

*Corresponding Author: bram.dewinter@earth.ox.ac.uk

Abstract

The crystallisation of Earth's ancient magma ocean may have generated long-lived chemical heterogeneity in the deep mantle. Geodynamic models suggest that such primordial reservoirs could persist for billions of years. If preserved, these domains should produce detectable seismic signatures and isotopic variability in the present-day mantle. However, seismic imaging reveals no widespread evidence for compositionally distinct structures, and mantle-derived rocks exhibit limited variability in the stable isotopes of major elements such as Mg and Si, as expected for primordial structures. This discrepancy raises the question of whether large primordial reservoirs are retained until the present-day Earth. Here, we quantify equilibrium Mg and Si isotope fractionation between bridgmanite and a silicate melt at lower-mantle conditions using combined molecular dynamics and density-functional theory calculations. We show that isotope fractionation remains significant under magma ocean conditions, for example, at 60 GPa, where $\Delta^{26}\mathrm{Mg}_{\mathrm{bdm-melt}} = -0.170 \pm 0.021‰$ and $\Delta^{30}\mathrm{Si}_{\mathrm{bdm-melt}} = -0.366 \pm 0.031‰$. Such fractionation would generate resolvable isotopic differences if substantial volumes of primordial bridgmanite were preserved to the present-day Earth. Combining these results, we demonstrate that the near-identical Mg and Si isotope compositions of the Bulk Silicate Earth and the Moon constrain the amount of bridgmanite-rich cumulates in present-day mantle to 4.1 ± 4.7 wt% (0–8.8 wt% within uncertainties).

We therefore conclude that primordial bridgmanite-rich regions are likely negligible to minor in volume and play a minor role in shaping current mantle structure and dynamics.

Keywords: Magma Ocean, Bridgmanite, stable isotopes, DFT, Mg isotopes, Si isotopes

6.1 Introduction

Earth likely experienced one or more periods of partial or complete melting (Canup, 2004; Nakajima & Stevenson, 2015), but the fate of chemical differences formed during these times remains unclear. The Moon-forming impact is believed to have released enough energy to create a deep, possibly global, magma ocean with temperatures above 3000–4500 K (Andrault et al., 2011; Canup, 2004, 2008; Ćuk & Stewart, 2012; Solomatov & Moresi, 2000). As this magma ocean cooled, crystallisation began in the mantle, either from the bottom up (Solomatov & Stevenson, 1993) or top down (Andrault et al., 2011; Elkins-Tanton et al., 2011), depending on convection and cooling rates (Caracas et al., 2019; Labrosse et al., 2007). Regardless of the crystallisation process, experimental and theoretical research shows that bridgmanite ($MgSiO_3$) is the first major phase to crystallise under lower mantle pressures (Andrault et al., 2016; Caracas et al., 2019; Ito & Takahashi, 1989; Wood et al., 2006). The formation and separation of bridgmanite-rich cumulate layers during this period could create long-lasting compositional heterogeneities that might be preserved as bridgmanite-enriched ancient mantle structures, or BEAMS (Ballmer et al., 2017; Gülcher et al., 2021).

Despite the potential for early-formed heterogeneities, vigorous convection within the magma ocean is expected to promote efficient mixing and chemical homogenisation (Abe, 1997; Solomatov & Moresi, 2000; van Keken et al., 2002). However, more recent geodynamic models show that mixing is neither uniform nor complete but instead depends strongly on the physical properties of the heterogeneities, and dense or viscous bridgmanite-enriched domains may resist entrainment and survive as

coherent structures in the lower mantle, with larger volumes preferentially preserved (Gülcher et al., 2021). This is consistent with geochemical evidence, including high $^{3}He/^{4}He$ ratios that require long-lived, undegassed mantle reservoirs (Mukhopadhyay, 2012) and ^{142}Nd anomalies indicating silicate differentiation within the first ∼30 Myr of Earth's history and the subsequent preservation of distinct domains (Boyet & Carlson, 2005; Rizo et al., 2016). This assumes that none of the noble-gas signatures originates from exchange with the core, as suggested by Bouhifd et al. (2013)

These findings suggest that primordial geochemical reservoirs may still exist in Earth's mantle, but the current volume required to verify their plausibility remains unknown. Resolving this uncertainty requires quantitative geochemical tracers that directly link magma ocean crystallisation processes to present-day mantle compositions. Most existing models focus on trace-element partitioning and radiogenic-isotope evolution, with comparatively little attention to stable-isotope behaviour in the lower mantle. In these models, it is assumed that fractionation of Mg and Si isotopes between the primordial reservoir and the rest of the mantle is minimal. However, computational studies indicate that significant fractionations can occur through equilibrium isotope fractionation when phases vary in bonding environment and coordination (De Winter et al., submitted; Walker et al., 2026). Even small fractionation factors for Mg and Si, crucial to bridgmanite, could create detectable isotopic differences in Earth's overall composition during crystallisation. Here, we calculate the equilibrium isotope fractionation of Mg and Si between bridgmanite and melt under lower-mantle conditions using first-principles methods. These findings, incorporated into crystallisation models, enable an assessment of how much primordial material remains in Earth's current mantle by comparing Earth's and the Moon's bulk compositions. This approach can test the hypothesis that large, primordial bridgmanite-rich cumulate structures could still be hidden deep within the mantle.

6.2 Methods

We conducted molecular dynamics simulations combined with DFT calculations, following similar methodologies to De Winter et al. (submitted) and Rabin et al. (2023), on a pyrolytic iron-free composition, similar to melts expected in Earth's magma ocean (McDonough & Sun, 1995). Our simulations were run at 4000 K at 40, 60, and 80 GPa in cells containing 120 atoms. The structure was equilibrated under these conditions for 10 ps to capture a broad range of melt structural environments. Details of the equilibrium protocol and parameters used can be found in the Supplementary Information (SI) and are the same as those used by De Winter et al. (submitted).

For the melt, we selected five static snapshots at each pressure from the MD trajectories, after 2 ps of simulation time, to allow the system to reach equilibrium in the liquid state, as recommended by previous studies (Rabin et al., 2023). We tested the validity of the liquid state with RDF, MSD and diffusion coefficients (SI). These snapshots were subsequently structurally relaxed by optimising atomic positions until the residual atomic forces dropped below 10^{-3} eV.

To assess both Si and Mg isotope fractionation, we calculated harmonic vibrational frequencies and the reduced partitioning functions (β) using DFT, employing the PBESOL functional (Perdew et al., 2008) and the CASTEP phonons module. We calculated β for Mg- and Si-sites in the structure, then averaged the site- and snapshot-level values to obtain a single β and its standard error for the pyrolitic melt structures at all pressures. These standard errors are considered for all fractionation factors and additional calculations throughout the study. The computational setup, including plane-wave cutoffs, pseudopotentials, k-point sampling, and convergence criteria, is described in the SI.

β-factors for crystalline bridgmanite were computed using the PBESOL functional at pressures between 25 and 140 GPa. These mineral β-factors are used for mineral–melt fractionation calculations. In both melt and mineral calculations, temperature-dependent β-values were fitted to simple polynomials for mineral–melt

fractionation analysis (see Table 6.1). Complete sets of coefficients for all melt environments and mineral sites are provided in the SI.

6.3 Results

6.3.1 Equilibrium isotope fractionation at lower mantle conditions

The computational approach described above allows direct quantification of equilibrium isotope fractionation between bridgmanite and the melt under lower-mantle conditions. We calculated the $\Delta^{26}\mathrm{Mg}_{\mathrm{bdm-melt}}$ and $\Delta^{30}\mathrm{Si}_{\mathrm{bdm-melt}}$ for 40–80 GPa and 2000–4000 K with a pyrolytic melt composition. The results are shown in Table 6.1 and Figure 6.1, with individual β values for snapshots shown in the Supplementary Information. The calculated isotope fractionation factors ($\Delta_{\mathrm{bdm-melt}}$) are negative under all conditions and decrease in magnitude with increasing temperature, as expected for equilibrium fractionation (Urey, 1947). In contrast to lower-pressure conditions (e.g., 1 atm; (De Winter et al., submitted)), the fractionation factor remains large and measurable even at high temperature. For example, at 40 GPa and 4000 K, $\Delta^{26}\mathrm{Mg}_{\mathrm{bdm-melt}} = -0.1387 \pm 0.015‰$. Across all pressures Figure 6.1, the magnitude of fractionation increases with pressure for both $\Delta^{26}\mathrm{Mg}_{\mathrm{bdm-melt}}$ and $\Delta^{30}\mathrm{Si}_{\mathrm{bdm-melt}}$.

Furthermore, we used the magma-ocean liquidus from Andrault et al. (2011) to define the equilibrium temperature and calculate $\Delta^{26}\mathrm{Mg}_{\mathrm{bdm-melt}}$ and $\Delta^{30}\mathrm{Si}_{\mathrm{bdm-melt}}$ during bridgmanite crystallisation in a cooling magma ocean, noting that, in a two-phase system, the temperature follows the liquid rather than the adiabat. While this liquidus is unlikely to represent conditions at depth in Earth during a magma ocean, it provides a maximum equilibration temperature and thus a lower bound on the fractionation factors. These values are shown in Figure 6.1 for each adiabatic line and its respective pressure.

These results allow comparison of our Mg-values with those of Walker et al. (2026), although an important methodological difference must be noted. Walker et al. (2026) used mineral substitutions based on coordination match with melts

as predicted by de Koker et al. (2008), whereas we calculate melt β directly from MD simulations. Furthermore, Walker et al. (2026) used the PBE functional, whereas we employ the PBESOL functional. PBE is known to underestimate the volume of crystals and hence the Mg isotope fractionation in crystalline phases by approximately 0.05–0.07‰ at 1500 K between forsterite and diopside (De Winter et al., in review). The calculated results here are in a similar order to those of Walker et al. (2026), but are slightly more negative.

6.3.2 Relationship to structural melt parameters

Molecular dynamics simulations reveal that the pyrolytic melt exhibits a broader range of local structural environments for Mg and Si than the bridgmanite crystalline phase. For magnesium, the average bond length decreases with increasing pressure, from 2.052 Å at 40 GPa to 1.988 Å at 80 GPa. This trend is also reflected in the average coordination number (CN), which increases from 5.938 at 40 GPa to 6.656 at 60 GPa, then to 6.917 at 80 GPa. This behaviour is consistent with previous simulations of silicate melts, which show that Mg exhibits a continuously evolving coordination environment, typically increasing from 5–6 at ambient pressures to 6–7 at higher pressures, accompanied by gradual bond compression (de Koker et al., 2008; Ghosh & Karki, 2011; Solomatova & Caracas, 2019; Stixrude & Karki, 2005).

In contrast, Si–O exhibits a gradual increase in bond length from 40 GPa (average Si–O = 1.693 Å) to 80 GPa (average Si–O = 1.714 Å), associated with a marked increase in coordination number (CN) from 4.688 to 5.542. This behaviour reflects a pressure-induced structural reorganisation, where the transition to higher Si coordination results in longer average bond distances due to geometric and electronic redistribution. Similar behaviour has been widely reported in other studies, in which coordination changes at 50 GPa (from fourfold to higher coordination) lead to a transient increase in the Si–O bond length. Similar behaviour of the Si–O bond length during coordination changes has been widely observed in high-pressure melts and glasses (de Koker et al., 2008; Prescher et al., 2017; Solomatova & Caracas,

2019; Stixrude & Karki, 2005). An overview of all CN, with comparisons, is given in Table 6.2.

Figure 6.2 shows $1000 \ln \beta$, averaged over Mg–O and Si–O bond lengths for individual melt sites, grouped by coordination number across snapshots at different pressures. For both isotopes, β increased with decreasing bond length, consistent with the expectation that heavier isotopes are preferentially situated in stiffer vibrational environments. Coordination number also exerts a systematic effect: higher-coordination-number sites exhibit higher β-values than lower-coordination-number sites, even when bond lengths are the same.

To assess the influence of coordination and bond length relative to second-order parameters, such as polyhedral distortion, we regressed against the ionic model of Young et al. (2015), similar to the statistical analysis performed in De Winter et al. (submitted). The analysis was performed across different groups of CN sites, and we calculated bond length and coordination number. The difference between the calculated β and ionic model values (β_{residual}) was treated as a secondary control. This residual value was seen as the factor that could not be explained by CN or bond length.

This analysis showed that, on average across all CN groups, CN and bond length explain 97.75% of the variance in Si, with the remaining 2.3% accounted for by second-order parameters. For Mg, this is 97.5% for CN and bond length, and 2.5% for β-residual. While average values plot very close to ionic fits, the individual Mg-sites show high degrees of polyhedral distortion, with average std. error on bond length = 0.169 ± 0.03. A previous study by De Winter et al. (submitted) found that this polyhedral distortion is the most important variable, along with bond length and coordination number, for determining β values at individual sites.

Overall, however, these results show that under high-pressure conditions, Mg and Si isotope fractionation between minerals and silicate melts can be understood predominantly in terms of variations in bond length and coordination number, far more than in lower-pressure basaltic melt compositions (De Winter et al., submitted).

6.4 Discussion

6.4.1 High-pressure isotope fractionation

These results have important implications for isotope behaviour during magma-ocean crystallisation and for the preservation of primordial mantle heterogeneity. Equilibrium isotope fractionation between bridgmanite and coexisting silicate melt remains significant under lower mantle conditions, even at temperatures approaching those of a global magma ocean. Along the magma ocean liquidus Andrault et al. (2011), fractionation remains significant at temperatures of ca. 3100–4000 K and pressures of 40–80 GPa. Mineral–melt isotope fractionation factors are $\Delta^{26}\mathrm{Mg}_{\mathrm{bdm-melt}} = -0.1387 \pm 0.015‰$ and $\Delta^{30}\mathrm{Si}_{\mathrm{bdm-melt}} = -0.4358 \pm 0.030‰$ at 40 GPa, with similar order values at 60 and 80 GPa (Figure 6.1). Under these conditions of a molten Earth magma ocean, fractionation remains clearly non-zero. This contrasts with previous studies, in which assumptions based on calculations using mineral analogues suggested little to no isotope fractionation during magma-ocean crystallisation (Huang et al., 2014). These findings were then used to explain how core exsolution could generate the negative δ^{30}Si component observed in ocean-island basalt samples (Deng et al., 2025).

The significant fractionations reflect the structural contrast between crystalline bridgmanite and coexisting silicate melt at high pressure. Although equilibrium fractionation generally decreases with temperature following a $1/T^2$ relationship (Urey, 1947), it remains non-zero here because bridgmanite has a much stiffer, more highly coordinated bonding environment than the melt (Horiuchi et al., 1987; Katsura, 2025; Schauble, 2011; Walker et al., 2026). The relevant quantity is therefore the coordination- and bond-stiffness-difference between the two phases, rather than the coordination number considered in isolation. This phase contrast also varies with pressure, because the melt structure evolves substantially across 40–80 GPa as Mg and Si coordination increase with compression (de Koker et al., 2008; Solomatova & Caracas, 2019). As a result, the bridgmanite–melt fractionation

factors remain significant along the magma-ocean liquidus at 40–80 GPa (Andrault et al., 2011), even at temperatures approaching those of a global magma ocean.

6.4.2 Magma ocean differentiation

To interpret the isotope fractionation results in a planetary context, we consider a model of magma ocean differentiation in the lower mantle following a Moon-forming impact (Canup, 2004). In this model, a deep, largely molten mantle cools and crystallises under pressures to the present-day lower mantle (25–135 GPa), with early crystallisation dominated by bridgmanite, the stable phases throughout most of these pressure conditions (Andrault et al., 2016; Ito & Takahashi, 1989). We focus here on the 40–80 GPa range because it captures the mid- to deep-lower mantle where (i) bridgmanite is the dominant crystallising phase, (ii) melt–crystal density contrasts are small and allow for crystal–melt segregation, and (iii) a large fraction of the mantle volume resides (Caracas et al., 2019; Labrosse et al., 2007). Crystallisation is assumed to occur in a vigorously convecting, two-phase system of crystals and melt (Solomatov & Stevenson, 1993), where temperature follows the liquidus rather than an adiabat, such that coexisting crystals and melt remain in near-equilibrium during solidification (Andrault et al., 2011). As cooling proceeds, bridgmanite crystallises from the melt and may segregate to form cumulate layers, while residual melt evolves compositionally and isotopically.

The presence of a significantly large bridgmanite–melt fractionation implies that a magma ocean inevitably generates isotopically distinct reservoirs during crystallisation and cooling. Crystallisation models provide a direct framework for linking these isotope fractionation to large-scale mantle differentiation. We considered the first 50% of crystallisation, during which the melt fraction decreases from 1 to 0.5, and crystallisation is likely a batch process (Solomatov & Stevenson, 1993) involving bridgmanite, the dominant crystallisation phase (Ito et al., 2004). We used fractionation factors of 80 GPa for Si and 60 GPa for Mg, as these represent the minimum values during magma ocean crystallisation. Results with other pressures are given in Table 6.3. The models show that equilibrium fractionation alone is

enough to generate substantial isotopic separation between coexisting reservoirs (Figure 6.3). Relative to the initial mantle composition, here shown as BSE for Mg (Liu et al., 2023) and Si (Liu et al., 2025), the residual melt evolves towards heavier compositions, reaching +0.1‰ for Mg and +0.25‰ for Si after 50% crystallisation of Earth's magma ocean, assuming bridgmanite crystals remain segregated from the residual melt while in equilibrium with the melt. The bridgmanite cumulates are isotopically lighter than the initial mantle composition, with Mg isotopic values ranging from −0.3 to −0.1‰ and Si isotopic values from −0.6 to −0.3‰ across 0 to 50% crystallisation. The magnitude of this isotopic fractionation is largely insensitive to the presence of additional phases. Incorporation of co-crystallising ferropericlase at the 10 wt% level produces only minor modifications to the bulk evolution (Walker et al., 2026), indicating that bridgmanite dominates the isotopic budget during early crystallisation. We therefore did not include any ferropericlase in our models.

If bridgmanite cumulates are included within larger structures like BEAMS (Ballmer et al., 2017; Gülcher et al., 2021), they could cause the bulk composition of the accessible mantle to diverge from the original mantle composition of a magma ocean. Any subsequent deterioration and mixing of BEAMS would erode this signal, thereby buffering the initial differences. While not the main subject of this paper, these calculations also reveal a significantly elevated heavy-isotope ratio in residual melts, leading to potentially heavy signatures in mantle structures that result from the accumulation of dense residual melt, such as the proposed Basal Magma Ocean structures (Boukaré et al., 2025; Caracas et al., 2019; Labrosse et al., 2007). However, the extent of this signature depends on the ongoing crystallisation of residual melt in the deepest part of the mantle and on the isotope fractionation factors of davemoaite–melt and, potentially, post-perovskite–melt. These factors require more detailed and complex DFT calculations. Unlike bridgmanite, davemaoite exhibits a wider range of structurally and chemically distinct configurations at lower mantle conditions, arising from both lattice distortions and substitutional disorder. This configurational complexity introduces additional uncertainty in first-principles isotope calculations, as multiple local environments with comparable energies must be considered.

6.4.3 Limits on primordial reservoirs

Isotopic contrasts generated during magma ocean crystallisation can be directly compared with current mantle compositions to estimate the amount of primordial material preserved. We evaluate the isotopic fractionation model shown in Figure 6.3 by comparing it with modern compositions of the BSE and Bulk Silicate Moon (BSM). This comparison depends on the widely accepted idea that the Earth and Moon originated from a common reservoir during the Moon-forming impact, followed by large-scale melting and magma-ocean crystallisation (Canup, 2004; Ćuk & Stewart, 2012; Nakajima & Stevenson, 2015). In this context, any isotope fractionation during Earth's magma ocean differentiation must have occurred after the Earth–Moon system reached equilibrium and would produce detectable differences between the BSE and BSM if significant amounts of fractionated material were retained in Earth's mantle. The similarity observed between BSE and BSM compositions thus directly constrains the extent of such differentiation and the preservation of early reservoirs.

We chose here the studies that have employed double-spiking methodology for both BSM and BSE (Klaver et al., 2024; Liu et al., 2023, 2025), except for δ^{30}Si BSM values, where we selected the most recent measurements (Dauphas et al., 2015), as samples measured using the double-spiking methodology are not available. A complete compilation of BSM and BSE values is available in Supplementary Information. In Mg and Si isotopes, the differences between BSM and BSE are virtually indistinguishable, with the larger BSM uncertainties resulting in maximum differences of 0.024 ± 0.021‰ for Mg (Klaver et al., 2024; Liu et al., 2023) and 0.016 ± 0.018% for Si (Dauphas et al., 2015; Liu et al., 2025) while incorporating the standard errors of the values. The close similarity between the present-day sampled mantle (represented by BSE estimates) and the BSM limits the amount of primordial bridgmanite that remained after lunar formation and the onset of the magma ocean. Bridgmanite could have been mixed back into the mantle over time; therefore, our calculations provide the volume that could be in present-day Earth. Our model (Figure 6.3) indicates upper bounds of 12.0 ± 15.0 wt% (Mg) and 4.1 ± 4.7 wt% (Si)

for bridgmanite-rich material, consistent with the observed BSE–BSM similarity. At other pressures, this number is lower, ranging from 9.7 ± 11.9 wt% (Mg; 80 GPa) to 2.3 ± 2.7 wt% (Si; 40 GPa), as shown in Table 6.3.

Both Mg- and Si-based estimates overlap at zero, indicating that the data do not require a resolvable bridgmanite-rich reservoir. However, the Mg system yields a comparatively weak constraint due to its large uncertainty (12.0±15.0 wt%), whereas the Si system provides a more restrictive upper bound (4.1 ± 4.7 wt%). Because the Mg- and Si-derived estimates are statistically consistent yet differ in central value, we interpret the discrepancy as reflecting differences in isotope-system sensitivity and overprint history rather than a resolvable difference in bridgmanite abundance. Therefore, we regard the Si-based estimate as the most reliable constraint on the preserved fraction in the following sections.

Our data is consistent with Walker et al. (2026), which excludes cumulate reservoirs exceeding ∼20 wt% of the mantle and more tightly constrains the preserved fraction to 4.1 ± 4.7 wt% of bridgmanite-rich material in the present-day mantle, challenging the existence of large-scale bridgmanite-rich cumulate structures, such as the BEAMS concept (Ballmer et al., 2017). This upper bound is substantially smaller than the reservoir sizes commonly invoked in geodynamic models of bridgmanite-enriched ancient mantle structures (BEAMS), which typically require approximately 10–30% of the lower mantle to remain compositionally distinct to influence mantle dynamics (Ballmer et al., 2017; Gülcher et al., 2021). Consequently, our isotope constraints permit only the smallest proposed BEAMS reservoirs or require extensive subsequent remixing.

6.4.4 Finding traces of primordial bridgmanite

If such isotopically distinct bridgmanite-rich reservoirs are preserved, even in small amounts like calculated here, they should, in principle, be detectable in mantle-derived melts. Specifically, ocean-island basalts (OIB), which are generally thought to originate from deep mantle sources due to their primordial $^3He/^4He$ ratios (Mukhopadhyay, 2012) and other isotope systems, could, in principle, record the Mg

and Si isotope signatures of bridgmanite-rich cumulates. Given the magnitude of equilibrium fractionation predicted here (Figure 6.1), incorporation of even modest proportions of bridgmanite-derived material would alter the isotopic signatures away from standard mantle values.

However, OIB data do not show such signatures. Global databases indicate that OIB Mg and Si isotope compositions are largely identical to those of BSE, with variations within 0.05‰ (Liu et al., 2023, 2025). The absence of a resolvable isotopic signal therefore places strong constraints on the contribution of primordial bridgmanite to plume source regions.

First, any isotopic contrast is likely diluted through interaction with the surrounding mantle and melt–rock exchange during ascent (Liu et al., 2022, 2023, 2026; van Keken et al., 2002). This is supported by the small quantities of primordial bridgmanite calculated here, which, if included, would constitute only minor parts of the melt products. An additional possibility is that isotopically light signatures are buffered by interaction with isotopically heavier mantle components. For example, an isotopically light bridgmanite component differing by 0.4% in δ^{30}Si would require approximately twenty parts ambient mantle to reduce the anomaly below the current analytical resolution of 0.02%. Although this estimate is approximate, it illustrates how even preserved primordial material could become effectively invisible following modest mantle mixing. Currently, the results needed to quantify this, such as calculating residual melt isotope factors, are unavailable, but future research could address this.

Instead, any measurable signatures of primordial bridgmanite are more likely to be preserved in residual melt pockets trapped between early-formed megacryst bridgmanite crystals (Deng et al., 2026). Such pockets could retain isotopically heavy signatures generated during magma ocean crystallisation, although their contribution to present-day melts remains uncertain.

6.4.5 Implications for lower mantle structure

These constraints on the detectability of bridgmanite-derived signatures have direct implications for the structure and evolution of the lower mantle. The combined constraints from equilibrium isotope fractionation, magma-ocean crystallisation models, and the absence of bridgmanite-related signals in OIB offer a coherent framework for evaluating the role of primordial heterogeneity in the present-day mantle (Figure 6.4). The 4.1 ± 4.7 wt% limit indicates a minor geochemical reservoir rather than a major primordial component of the mantle. This implies that any preserved bridgmanite-rich reservoirs are volumetrically limited and inefficiently sampled by mantle melting.

Geodynamic models indicate that compositionally different, bridgmanite-enriched regions may persist in the lower mantle over geological timescales, particularly if they possess sufficient density or viscosity contrasts (Ballmer et al., 2017; Gülcher et al., 2021). However, the isotopic data here show these domains cannot make up a large part of the mantle without causing detectable bulk isotopic compositional shifts. Instead, their contribution must remain $< 4.1 \pm 4.7$ wt% or be continuously reprocessed and mixed into the surrounding mantle. These findings align with seismic observations, which indicate that the lower mantle is largely laterally homogeneous aside from prominent structures such as LLSVPs and subducted slabs (e.g., (Garnero et al., 2016; Ritsema et al., 2011)), with heterogeneity predominantly explained by thermal variations rather than widespread compositional differences (Koelemeijer et al., 2018).

Overall, these results support a model in which early-formed bridgmanite-rich cumulates are largely homogenised during mantle evolution, with only small, dynamically isolated remnants preserved. However, these remnants have little influence on the overall Mg and Si isotope composition of the bulk (Figure 6.4). Stable isotope systematics, therefore, provide a bulk constraint on the scale of primordial heterogeneity, indicating that large bridgmanite-rich reservoirs do not dominate the present-day mantle. These stable-isotope constraints should also be considered alongside previous geochemical observations. Long-lived radiogenic

isotope systems (e.g. Sm–Nd, Lu–Hf) and incompatible trace-element systematics generally show little evidence that magma-ocean differentiation generated large preserved mantle reservoirs (Corgne et al., 2005; Halliday et al., 1995). Our results are consistent with these observations because they imply that only a small fraction (< 5 wt%) of isotopically distinct bridgmanite-rich material could remain isolated. Consequently, stable isotope systematics do not require a fundamentally different interpretation from radiogenic isotope evidence but instead provide an independent quantitative constraint on the maximum size of primordial reservoirs.

While the calculations presented here are based on simplified iron-free compositions, a comparative study at 1 atm for basaltic systems revealed little difference between iron-free and melt structures that included iron (De Winter et al., submitted). Future work should extend isotope fractionation to more complex lower mantle phases, such as davemaoite and post-perovskite, and integrate these results with geodynamic models to further constrain the generation and preservation of primordial heterogeneity.

6.5 Conclusion

We have performed *ab initio* calculations of Mg and Si isotope fractionation between bridgmanite and coexisting silicate melt under lower mantle conditions, with pressures between 40 and 80 GPa and temperatures up to 4000 K. Along a standard magma ocean adiabat, the fractionation factors of Δ^{26}Mg and Δ^{30}Si between bridgmanite and melt are approximately -0.200 and -0.246‰ for Mg, and -0.387 and -0.685‰ for Si, respectively. These results demonstrate that pressure effects overcome high temperatures and maintain significant isotope fractionation in the lower mantle.

We then combined these fractionation factors with crystallisation models to quantify the isotopic evolution of the cooling Earth magma ocean. During the crystallisation, the residual melt evolves to heavier compositions of $+0.1$‰ for Mg and $+0.25$‰ for Si. Bridgmanite cumulates become isotopically lighter, with -0.25‰ for Mg and -0.5‰ for Si. These results show that bridgmanite

crystallisation inevitably generates isotopic differences during differentiation of a deep magma ocean.

By applying these constraints alongside observed similarities between BSE and BSM, we estimate that up to 4.1 ± 4.7 wt% of bridgmanite-rich cumulates can be retained in the current mantle without causing significant isotopic differences. This allows for a negligible to minor volume of BEAMS on today's Earth but rules out the presence of large, unmixed reservoirs exceeding 4.1 ± 4.7 wt% (0–8.8 wt% within uncertainties). The absence of deviations between ocean island basalts and BSE indicates that bridgmanite-rich cumulate reservoirs are either volumetrically minor, inefficiently sampled, or isotopically buffered during mantle evolution. The refractory nature of bridgmanite, combined with melt–rock interaction and long-term convective mixing, likely suppresses the transfer of its isotopic signature into mantle-derived melts.

Overall, these findings demonstrate that equilibrium Mg and Si isotope fractionation during magma ocean crystallisation offers a quantitative approach to estimate the volume of preserved primordial mantle heterogeneity. Although bridgmanite-rich cumulates may remain in minor portions of the lower mantle, their impact on the overall mantle composition is negligible, and their isotopic signature is mostly concealed by later mantle processing. These results demonstrate that stable isotope systematics provide a robust, quantitative constraint on the scale of primordial heterogeneity remaining in Earth's mantle.

CRediT authorship contribution statement

Bram de Winter: Writing – original draft, Methodology, Conceptualisation. Andrew M. Walker: Writing – review & editing, methodology, conceptualisation, funding acquisition. Elena Melekhova: Writing – review & editing. Tim Elliott: Writing – review & editing, conceptualisation, and funding acquisition.

Acknowledgements

This work was funded by the European Research Council (ERC) under the ERC Advanced Grant 883351, NONUNE, awarded to Tim Elliott, and by BdW, which received financial support through an Oxford Radcliffe Scholarship from University College, Oxford. For Open Access, the authors have applied a CC BY public copyright licence to any Author Accepted Manuscript (AAM) version arising from this submission. The authors would like to acknowledge the use of the University of Oxford Advanced Research Computing (ARC) facility and the ARCHER2 UK National Supercomputing Service (`https://www.archer2.ac.uk`) in carrying out this work.

Bibliography

Abe, Y. (1997). Thermal and chemical evolution of the terrestrial magma ocean. *Physics of the Earth and Planetary Interiors*, *100*(1), 27–39.

Andrault, D., Bolfan-Casanova, N., Nigro, G. L., Bouhifd, M. A., Garbarino, G., & Mezouar, M. (2011). Solidus and liquidus profiles of chondritic mantle: Implication for melting of the Earth across its history. *Earth and Planetary Science Letters*, *304*(1), 251–259.

Andrault, D., Monteux, J., Le Bars, M., & Samuel, H. (2016). The deep Earth may not be cooling down. *Earth and Planetary Science Letters*, *443*, 195–203.

Ballmer, M. D., Houser, C., Hernlund, J. W., Wentzcovitch, R. M., & Hirose, K. (2017). Persistence of strong silica-enriched domains in the Earth's lower mantle. *Nature Geoscience*, *10*(3), 236–240.

Bouhifd, M. A., Jephcoat, A. P., Heber, V. S., & Kelley, S. P. (2013). Helium in Earth's early core. *Nature Geoscience*, *6*(11), 982–986.

Boukaré, C.-É., Badro, J., & Samuel, H. (2025). Solidification of Earth's mantle led inevitably to a basal magma ocean. *Nature*, 1–6.

Boyet, M., & Carlson, R. W. (2005). ^{142}Nd Evidence for Early (>4.53 Ga) Global Differentiation of the Silicate Earth. *Science*, *309*(5734), 576–581.

Canup, R. M. (2004). Simulations of a late lunar-forming impact. *Icarus*, *168*(2), 433–456.

Canup, R. M. (2008). Lunar-forming collisions with pre-impact rotation. *Icarus*, *196*, 518–538
ADS Bibcode: 2008Icar..196..518C.

Caracas, R., Hirose, K., Nomura, R., & Ballmer, M. D. (2019). Melt–crystal density crossover in a deep magma ocean. *Earth and Planetary Science Letters*, *516*, 202–211.

Corgne, A., Liebske, C., Wood, B. J., Rubie, D. C., & Frost, D. J. (2005). Silicate perovskite-melt partitioning of trace elements and geochemical signature of a deep perovskitic reservoir. *Geochimica et Cosmochimica Acta*, *69*(2), 485–496.

Ćuk, M., & Stewart, S. T. (2012). Making the Moon from a Fast-Spinning Earth: A Giant Impact Followed by Resonant Despinning. *Science*, *338*(6110), 1047–1052.

Dauphas, N., Poitrasson, F., Burkhardt, C., Kobayashi, H., & Kurosawa, K. (2015). Planetary and meteoritic Mg/Si and δ^{30}Si variations inherited from solar nebula chemistry. *Earth and Planetary Science Letters*, *427*, 236–248.

de Koker, N. P., Stixrude, L., & Karki, B. B. (2008). Thermodynamics, structure, dynamics, and freezing of Mg2SiO4 liquid at high pressure. *Geochimica et Cosmochimica Acta*, *72*(5), 1427–1441.

De Winter, B., Walker, A. M., Melekhova, E., & Elliott, T. (submitted). Five-fold Mg in silicate melts drives non-zero olivine-melt isotope fractionation. *Geochemical Perspectives Letters*.

De Winter, B., Walker, A. M., Melekhova, E., Liu, X.-N., & Elliott, T. (in review). The magnitude of equilibrium isotope fractionation of Mg between forsterite, diopside and melt at liquidus temperatures. *Geochimica et Cosmochimica Acta*.

Deng, J., Hu, J., Shi, Y., Lee, J., Niu, H., & Stixrude, L. (2026). The potential for bridgmanite megacrysts to drive magma ocean segregation. *Nature*, *650*(8101), 361–366.

Deng, J., Miyazaki, Y., Yuan, Q., & Du, Z. (2025). Deep mantle heterogeneities formed through a basal magma ocean contaminated by core exsolution. *Nature Geoscience*, *18*(10), 1056–1062.

Elkins-Tanton, L. T., Weiss, B. P., & Zuber, M. T. (2011). Chondrites as samples of differentiated planetesimals. *Earth and Planetary Science Letters*, *305*(1), 1–10.

Garnero, E. J., McNamara, A. K., & Shim, S.-H. (2016). Continent-sized anomalous zones with low seismic velocity at the base of Earth's mantle. *Nature Geoscience*, *9*(7), 481–489.

Ghosh, D. B., & Karki, B. B. (2011). Diffusion and viscosity of Mg2SiO4 liquid at high pressure from first-principles simulations. *Geochimica et Cosmochimica Acta*, *75*(16), 4591–4600.

Gülcher, A. J. P., Ballmer, M. D., & Tackley, P. J. (2021). Coupled dynamics and evolution of primordial and recycled heterogeneity in Earth's lower mantle. *Solid Earth*, *12*(9), 2087–2107.

Halliday, A. N., Lee, D.-C., Tommasini, S., Davies, G. R., Paslick, C. R., Godfrey Fitton, J., & James, D. E. (1995). Incompatible trace elements in OIB and MORB and source enrichment in the sub-oceanic mantle. *Earth and Planetary Science Letters*, *133*(3), 379–395.

Horiuchi, H., Ito, E., & Weidner, D. J. (1987). Perovskite-type MgSiO 3 ; single-crystal X-ray diffraction study. *American Mineralogist*, *72*(3-4), 357–360.

Huang, F., Wu, Z., Huang, S., & Wu, F. (2014). First-principles calculations of equilibrium silicon isotope fractionation among mantle minerals. *Geochimica et Cosmochimica Acta*, *140*, 509–520.

Ito, E., Kubo, A., Katsura, T., & Walter, M. J. (2004). Melting experiments of mantle materials under lower mantle conditions with implications for magma ocean differentiation. *Physics of the Earth and Planetary Interiors*, *143–144*, 397–406.

Ito, E., & Takahashi, E. (1989). Postspinel transformations in the system Mg2SiO4-Fe2SiO4 and some geophysical implications. *Journal of Geophysical Research: Solid Earth*, *94*(B8), 10637–10646.

Katsura, T. (2025). Phase relations of bridgmanite, the most abundant mineral in the Earth's lower mantle. *Communications Chemistry*, *8*(1), 28.

Klaver, M., Klemme, S., Liu, X.-N., Hin, R. C., Coath, C. D., Anand, M., Lissenberg, C. J., Berndt, J., & Elliott, T. (2024). Titanium-rich basaltic melts on the Moon modulated by reactive flow processes. *Nature Geoscience*, 1–6.

Koelemeijer, P., Schuberth, B. S. A., Davies, D. R., Deuss, A., & Ritsema, J. (2018). Constraints on the presence of post-perovskite in Earth's lowermost mantle from tomographic-geodynamic model comparisons. *Earth and Planetary Science Letters*, *494*, 226–238.

Labrosse, S., Hernlund, J. W., & Coltice, N. (2007). A crystallizing dense magma ocean at the base of the Earth's mantle. *Nature*, *450*(7171), 866–869.

Liu, X.-N., Hin, R., Coath, C., van Soest, M., Melekhova, E., & Elliott, T. (2022). Equilibrium olivine-melt Mg isotopic fractionation explains high δ^{26}Mg values in arc lavas. *Geochemical Perspectives Letters*, *22*, 42–47.

Liu, X.-N., Hin, R. C., Coath, C. D., Bizimis, M., Su, L., Ionov, D. A., Takazawa, E., Brooker, R., & Elliott, T. (2023). The magnesium isotopic composition of the mantle. *Geochimica et Cosmochimica Acta*, *358*, 12–26.

Liu, X.-N., Hin, R. C., Coath, C. D., Onyett, I., Rogers, B., Lewis, J., & Elliott, T. (2026). Magnesium isotope heterogeneity in oceanic island basalts. *Earth and Planetary Science Letters*, *684*, 120010.

Liu, X.-N., Klaver, M., Hin, R. C., Coath, C. D., Bizimis, M., Ionov, D. A., & Elliott, T. (2025). Si isotope composition of Earth's mantle and oceanic basalts. *Geochimica et Cosmochimica Acta*.

McDonough, W., & Sun, S. (1995). The composition of the Earth. *Chemical Geology*, *120*(3-4), 223–253.

Mukhopadhyay, S. (2012). Early differentiation and volatile accretion recorded in deep-mantle neon and xenon. *Nature*, *486*(7401), 101–104.

Nakajima, M., & Stevenson, D. J. (2015). Melting and mixing states of the Earth's mantle after the Moon-forming impact. *Earth and Planetary Science Letters*, *427*, 286–295.

Perdew, J. P., Ruzsinszky, A., Csonka, G., Vydrov, O. A., Scuseria, G. E., Constantin, L. A., Zhou, X., & Burke, K. (2008). Restoring the Density-Gradient Expansion for Exchange in Solids and Surfaces. *Physical Review Letters*, *100*(13), 136406.

Prescher, C., Prakapenka, V. B., Stefanski, J., Jahn, S., Skinner, L. B., & Wang, Y. (2017). Beyond sixfold coordinated Si in SiO2 glass at ultrahigh pressures. *Proceedings of the National Academy of Sciences*, *114*(38), 10041–10046.

Rabin, S., Blanchard, M., Pinilla, C., Poitrasson, F., & Grégoire, M. (2023). Iron and silicon isotope fractionation in silicate melts using first-principles molecular dynamics. *Geochimica et Cosmochimica Acta*, *343*, 212–233.

Ritsema, J., Deuss, A., van Heijst, H. J., & Woodhouse, J. H. (2011). S40RTS: A degree-40 shear-velocity model for the mantle from new Rayleigh wave dispersion, teleseismic traveltime and normal-mode splitting function measurements. *Geophysical Journal International*, *184*(3), 1223–1236.

Rizo, H., Walker, R. J., Carlson, R. W., Touboul, M., Horan, M. F., Puchtel, I. S., Boyet, M., & Rosing, M. T. (2016). Early Earth differentiation investigated through ^{142}Nd, ^{182}W, and highly siderophile element abundances in samples from Isua, Greenland. *Geochimica et Cosmochimica Acta*, *175*, 319–336.

Schauble, E. A. (2011). First-principles estimates of equilibrium magnesium isotope fractionation in silicate, oxide, carbonate and hexaaquamagnesium(2+) crystals. *Geochimica et Cosmochimica Acta*, *75*(3), 844–869.

Solomatov, V. S., & Moresi, L.-N. (2000). Scaling of time-dependent stagnant lid convection: Application to small-scale convection on Earth and other terrestrial planets. *Journal of Geophysical Research: Solid Earth*, *105*(B9), 21795–21817.

Solomatov, V. S., & Stevenson, D. J. (1993). Nonfractional crystallization of a terrestrial magma ocean. *Journal of Geophysical Research: Planets*, *98*(E3), 5391–5406.

Solomatova, N., & Caracas, R. (2019). Pressure-Induced Coordination Changes in a Pyrolitic Silicate Melt From Ab Initio Molecular Dynamics Simulations. *Journal of Geophysical Research: Solid Earth*, *124*(11), 11232–11250.

Stixrude, L., & Karki, B. (2005). Structure and Freezing of MgSiO3 Liquid in Earth's Lower Mantle. *Science*, *310*(5746), 297–299.

Urey, H. C. (1947). The thermodynamic properties of isotopic substances. *Journal of the Chemical Society (Resumed)*, (0), 562–581.

van Keken, P. E., Hauri, E. H., & Ballentine, C. J. (2002). Mantle Mixing: The Generation, Preservation, and Destruction of Chemical Heterogeneity. *Annual Review of Earth and Planetary Sciences*, *30*(Volume 30, 2002), 493–525.

Walker, A. M., Hin, R. C., & Elliott, T. (2026). Controls on Mg isotopic fractionation between deep mantle phases and relict signatures of a terrestrial magma ocean. *Geochimica et Cosmochimica Acta*, *425*, 131–142.

Wood, B. J., Walter, M. J., & Wade, J. (2006). Accretion of the Earth and segregation of its core. *Nature*, *441*(7095), 825–833.

Young, E. D., Manning, C. E., Schauble, E. A., Shahar, A., Macris, C. A., Lazar, C., & Jordan, M. (2015). High-temperature equilibrium isotope fractionation of non-traditional stable isotopes: Experiments, theory, and applications. *Chemical Geology*, *395*, 176–195.

Figures & Tables

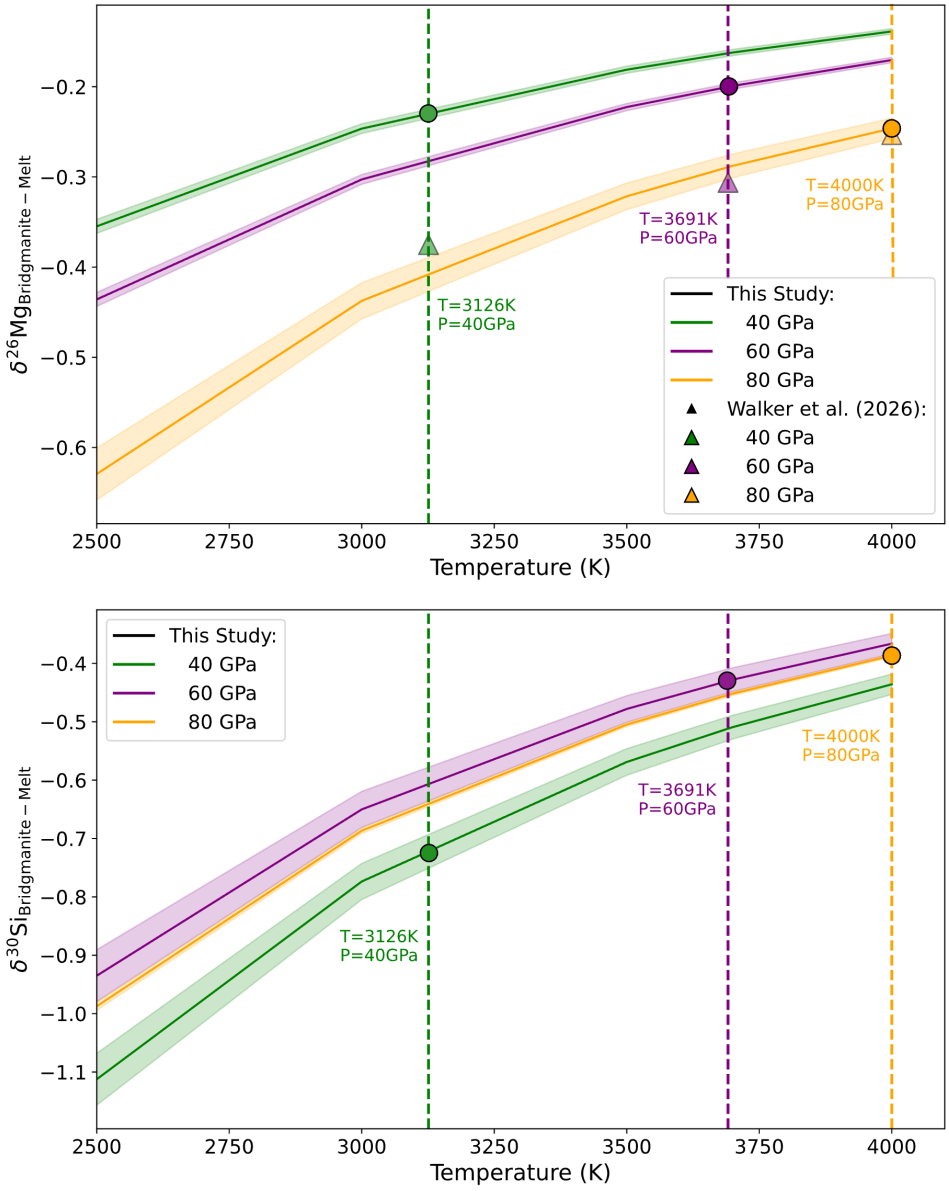


Figure 6.1: Temperature dependence of equilibrium isotopic fractionation between bridgmanite and melt for (a) Si (δ^{30}Si) and (b) Mg (δ^{26}Mg) at 40, 60, and 80 GPa. Solid lines show results from this study, with shaded bands indicating associated uncertainties. Colored symbols mark fractionation values at representative mantle temperatures along each isobar (vertical dashed lines). Triangles denote Mg results from (Walker et al., 2026) for comparison.

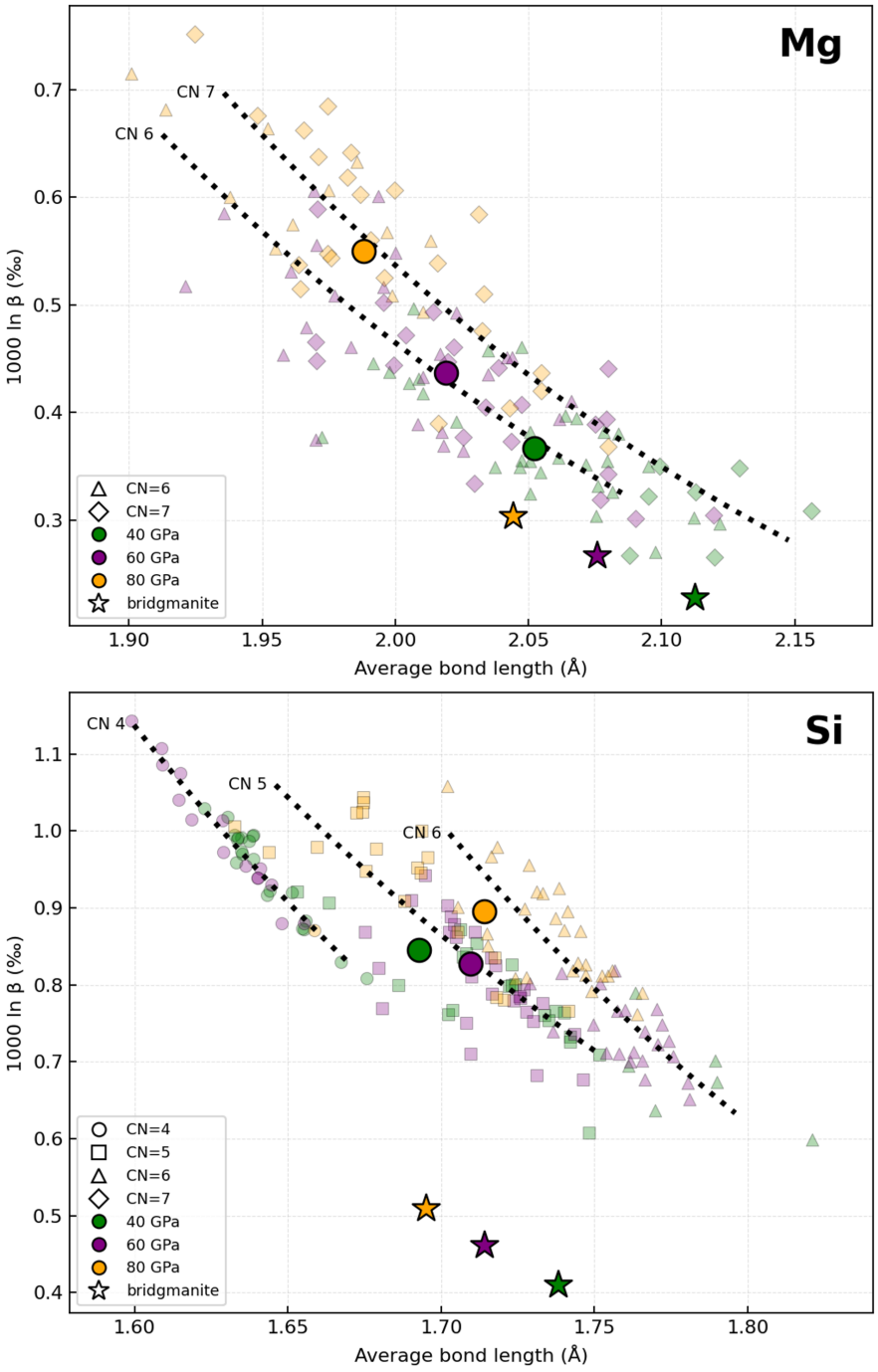


Figure 6.2: Relationship between average bond length and isotopic fractionation expressed as $1000\ln(\beta)$ for (a) Si- and (b) Mg-bearing phases. Symbols denote coordination numbers (CN) as indicated, while colours represent different pressure conditions (40, 60, and 80 GPa). Large colored markers highlight selected high-pressure phases, and star symbols indicate bridgmanite compositions. Dashed curves correspond to theoretical fractionation trends for different coordination environments.

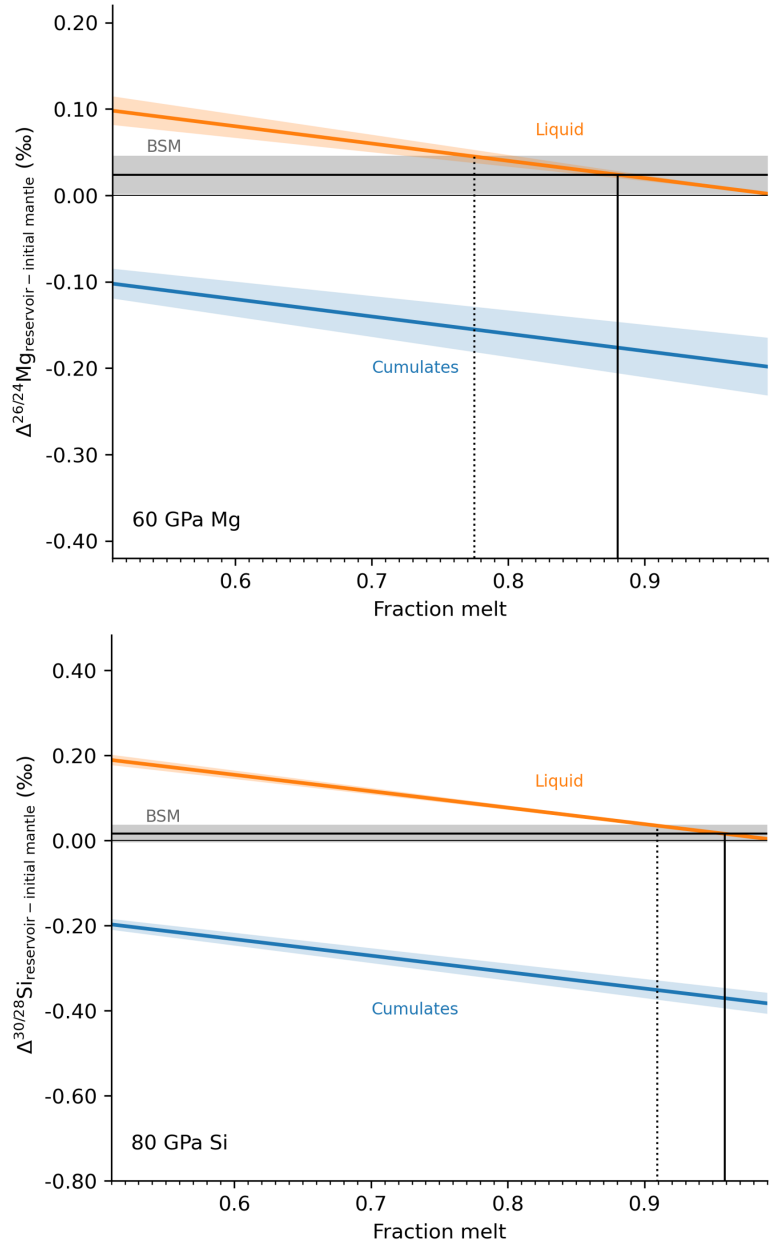


Figure 6.3: Evolution of isotopic composition during fractional crystallisation as a function of melt fraction. The top panel shows Δ^{26}Mg and the bottom panel shows Δ^{30}Si (both reported relative to initial mantle composition, ‰). The orange curves represent the composition of the instantaneous (residual) melt, while the blue curves show the isotopic composition of bridgmanite cumulates crystallising out of the pyrolitic melt. Shaded regions indicate model uncertainty. The grey horizontal band marks the BSM reference range. As the melt fraction increases, instantaneous melts approach the initial composition, whereas cumulative melts remain isotopically lighter.

Table 6.1: Polynomial fitted constants for $1000\ln\beta = AT^{-6} + BT^{-4} + CT^{-2}$ for Mg and Si isotopes in bridgmanite and coexisting melt at 40, 60 and 80 GPa. Fits are calibrated over the temperature range 2000–4000 K, where T is in Kelvin. Coefficients A, B and C are reported with their 1σ regression uncertainties. Corresponding values of $1000\ln\beta$ at 4000 K are listed for both phases, with melt uncertainties reflecting the standard error of the mean from independent calculations. Bridgmanite–melt equilibrium fractionation factors ($\Delta^{26}\mathrm{Mg}_{\mathrm{bdm-melt}}$ and $\Delta^{30}\mathrm{Si}_{\mathrm{bdm-melt}}$) are additionally expressed as inverse-square temperature relationships of the form $(a \pm \sigma) \times 10^5/T^2$, where uncertainties represent 1σ errors from linear regression.

		A	s.e.	B	s.e.	C	s.e.	$1000\ln\beta$ (4000 K)
Mg								
Melt	40 GPa	1.85×10^{15}	5.32×10^{14}	-8.31×10^{10}	1.85×10^{8}	7.74×10^{6}	1.40×10^{1}	0.3665 ± 0.015
	60 GPa	3.24×10^{15}	3.50×10^{13}	-1.20×10^{11}	1.22×10^{7}	8.95×10^{6}	9.21×10^{-1}	0.445 ± 0.021
	80 GPa	4.82×10^{15}	3.08×10^{14}	-1.59×10^{11}	1.07×10^{8}	1.03×10^{7}	8.09×10^{0}	0.558 ± 0.0206
Bridgmanite	40 GPa	4.59×10^{14}	2.89×10^{14}	-3.90×10^{10}	1.01×10^{8}	3.65×10^{6}	7.61×10^{0}	0.2278
	60 GPa	1.01×10^{15}	3.24×10^{14}	-5.24×10^{10}	1.13×10^{8}	4.27×10^{6}	8.52×10^{0}	0.2669
	80 GPa	2.13×10^{15}	1.31×10^{14}	-6.80×10^{10}	4.54×10^{7}	4.87×10^{6}	3.44×10^{0}	0.2669
Si								
Melt	40 GPa	1.36×10^{16}	1.82×10^{14}	-3.3×10^{11}	6.31×10^{7}	1.38×10^{7}	4.78×10^{0}	0.8456 ± 0.030
	60 GPa	1.62×10^{16}	1.06×10^{14}	-3.7×10^{11}	3.68×10^{7}	1.48×10^{7}	2.79×10^{0}	0.835 ± 0.031
	80 GPa	2.01×10^{16}	1.96×10^{14}	-4.2×10^{11}	6.82×10^{7}	1.59×10^{7}	5.16×10^{0}	0.898 ± 0.022
Bridgmanite	40 GPa	3.99×10^{15}	2.65×10^{14}	-1.19×10^{11}	9.21×10^{7}	6.56×10^{6}	6.97×10^{0}	0.4098
	60 GPa	5.85×10^{15}	4.20×10^{14}	-1.55×10^{11}	1.46×10^{8}	7.40×10^{6}	1.10×10^{1}	0.4617
	80 GPa	7.49×10^{15}	2.61×10^{14}	-1.85×10^{11}	9.06×10^{7}	8.16×10^{6}	6.86×10^{0}	0.5093
$\Delta^{26}\mathrm{Mg}_{\mathrm{bdm-melt}}$	40 GPa			$(-22.180 \pm 0.004) \times 10^5/T^2$				-0.1387 ± 0.015
	60 GPa			$(-27.249 \pm 0.007) \times 10^5/T^2$				-0.1704 ± 0.021
	80 GPa			$(-39.359 \pm 0.016) \times 10^5/T^2$				-0.2462 ± 0.020
$\Delta^{30}\mathrm{Si}_{\mathrm{bdm-melt}}$	40 GPa			$(-69.602 \pm 0.059) \times 10^5/T^2$				-0.4358 ± 0.030
	60 GPa			$(-58.494 \pm 0.044) \times 10^5/T^2$				-0.3662 ± 0.031
	80 GPa			$(-61.769 \pm 0.046) \times 10^5/T^2$				-0.3867 ± 0.022

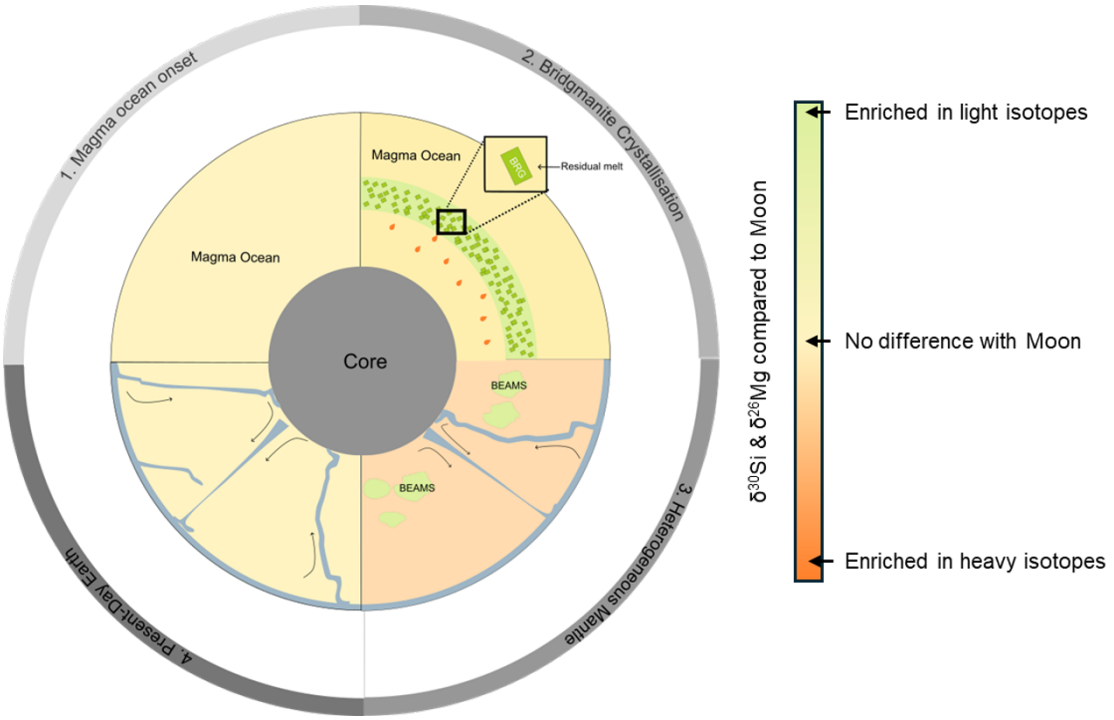


Figure 6.4: Schematic of planetary differentiation from magma ocean onset to long-term mantle evolution. The four quadrants illustrate successive stages: (1) magma ocean onset, (2) bridgmanite crystallisation and formation of a basal residual melt layer enriched in light isotopes (green), (3) heterogeneous mantle development with preserved BEAMS domains over the 4.4 Gyr following magma-ocean crystallisation, and (4) present-day Earth structure.

Table 6.2: Average coordination numbers (CN) of Mg and Si in silicate melt at 40–80 GPa from this study and previous computational studies. Values represent mean coordination numbers; literature values are approximate ranges from Solomatova and Caracas (2019) and Stixrude and Karki (2005).

	40 GPa	60 GPa	80 GPa
Mg – This study	5.938	6.656	6.917
Mg – Solomatova and Caracas (2019)	∼6.5	∼7.0	∼7.1
Si – This study	4.688	5.109	5.542
Si – Solomatova and Caracas (2019)	∼4.6	∼5.3	∼5.45
Si – Stixrude and Karki (2005)	∼4.5	∼5.1	∼5.6

Table 6.3: Bridgmanite (BDM) fraction calculated using the Walker et al. (2026) model for Si- and Mg-bearing systems at different pressures (P) and temperatures (T). $\Delta_{\text{bdm-melt}}$ represents the partitioning difference between Bdm and melt; maximum Bdm fraction values are reported with associated uncertainties. Negative values of the maximum Bdm fraction are physically plausible and indicate conditions where residual melt is retained (e.g., in a basal magma ocean). However, the lower bound for bridgmanite-rich cumulates is taken as 0. Results correspond to the conditions shown in Figure 6.3.

	P (GPa)	T (K)	$\Delta_{\text{bdm-melt}}$ (‰)	Max bridgmanite fraction (wt%)
Si	40	3126	-0.685	2.3 ± 2.7
	60	3691	-0.430	3.7 ± 4.2
	80	4000	-0.387	4.1 ± 4.7
Mg	40	3126	-0.218	11.0 ± 11.7
	60	3691	-0.200	12.0 ± 15.0
	80	4000	-0.246	9.7 ± 11.9

Appendix: Supplementary Information

1. Computational methods: Molecular Dynamics and DFT

All calculations in this study were performed using density functional theory (DFT) with the CASTEP software, following a workflow similar to that described in De Winter et al. (submitted). More details on the workflow and the methodology can be found in this paper.

Here, *ab initio* molecular dynamics (DFT-MD) simulations were used to generate equilibrated silicate melt structures that sample the range of local coordination environments in the liquid. A series of atomic configurations was extracted from these MD trajectories and treated as static snapshots for site-specific DFT calculations to calculate vibrational properties, following the methodology developed by Rabin et al. (2023). Equilibrium isotope fractionation factors (β) were calculated from these vibrational calculations using isotopic mass substitution, as seen in previous studies (Huang et al., 2013, 2014; Rabin et al., 2023; Schauble, 2011; Walker et al., 2026; Wang et al., 2023).

First-principles calculations were performed using DFT (Hohenberg & Kohn, 1964; Kohn & Sham, 1965) within a plane-wave formalism (Payne et al., 1992) as implemented in CASTEP (Clark et al., 2005). Both mineral and melt DFT calculations were performed using the Perdew–Burke–Ernzerhof for solids (PBESOL; (Perdew et al., 2008)). The PBESOL functional was selected due to its improved performance for solid-state structures and vibrational properties (De Winter et al., in review). We used norm-conserving pseudopotentials (Troullier & Martins, 1991) with valence configurations including O 2p, Si 3s–3p, Mg 3s, Ca 3s, and Al 3s–3p electrons. Due to the large size ($\sim$120 atoms) of the melt supercells, Brillouin zone sampling is limited, and Γ-point phonon calculations provide an adequate representation of vibrational properties for isotope fractionation calculations. Plane-wave energy cutoffs of 900 eV for bridgmanite and 500 eV for melt structures

were chosen based on convergence testing to ensure reliable forces and vibrational frequencies (De Winter et al., submitted, in review).

Molecular Dynamics simulations

Molecular dynamics (MD) simulations were used to generate equilibrated silicate melt structures suitable for snapshot-based isotope fractionation calculations. All simulations began from a crystalline bridgmanite supercell containing 120 atoms, constructed to ensure realistic initial atomic separations and to avoid unphysical short-range interactions and subsequent failures. The initial crystalline structure was fully melted using canonical ensemble (NVT) simulations at 8000 K for 10 ps. Temperature control was achieved using a Nosé–Hoover thermostat (Hoover, 1985; Nosé, 1984), which provides correct sampling of the canonical ensemble and energy exchange between the system and the thermal reservoir. Melt equilibration was assessed through monitoring of equilibrated total energy, temperature stability, radial distribution functions (Figure 6.6 & Figure 6.7), and atomic diffusion behaviour (see next section). When equilibration criteria were not satisfied, additional high-temperature NVT simulations were performed until a stable molten structure was obtained.

Target melt composition (pyrolytic melt based on McDonough and Sun (1995)) was produced by atomic substitution applied to the equilibrated melt structure. The melt composition corresponds to a pyrolitic mantle composition based on McDonough and Sun (1995), with major-element proportions of Mg, Si, Ca, and Al representative of the BSE, corrected for the removal of Fe. Compositional adjustments were performed using a custom Python workflow that modifies cation proportions and writes `-cell` files, which are then used for MD simulations. Following atomic substitution, our melt structures were re-equilibrated at 8000 K to remove any artefacts introduced by the composition change. The simulation was then cooled to 4000 K. Additional NVT simulations at 4000 K (10 ps) were performed to ensure stability.

Because melt structure is strongly dependent on volume, simulation cell parameters were optimised using isothermal–isobaric (NPT) simulations at 4000 K. Pressure was controlled using a Parrinello–Rahman barostat (Parrinello & Rahman, 1981) with NPT simulations running for 10 ps and repeated until the average pressure converged to 1 GPa. The final MD trajectories were produced in the NVT ensemble at 4000 K for up to 20 ps. Integration steps of 0.001 ps (1 fs) were chosen, following the methodology from Rabin et al. (2023).

Our snapshot selection was extracted from the equilibrated NVT MD trajectories. We selected 3 snapshots for each pressure for further calculations due to the computationally expensive DFT geometry optimisation steps. Although only a limited number of snapshots were used, these were selected from equilibrated MD trajectories and span the range of local coordination environments present in the melt. The resulting standard errors are small, indicating that the sampled configurations capture the dominant structural variability.

Melt snapshot calculations

Each melt snapshot was optimised at its respective pressure with fixed cell parameters. Although these optimised structures are formally glasses rather than liquids, previous studies have demonstrated that their local structural environments are representative of the parent melt (Rabin et al., 2023), supporting their use in snapshot-based vibrational calculations.

The *ab initio* treatment of equilibrium isotope fractionation follows established approaches for Mg and Si isotopes in silicate minerals and melts (De Winter et al., submitted, in review; Huang et al., 2013, 2014; Rabin et al., 2021; Schauble, 2011; Walker et al., 2026). Density functional theory calculations were performed using CASTEP. We used variational Density Functional Perturbation Theory (DFPT: (Gonze, 1997; Gonze & Lee, 1997; Refson et al., 2006)) on a Γ-centred $1 \times 1 \times 1$ q-point grid for the 120-atom melt supercells. Given the large real-space dimensions of the melt cells, Brillouin zone sampling is correspondingly small,

and Γ-point phonons provide an adequate description of vibrational properties for isotope fractionation calculations.

Phonon frequencies were computed in a single CASTEP thermodynamics calculation for each structure. Isotope fractionation factors were subsequently derived using a custom post-processing script. This script takes the force constant matrix obtained from the original calculations and reconstructs the dynamical matrix after applying isotopic mass substitutions. The vibrational frequencies are then recalculated from the updated dynamical matrix, while the force constants remain unchanged. This procedure allows reduced partition function ratios (β, eq. 1) to be evaluated for all isotopes and crystallographic sites from a single phonon calculation, within the harmonic approximation (at fixed equilibrium structure) and following the Bigeleisen–Mayer equation (Young et al., 2015). Final β-values were obtained by averaging over all snapshots (or crystallographic sites, where applicable), with uncertainties estimated as the standard error of the mean. Uncertainties in β-values are reported as the standard error of the mean across snapshots or crystallographic sites. These uncertainties are propagated through all subsequent fractionation calculations, assuming independent errors. β is defined as the reduced partition function ratio calculated from vibrational frequencies using the Bigeleisen–Mayer formulation:

$$\beta(X,Y,Y^*) = \prod_{i=1}^{N_q} \left[\prod_{j=1}^{3N_{\mathrm{at}}} \left(\frac{\omega^*_{i,j}}{\omega_{i,j}} \frac{e^{-h\omega^*_{i,j}/(2kT)}}{1-e^{-h\omega^*_{i,j}/(2kT)}} \frac{1-e^{-h\omega_{i,j}/(2kT)}}{e^{-h\omega_{i,j}/(2kT)}} \right) \right]^{w_i} \quad (1)$$

Mineral calculations (bridgmanite)

In addition to melt calculations, first-principles DFT calculations were performed on crystalline bridgmanite ($MgSiO_3$) to obtain equilibrium isotope fractionation factors for both Mg and Si. Bridgmanite was modelled in the orthorhombic *Pnma* structure and treated as an iron-free $MgSiO_3$ endmember. Initial crystal structures were obtained from the American Mineralogist Crystal Structure Database and fully optimised for pressures between 0 and 140 GPa. Geometry optimisation involved relaxing both atomic positions and cell parameters until residual forces

were below 1×10^{-4} eV Å^{-1}, stresses were below 0.05 GPa, and total energy changes were below 1×10^{-5} eV.

Calculations employed the Perdew–Burke–Ernzerhof for solids (PBESOL; (Perdew et al., 2008)) exchange–correlation functional. Norm-conserving pseudopotentials and plane-wave cutoffs sufficient to converge phonon frequencies were utilised, with Brillouin-zone sampling using Monkhorst–Pack grids suitable for each crystal structure. Specifically, a $4 \times 4 \times 2$ k-point grid was employed for our bridgmanite calculations.

Phonon frequencies were calculated using density functional perturbation theory (Gonze & Lee, 1997) with a $4 \times 4 \times 4$ q-point grid, using a fine grid multiplied by 3. Isotopic fractionation factors for Mg and Si were obtained by substituting isotopic masses at the relevant crystallographic sites while keeping force constants unchanged (eq. 1). The calculated β-factors are consistent in magnitude and temperature dependence with previous DFT studies (e.g., (Huang et al., 2014; Walker et al., 2026)), supporting the reliability of the computational approach (Figure 6.5). Small systematic offsets between studies likely reflect differences in exchange–correlation functional, structural models, and treatment of vibrational properties.

2.Validation of melt structure

The structure of the pyrolytic melt was characterised using radial distribution functions (RDFs), coordination-number (CN) statistics, and mean squared displacements (MSD) computed from the equilibrated portion of the molecular-dynamics trajectory (Figure 6.6 & Figure 6.7).

Pressure-dependent evolution of Si and Mg melt structures

The Si–O RDF shows a distinct first peak centred near ~ 1.6 Å across all pressures (40–80 GPa), consistent with dominant tetrahedral coordination. However, under increasing pressure, the first peak becomes slightly wider, and its height decreases, indicating a gradual change in tetrahedral coordination and the onset of higher coordination states. Similar pressure-induced coordination changes in silicate melt

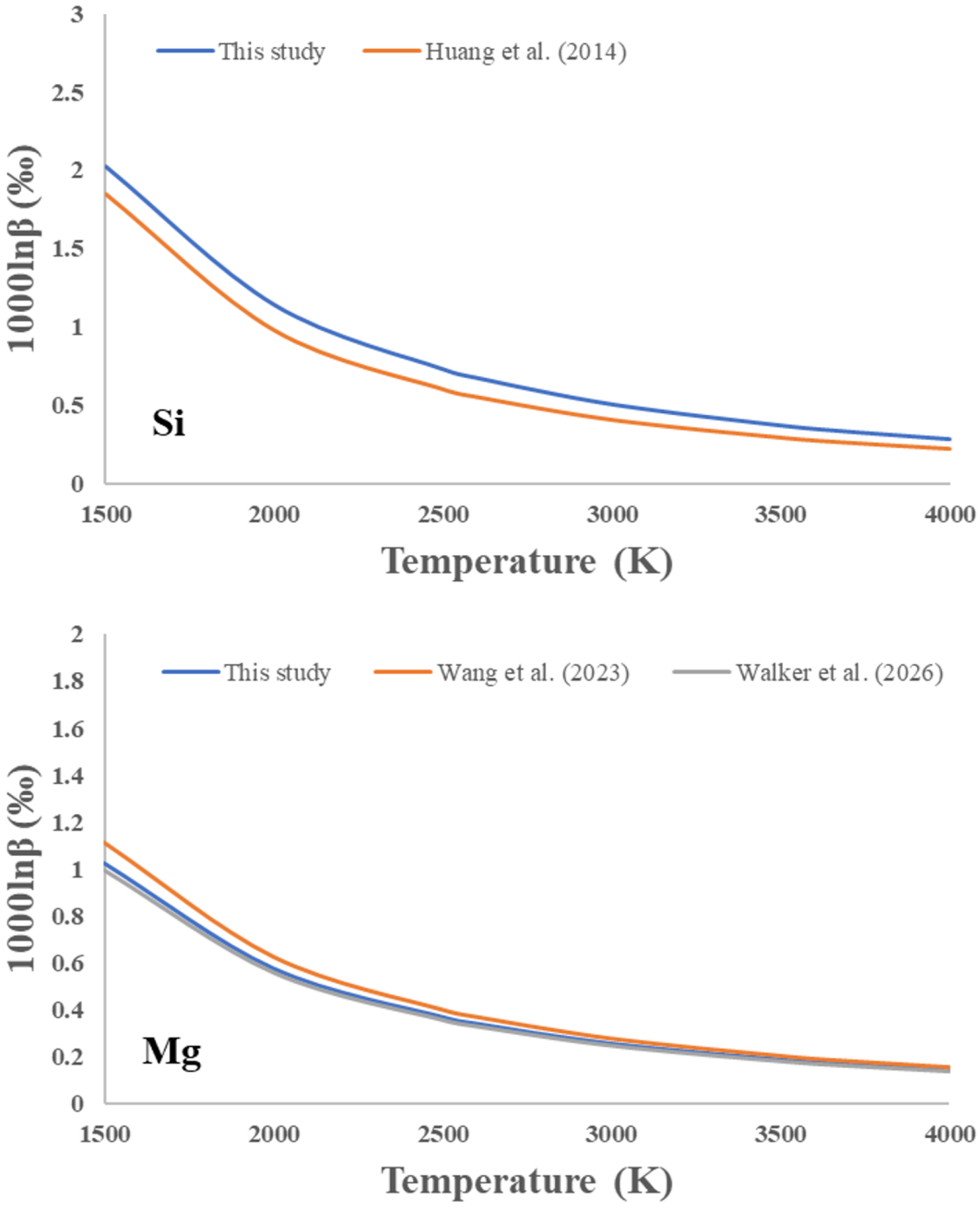


Figure 6.5: Temperature dependence of reduced partition function ratios ($1000 \ln \beta$) for Mg (top) and Si (bottom) at 0 GPa for bridgmanite. Results from this study are compared with literature calculations.

have been reported in other experimental and computational studies (Guillot & Sator, 2007; Sanloup et al., 2013; Solomatova & Caracas, 2019).

In contrast, the Mg–O RDF displays a broader, more pressure-sensitive first peak around 2.0 Å. As pressure increases from 40–80 GPa, the average distance decreases, indicating compression of the Mg–O bond. At higher pressure, a modest increase in peak intensity is observed, consistent with the shift in average coordination number from predominantly 5 to 6. This behaviour is consistent with previous findings where Mg adapts its coordination environment under pressure to accommodate increased density (de Koker et al., 2008; Stixrude et al., 2009).

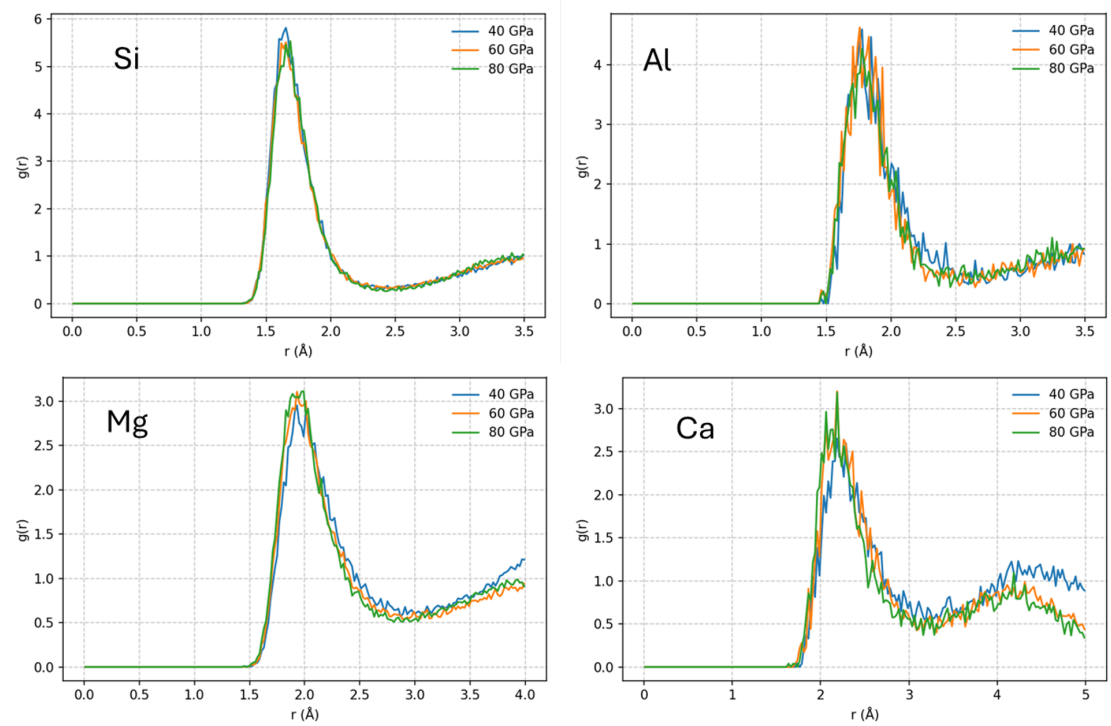


Figure 6.6: Cation–oxygen radial distribution functions (RDF) for Si, Al, Mg, and Ca obtained from the equilibrated segment of the molecular-dynamics trajectory.

Diffusion coefficients

Diffusion coefficients for individual atomic species were calculated from the MSD curves shown in the Figure 6.7. Diffusion coefficients were derived using the Einstein relation:

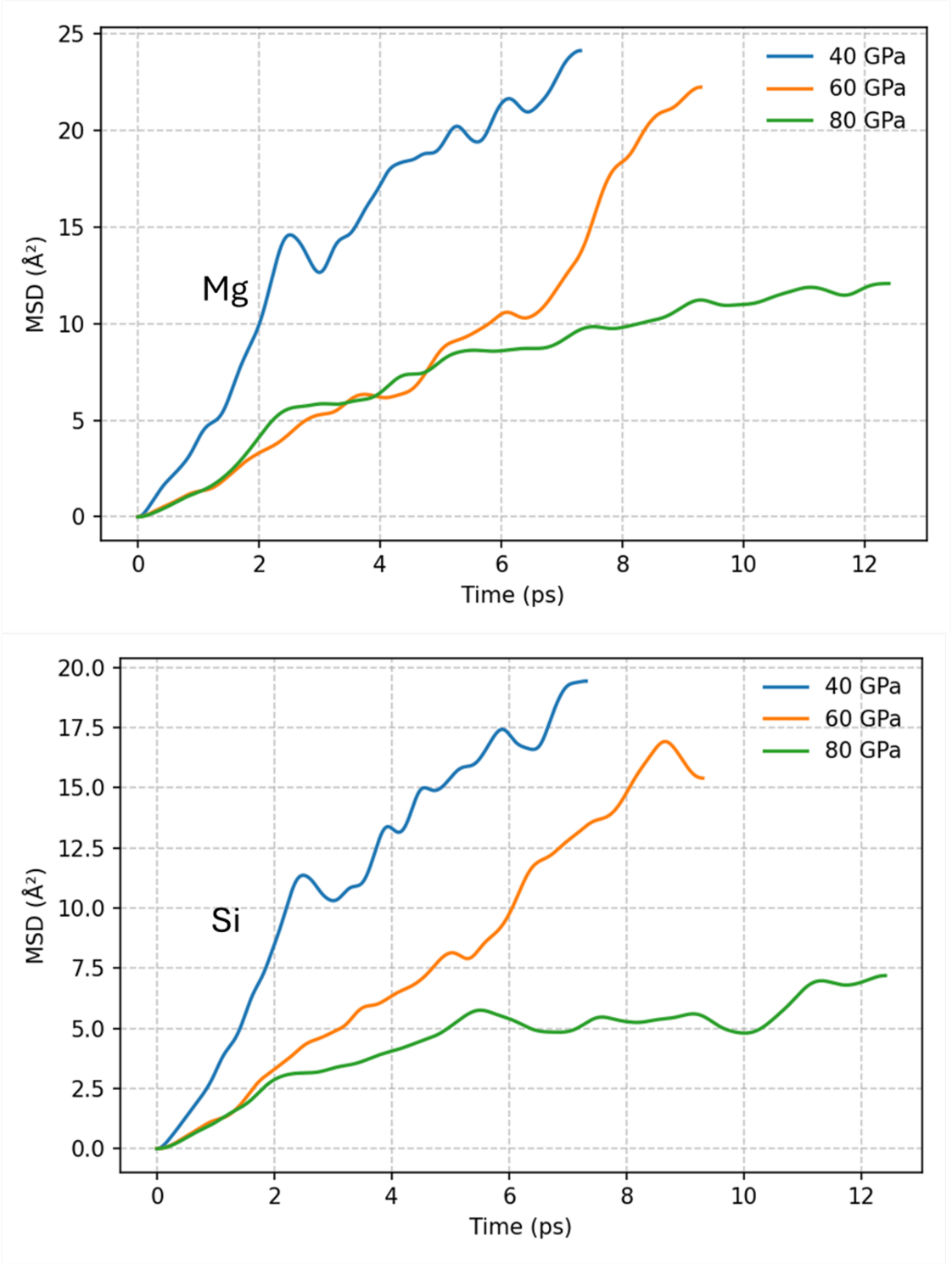


Figure 6.7: Mean squared displacement (MSD) of Al, Ca, Mg, O, and Si atoms as a function of time for the full molecular-dynamics trajectory. MSDs are computed relative to the initial configuration.

$$D = \frac{1}{6}\frac{d}{dt}r^2(t) \tag{2}$$

by fitting to MSD curves over the 2–8 ps interval. Because MD simulations are limited in time, these diffusion coefficients should primarily be used to compare atomic species. The data show a clear decrease in both species with increasing pressure. Mg exhibits higher mobility than Si at all pressures, with D decreasing from $\sim 5.2 \times 10^{-9}$ to $\sim 2.1 \times 10^{-9}$ $\mathrm{m^2\,s^{-1}}$ between 40 and 80 GPa, while Si decreases from $\sim 4.2 \times 10^{-9}$ to $\sim 1.1 \times 10^{-9}$ $\mathrm{m^2\,s^{-1}}$ over the same range.

The calculated diffusion coefficients ($\sim 10^{-9}$–10^{-10} $\mathrm{m^2\,s^{-1}}$) are consistent with *ab initio* simulations of $MgSiO_3$ melts at deep mantle conditions, which report diffusivities of $\sim 10^{-9}$ $\mathrm{m^2\,s^{-1}}$ (Wan et al., 2007). The higher mobility of Mg relative to Si agrees with first-principles studies of silicate melt (X. Liu et al., 2018). At the same time, the observed pressure dependence, including possible non-monotonic behaviour, is consistent with previous simulations showing structural control on transport properties (de Koker et al., 2008; Luo et al., 2020).

Table 6.4: Diffusion coefficients in basaltic melt.

Element	Pressure (GPa)	This study – D ($\mathrm{m^2\,s^{-1}}$)
Mg	40	5.2×10^{-9}
	60	3.9×10^{-9}
	80	2.1×10^{-9}
Si	40	4.2×10^{-9}
	60	3.2×10^{-9}
	80	1.1×10^{-9}

3. Isotope fractionation calculations

Ionic model

We employed an ionic model following the approach of Young et al. (2015), but modified to better capture the behaviour of melt environments. Rather than fitting a single force constant per coordination number, we allow the effective force constant to vary continuously with bond length and coordination environment. The

model was applied to Si (CN = 4, 5, 6) and Mg (CN = 6, 7), using individual β-values from single sites.

Following the classical Bigeleisen and Mayer (1947) formulation, the reduced partition function ratio for a given site can be written as:

$$\beta^{\text{ionic}} = 1 + \frac{1}{24}\left(\frac{h}{k_B T}\right)^2 \frac{K_f}{4\pi^2}\left(\frac{1}{\mu_i} - \frac{1}{\mu_0}\right), \tag{6.1}$$

where h is Planck's constant, k_B is the Boltzmann constant, T is temperature, and μ_i and μ_0 are the reduced masses of the substituted and reference isotopes, respectively.

In contrast to a fixed harmonic force constant, we express K_f in terms of an effective ionic interaction:

$$K_f \propto \frac{z_1 z_2}{r^3}, \tag{6.2}$$

where r is the average bond length and z_1, z_2 are effective ionic charges. The charges are parameterised through an effective ionicity term ζ, such that:

$$z_1 = \zeta \cdot Z_1, \qquad z_2 = \zeta \cdot Z_2, \tag{6.3}$$

with Z_1, Z_2 as the formal charges of the cation and anion.

To account for structural variability, ζ is allowed to vary linearly with bond length within each coordination environment:

$$\zeta(r) = \zeta_0 + \zeta_r\, r. \tag{6.4}$$

The parameters ζ_0 and ζ_r were fitted independently for each coordination number group. For Mg, CN = 6 and 7 were fitted, whereas CN = 5 was excluded due to limited, scattered data. For Si, CN = 4, 5, and 6 were retained.

Fits were performed over restricted bond-length ranges corresponding to the central distribution of each dataset (typically the 5–95% range, with additional constraints applied where necessary). For example, Mg CN = 6 fits were restricted to $r \leq 2.07$ Å, and Mg CN = 7 fits were weighted toward the higher-β population near $r \sim 2.0$ Å to represent the dominant melt coordination environment better.

This formulation removes the need for a single, fixed harmonic force constant per coordination number and instead captures both bond-length- and coordination-dependent variations in vibrational stiffness. The resulting fits, when sufficient data are available, reproduce the observed trends in β across coordination environments and are shown in Figure 6.6.

Effects of coordination number, bond length and residual forces on β

To calculate the variance explained by the ionic model (and therefore CN and bond length), we used a regression model. To evaluate structural effects not captured by bond length and coordination number, residual β-values were defined as:

$$\beta_i^{\text{residual}} = \beta_i^{\text{DFT}} - \beta_i^{\text{ionic}}(\text{CN},\ \text{bond length}) \tag{6.5}$$

where β_i^{ionic} is the predicted value from the coordination-restricted ionic fit (Eq.6.1). In this framework, the ionic model captures the first-order effect of coordination number on isotope fractionation. In contrast, the residual term captures intra-group variability. Inspection of the data shows that this residual is strongly correlated with bond length, with shorter bonds corresponding to higher *beta* values. This behaviour is consistent with theoretical expectations: shorter bonds correspond to stiffer force constants and higher vibrational frequencies, which preferentially stabilise heavier isotopes.

To quantify these relationships, we performed linear regressions of β on coordination number and average bond length for each element at all pressures. This allowed us to partition the variance in β into contributions from (i) coordination number, (ii) bond length, and (iii) unexplained residual variance. The latter term represents higher-order structural effects not captured by the first two descriptors, including angular distortions, bond-length distributions, and second-neighbour interactions.

The analysis shows that, averaged over all coordination environments and pressures, β in Si is explained to 97.75% by coordination number and bond length, with only 2.25% attributed to residual effects. For Mg, the corresponding values

are 97.5% explained by coordination number and bond length, and 2.50% residual. These results demonstrate that, under high-pressure conditions, isotope fractionation in silicate melts is overwhelmingly controlled by local structural parameters, with bond length providing the dominant contribution within coordination groups.

The relatively small magnitude of the residual term indicates that higher-order structural effects play only a minor role at high pressure. This contrasts with lower-pressure melt compositions, where greater structural variability leads to a larger contribution from such effects (De Winter et al., submitted).

Element	CN	n	β (average)	β_{ionic} (average)	Ionic (%)	Residual (%)
Mg	6	70	0.4264	0.414	97.2	2.8
Mg	7	53	0.4659	0.458	98.3	1.7
Si	4	37	0.9646	0.915	94.8	5.2
Si	5	68	0.8400	0.829	98.7	1.3
Si	6	55	0.7958	0.796	100.0	0.0

Table 6.5: Mean ionic (β_{ionic}) and residual ($\beta_{\mathrm{residual}}$) contributions to $1000 \ln \beta$ as a function of coordination number (CN) for Mg and Si. Values are averaged over all configurations within each CN; percentages indicate the relative contribution of each term to the total β, and n denotes the number of data points.

4. Additional figures/tables

Figure 6.8 compiles published estimates of $\delta^{26/24}\mathrm{Mg}_{\mathrm{DSM\text{-}3}}$ and $\delta^{30/28}\mathrm{Si}_{\mathrm{NBS28}}$ for the Moon and Earth. While reported values show some spread between studies, the overall ranges for lunar and terrestrial compositions overlap within uncertainty for both isotope systems. For this study, we adopt representative bulk compositions based on recent high-precision datasets. Specifically, we use the bulk silicate Moon (BSM) estimate of Klaver et al. (2024) and the bulk silicate Earth (BSE) estimate of X.-N. Liu et al. (2023) for Mg isotopes. For Si isotopes, we adopt the BSM value of Dauphas et al. (2015) and the BSE value of X.-N. Liu et al. (2025). These choices are consistent with the most recent and internally consistent datasets and fall within the range of previously reported values shown in Figure 6.8.

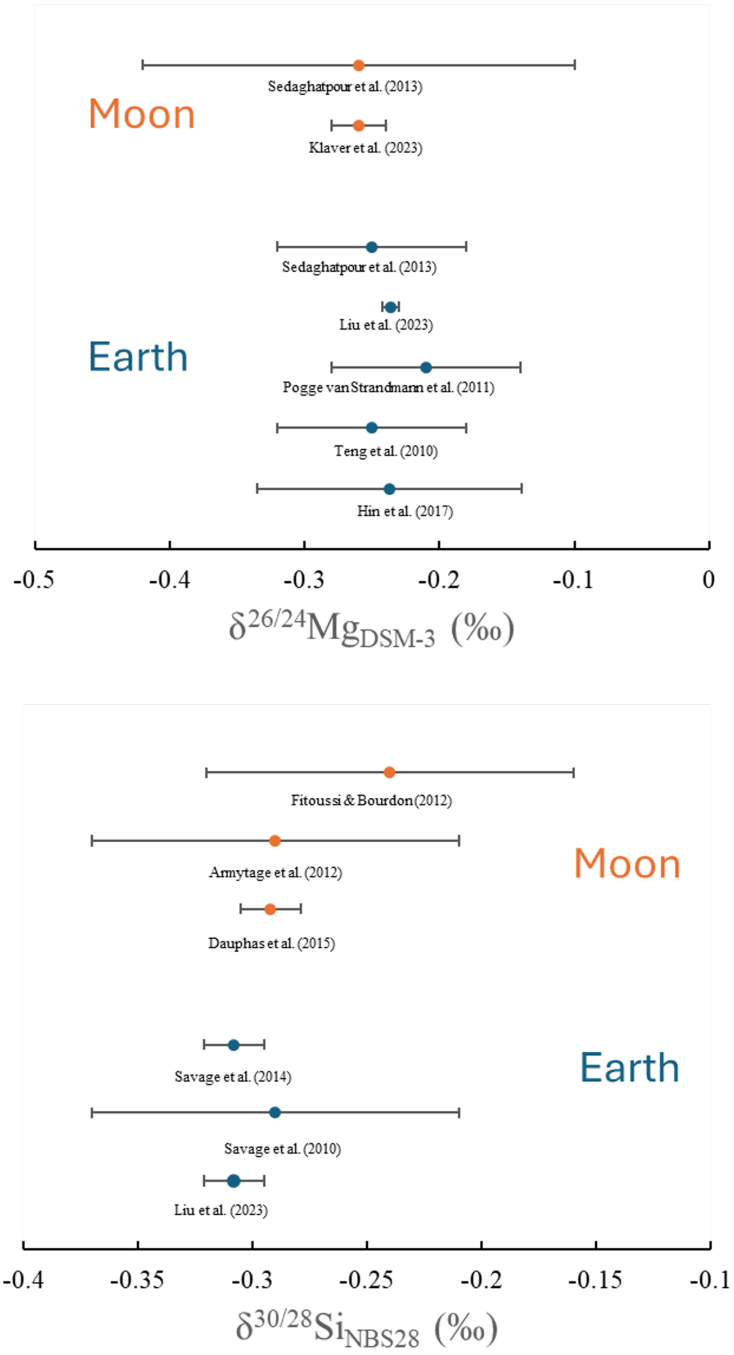


Figure 6.8: Compilation of published BSE and BSM isotope compositions for Mg and Si. Top: δ^{26}Mg (DSM3); Bottom: δ^{30}Si (NBS28). Points represent literature estimates, and horizontal bars denote reported uncertainties (1σ or as given in original studies). Earth estimates (blue) and Moon estimates (orange) are indistinguishable within uncertainty for both isotope systems, highlighting the isotopic similarity of the two bodies.

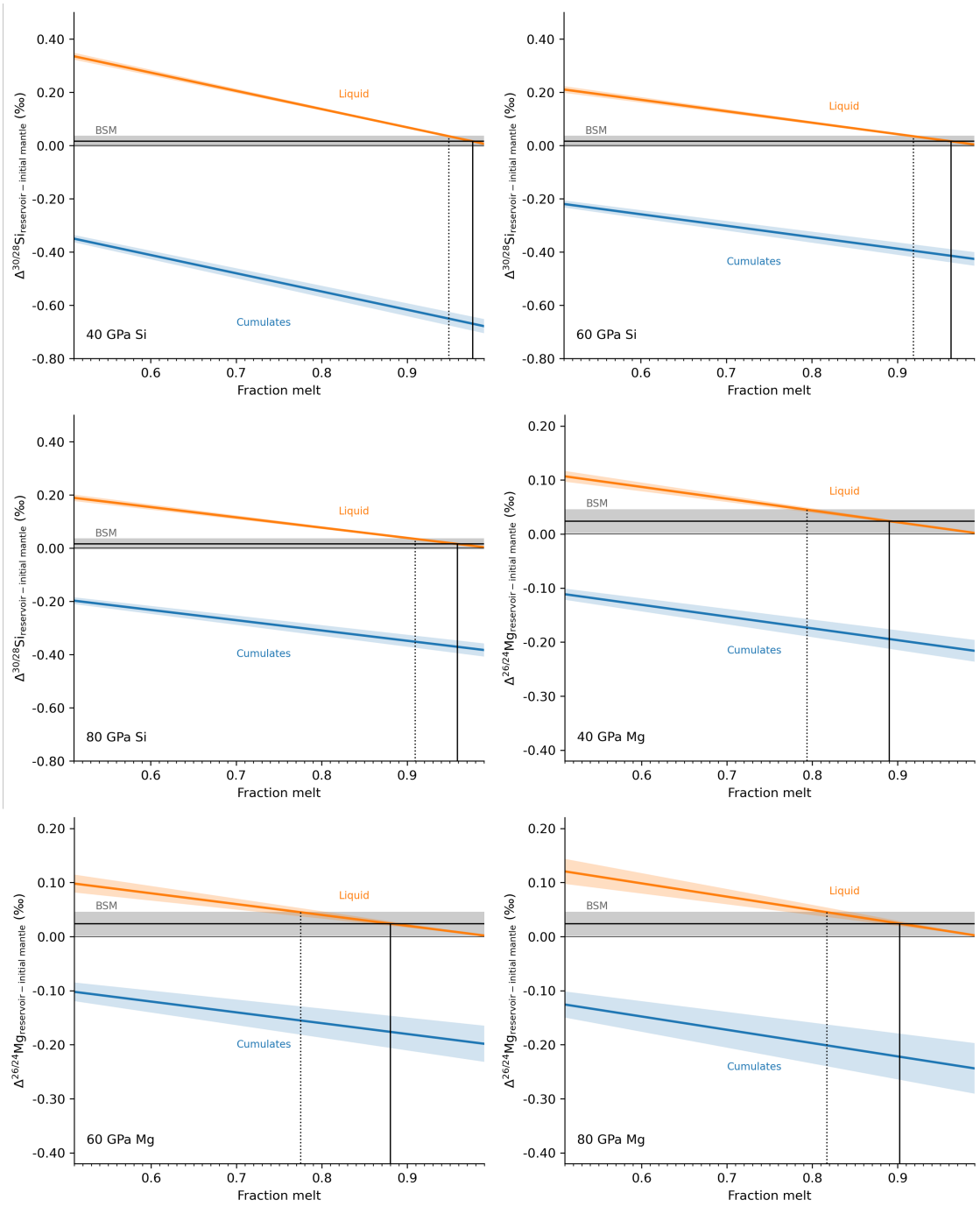


Figure 6.9: Evolution of isotopic composition during fractional crystallisation as a function of melt fraction. The top three panels show Δ^{30}Si, and the bottom three panels show Δ^{26}Mg (both reported relative to initial mantle composition, ‰). The orange curves represent the composition of the instantaneous (residual) melt, while the blue curves show the isotopic composition of the bridgmanite cumulates segregated from the melt. Shaded regions indicate model uncertainty. The grey horizontal band marks the BSM reference range.

Bibliography

Bigeleisen, J., & Mayer, M. G. (1947). Calculation of Equilibrium Constants for Isotopic Exchange Reactions. *Journal of Chemical Physics*, *15*, 261–267 ADS Bibcode: 1947JChPh..15..261B.

Clark, S. J., Segall, M. D., Pickard, C. J., Hasnip, P. J., Probert, M. I. J., Refson, K., & Payne, M. C. (2005). First principles methods using CASTEP. *Zeitschrift für Kristallographie - Crystalline Materials*, *220*(5-6), 567–570.

Dauphas, N., Poitrasson, F., Burkhardt, C., Kobayashi, H., & Kurosawa, K. (2015). Planetary and meteoritic Mg/Si and δ^{30}Si variations inherited from solar nebula chemistry. *Earth and Planetary Science Letters*, *427*, 236–248.

de Koker, N. P., Stixrude, L., & Karki, B. B. (2008). Thermodynamics, structure, dynamics, and freezing of Mg2SiO4 liquid at high pressure. *Geochimica et Cosmochimica Acta*, *72*(5), 1427–1441.

De Winter, B., Walker, A. M., Melekhova, E., & Elliott, T. (submitted). Five-fold Mg in silicate melts drives non-zero olivine-melt isotope fractionation. *Geochemical Perspectives Letters*.

De Winter, B., Walker, A. M., Melekhova, E., Liu, X.-N., & Elliott, T. (in review). The magnitude of equilibrium isotope fractionation of Mg between forsterite, diopside and melt at liquidus temperatures. *Geochimica et Cosmochimica Acta*.

Gonze, X. (1997). First-principles responses of solids to atomic displacements and homogeneous electric fields: Implementation of a conjugate-gradient algorithm. *Physical Review B*, *55*(16), 10337–10354.

Gonze, X., & Lee, C. (1997). Dynamical matrices, Born effective charges, dielectric permittivity tensors, and interatomic force constants from density-functional perturbation theory. *Physical Review B*, *55*(16), 10355–10368.

Guillot, B., & Sator, N. (2007). A computer simulation study of natural silicate melts. Part II: High pressure properties. *Geochimica et Cosmochimica Acta*, *71*(18), 4538–4556.

Hohenberg, P., & Kohn, W. (1964). Inhomogeneous electron gas. *Physical Review*, *136*(3B), B864.

Hoover, W. G. (1985). Canonical dynamics: Equilibrium phase-space distributions. *Physical Review A*, *31*(3), 1695–1697.

Huang, F., Chen, L., Wu, Z., & Wang, W. (2013). First-principles calculations of equilibrium Mg isotope fractionations between garnet, clinopyroxene, orthopyroxene, and olivine: Implications for Mg isotope thermometry. *Earth and Planetary Science Letters*, *367*, 61–70.

Huang, F., Wu, Z., Huang, S., & Wu, F. (2014). First-principles calculations of equilibrium silicon isotope fractionation among mantle minerals. *Geochimica et Cosmochimica Acta*, *140*, 509–520.

Klaver, M., Klemme, S., Liu, X.-N., Hin, R. C., Coath, C. D., Anand, M., Lissenberg, C. J., Berndt, J., & Elliott, T. (2024). Titanium-rich basaltic melts on the Moon modulated by reactive flow processes. *Nature Geoscience*, 1–6.

Kohn, W., & Sham, L. J. (1965). Self-Consistent Equations Including Exchange and Correlation Effects. *Physical Review*, *140*(4A), A1133–A1138.

Liu, X., Qi, Y., Zheng, D., Zhou, C., He, L., & Huang, F. (2018). Diffusion coefficients of Mg isotopes in MgSiO3 and Mg2SiO4 melts calculated by first-principles molecular dynamics simulations. *Geochimica et Cosmochimica Acta*, *223*, 364–376.

Liu, X.-N., Hin, R. C., Coath, C. D., Bizimis, M., Su, L., Ionov, D. A., Takazawa, E., Brooker, R., & Elliott, T. (2023). The magnesium isotopic composition of the mantle. *Geochimica et Cosmochimica Acta*, *358*, 12–26.

Liu, X.-N., Klaver, M., Hin, R. C., Coath, C. D., Bizimis, M., Ionov, D. A., & Elliott, T. (2025). Si isotope composition of Earth's mantle and oceanic basalts. *Geochimica et Cosmochimica Acta*.

Luo, H., Karki, B. B., Ghosh, D. B., & Bao, H. (2020). First-principles computation of diffusional Mg isotope fractionation in silicate melts. *Geochimica et Cosmochimica Acta*, *290*, 27–40.

McDonough, W., & Sun, S. (1995). The composition of the Earth. *Chemical Geology*, *120*(3-4), 223–253.

Nosé, S. (1984). A molecular dynamics method for simulations in the canonical ensemble. *Molecular Physics*, *52*(2), 255–268.

Parrinello, M., & Rahman, A. (1981). Polymorphic transitions in single crystals: A new molecular dynamics method. *Journal of Applied Physics*, *52*(12), 7182–7190.

Payne, M. C., Teter, M. P., Allan, D. C., Arias, T. A., & Joannopoulos, J. D. (1992). Iterative minimization techniques for ab initio total-energy calculations: Molecular dynamics and conjugate gradients. *Reviews of Modern Physics*, *64*(4), 1045–1097.

Perdew, J. P., Ruzsinszky, A., Csonka, G., Vydrov, O. A., Scuseria, G. E., Constantin, L. A., Zhou, X., & Burke, K. (2008). Restoring the Density-Gradient Expansion for Exchange in Solids and Surfaces. *Physical Review Letters*, *100*(13), 136406.

Rabin, S., Blanchard, M., Pinilla, C., Poitrasson, F., & Gregoire, M. (2021). First-principles calculation of iron and silicon isotope fractionation between Fe-bearing minerals at magmatic temperatures: The importance of second atomic neighbors. *Geochimica et Cosmochimica Acta*, *304*, 101–118.

Rabin, S., Blanchard, M., Pinilla, C., Poitrasson, F., & Grégoire, M. (2023). Iron and silicon isotope fractionation in silicate melts using first-principles molecular dynamics. *Geochimica et Cosmochimica Acta*, *343*, 212–233.

Refson, K., Tulip, P. R., & Clark, S. J. (2006). Variational density-functional perturbation theory for dielectrics and lattice dynamics. *Physical Review B*, *73*(15), 155114.

Sanloup, C., Drewitt, J. W. E., Konôpková, Z., Dalladay-Simpson, P., Morton, D. M., Rai, N., van Westrenen, W., & Morgenroth, W. (2013). Structural change in molten basalt at deep mantle conditions. *Nature*, *503*(7474), 104–107.

Schauble, E. A. (2011). First-principles estimates of equilibrium magnesium isotope fractionation in silicate, oxide, carbonate and hexaaquamagnesium(2+) crystals. *Geochimica et Cosmochimica Acta*, *75*(3), 844–869.

Solomatova, N., & Caracas, R. (2019). Pressure-Induced Coordination Changes in a Pyrolitic Silicate Melt From Ab Initio Molecular Dynamics Simulations. *Journal of Geophysical Research: Solid Earth*, *124*(11), 11232–11250.

Stixrude, L., de Koker, N., Sun, N., Mookherjee, M., & Karki, B. B. (2009). Thermodynamics of silicate liquids in the deep Earth. *Earth and Planetary Science Letters*, *278*(3), 226–232.

Troullier, N., & Martins, J. L. (1991). Efficient pseudopotentials for plane-wave calculations. *Physical Review B*, *43*(3), 1993–2006.

Walker, A. M., Hin, R. C., & Elliott, T. (2026). Controls on Mg isotopic fractionation between deep mantle phases and relict signatures of a terrestrial magma ocean. *Geochimica et Cosmochimica Acta*, *425*, 131–142.

Wan, J. T. K., Duffy, T. S., Scandolo, S., & Car, R. (2007). First-principles study of density, viscosity, and diffusion coefficients of liquid MgSiO3 at conditions of the Earth's deep mantle. *Journal of Geophysical Research: Solid Earth*, *112*(B3).

Wang, W.-Y., Kang, J.-T., & Huang, F. (2023). How precise and how accurate can magnesium isotope analysis be by the sample-standard bracketing method? *International Journal of Mass Spectrometry*, *491*, 117102.

Young, E. D., Manning, C. E., Schauble, E. A., Shahar, A., Macris, C. A., Lazar, C., & Jordan, M. (2015). High-temperature equilibrium isotope fractionation of non-traditional stable isotopes: Experiments, theory, and applications. *Chemical Geology*, *395*, 176–195.

"Somewhere, something incredible is waiting to be known."

— Carl Sagan

7 Conclusions and Outlook

7.1 Conclusions

The purpose of this thesis was to better understand the processes controlling Mg and Si isotope fractionation during magmatic differentiation and planetary evolution, with particular importance to magma ocean crystallisation and the preservation of primordial mantle heterogeneity. A combined approach of high-temperature experiments, molecular dynamics simulations, and first-principles calculations was developed to resolve both the magnitude of equilibrium isotope fractionation and the fundamental controls governing the isotope fractionation of Mg and Si. This method was used to quantify whether early-formed bridgmanite-rich cumulate reservoirs can be preserved in the present-day mantle.

In Chapter 3, the equilibrium Mg isotope fractionation between minerals and melt at high temperature was studied with a combined experimental and computational approach. Near-liquidus synthesis experiments were performed in the CMAS system, showing that mineral–melt fractionation at high temperatures is small yet measurable. $\Delta^{26}\mathrm{Mg}_{\text{ol-melt}} = -0.058 \pm 0.032\,‰$ and $\Delta^{26}\mathrm{Mg}_{\text{cpx-melt}} = 0.060 \pm 0.034\,‰$, corresponding to $\Delta^{26}\mathrm{Mg}_{\text{cpx-ol}} = 0.118 \pm 0.045\,‰$. These values confirm that equilibrium fractionation can persist at magmatic temperatures and are of a similar order as isotopic variability observed in natural mantle-derived samples

(Liu et al., 2023, 2026). Comparison with DFT calculations shows that accurate reproduction of these fractionation factors can be achieved with a combination of the PBESOL functional, explicit treatment of thermal expansion, and site averaging for forsterite. These findings show that DFT methods can reliably predict equilibrium isotope fractionation, provided the structural and thermodynamic parameters are appropriately selected. This chapter establishes a quantitative basis for interpreting Mg isotope signatures in high-temperature magmatic processes.

In Chapter 4, molecular dynamics simulations coupled with DFT calculations were used to examine in greater detail how structural factors influence isotope fractionation in silicate melt. This marks an important advance, as the isotopic behaviour of Mg had not been directly computed from atomistic melt structures before, and such a detailed analysis based on single-site calculations had not been conducted for Si. Silicate melts are complex and disordered and therefore require a statistical description of local atomic environments and their respective vibrational properties. The results show that basaltic melts exhibit a heterogeneous distribution of coordination environments, with Mg in five- and six-fold coordination states, at 53% and 47%, respectively, at 1 atm. In contrast, Mg in crystalline phases such as olivine and clinopyroxene is exclusively six-fold coordinated. This coordination contrast leads to systematic differences in β-values, with five-fold coordinated Mg sites showing higher β-values than six-fold coordinated sites, even where bond lengths are comparable. When averaged across the melt structure, the bulk β_{melt} value is higher than that of the minerals, yielding a non-zero equilibrium $\Delta^{26}\mathrm{Mg}_{\mathrm{ol\text{-}melt}}$ observed in both experimental and natural datasets. Further analysis shows that the Mg–O bond length exerts the dominant control on isotope fractionation, with coordination number acting as a secondary parameter. At the same time, polyhedral distortion contributes to second-order differences in β-values. In contrast, silicon exhibits less variation in coordination environments compared to minerals, where β-values are dominated by bond length variation. Consequently, Si isotope fractionation shows minimal mineral–melt fractionation at near-liquidus temperatures. These differences highlight that isotope fractionation is inherently connected to the variety of local

environments in silicate melt. Crucially, the study indicates that coordination state and bond length directly affect isotope fractionation, with potentially greater fractionations occurring during magmatic processes where larger differences in coordination number, caused by pressure, are observed.

In Chapter 4, this computational approach has been extended to lower-mantle conditions to quantify Mg and Si isotope ratios during magma-ocean crystallisation and to constrain the volume of primordial mantle reservoirs in the present-day mantle. DFT calculations show that equilibrium fractionation between bridgmanite and silicate melt remains large and measurable at pressures of 40–80 GPa and temperatures up to 4000 K, with values such as $\Delta^{26}\mathrm{Mg}_{\mathrm{bdm\text{-}melt}} = -0.1704 \pm 0.021\,‰$ and $\Delta^{30}\mathrm{Si}_{\mathrm{bdm\text{-}melt}} = -0.3662 \pm 0.031\,‰$ at 60 GPa. These values are substantially larger than mineral–melt values observed at ambient pressure and reflect the increased structural contrast between crystalline bridgmanite and high-pressure silicate melt. The pressure-driven increases in coordination number and bond compression in melt, compared to the more rigid structure of bridgmanite, maintain large differences in vibrational properties even at extremely high temperatures. This shows that pressure effects offset the expected reduction in isotope fractionation with increasing temperature, ensuring that isotopic differences are generated during all phases of Earth's magma ocean crystallisation.

These fractionation factors were incorporated into crystallisation models, which show that magma-ocean cooling and subsequent crystallisation produce substantial isotopic differences between coexisting reservoirs: bridgmanite cumulates and residual melt. In the initial crystallisation stages, residual melt tends to develop heavier compositions, reaching around $+0.1\,‰$ for Mg and $+0.25\,‰$ for Si relative to initial mantle values. Meanwhile, bridgmanite-rich cumulates become isotopically lighter, with Mg and Si values dropping to $-0.25\,‰$ and $-0.5\,‰$, respectively, relative to the original mantle. These results suggest that equilibrium fractionation alone is sufficient to generate substantial isotopic heterogeneity in a crystallising magma ocean.

However, comparison with the observed similarity between Bulk Silicate Earth and Bulk Silicate Moon indicates that such heterogeneity is not preserved at large scales in the present-day mantle. The results show that no more than 4.1 ± 4.7 wt% (0-8.8 wt% within uncertainties) of bridgmanite-rich material can be retained without producing isotopic differences larger than observed. This constraint implies that large-scale primordial reservoirs, such as BEAMS (Ballmer et al., 2017), have been homogenised by mantle convection if they were ever stable in the mantle. At the same time, it allows the possibility that small, isolated remnants of primordial material may still exist, though volumetrically minor and inefficiently sampled by mantle melting processes.

In summary, this work provides evidence that equilibrium isotope fractionation is not negligible at high temperatures and is controlled by atomic-scale structural differences between the phases involved. Stable isotopes of major elements such as Mg and Si thus provide a quantitative constraint on the scale of primordial heterogeneity in Earth's mantle. Ultimately, the results demonstrate that Earth's isotopic composition is rooted in the structure of silicate melt and minerals, and that while early differentiation processes generate significant isotopic contrasts, their signatures are largely erased or diluted during subsequent mantle evolution.

7.2 Future Work

The results presented in this work aim to use stable-isotope studies to resolve small equilibrium fractionation in simplified systems and to provide insights within a broader planetary context. However, extending this approach to address the complexity of planetary differentiation fully requires integration across chemical compositions, temperatures, and 3D geodynamic models. The following research directions are partly based on a series of postdoctoral research proposals developed during this PhD, which collectively outline a future research direction aimed at advancing isotope geochemistry into a predictive tool for planetary evolution.

Integrating atomistic isotope systematics into predictive geodynamical models

A central challenge identified in this thesis is the limited scalability of DFT calculations. While DFT and MD simulations provide precise constraints on isotope fractionation, their computational cost restricts the usage of a full pressure–temperature–composition space relevant to planetary interiors and geodynamical models (Boukaré et al., 2025; Caracas et al., 2019; Gülcher et al., 2021). The results in this thesis show that, within the studied compositions and limitations, isotope fractionation can largely be described using a limited number of parameters: bond length and coordination number explain ca. 95% of the variance in β-values in high-pressure systems.

Building on this, future work could focus on developing data-driven predictive models that combine DFT-derived datasets with machine learning techniques in a multidimensional parameter space during the crystallisation of a magma ocean. Such models would allow isotope fractionation to be predicted for all pressure–temperature–composition conditions in Earth's magma ocean. A key application is the integration of mantle convection and magma ocean crystallisation into geodynamical models, such as those developed by Boukaré et al. (2025). Embedding structure-based fractionation laws into these models would enable isotope tracking and assessment of isotopic values of different reservoirs within Earth's mantle.

The models developed in this work were intentionally based on simplified iron-free systems. However, natural mantle materials exhibit much greater compositional complexity, including variable Fe concentrations, redox conditions, and the presence of additional phases, such as lower mantle ferropericlase and davemaoite. Physicochemical conditions (e.g., temperature, pressure, and melt composition) influence melt structure and coordination, and therefore isotope fractionation. In addition, the presence of other solid phases must be considered, as these will affect isotope partitioning between solids and the residual melt. Future work should extend MD–DFT simulations to include Fe-bearing melt and minerals, as iron is likely to influence coordination states and bonding environments in both phases.

As shown by Rabin et al. (2023), compositional effects may alter fractionation factors by 0.05–0.15 ‰ in silicate melt, while in minerals a smaller effect is expected (Chapter 3). In addition, other high-pressure phases such as davemoite and post-perovskite should be considered.

Metal–silicate isotope fractionation and core formation

While this study focused primarily on silicate melt and minerals, a major unresolved question in planetary science concerns the role of metal-silicate isotope fractionation and light-element partitioning during core formation. The isotopic composition of Bulk Silicate Earth for Si is offset by 0.35 ‰ from enstatite chondrites (Onyett et al., 2023). It is commonly attributed to isotope fractionation between the metal and silicate phases during the incorporation of Si as a light element into metal phases. However, the magnitude and pressure dependence of metal–silicate fractionation remain poorly constrained, as existing experiments are limited to pressures below 7 GPa.

Future research should therefore focus on combining a similar experimental-computational approach to constrain isotope fractionation under core-formation conditions. MD simulations could be run on the liquid metal phase rather than on the β-values of the silicate melt calculated in this thesis.

If a better constraint for metal–silicate fractionation is known, the constraint could be used to model the difference between BSE and enstatite chondrites in multiparameter space between magmatic differentiation and primordial reservoirs (this thesis), core formation and volatile loss (Hin et al., 2017). An earlier attempt was made, but it is not shown in this thesis. The model was hindered by large uncertainties in metal–silicate isotope fractionation factors. Despite this, calculations suggested possible combinations in which a small amount of Si (wt%) in the core, with moderate amounts of volatile loss and active components of a Basal Magma Ocean, could explain both Mg and Si isotope differences between BSE and enstatite chondrites. This model needs to be developed in

more detail, with reduced uncertainties in input parameters such as $\Delta^{30}Si_{metal\text{-}silicate}$ and $\Delta^{30}Si_{vapour\text{-}melt}/\Delta^{26}Mg_{vapour\text{-}melt}$ values.

Thanks to Jon Wade (Oxford), James Bryson (Oxford), and Anat Shahar (Carnegie) for their feedback and brainstorming on this research proposal.

Experimental constraints on planetary differentiation: the Moon as test case

An important extension of this work is the application of isotope fractionation approaches to other planetary bodies, in particular the Moon. The near-identical Mg and Si isotope compositions of Earth and the Moon (see Chapter 5) are often interpreted as evidence of efficient equilibrium during the Moon-forming event. However, this interpretation relies on the assumption that isotope fractionation during the early stages of magma ocean crystallisation, when olivine and pyroxene crystallise and segregate, is negligible.

We show in this study that both $\Delta^{26}Mg_{ol\text{-}melt}$ and $\Delta^{26}Mg_{cpx\text{-}melt}$ are non-zero and should be accounted for in crystallisation models. The remaining fractionation factor to consider is $\Delta^{26}Mg_{opx\text{-}melt}$, which has not been measured experimentally. A study could aim to test this assumption by experimentally determining orthopyroxene–melt Mg and Si isotope fractionations.

These experiments would focus on reproducing crystallisation pathways from the onset of the magma ocean through to the formation of lunar samples, including high- and low-Ti basalts, allowing direct comparison with lunar samples. By quantifying all the mineral–melt isotopic fractionation factors, this work would provide constraints on the evolution of the lunar mantle and assess whether subtle isotopic differences between Earth and Moon should be considered.

Thanks to Helen Williams (Cambridge) and Corliss I Sio (Toronto) for their feedback and brainstorming during this proposal.

Bibliography

Ballmer, M. D., Houser, C., Hernlund, J. W., Wentzcovitch, R. M., & Hirose, K. (2017). Persistence of strong silica-enriched domains in the Earth's lower mantle. *Nature Geoscience*, *10*(3), 236–240.

Boukaré, C.-É., Badro, J., & Samuel, H. (2025). Solidification of Earth's mantle led inevitably to a basal magma ocean. *Nature*, 1–6.

Caracas, R., Hirose, K., Nomura, R., & Ballmer, M. D. (2019). Melt–crystal density crossover in a deep magma ocean. *Earth and Planetary Science Letters*, *516*, 202–211.

Gülcher, A. J. P., Ballmer, M. D., & Tackley, P. J. (2021). Coupled dynamics and evolution of primordial and recycled heterogeneity in Earth's lower mantle. *Solid Earth*, *12*(9), 2087–2107.

Hin, R. C., Coath, C. D., Carter, P. J., Nimmo, F., Lai, Y. J., Pogge von Strandmann, P. A., Willbold, M., Leinhardt, Z. M., Walter, M. J., & Elliott, T. (2017). Magnesium isotope evidence that accretional vapour loss shapes planetary compositions. *Nature*, *549*(7673), 511–527.

Liu, X.-N., Hin, R. C., Coath, C. D., Bizimis, M., Su, L., Ionov, D. A., Takazawa, E., Brooker, R., & Elliott, T. (2023). The magnesium isotopic composition of the mantle. *Geochimica et Cosmochimica Acta*, *358*, 12–26.

Liu, X.-N., Hin, R. C., Coath, C. D., Onyett, I., Rogers, B., Lewis, J., & Elliott, T. (2026). Magnesium isotope heterogeneity in oceanic island basalts. *Earth and Planetary Science Letters*, *684*, 120010.

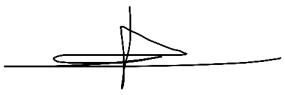
Onyett, I. J., Schiller, M., Makhatadze, G. V., Deng, Z., Johansen, A., & Bizzarro, M. (2023). Silicon isotope constraints on terrestrial planet accretion. *Nature*, *619*(7970), 539–544.

Rabin, S., Blanchard, M., Pinilla, C., Poitrasson, F., & Grégoire, M. (2023). Iron and silicon isotope fractionation in silicate melts using first-principles molecular dynamics. *Geochimica et Cosmochimica Acta*, *343*, 212–233.

Statement of Authorship for joint/multi-authored papers for PGR thesis

Title of Paper	The magnitude of equilibrium isotope fractionation of Mg between forsterite, diopside and melt at liquidus temperatures.
Publication Status	Submitted for Publication
Publication Details	Submitted to GCA, rejected and due for resubmission. Preprint available on https://eartharxiv.org/

Student Confirmation

Student Name:	Bram de Winter		
Contribution to the Paper	In this paper, I designed and conducted the experiments, performed DFT calculations and additional models, and wrote the initial manuscript. After the co-author review, I revised the manuscript accordingly. The paper was submitted to Geochemica et Cosmochemica Acta but was rejected due to a typo in the supplementary material. The feedback from this submission has been integrated into the chapter and manuscript included in the thesis. The revised manuscript is planned for submission to GCA following the thesis submission.		
Signature 		Date	11-04-2026

Supervisor Confirmation

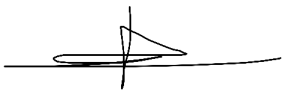
By signing the Statement of Authorship, you are certifying that the candidate made a substantial contribution to the publication, and that the description described above is accurate.

Supervisor name and title: Dr. Andrew Walker		
Supervisor comments This work was undertaken by, and the manuscript was written by, Bram. After lengthy review, GCA rejected the first submission because of a mismatch between the supplementary material and the main text (digits mixed up in a number) and because of questions around equilibration of the experimental samples but the editor seems supportive of resubmission.		
Signature 	Date	13/4/2026

Statement of Authorship for joint/multi-authored papers for PGR thesis

Title of Paper	Variable coordination number controlling equilibrium isotope fractionation between minerals and melt
Publication Status	Unpublished and unsubmitted work written in a manuscript style
Publication Details	Manuscript expected to be submitted in weeks after thesis submission date to Geochemical Perspective Letters (GPL)

Student Confirmation

Student Name:	Bram de Winter		
Contribution to the Paper	In this paper, I performed molecular dynamics simulations and site-specific DFT calculations to determine isotope fractionation factors in silicate melts. I was responsible for analysing the structural data, including coordination environments and bond-length distributions, and for developing the framework linking melt structure to isotope fractionation. I wrote the initial manuscript, including the interpretation of results and development of the conceptual model. Following co-authors' feedback, I revised the manuscript and added additional analysis to clarify the roles of coordination number and melt heterogeneity. The manuscript is currently in preparation for submission.		
Signature 		Date	11-04-2026

Supervisor Confirmation

By signing the Statement of Authorship, you are certifying that the candidate made a substantial contribution to the publication, and that the description described above is accurate.

Supervisor name and title: Dr. Andrew Walker		
Supervisor comments After discussion of the methodology, Bram undertook the calculations described in this manuscript. The manuscript was written by Bram and has been revised following several rounds of feedback.		
Signature 	Date	13/4/2026

Statement of Authorship for joint/multi-authored papers for PGR thesis

Title of Paper	Mg–Si isotopes tightly constrain the primordial bridgmanite reservoir in the present-day Earth's mantle
Publication Status	Unpublished and unsubmitted work written in a manuscript style
Publication Details	Manuscript expected to be submitted in next month after thesis submission date to Earth and Planetary Science Letters (EPSL)

Student Confirmation

Student Name:	Bram de Winter		
Contribution to the Paper	In this paper, I carried out molecular dynamics simulations and DFT calculations to determine equilibrium Mg and Si isotope fractionation under lower-mantle conditions. I implemented isotope fractionation modelling and performed mass-balance calculations to constrain the volumes of primordial bridgmanite-rich reservoirs in the present-day mantle. I led the interpretation of the results in the context of magma ocean crystallisation and mantle evolution. I wrote the initial manuscript and revised it following co-author input, including integrating geodynamic and geochemical implications. The manuscript is currently in preparation for submission.		
Signature 		Date	11-04-2026

Supervisor Confirmation

By signing the Statement of Authorship, you are certifying that the candidate made a substantial contribution to the publication, and that the description described above is accurate.

Supervisor name and title: Dr. Andrew Walker		
Supervisor comments After discussion of the methodology, Bram undertook the calculations described in this manuscript. The manuscript was written by Bram and has been revised following a single round of feedback.		
Signature 	Date	13/4/2026